UNIVERSITY OF OKLAHOMA

GRADUATE COLLEGE

MULTIPHYSICS ANALYSIS OF HIGH DIFFERENTIAL PRESSURE ELECTROZIPPER PERISTALTIC MICROPUMP

A DISSERTATION

SUBMITTED TO THE GRADUATE FACULTY

in partial fulfillment of the requirements for the

Degree of

DOCTOR OF PHILOSOPHY

By

CARLOS BORRAS PINILLA
Norman, Oklahoma
2012

MULTIPHYSICS ANALYSIS OF HIGH DIFFERENTIAL PRESSURE ELECTROZIPPER PERISTALTIC MICROPUMP

A DISSERTATION APPROVED FOR THE SCHOOL OF AEROSPACE AND MECHANICAL ENGINEERING

BY

_____
Dr. HAROLD L. STALFORD, Chair

_____
Dr. KUANG-HUA CHANG

_____
Dr. RONG Z. GAN

_____
Dr. FENG C. LAI

_____
Dr. JOHN P. ALBERT

ACKNOWLEDGEMENTS

I would like to thank my advisor, Dr. Harold Stalford, for his support and encouragements throughout my dissertation research. I have really enjoyed working with all of other student during the time I stayed in Norman, learning and sharing knowledge with them, and my good friends in the AME shop, Billy Mays and Greg Williams and the AME professors and staff. I could not have done this without support and sacrifice of my family and so many good friends and the loved ones.

TABLE OF CONTENTS

LIST OF FIGURES.

LIST OF TABLES

ABSTRACT

The problem investigated in this dissertation is that of designing and developing a micropump for on-chip applications that have requirements for simultaneous high differential pressures and high flow rates, particularly for gas flow applications. In the literature, there are designs that provide high differential pressures at low flow rates and there are designs that provide for high flow rates at low differential pressures. Developing on-chip design solutions for both simultaneously is currently a wide open research area. It is a challenging research area in nanotechnology and microelectromechanical systems (MEMS) to develop on-chip micropump solutions that provide for simultaneous high differential pressures and high flow rates. The research in this dissertation considered this interesting and challenging research problem and focused its thesis on developing such performance requirementsfor peristaltic micropumps using the so-called “electrozipper” mechanism approach. The electrozipper mechanism uses electrostatic forces to bring two surfaces together for pumping fluids by zippering them together by starting at one end and finishing up at the far end, not dissimilar from the result of squeezing out toothpaste from a tube by rolling the tube up. The main pursuit of the research in this dissertation is to derive designs that yield high differential pressures and high flow rates simultaneously, particularly, differential pressures greater than 1 atm (one atmospheric pressure) with flow rates in the range 1-1000 SCCM (cubic centimeters per minute at standard atmospheric conditions).

A critical parameter that limits the performance of electrozipper-based mechanisms is the voltage dielectric breakdown factor of the semiconductor dielectric material used to insulate the voltage potential differences between the two electrozippering surfaces. Silicon dioxide (SiO_2) is selected as the dielectric material that has a voltage dielectric breakdown factor greater than 1 volt per nanometer (nm). All micropump designs of this dissertation are limited to 1 volt per nanometer to stay below the voltage dielectric breakdown factor of Silicon dioxide. The baseline value for the dielectric thickness is taken to be 200 nm. As a result, the applied voltage is limited to a maximum of 200 volts.

Baseline design parameters of the micropump chamber geometry include micropump plate radius = 1 mm and chamber height = 20 microns. Micropump plate thicknesses of 2, 4, 6, 8, and 10 microns are considered throughout the investigation. Extensive multiphysics 2D simulations are performed on the baseline configuration for intake and outlet power strokes. One of the contributions of the research work is the development of simulation models for simulating the multiphysics interactions of electrostatics, structures, fluid flow, and moving boundaries of the micropump. Another contribution is the derivation of analytical models for the intake and outlet power strokes. The results from the multiphysics simulations and that from the analytical models are shown to agree within a few per cent for all cases treated.

Another contribution is that of considering preloaded tension (i.e., preloaded residual stresses) in the micropump plate as an additional baseline design parameter and

showing that micropump performance (i.e., higher differential pressures and flow rates) is significantly improved under such preloaded conditions. It is shown that preloaded tension in the plate can be used as stored energy to balance out the applied voltage requirements of the intake and power strokes and thereby increase micropump performance and reduce power requirements. With the employment of preloaded residual stress, differential pumping pressures greater than 1.5 atm are shown to be achievable for a 10 micron plate thickness and, for such cases, it is shown that fatigue safety limits are satisfied for multimillions life-cycles.

The new vacuum micropump concept is proposed for the sensor industry to handle large differential pressures (1 atm) at the outlet and achieving very low absolute pressures at the inlet reservoir. The baseline design is shown to provide 10^{-3}Torr vacuum pressures in the presence of leak back rates for plate surface roughness height factors in the range from 1-10 nm. And, it is shown that high vacuum pressures (e.g., 10^{-6} to 10^{-9}Torr) are achievable by cascading two such micropumps. A detailed method is provided to study different design alternatives for vacuum micropump applications.

Non-dimensional ratios in the analytical equations are used to extrapolate the performance of designs beyond that of the baseline configuration and tailor designs for particular differential pressure/flow rate performances and size requirements. This design approach saves the enormous computational time required by multiphysics simulations. Two designs applications are considered to meet high flow rates with

high differential pressures. One is pumping down a 1 Torr inlet reservoir to a 1 atm outlet reservoir and the second application considered is that of pumping a 1 atm inlet reservoir to a 2 atm outlet reservoir. Designs with flow rates in the range 1-1000 SCCM are shown to be achievable

CHAPTER 1

MULTIPHYSICS DYNAMIC ANALYSIS OF MICRO-PUMP

INTRODUCTION

1.1 Introduction to Micropumps.

Stimulated by the need for an implantable insulin pump for diabetic patients, the first micropump was fabricated about three decades ago. Smits developed the principle of a peristaltic piezoelectric fluid pump in the early 1980s at Stanford University and was granted a patent in the Netherlands in 1985. Smits and his students continued with that direction of research at the University of Twente (e.g., 1988 H.T.G. van Lintel, F.C. M. van de Pol, and S. Bouwstra) for developing a micropump based on micromachining of silicon and thin-film techniques. In 1989, Smits reported on a piezoelectric micropump with microvalves with water flow rates up to 3 microliters per minute at pressures of 0.8 psi.

Hundreds of micropump designs and concepts have been reported on in the past several decades. The various mechanisms used in developing micropump devices include shape memory alloy, thermopneumatic, ultrasonic, electromagnetic, electrokinetic, piezoelectric, electroosmotic, electrostatic, electrochemical, and electrohydrodynamic. Currently, there are needs in the micro-chemlab field of chemical detectors to design a monolithically integrated low-power micropumps that can be able to pump air or fluid with a flow rate around 1 milliliters per minute at a differential pressure higher than 1 psi. New areas of research for chemical and biological analysis

require reliable designs of micropump for micro lab on a Chip [Paul C. H. Li, 2006]. Micropumps are desired that can achieve high flow rates at higher differential pressures keeping small sizes to fit within chip area of 13 mm by 13 mm. In this work, the electrostatic mechanism is considered in developing micropump designs for meeting the performance requirements in the microchemlab field since the electrostatic mechanism has relatively good power density and it has low power dissipation effects. Electrostatic actuation has proved to be very reliable and it has very simple mechanics.

Currently, the major focus of micropump research concentrated on fabrication issues and proof-of-concept ideas. It has neglected to a large extent the computational modeling of the coupling multiphysics of micro-fluidics systems. We plan to consider analysis and computational modeling based on the equations of motion of a coupled microfluidics system, covering the multiphysics interactions of mechanics, solid mechanics, and electrostatics.

Microfluidics has experienced exponential growth in the past decade to assist in forming the now well established MEMS area (Nguyen and Wereley, 2002; Francis et al., 2002; Gad-El-Hak, 1999). The Microfluidics term is defined as "A new research discipline dealing with transport phenomena and fluid–based devices at microscopic length scale" (Nguyen and Wereley, 2002).

In the miniaturization of systems, microfluidics is an important research area of development, yielding new applications and dealing with multiphysics effects that could

be neglected in the macro fluidics world. Examples of such multiphysics effects are: electrokinetic, acoustic streaming, magneto hydrodynamic, and electrochemical effects (Nguyen 2002; Gad-El-Hak, 1999; Gravesen et al., 1993).

At the present time, researchers have the challenge to design and built a complete microfluidic Lab system together with other applications that include a micro Lab for DNA analysis, Micro mixers, separators, drug delivery systems, protein analysis, and chromatography analysis.

Even though a large number of publications dealing with micropump research can be found in the literature, very few designs have been successful in terms of function ability, reliability, efficiency, and useful fluid power output as well as less complicated fabrication procedure.

Even though there are many publications and excellent review papers (e.g., Gravesen et al., 1993; Nguyen 2002; Shoji and Esahi 1994; Ho and Tai, 1996), microfluidics is increasing as a rich open area of research. There are many issues to be addressed and problems to be solved that are commonly related such as improving the overall efficiency of the micropump, optimizing the design of the actuator, and better understanding and modeling of the multi-physics of micropump systems. Unlike that of the macropump, the multiphysics interactions of fluid, structural and electrical coupling cannot be neglected in the analysis in the micro domain.

We propose to develop a new micropump device that possesses design simplicity. It is well suitable for fabrication with standards procedure in the IC industry. Unlike other designs it will use a flat plate like diaphragm for the pump chamber and valves, which is easy to fabricated compare with the generalized curved electrodes of other designs (e.g., Cabuz, 2001; Najafi, 2003).

For the purpose of developing optimal operation of a flat membrane, we develop the novel idea of using switching sequence of electrostatics-based curved actuator type for the intake stroke to generate the opening volumes and another electrostatics-based actuator type for the pressure stroke to generate differential pressures. Opening and closing of the micropump are based on electrostatic forces. And they used the electro-zipper concept.

An actuator concept that use a curved and a flat electrode based on the parallel plate approach is designed to generate the volumes in the intake stroke. This new electrostatics-based actuator can be monolithically integrated with microfluidic systems.

We employ the "electrozipper" actuator to generate differential pressures during the pressure stroke as well as opening the membrane during the intake stroke. We show using rough calculations that our novel approach can meet the performance needs of microchemlabs (i.e., gas chromatography analyzer in a chip). We propose to use computationally multiphysics and to establish better understanding of the dynamic behavior and performance of our novel design.

1.2 Literature Review

Micropumps and microvalves are one of main components in any microfluidic system. Micropumps require input power to transfer energy to fluid. As a result, it will generate flow and pressure as useful output power. The literature survey on micropumps shows that micropumps are usually classified in two basic categories: mechanical pumps and non-mechanical pumps (Francis et al., 2002; Nguyen 2002). The mechanical pump involves some moving part during the energy transfer and the literature describes three different kinds of mechanical micropumps that have been developed. These are; peristaltic, reciprocating and rotary pumps.

The peristaltic pumps use either piezoelectric actuation or thermopneumatic actuation to force fluid flow by waves of mechanical contraction. The control of peristaltic pumps are involved and their structures are complicated in design, (Francis et al., 2002; Berg 2003). Currently, peristaltic micropumps develop large flows due to the large deformation of the flexible membrane material, but usually low pressures.

Reciprocating pumps (e.g., valve-less pumps) deliver flow using flexible diaphragms or diffuser/nozzle types driven by an actuator (e.g., pneumatics, electrostatic, piezoelectric and thermo-pneumatic). Three of the biggest shortcomings associated with valve-less pumps are leakage (i.e., back flow), difficulty in priming, and susceptibility to cavitations, (Francis et al 2002). Reciprocating pumps have a considerably advantage respect to the other two kind of pumps in terms of function ability and simple concept with a few moving parts. However the main advantage of this kind of pump is that it uses the large surface ratio of the structure to transfer energy.

Reciprocating pump can be fabricated with different MEMS technology like surface micromachining (Lithography), and LIGA (X-ray lithography, electrodeposition, and molding). Many papers have been published using this concept, (Francis, et al., 2002; Nguyen, 2002).

A few rotary positive displacement pumps have been fabricated using LIGA technology (Andrew 1997; Dopper 1997). These require assembly utilizing mechanical jigs. The microgear pump design by (Dopper 1997) has been designed for dosing of viscous fluids and its dimensions are more in the centimeter range (miniaturize size), reducing the effect of the very large viscous drag force at the microscopy size. The main drawback is that this kind of pump requires a large energy input to overcome the viscous force on the fluid at small scale and because of several internal moving parts with small separation between them the dissipative force are large especially if the dimensions are getting smaller. Not a single successful rotary pump is reported on at the micron scale due to the viscous forces of the fluid at the micro level.

Fig. 1.0, which is taken from (Francis, et al., 2002), shows that the pumping principle of "Reciprocating Displacement" has received the greatest amount of micropump development over the period 1989-2002. Among various working principles, the most promising principle approach is the diaphragm reciprocal actuation (Ritcher, et al., 1998). The rotary positive displacement principle has received the least amount of research work because of its high power input requirement to overcome the high fluidic impedance (Nguyen et al., 2002) at micro scale.

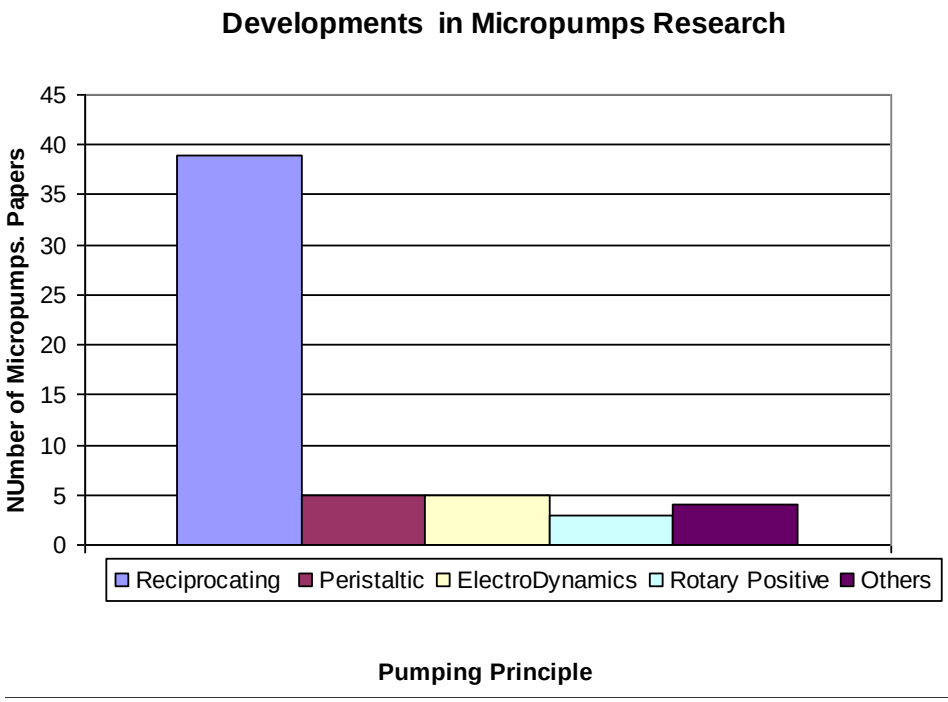

Fig. 1.0. Micropump Developments Based on Pumping Principle, (Francis, et al., 2002)

There is also a significant interest in Micro-fluid actuators/motors that extract energy from pressurized, flowing fluids and supply force and mechanical power as output. However, rotary type micro-fluid actuators/motors fabricated using surface micro-machining technology (i.e., 100-1500 microns height scale) have been the least developed. One micro-actuator with rotary micro-gears fabricated using LIGA (X-ray lithography, electrodeposition, and molding) technique has been developed, (Dooper 1997). A gear micro motor using surface micro machined techniques from Berkeley sensor and actuator center was developed (Leslie, 1991). Both works, without providing detailed performance analysis, demonstrated that micro-fluid device can be used as sensors for micro-flow in an ambient that contains substance harmful to electronics, explosive or flammable environments or in medical or biological applications (e.g.,

micro-mixing and drug delivery). These devices work as hydraulic motors (see Fig. 1.1) and the transfer energy from the fluid to the mechanical output energy.

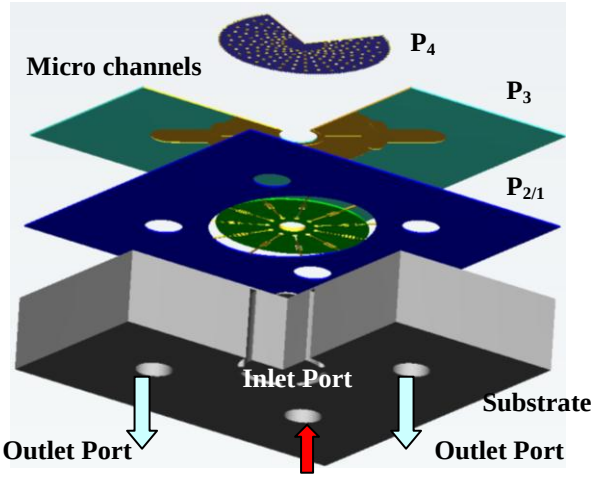

Fig. 1.1. Exploded and Cut View of the Rotary Vane Micro-Motor idea.

One of the main drawback of these design working as a micropump is that they require a large amount of energy to overcome the friction and drag viscous forces at small scale. Besides, most of these designs involve several moving parts. Therefore the probability of failure in the system is also high.

The actuator types that have been fully developed in surface micromachining technology are thermal-based actuators (Comtois, 1995; Que, 1999), electrostatic-based actuators (e.g., Tang, 1990; Johnson, William A., 1995), high performance comb drive (e.g., Rodgers, M. Steven, 2000), and torsional ratchet actuator (TRA) (Barnes, Stephen M., 2000). Other actuator types that have been developed are 100 times larger (millimeters heights scale) using LIGA technologies. Examples are electromagnetic micromotor (Yang, Chunsheng, 2001) and microturbine research at MIT (Epstein, A.H., 1997; Lue G.

Fréchette, Lue G. 2000; Schmidt, Martin A. 2001). These MEMS devices require costly assembly processes after fabrication. Microturbo machineries (millimeter device heights) have been developed based on turbine engines, turbo generators and rocket engines technologies, (Epstein, A.H., 1997; Schmidt, Martin A., 2001).

1.3 Review of Mechanical Micropumps

Several review papers have already been published in micropumps, (Nguyen, 2002; Gravesen, 1993; Ho, et al., 1996).

Almost all the papers show the design, performance, and characterization as well as the fabrication process that the researches have used to accomplish the functionalities and design's requirements. Developments in manufacturing processes and successful fabrication therein have created small devices (Angell, Terry and Barth, 1983; Gabriel et al., 1988, 1992, 1995; Hogan, 1996; Amato, 1998) such as electrostatic, magnetic, electromagnetic, pneumatic and thermal actuators, motors, valves, gears, cantilevers, diaphragms with dimension on the order of a hundred microns (Francis, et al., 2002; Nguyen, 2002).

It can be noted that in these paper the authors are eager to publish their research about new working concepts of the micro pump and new design ideas. But, in most of the cases they just ignored the mathematical modeling of the devices that explained some of the behavior. Very few authors have published detail mathematical modeling of these devices.

The mathematically modeling of these systems are very challenging and require a dedicated effort to explain some of the behavior of coupling systems with different domain of physics-science (knowledge) interacting each other.

These micropumps can be categorized by their pumping principles as we said above: Mechanical and non-mechanical. Usually a non-mechanical pump implies that there are no moving parts involve during the power transfer of the system.

A survey through the literature reveals that there are at least three kinds of mechanicals micropumps have been developed: peristaltic, reciprocating and rotary pumps, that use several way of actuation like electrostatic (Zengerle, 1995, 1992,), (Cabuz 2002), (Najafi, 2003), Piezoelectric (Lintel, 1988), (Koch 1997, 1998, 1999), pneumatic (Schwesinger, Norbert et al 1998), thermo-pneumatic (Bustengs, B., 1994) electromagnetic (Lemoff, 2000) and TINi based (Makino, 2001, 1998), (Pelesko, 2002), (Senturia, 2001), (Nguyen and Wereley, 2002)

On the other hand, Non Mechanical Micropumps can be classified as Electrohydrodynamic (EHD) micropump, Electroosmotic Micropumps, Ultrasonic Micropumps, Magnetohydrodynamic (MHD) Micropumps (Francis et al 2002).

With the purpose of our work, we are going to concentrate only to the mechanical micropump because they can provide relative large flow rates compared with the non-mechanical pump whose applications are limited by nanoliter scale range.

Mechanical micropumps usually are composed of moving chambers that change periodically its volume in order to create a relative constant flow rate. Maximum

pressure depends of the actuator-force mechanism that supplies power to the micropump. The design of the valves must be carefully chosen. They could be passive or active design's valves (Francis et al., 2002). Several kinds of actuators have been designed to accomplish this task such as: electrostatic, piezoelectric, pneumatic, and thermo-pneumatics (Francis et al., 2002; Gad-el-Hak, 2001; Nguyen, 2002; Lemoff, 2000). However, the ones most often used are electrostatic and piezoelectric actuators.

Because of very high viscous forces in micro channels, the mechanical pumps are applied mostly to macro scale and some of them at micro-level. However, those which apply to micro level keep large dimensions respect to the micro dimension. They can fill the gap between macroscale pump and micropumps. The mechanical micropumps can have a flow rate range from 10μl/min up to 10ml/min (Francis et al., 2002; Nguyen 2002). For flows greater than 10ml/min miniaturized or macroscale pump can be used (Nguyen 2002).

Mechanical micropumps share the same transfer fluid power principle as their cousin in the macro world. However, there is a need of an actuator to transfer electric energy into hydraulic energy and later on into mechanical useful work. The actuator could be external or integrated actuator (e.g., Shoji and Esashi, 1994). External actuators tend to be slower and too big compared with the dimensions of the micropump. But, they can develop large forces as well as stroke length. In contrast, integrated actuators are designed with the pump on a single micromachined chip. The time response is faster and the dimensions are smaller compare with the external

actuator, but they usually generate smaller forces and shorter stroke lengths. Therefore, they are in the range of low power (Nguyen 2002; Francis et al 2002).

For gas pumping applications, electrostatic or piezoelectric driven membranes are frequently used (Francis, et al., 2002).

Smits, Jan G, was the first to develop a piezoelectric micropump with surface micromachining of silicon in 1980, However He did not published his work until 1989 (Smits, 1989). Van Lintel published the first successful piezoelectric micropump in 1988 (Van Lintel, et al., 1988). Van Lintel was a student of Smits and He continued his work on the possibility of realizing a micropump based on micromachining of silicon and thin-film techniques. Both design use a silicon membrane as a diaphragm and a piezoelectric effect to actuate it. Some of the characteristic of these micropumps are describe on Table 1.0. The applications of these first works were for delivery insulin at low flow rate. Both design use the principle of a peristaltic piezoelectric fluid pump, it was developed by Smits at Stanford University in 1980 (Van Lintel, 1988).

Table 1.0. Performance summary of the first Diaphragm piezoelectric micropump by Van Lintel, et al., 1988 and Smits, 1989.

Pump Characteristic.	Piezoelectric: Van Lintel 1988	Piezoelectric micropump Smits, 1989
Fluid Media	Water	Water
Flow rate [ml/min]	0.05	0.03
Pressure [Kpa] [cms H_20]	6.86 [70]	5.8 [60]
Input Power [mwatts]	N/A	N/A
Output Power[mwatts]	5.7E-03	2.9E-03
Frequency range[Hz]	0.1	15
Voltage [vol}	100	80
Volume/stroke [µliters]	0.083	N/A
Dimensions[µmxµmxµm]	12,500x12,500x0,130	N/A
Check Valve	Build in	Build in
Volumetric efficiency[%]]	N/A	N/A
Total efficiency[%]	N/A	N/A
Fabrication Process	Micromachining Silicon	Micromachining Silicon

A micropump design thought to hold some promise was the diaphragm pump by Cabuz, C., William R. Herb, Eugen I. Cabuz, Son Thai Lu. (2001). It was developed at Honeywell laboratories and it uses a curved electrode wall. Fig. 1.2 shows the concept. This pump uses two diaphragms and can produce up to 30 ml/min of flow with power consumption of 8 mwatts. Even though the authors claim that its dimension belongs to the micro-level the size of this particular design more in the macro domain: 15x15x1 mm^3. One of its downsides is its leaky concept.

The volumetric efficiency is almost 99% and it has zero dead volume. But the total efficiency [equation 2.0] is about 11.5 %.

$$\eta_t = \frac{P_{Hyd.output}}{P_{Input}} = \frac{\Delta P * Q}{P_{input}} \tag{2.0}$$

The pump chamber is made by injection of plastic. The material chosen for the diaphragm is made out of metallized kapton. The assembly of this pump is done carefully by hands.

This is one of the most promising micro pumps that someone has design so far; it is efficient and relatively simple even though has leaks. It is very well know in the literature; researchers use it as a reference on design. However, this work (Cabuz 2002) lacks of mathematic modeling to explain its performance. Furthermore, since it requires manually assembly it is not a good choice for high production and manufacturing.

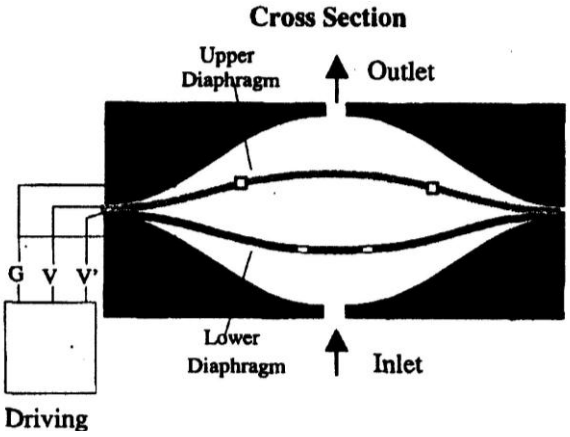

Fig. 1.2 Cabuz's micro pump design. Showing the successful curved electrode feature and double membrane (Cabuz, C. 2002)

One of the main drawbacks of the Cabuz's micro pump besides being leaky is that this pump requires accurate manual mechanical assembly. The fabrication process

is not standard. The electrodes are fabricated by casting. The displacement volume is 5.5 µliters and the flow rate is 28.2 ml/min at 66 Hz with 200 V. The fluid media is gas (air).

The pressure developed during the test is about 20 cm H_20 (1.96KPa). Table 1.1 shows some data extracted from papers about this micropump.

Table 1.1. Performance summary of the Dual Diaphragm Pump, Cabuz's Micropump. [CABUZ, et al. 2002]

Pump Characteristic.	The Dual Diaphragm Pump
Fluid Media	Gas - Air
Flow rate [ml/min]	28.2
Pressure [Kpa] [cms H_20]	1.96 [20]
Input Power [mwatts]	8
Output Power[mwatts]	0.92
Frequency range[Hz]	37 ~ 95
Voltage [vol}	200
Volume/stroke [µliters]	5.5
Dimensions[µmxµmxµm]	15,000x15,000x1,000
Check Valve	Build in
Volumetric efficiency[%]]	99
Total efficiency[%]	11.5
Fabrication Process	Plastic_Injection molding. and Mech Assembly

A recent patent by Najafi, Khalil 2003 shows the design of a new micropump that uses a flat parylene membrane that is placed on top of curved electrodes. This work is an improvement of Cabuz's work. They also design a similar curved electrode-chamber,

like that of the Cabuz's idea (Cabuz, 2002). They claim in their patent that it is not possible to design a flat membrane based on parallel plate electrostatic forces to produce the require stroke without consuming too much energy. However, there is no detailed information about its performance and math modeling is also lacking.

An electrostatic micropump was developed in the Fraunhofer Institute for Solid State Technology, Germany (Zengerle, 1992). The diaphragm pump was built using bulk micromachined techniques with dimensions 7x7x2 mm^3 (four micromachined silicon chips); it is claimed to be the first application of electrostatic actuation in micropumps. The dimension of the membrane is 4x4 mm^2 with 25 μm thickness. The liquid used for pumping is DI water. But it can pump saline solutions. The volume of the stroke is measured to be in the range of 10nl to 50 nl. At 25Hz with 170 V, the micropump can deliver 70 μl/min when the maximum frequency is up to 100 Hz. No mathematical model is shown in the paper, only micropump characterization. Table 1.2 shows performance.

Similar designs as before by the same researchers (R. Zengerle, S. Kluge, M. Richer, A. Richter, 2001) show a bidirectional silicon micropump with an electrostatically actuated diaphragm type. Table 1.3 shows the performance of this micropump. At low frequency [0.1Hz-800 Hz], it works in forward mode, delivering 850 μl/min with maximum backpressure of 310 hPa (310 cm H_2O). At a supply voltage of 200V the power is estimated less than 1 mwatt. There is no information about the dimensions of the micropump and none about the flat valve. But some parameters can

be estimated using the data provided by the paper. Also, it lacks for mathematical modeling.

Table 1.2. Performance summary of the Micro Membrane Pump (Zengerle, 1992).

Pump Characteristic.	Micro Membrane Pump
Fluid Media	Water (estimate}
Flow rate [ml/min]	0.100
Pressure [Kpa] [cms H_20]	10 [100]
Input Power [mwatts]	N/A
Output Power[mwatts]	0.016
Frequency range[Hz]	25~100
Voltage [vol}	170
Volume/stroke [µliters]	0.01~0.05
Dimensions[µmxµmxµm]	7,000x7,000x2,000
Check Valve	Build in: Flat valves.
Volumetric efficiency[%]]	N/A
Total efficiency[%]	N/A
Fabrication Process	Bulk Silicon Micromachined.

A surface machined micromechanical (photolithography techniques) membrane pump by Jack W. Judy, Takashi Tamagawa, and Dennis L. Polla. 1991. This work shows an electrostatic membrane pump design. This pump uses an actuation voltage of 50 V with stroke displacement being measured in the range of 12nl/min to 640 nl/min. Table 1.4 summarize the performance of this micropump.

Table 1.3. Performance summary of the directional diaphragm micro-pump (Zengerle, 2001).

Pump Characteristic.	Bidirectional Silicon Micropump
Fluid Media	Water (estimate}
Flow rate [ml/min]	0.850
Pressure [Kpa] [cms H_20]	31 [310]
Input Power [mwatts]	1mwatts
Output Power[mwatts]	0.439
Frequency range[Hz]	Low [0.1 ~850] High [2KHz- 6KHz]
Voltage [vol}	200
Volume/stroke [µliters]	N/A
Dimensions[µmxµmxµm]	N/A
Check Valve	Build in
Volumetric efficiency[%]]	N/A
Total efficiency[%]	43.9
Fabrication Process	Bulk Silicon Micromachined

Three different membrane sizes were tested [100x100µm, 200x200µm, and 400x400µm] to show how they affect the flow rate characteristic. This micropump only can pump non-hydrophobic fluid due to the large surface tension because of the micro scale cross-section pump. Also no information available for pressure and frequency ranges during the performance of this design. Beside, no mathematical model has been given.

Table 1.4. Performance summary of the surface machined membrane pump (Judy, W., 1991)

Pump Characteristic.	Surface Machined Membrane Pump
Fluid Media	Water and gas
Flow rate [ml/min]	N/A
Pressure [Kpa] [cms H_20]	N/A
Input Power [mwatts]	N/A
Output Power[mwatts]	N/
Frequency range[Hz]	N/A
Voltage [vol}	50~ 75
Volume/stroke [µliters]	0.012~0.640
Dimensions[µmxµmxµm]	400x 400 x NA only Membrane size.
Check Valve	Build in: Flat valves.
Volumetric efficiency[%]]	N/A
Total efficiency[%]	N/A
Fabrication Process	Surface machined. Lithography

A design and simulation of an electrostatic actuated micro pump for drug delivery applications was presented by Bourouina, T., Alan Bosseboeuf, and Jean Paul Grandchamp (1997). The micropump works with only one valve (normally closed), the device is made of three micromachined superimposed silicon wafers. The dimensions are 5x5xNA mm^3. The flow rate was measure to be around 10 ~100 nl/min. A working voltage of 10V was used. The height of the micro channel is around 10 µm. An electrical network model is presented based on analogies of electric networks and mechanical fluidic, and structure elements. Table 1.5 shows performance for this pump.

The simulation frequencies range is from 5 to 100 Hz. The main application for this micro pump is for drug delivery.

Table 1.5. Performance summary of the Electrostatic Pump (Bourouina, 1997)

Pump Characteristic.	Design electrostatic micropump [14]
Fluid Media	Water
Flow rate [ml/min]	0.01 ~ 0.1
Pressure [Kpa] [cms H_20]	N/A
Input Power [mwatts]	N/A
Output Power[mwatts]	
Frequency range[Hz]	5 ~ 100 (simulations)
Voltage [vol}	10 V
Volume/stroke [µliters]	N/A
Dimensions[µmxµmxµm]	5000x 5000 x NA only Membrane size.
Check Valve	Only one Flat valve.
Volumetric efficiency[%]]	N/A
Total efficiency[%]	N/A
Fabrication Process	Surface micro- machined.

Another reciprocal micropump is "*The first self priming and Bidirectional valve less diffuser micropump for both liquid and gas*" by Wouter Van der Wijingaart, Helene Anderson, Peter Enoksson, Kjell Noren and Goran Stemme (2000). It was developed at the Royal Institute of technology. Stockholm, Sweden. This pump is a reciprocal type diffuser pump that uses a piezo-disc diaphragm to create the displacement of the chamber. Figs. 1.3 and 1.4 show the schematic of this micropump. The pump was made

out of silicon-glass stack and fabricated using Deep Reactive Ion etching process (DRIE) (Wijngaart, 2000).

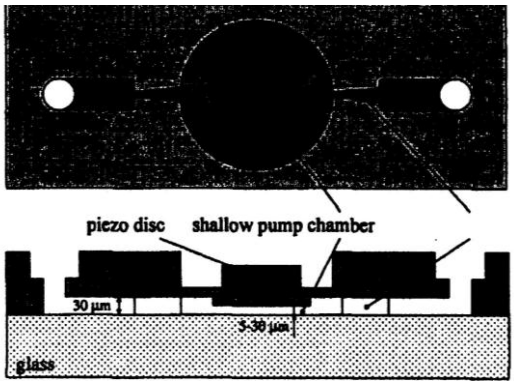

Fig. 1.3. Schematic of the diffuser micro pump. (Taken from Wijingaardt, 2000)

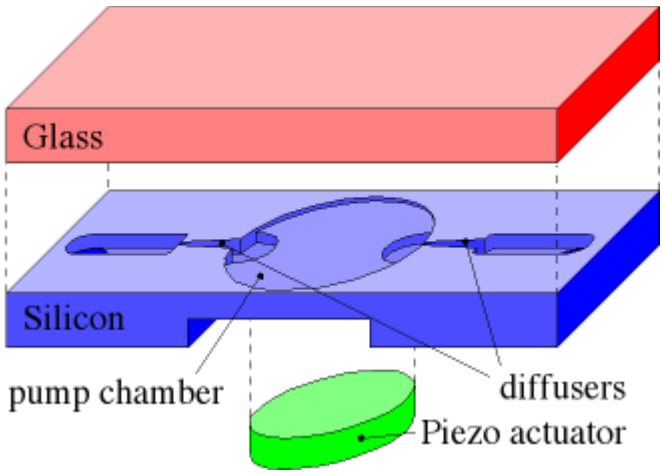

Fig. 1.4. Exploded view of the diffuser Micro pump, taken from Wijngaart, 2000.

The dimensions provided in the research work are only related with the piezo disk used and those are 4mm diameter and 100 µm thick and the channel depth for the diffuser is around 30 µm deep and wide. Estimation of the size of the pump without the

glass cover would be approximately 10mmx6mmx0.3 mm^3 according with some sketch provided (Wijngaart, 2000), but there is not sufficient data available.

The pump can work either in water or air; for water fluids, the maximum pressure reached is around 5 kPa with a flow rate of 30 µliters/min. Therefore the hydraulic power generated is around 0.025 mwatts. For air the pressure reached is also around 5 kPa and the flow rate recorded was about 545 µliters/min. Fig. 1.5 shows the working principle.

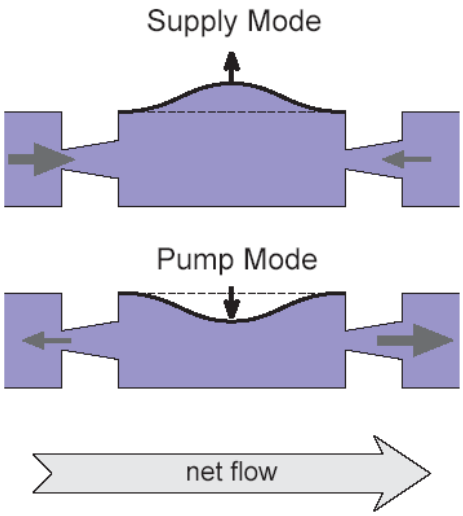

Fig. 1.5. Principle of the diffuser Micro pump, taken from [Wijngaart, 2002].

Assuming uncompressed fluid, the useful power generated is around 0.454 mwatts. The paper lacks of detailed recorded and measured data.

Another good example of a diaphragm type of micropump design is the NiTi/Si Diaphragm micropump. Several pumps have been fabricated successfully with NiTi/Si composite diaphragm (Xu Dong, 2001; Eiji Makino, 1998, 2001; Kahn, H., 1998).

Table 1.6. Performance of diffuser type of micro pump, (Wijingaardt, 2000).

Pump Characteristic.	The first self priming and Bidirectional valve less diffuser micropump for both liquid and gas [6]
Fluid Media	Air and Water
Flow rate [ml/min]	545/air 30/water
Pressure [Kpa] [cms H_20]	5 [[51]
Input Power [mwatts]	N/A
Output Power[mwatts]	0.45 / air 0.05/water
Frequency range[Hz]	[10-33,000]
Voltage [vol}	125
Volume/stroke [µliters]	N/A
Dimensions[µmxµmxµm]	10,000x6,000x300 (estimation)
Check valves	No, diffuser type.
Volumetric efficiency[%]	N/A
Total efficiency[%]	N/A
Fabrication Process	Deep Reactive Ion etching process (DRIE)

A novel micropump using NiTi/Si diaphragm was developed at Shanghai Jiao Tong University (Xu, 2001). The dimension of the micro pump is 6mmx6mmx1.5mm and specific dimension for the composite diaphragm is 3mm x 3 mm x 20 µm basically, it is a deformable chamber with two flat check valve made out of silicon, see Fig. 1.6.

The fabrication process is silicon micromachining and Au-Si eutectic bonding. The maximum flow rate recorded was around 340 µliter/min and maximum working frequency of 100 Hz. The paper show excellent actuation performance using the

composite material. The actuation mechanism is thermo-mechanical response of the thin-films material. Another micro diaphragm pump using similar approach was developed by (Makino, 2001). The drawbacks of this micropump are high consuming power and large response times. It needs to wait for the membrane material to cool down to a flat state before current can be applied again to heat it back up into a bending state and repeat the cycle.

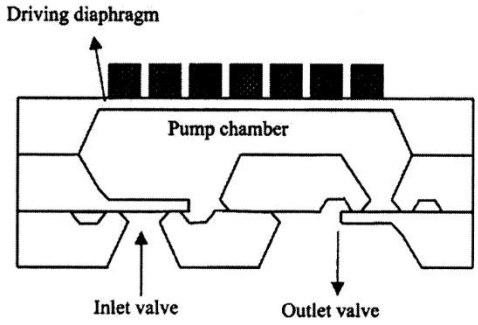

Fig. 1.6. Sketch of NiTi/Si diaphragm Micropump, taken from [Xu Dong, 2001]

Several papers have been reported about the design of peristaltic pumps. The fundamental principle is to squeeze the fluid out. The backpressure for this kind of micro pump is very low. Usually, they optimize the displacement rather than the high pressure (Francis et al., 2002).

An improved two stage discrete peristaltic micropump was developed and presented by Berg, J.M., 2003. And, they used compressed nitrogen gas as the pneumatic actuator. The maximum flow was 7ul/min at 227 Pa.

Rotary Pumps is another type of mechanical pump and it uses the same principle as the macro pumps. They add energy to the fluid by using momentum or positive displacement of the chambers. Several papers have presented designs. [Ahn, et al., 1995] presented a micropump with turbine as rotor and it uses an electromagnetic field

to create the motion of the turbine. It added momentum to the fluid by means of the motion of the rotor which is rotate at 5000 RPM. At maximum pressure is 10KPa. However, there is little attention in developing a rotary micropump. This is because when the dimension of the sliding moving parts are reduced to the range of a few micron gap, the viscous shear forces become large, creating a large drag force on the rotor with the result that most of the energy is expended just to overcome the viscous forces.

But a microfluidics design working as an actuator can be used in a sensor devices for good advantage. For instance a viscous drag spiral pump that uses this principle to pump and has been fabricated by polysilicon surface micromachining process is reported in Kilani, 2002.

Table 1.7. Comparison between actuation mechanisms, [Francis, et al., 2002].

Actuation Methods	**Pressure**	**Displacement**	**Response Time**	Comments
Electrostatic	Small	Very small	Very fast	Micromachinable Surface MicroM.
Piezo-electric	Small	Medium	Fast	External actuation
Stack type piezoelectric	Very Large	Very small	Fast	External actuation
Shape Memory Alloy	Large	Large	Slow	External actuation
Thermo-pneumatic	Large	Medium	Medium	Micromachinable.
Pneumatic	Small	Large	Slow	External actuation
Note Pressure; Very large P>9810 KPa, Large 9810>P>98.1, Medium: 98.1>P>49 . Small: 49>P. Displacement; Large d>100mm, Medium 100>d>30, Small: 30>d>10, Very small: 10>d. Response Time; Very fast: t<0.1 ms, Medium: 1 sec>t>1 ms, slow: t>1 s,. [Shoji and Esashi 1994]				

The most used actuation means for diaphragm micropump have been electrostatic and piezoelectric actuators because of its good response performance. Therefore, they can handle high frequency membrane oscillation, which means the

capability to delivery high flow rates. Furthermore, the fabrications of the electrostatic actuators are compatible with most of the standard MEMS fabrication techniques. On the other hand, the maximum pressure is directly related with the force that the actuator can developed. Fig. 1.7 summarizes of the most important micropumps development on the past decades.

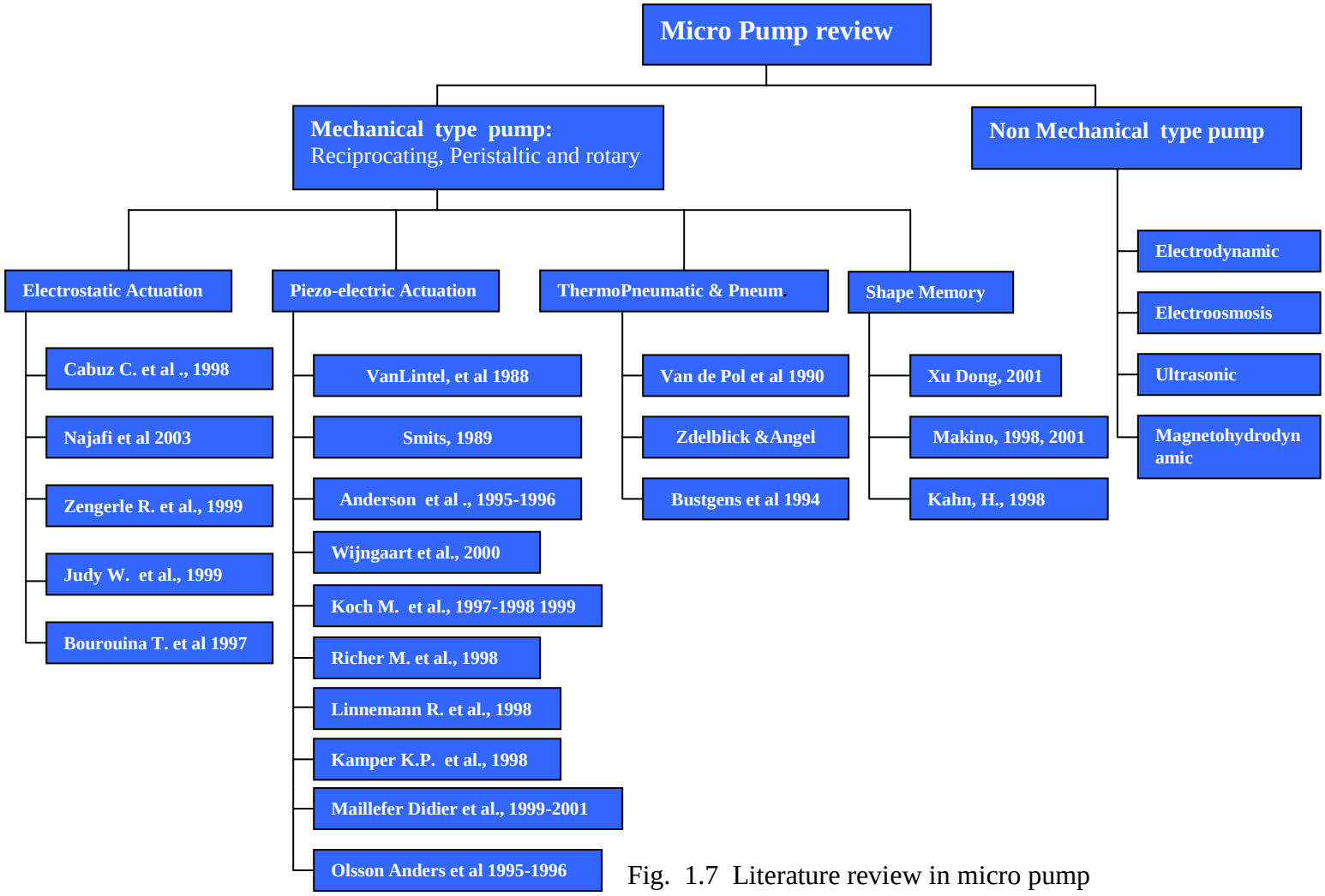

Fig. 1.7 Literature review in micro pump

Table 1.8 Micro Pump review features

		Micro - Pump Review											
	Media	Physical Features											
Pump design.	Gas/Water.	Flow [ml/M]	Press.[kPa]	P In[mW]	P out [mW]	Freq.[Hz]	Volt [V]	Structure	Vol/Stroke[µlt]	Area [µm]	height[µm]	Valve	Fabrication Process
Electrostatic actuation													
Dual Diaphragma [Cabuz, 2001]	Air	28.2	196	8	0.92	[37~95]	200	Simple	5.5	150000x150000	1000	Build in	Plastic_Injection molding/Mech Assembly
Bidirec. Silicon µpump[Zengerle 1995]	Water	0.85	31	1	0.439	[0.1-850][2K~5K]	200	Simple	N/A	N/A	N/A	Build in	Bulk Silicon Micromachined
Micro Membrane Pump [Zengerle 1992]	Water	0.1	10	N/A	0.015	25~100	170	Simple	0.01-0.05	7000x7000	2000	Build in	Bulk Silicon Micromachined
Surface Mach. Mem Pump [Judy 1991	Gas/Water	N/A	N/A	N/A	N/A	N/A	50~75	simple	0.012~0.640	400x400	N/A	Active Val.	Surface machined. Lithography
D.electros. µpump [Borouina 1997]	Water	0.01-0.1	N/A	N/A	N/A	5~100 Simul	10	Simple	N/A	5000x5000	N/A	One Flat V.	Surface Micromachined
Piezo Electric actuation													
Van Lintel, et al., 1988	Water	0.05	68	N/A	N/A	0.1	100	Simple	0.083	12500x12500	130	built in	Silicon Micromachining
Smits, J.G., 1989	Water	0.03	5.8	N/A	N/A	15	80	Simple	N/A	N/A	N/A	built in	Silicon Micromachining
Anderson Olsson et al 1995 [1]	Water	16	16.6	N/A	N/A	540	130	Simple	N/A	D 13000	N/A	Built in	DRIE:Deep Reactive Ion Etching
Anderson Olsson et al 1996 [2]	Wat&Meth	0.23	16.6	N/A	N/A	1318 Meth-1198 Wat	120 PP	Simple	N/A	D 6000	N/A	Built in	DRIE:Deep Reactive Ion Etching
Wijngaart et al 2000[3]	Air/Water	30	5	N/A	N/A	10~33000	125	Simple	N/A	10000x6000	300	Built in	DRIE:Deep Reactive Ion Etching
M Koch et al 1997 [4]	Water	0.9	70	N/A	N/A	0~1000	40 max	simple	N/A	8000x4000	50,60,90	Built in	Surface micromachined.
M Richer et al 1998 [5]	Gas/Water	0.7	1	N/A	N/A	220	50~75	Simple	0.085	N/A	N/A	Built in	Silicon Micromachining
R. Linnemann et al 1998 [6]	Air	1	100	N/A	N/A	200	40 ~120 Rec	Simple	N/A	N/A	N/A	Built in	Silicon Micromachining
Michael koch et al 1998 [7]	Ethanol	0.12	2	N/A	N/A	200	600 PP	Simple	N/A	8000x4000	70	Built in	Silicon Micromachining hybrid
K.P. kamper et al 1998 [8]	Gas/Water	0.4	210	N/A	N/A	70	N/A	Simple	N/A	D 10000	250	Built in	Micro Mold Injection & Laser
M. Koch et al 1999 [9]	Ethanol	0.49	2.5	N/A	N/A	4000	240	Simple	N/A	35000x30000	100	Built in	Micromachined
Didier Maillefer et al 1999&2001[10-11]	Gas/water	0.033	10	N/A	N/A	1	N/A	Simple	0.16	6000x10000	N/A	Built in	SOI & DRIE

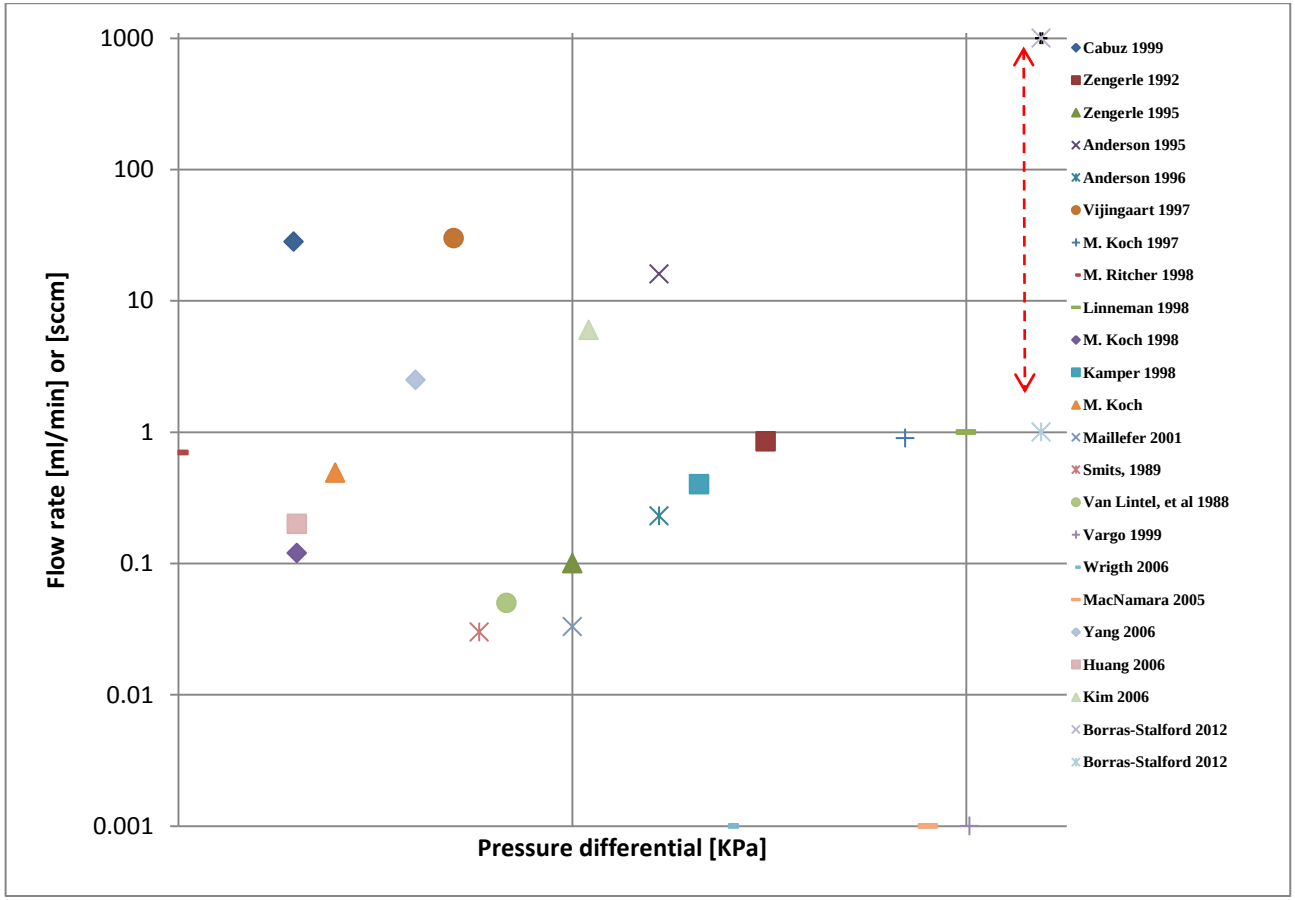

Fig. 1.8. Micro Pump review: Electrostatic and Piezo-electric diaphragm type pumps.

1.4 Non Mechanical Pumps.

These pumps do not have moving parts during the energy transfer process and the principles of this category is to add momentum energy to the fluid by transferring energy from any energy source available (Nguyen, 2002). However, the flow rates are very low compare with mechanical pumps. Usually, the flow rate is less than 10 μl/min [3]. Non-mechanical pumps are: Electrohydrodynamic pump (EHD), electrokinetic pumps, phase transfer pumps, ultrasonic pumps, electro-wetting pump, electrochemical pumps, magnetohydrodynamic pump (MHD). These micropumps have the research potential to develop the technology at the nanoscale. (Francis, et al., 2002).

1.5 Objectives.

The main goal of the proposed research is to develop a novel monolithically integratable low-power micro-diaphragm pump with applications to microchemlab systems. Furthermore, a new 3D model of micro pump system will be developed and designed based on electrostatic curved drive electrodes concept as well as electrostatic parallel plate attraction forces to power not only the pump but also operate the built-in microvalves.

The integrated microvalves will also use the same actuation concept developed for the micro-diaphragm pump motion.

Specific aims of the proposed research work are:

a) Design a novel micropump based on a diaphragm and reciprocal type of mechanical pump.

b) Design an electrostatic actuator for the membrane-plate diaphragm based on a curved electrode drive idea, and "electrozipper" concept. The curved electrode drive will actuate the diaphragm during the intake stroke of the micropump and the electrostatic actuator will actuate the diaphragm during the power stroke of the micropump, both intake and power stroke use the zipper idea.

c) A multi-physics system or computational fluid, structure and electrical dynamic interaction will be developed to simulate the dynamic and predict the behavior of the micro pump system. The development of a computational tool will optimize the micropump designs for better performance, lower cost, and higher reliability modeling.

d) The designs of micro-actuators and micro-pump devices will take and follow the rules for fabrication by Sandia's surface micro-machining technology.

e) Characterize performance of designs and validate models and theory through computational simulations.

1.6 Contribution.

The proposed research will establish a new field of knowledge, research, and applications in micro-fluidic actuator development at the microscale using fluid as a medium for low-cost, high-performance energy transfer. It will also develop and clarify the concepts of computational fluid dynamics modeling for micro-fluid power devices. It will pave the way for a host of new innovative single-chip applications of micro-

chemical lab system, micro-positioning, micro-mixing, micro-flow, micro-fluid power, and vacuum micropumps applications, and micro-sensing devices.

This research work has the potential of making several contributions to the field of microfluidics and multiphysics simulations.

First, the main contribution is the presentation of a novel micropump in a chip that uses electrostatic force by mean of curved and flat electrode to generate a peristaltic motion that squeezes out the fluid. The electrostatic force produces a zipper concept and it provides the actuation on the diaphragm of the pump. Currently, in the literature researchers have developed the curved electrode-chamber (Cabuz 2001; Najafi 2003) as one of the best ways to generate volumes in the actuation of the diaphragm of the micro pump. It is generally believed by the micropump community that a flat membrane cannot be utilized electrostatically to generate large flow rates and large differential pressures (e.g., Najafi 2003). Based on our rough calculations, we have established that this belief is false.

Second, the contribution is the design of a new way of closing the chambers by mean of electrostatic forces that squeeze the fluid out in the right direction by means of the zipper motion idea (Gilbert 1996; Ionis 2002) and achieve high differential pressure above 100 KPa (1atm). Currently, there is high demand (e.g., sensors industry) for micropumps that can produce high vacuums.

Third, using the same new concepts as described above for the pumping chamber, the inlet and outlet valves will be designed as integrated parts of the system on the chip.

Fourth, a design and a modeling procedure based in CAD/CAE analysis will be carried out in order to accomplish and establish all requirements as well as the dynamic simulation of the micropump. It will provide the computational tools to predict the behavior and dynamic response of the system

1.7 Outline of the research.

This is a study in the area of microfluidics research. It is a multi-physics study: fluid dynamics, solid structure and electrostatics field interacting all together to form a Micro-Electro-Mechanical System (MEMS). The design of the micropump is based on the diaphragm and peristaltic concept and its design will be conducted by electro-mechanical analysis and computer aided design (CAD) as well as computer engineering design (CAE). The design of this micropump will follow suitable design rules for potential micro-fabrication using batch cut and surface micromachining techniques (e.g. SUMMiT V™, SwIFT™, DRIE). The methodology of this research project will be described as the following:

In Chapter 2, we present the literature review about microfluidics and microdevices with special attention paid to micropumps, their design parameters and modeling of micropumps that are relevant to the project.

In Chapter 3, we present the FEM simulation and the model validation for non-linear displacement thin plate, a thin non linear large displacement model simulation is compare with analytical equation available on literature.

In Chapter 4, we present the mathematical model and simulation of the 2D intake power stroke for the micropump will be described in this chapter. The intake power stroke of this micro-pump is based on electrostatic actuation and it will be analyzed under quasi-static condition, the mathematical model proposed is based on continuum solid mechanics, the inertial effect of the plate have been neglected and this model.

In Chapter 5, we present the analytical derivation of quadratic electrostatic distributive force model for the intake stroke. The 4^{th} order reduced von Kármán governing differential equations can be analytically integrated.

In Chapter 6, we present the analysis and electrostatics model of the 2-D curved actuator drive as well as the electro-zipper mechanism of an electrostatic force plate actuator that generates forces. Using a simplified 2 D static model for the plate analysis, it can be applied the reduced von Kármán governing differential equation, this equation is usually for thin plate that has bending stresses as well as stretching stresses due to the external pressure and initial small curvature.

In Chapter7, we compare analytical and simulation result for intake power stroke on the plate micropump with different cases. We compare bending stress σ_B results obtained from simulation with those generated using the analytical model.

In Chapter 8, we present the estimated voltage and breakaway points for intake power stroke. The analytical model is used to estimate the required voltage needed in completely opening up the intake chamber.

In Chapter 9, we present the mathematical analysis for the intake stroke. The results from the analytical modeling are compared with those from the multiphysics simulation. A quadratic approximation model of the electrostatic distributive force is presented therein.

In Chapter 10, we present the methodology for a baseline design using the non-dimensional parameters. The method is applied to size new micropumps beyond the baseline.

In Chapter 11, we present a new concept for vacuum micropump design that is targeted to produce 10^{-9} Torr by cascading two baseline pumps. The baseline design is applied to two different cases where the inlet reservoir has vacuum pressures of 10^{-6} Torr and 10^{-3} Torr. The leak rate for different surface roughness values is also taken into account.

In Chapter 12, we use the method described in chapter 10 to develop a novel design for achieving high pressure high flow rate [1-1000] SCCM micropump.

In Chapter 13, we present the conclusions of the research work.

1.8 Chapter Summary

During the past decades a large number of different kinds of micropumps have been developed. However, the most promising principle is the diaphragm type of micropump, because they use the surface ratio advantage to pump the fluid. They also keep simplicity in their basic design with no sliding parts. Having, no sliding parts, they reduce the viscous drag forces that are dominant in microfluidics.

The most efficiency, simple and common way to actuate these diaphragm-based micropumps is to use electrostatic forces and piezoelectric forces. These two have a potential in terms of response time, simplicity, relatively easy to fabricated, and compatibility with standards MEMS techniques.

There is a strong need for develop a micropump capable of providing a high differential pressure of 100KPa (1 atm). Currently, it is an open research area to study

and design micropumps capable of providing high differential pressure above 1 atm. New sensors have been developed that are required to work in vacuum against differential pressure at 1 atm in order to perform well.

Consider the following important question. Does there exist an on-chip micropump for application in gas micro-chromatography analysis that provides high differential pressures close to 1 atm? The literature review shows that diaphragm micropumps available provide either high pressures but very low flow rates or high flow rates but low pressures. There is nothing that gives a high flow rate and a high differential pressure in the range needed for application in gas chromatography analysis. Fig. 2.5 shows this conclusion.

The main goal of this proposed research is to design a novel micropump unit to delivery 5 ml/min and 100KPa (1 atm of air or a gas) differential pressure to be used in a MEMS sensor type that required vacuum pressure package. Furthermore, we consider the micropump arrays, coupled in series or in parallel to increase flow rate and/or pressure.

Table 1.8 and Fig. 1.8 show that in the middle region of the chart there is no design available.

The expected power consumption of the micropump will be in the low range of few mwatts.

CHAPTER 2

NOVEL MICROPUMP CONCEPT

2.1. Novel Micropump Design Concept.

This chapter presents the development and general design ideas of the new micro-pump concept. The material and fabrication process under consideration is compatible with surface micromachining of MEMS at Sandia National Laboratories. The main components of our micro-pump in a chip are: the plate the polysilicon curved electrode and flat electrode, electrical insulation layer (e.g., silicon nitrate), silicon substrate or base of the micro-pump. The study of the micropump concept will be split into its natural two stage strokes: intake stroke and power stroke.

2.2 Intake Stroke.

At the start of the intake sequence, the flat polysilicon plate rests on a nitrate electrical insulation layer as shown in Fig. 2.0. The curved electrode surface is coated by an insulation layer (e.g., nitrate layer) on the bottom surface of the electrode. The curved electrode section is connected to a bond pads, which is connected either to ground or a potential voltage and switched depending of the stroke sequence cycle. A dielectric glass-Pyrex separation at the edges is proposed as one candidate for electrically isolating the flat plate surface electrode from the upper curved drive structure electrode. The lower substrate electrode and the upper curved drive electrodes are each separated into three electrically insulated sections. It permits electrical control applied separately to the functions of inlet valve, outlet valve, and pumping chamber.

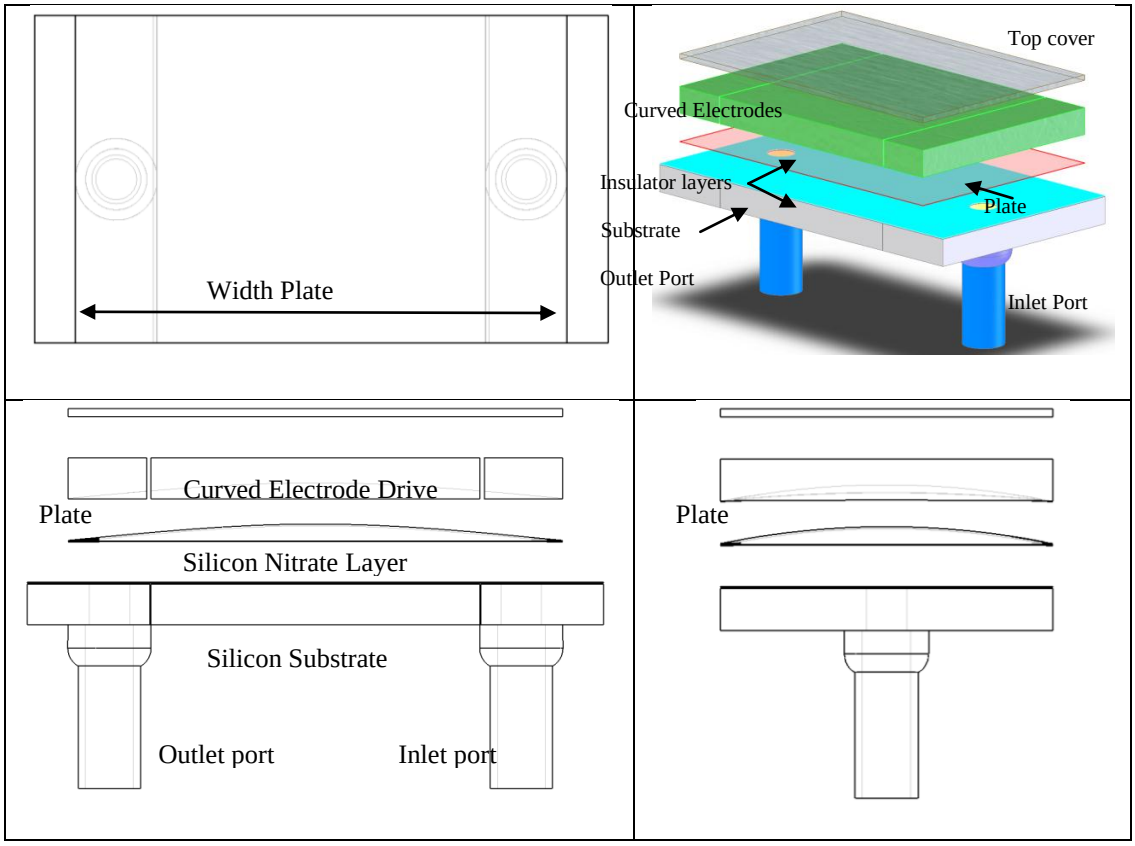

Fig. 2.0. View section of micropump on a chip and a curved actuator idea.

As soon as potential voltage difference is applied to the upper drive curved electrode, electrostatic forces develop between the plate and the upper curved electrode drive resulting in an upward force on the plate is held always to ground potential. The electrostatic force is inversely proportional to the square of the gap separation; the equation describing the electrical model is given in the following chapters. Therefore, the largest force is applied at the edges of the plate and acts to create an opening volume inside the chamber as the plate moves up. The forces pull up the plate from the outside edge in toward the middle of the plate suck in the fluid through the inlet opening valve

and at the same time venting out to atmosphere pressure the fluid in the upper chamber through the venting hole.

As a result, the plate will deflect upwards creating a volume between the plate and the nitrate layer which is then filled by the fluid coming through the inlet valve opening. This describes the opening and intake stroke sequence in one stage of the micropump.

2.3 Power Stroke

At the start of the power stroke motion, a voltage potential is applied to the flat substrate electrode while the plate electrode is maintained at ground reference. Therefore, the potential difference between the plate and the substrate generate electrostatic forces that pull down the plate toward the substrate and squeezes out the fluid through the outlet valve opening. The electrostatic force which is inversely proportional to the square of the gap separation causes that the largest force is applied again at the edges of the plate and acts to create large internal pressure inside the chamber as the plate closes down.

The forces push down the plate from the outside edge in toward the middle of the plate squeezing out the fluid through the outlet valve opening. The electrostatic forces increase as the gap distance decreases between the plate and the bottom of the chamber (i.e., nitrate layer). In other words, the electrostatic pressure will close the plate in a two-dimensional zipper motion.

The electrostatic variable pressure along the plate length chord will push down the plate as long as such pressures are greater than the fluid pressure inside the chamber and the viscous damping fluid resistant to flow. Therefore, the closing motion will start from the edge and move two-dimensionally toward the center of the plate. This motion is called the zipper motion because it acts just like the motion of a one-dimensional zipper. See Fig. 2.1.

In a worst case scenario, the pressures created by the electrostatic forces at the zipper's edge needs to be greater than the required differential pressure at the outlet. For example, if 100KPa (i.e., 1 atm) is required as differential pressure at the outlet as compared to the inlet, then it is necessary that the zipper pressure exceed 100KPa in order that the plate completely closes with the fluid being driven completely out through the opening in the outlet valve.

The zipper pressure is determined entirely by distance and electric potential across the nitrite layer or dielectric material.

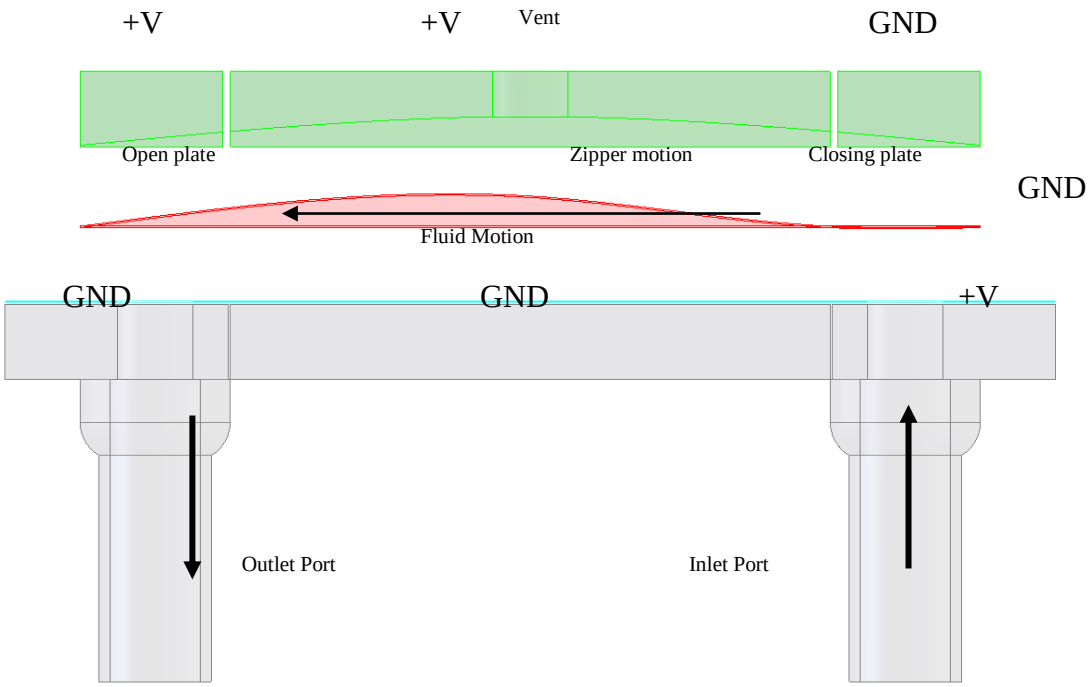

Fig. 2.1 Electrostatic pressure zips plate closed.

2.4 Inlet and Outlet Valves actuated mechanism.

There are two options that can be applied to this problem: Active and passive valves. Active valve designs will be based on the same concept as that used in the pumping chamber. Applying potential to the upper curved electrode will created a electrostatic pressure on the grounded flat plate that it will deflected the plate toward the upper electrode, allowing the fluid coming in as well as opening the valve. In order to close the valve, a potential will be applied to the lower electrode, as result, the electrostatic pressure will close the grounded flat plate in a zipper like motion squeezing out the fluid through the valve until is completely close.

The upper curved electrode drive is used to open a valve and therefore, allow the fluid fill out the expanded volume and the lower electro is used to close the valve as well as squeezing the fluid out in a zipper motion.

A simple passive flapper check valve will be considered and designed as an alternative to the active valve. By its very nature, flow is restricted to one direction.

A 3D CAD micropump model is presented in Fig. 2.2. During the inlet stroke process, the active inlet valve is forced open by applying a potential to upper curved electrode drive while the entire flat plate is held at ground potential and while the lower substrate electrodes under both the pumping chamber and the inlet valve are set to ground potential. The upper curved electrodes of both the inlet valve and the pumping chamber are held at high potential. The upper curved electrode of the outlet valve is kept at ground for the intake stroke and the substrate underneath the outlet valve is held at high potential to keep the outlet valve closed during the intake stroke.

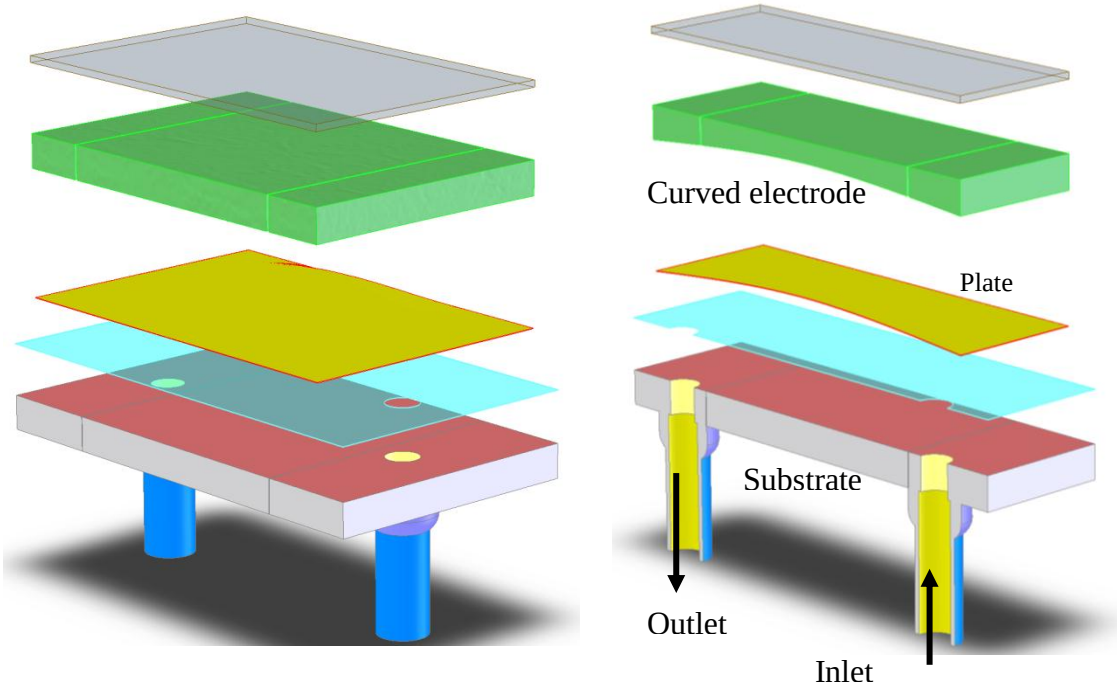

Fig. 2.2. 3D cross section plate configuration during inlet stroke.

We consider next the zipper closing motion of the outlet valve at the end of the pressure stroke. The lower substrate electrode underneath the outlet valve is held at high potential while the plate is maintained at ground potential, resulting in a zipper closing.

For the pressure stroke phase, the actuated valves switch their logical states. First, the intake valve's plate closes down via zipper motion while the pumping chamber remains open. Next, at the start of the pressure stroke, the outlet valve is opened by setting the upper curved electrode portion above of the outlet valve at high potential and grounding the substrate underneath it. During the next part of the pressure stroke, the lower electrode substrates underneath the inlet valve and the pumping chamber are held at the high potential while the entire plate is maintained at the ground

potential., resulting in a zipping close of the pumping chamber and forcing the fluid through the outlet.

2.5 Valve sequence control.

The micropump has three different segments or sections: Outlet valve section; pumping chamber section and inlet valve section. The flat plate electrode is always connected to ground potential in all sections. Therefore, for each section, the high potential control signal is applied to either the upper curved or to the lower substrate electrode. The three sections are electrically isolated and have independent switching control sequences. See Fig. 2.3.

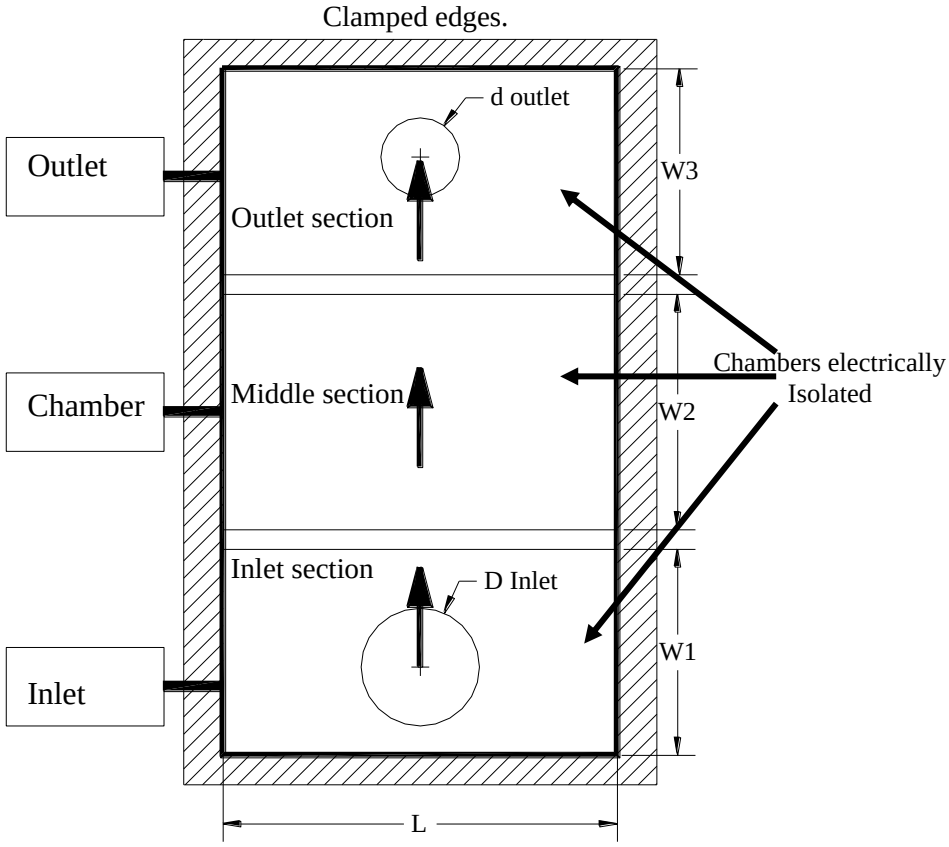

Fig. 2.3 Sketch of the micropump control concept.

Fig. 3.5 shows the direction of the flow, from the inlet valve to the outlet valve through the main pumping chamber during the stroke stage. The design must guarantee that the inlet clamped side of the plate on the pump closes first to squeeze out the fluid in the desired forward direction. Switching sequence will provide the closing and right sequence of pumping.

Switching either the upper curved electrode or the lower substrate electrode between ground and high potential determine the state (open and close) on the valve as well as that of the direction of deflection of the plate.

2.6. Intake stroke Valve control

The control stages of the intake stroke are shown in Fig. 2.4. It describes the sequence control of the valve acting during the intake stroke of the micro pump.

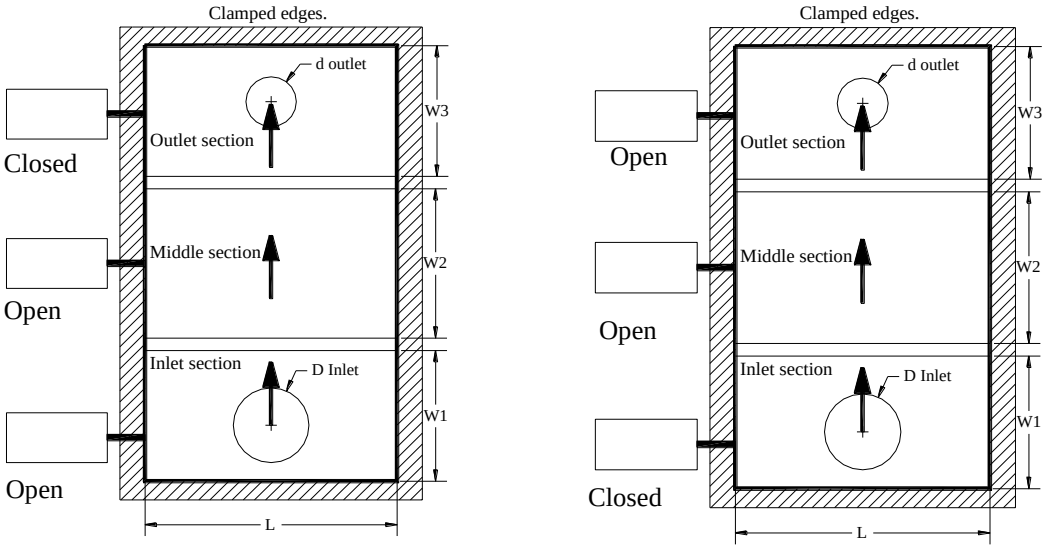

Intake Stroke
a)

End Intake stroke and start power stroke
b)

Fig. 2.4. Intake stroke valve control sequence concept: a) Initial intake stroke. b) End of the intake stroke.

Just before the intake stroke, the outlet valve is close by means of the zipper electrostatic attraction forces, between the flat plate and the high potential lower electrode status. During the initial intake stroke motion, the inlet valve as well as the pump chamber plate is pulled up by the upper curved electrode. At the end of the intake stroke and before the start of the pressure stroke, the inlet valve is closed by means of the zipper electrostatic attraction force and then the outlet valve switches to the open state by means of the activation of the last section upper curved electrode.

The pumping chamber plate which is still open at this point by the upper curved electrode, inlet and middle section drive is now ready to be closed by the zipper mechanism.

2.7. Power stroke valve control sequence.

The power stroke sequence control stage is shown in Fig. 2.5. It describes the sequence control of the valve acting during the power stroke stage of the micro pump.

During the initial power stroke motion, the inlet valve as well as the pump chamber plate is already open by mean the upper curved electrode and the outlet valve is still closed by means of the zipper electrostatic attraction forces between the plate and the flat electrode at that section. Switching potential in the last section to opening the outlet valve and switching in the first section to start closing in a zipper fashion, following by the switching the next middle section, it produce a squeeze fluid effect to pumping the fluid out.

At the end of the power stroke and before the start of next the intake stroke stage, then, the last section is switching to beginning to close as a result the plate is closed by the same zipper principle as well as the outlet is closed by means of the zipper electrostatic attraction force.

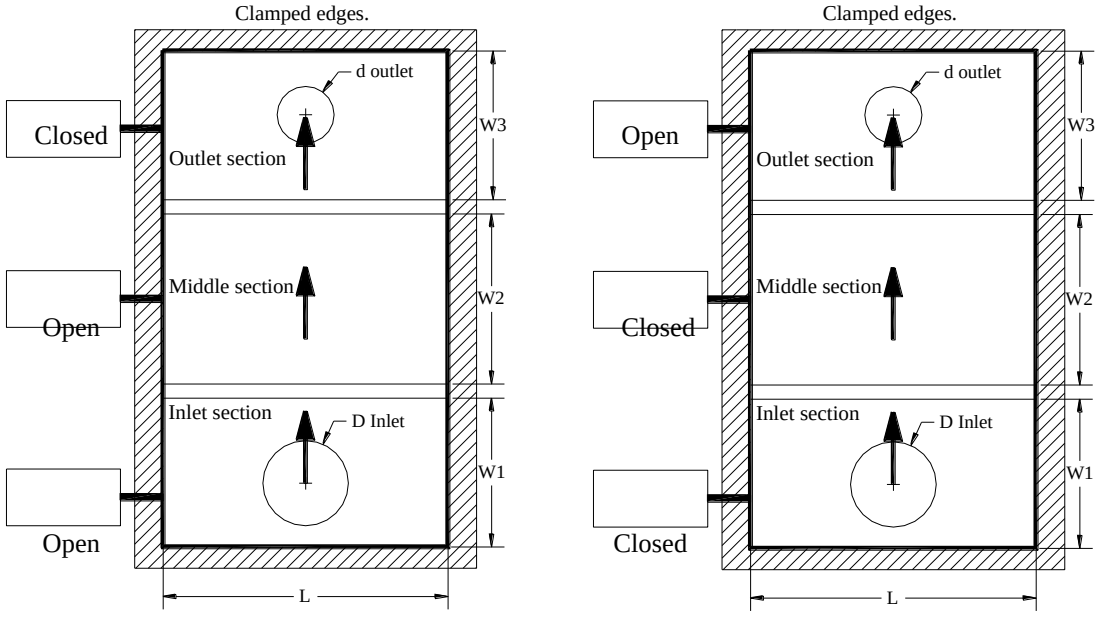

Start power stroke

End of power stroke

a)

b)

Fig. 2.5. Power stroke valve control sequence concept: a) Initial power stroke b) End of the power stroke.

Following the closing action of the inlet valve, the outlet valve is opened by means of the curved drive electrode at the first inlet section. At the end of the pressure stroke, the entire flat plate rests on the insulation layer.

2.8 Analysis of the micropump concept.

During the intake stroke some energy and differential voltage potential need to be applied in order to make the plate deform. A 3D FEM simulation model is developed base on the continuing static von Kármán plate equations; these equations are coupled, non-linear, partial differential equations that describe the non-linear, large deflection problem in thin plate. These simulations are conducted for validating the result with well known analytical solution and also for sizing and finding the magnitude order of pressure/force required to deflect the plate and to match the design requirements.

That deformation is related to the amount of the electrical field applied on the electrodes. In other words, based on the electrostatic forces and geometric characteristics, the voltage potential needs to be determined that will generate the desired pressure on the plate. From this we can find the magnitude of the electric field size require for design.

A 3D-square diaphragm model based on continuous non linear plate-plate will also be used to estimate dimensional parameters more accurately. Some of the dimensions from the previous analysis will also be used. The real 3D rectangular diaphragm model has no analytical solution. Therefore, computational and numerical modeling will be employed to study and understand the performance of the micro pump.

Similarly, the size of the electrical field will be determined for the power stroke. It will be estimated based on electrostatic forces generated in parallel plates using the

separation distance at the location of the zipper's closing edge. However the gap separation varies with the horizontal distance due to the upper curved electrode.

2.9 CAD/CAE Design process.

The overall design process of the proposed work includes CAD modeling and CAE analysis, design model definition, fluid, electrical and structural analysis, design optimization and design model update. The design process starts with a CAD model for visualization and sizing purposes from this CAD model a simplified and a design model definition parameter is constructed after some preliminary sizing by static analysis of the requirements.

The design model generation consists of design parameterized definition, allowing modification of the geometric variables for simulation analysis. The language for generating the CAD-Geometry for the model generation is Python which is coupled with the multiphysics software. Phyton is a language that allows creating a simplified 2D, CAD model with parameters, so they can be changed quickly to generate a new model for simulation or optimization purposes. The CFD +ACE software uses this CAD model to apply the physics and governing equation that the model requires. A flowchart design approach carry out during this work is shown in Fig. 2.6.

Models are simulated and performance results obtained by the computational engineering analysis a mutiphysics CFD +ACE software. We are going to propose the design and analysis of the system. Final designs for fabrication may be done by Sandia National Laboratories; they have the technology to fabricate micro-fluidics devices using novel surface micro-machine techniques.

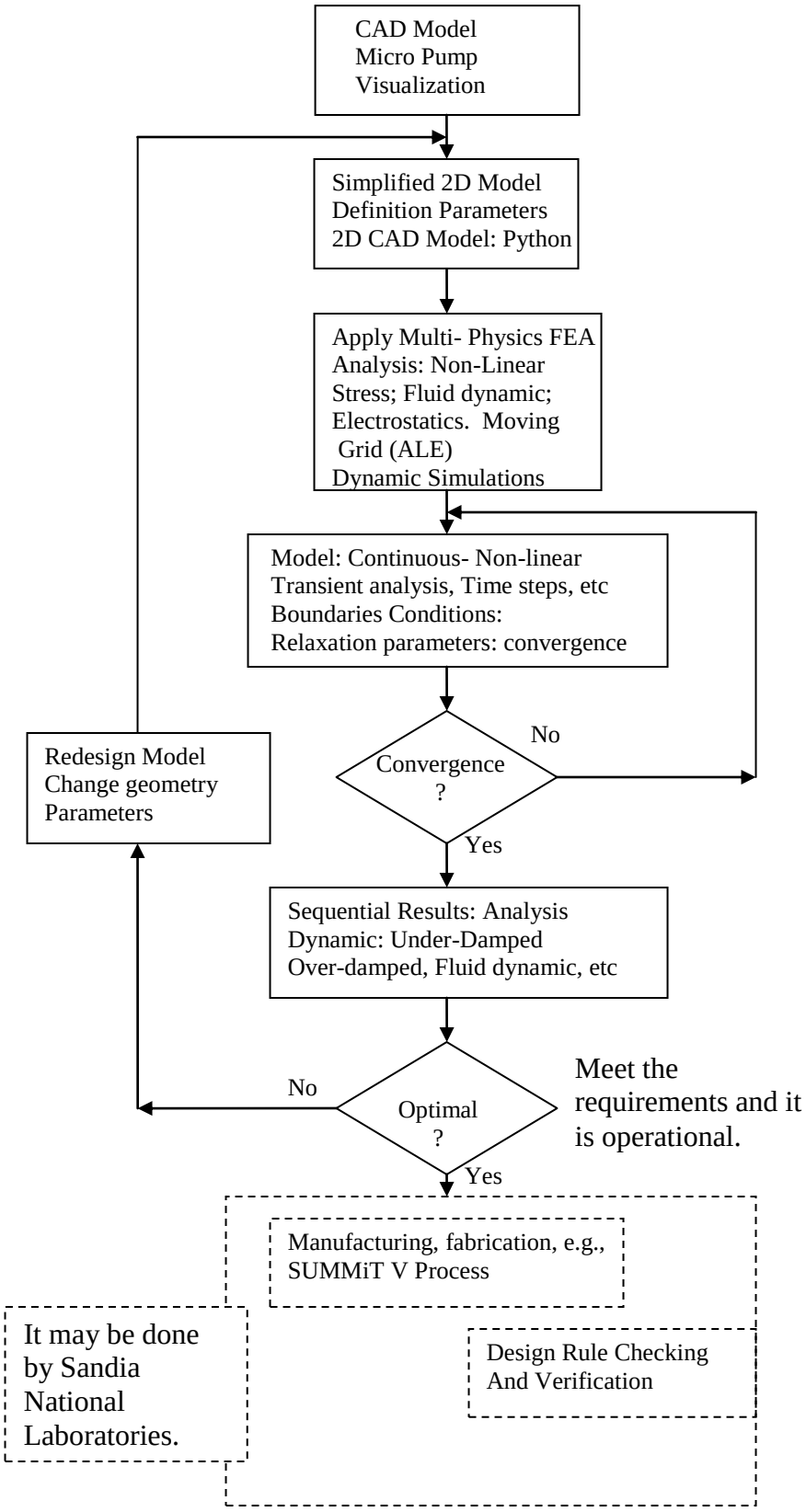

Fig. 2.6. Flow Chart of Design Process.

2.10 Field Strength of Dielectric Materials, and Electro-Zipper Pressure

The electrodes on the upper and lower chambers are coated with a dielectric material. The electro-zippering actuation of the plate against the dielectric is produced by applying a voltage ***V*** across the dielectric layer between the chamber electrodes and the plate; see Fig. 2.7.

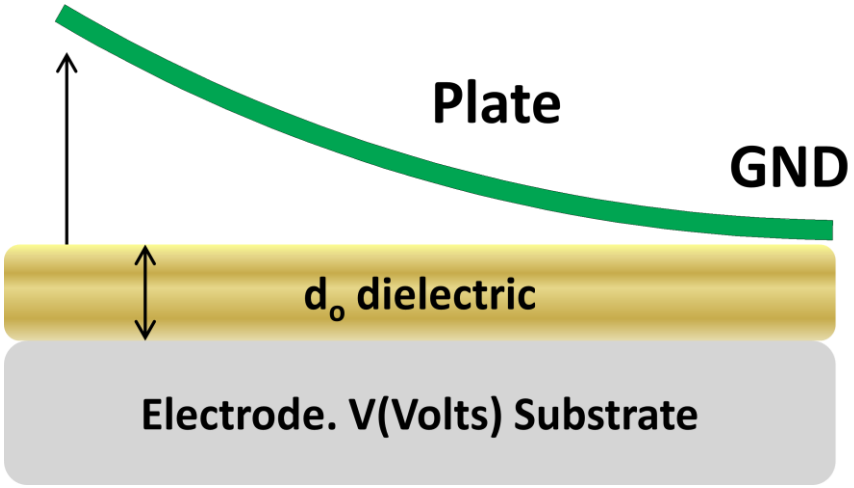

Fig. 2.7. Plate in contact with dielectric surface of electrode.

The grounded plate has contact with the dielectric surface, particularly at the outer edges of the pump chambers where the grounded plate is bonded to the surface of the dielectric material. With sufficient voltage across the dielectric, electro-zippering occurs at all edges of contact. The applied voltage ***V*** across the dielectric layer is limited by the breakdown voltage characteristics of the dielectric film material which is a function of the film thickness d_0 and the kind of dielectric material.

Candidates for the thin dielectric layer (see Fig. 2.8) include silicon dioxide (**SiO_2**), silicon nitride (Si_3N_4), and silicon oxynitride (SiON**)** (i.e., SiO_xN_y where ***x*** and ***y*** vary according to composition**).** In the literature**,** silicon nitride Si_3N_4 is often written as SiN_x with ***x***=1.33. The properties of silicon nitride SiN_x varies according to the ratio of N content to Si content (i.e., composition ***x*)**. We are interested in the breakdown voltages of these dielectrics (i.e., the maximum amount of applied voltage (volts) per nm of dielectric thickness).

The breakdown voltages are usually given in units of MV/cm (i.e., 100 volts/micron or 0.1 volts/nm**).** [Herman and Terry, 1991] developed a technique for PECVD (Plasma Enhanced Chemical Vapor Deposition) for the deposition of SiO2 that provided a breakdown field above 8.7 MV/cm (i.e., 0.87 volts/nm). [Sung, et al., 1993] demonstrated the growth of ultrathin 5nm-thick SiO_2 that had breakdown fields 12.6 to 13.4 MV/cm (i.e., 1.26 to 1.34 volts/nm).

[Morishita, et al., 1997] obtained a breakdown field strength of about 10 MV/cm for Si_3N_4 using atomic-layer chemical vapor deposition. [C. H. Ng, et al., 2003] achieved breakdown field strengths greater than 11MV/cm (i.e., 1.1 volts/nm) for PECVD depositions of 30nm-thick Si_3N_4 and SiON**.** [Tipirneni, et al., 2007] states that PECVD-deposited Si_3N_4 and SiO_2 generally have breakdown field strengths up to 12 MV/cm (i.e., 1.2 volts/nm)**.**

At Sandia, silicon oxynitride SiON is fabricated using the LPCVD method (Low pressure chemical vapor deposition) yielding breakdown voltages in the range 10-13

MV/cm (i.e., 1.0-1.3 volts/nm), e.g., Table II in [Habermehl, et al., 2005]. Therein, the composition $SiO_{0.60}N_{0.93}$ with 50nm thickness yielded breakdown voltage fields between 1.23 and 1.33 volts/nm.

Recently, Sandia fabricated SiON using the composition $SiO_{1.36}N_{0.42}$ with thicknesses 2-2.5 microns and the LPCVD method that held up to 3,000 volts without breakdown. Generally, the LPCVD method achieves higher breakdown field strengths than that of PECVD**.** The breakdown voltages 11.34-12.04 MV/cm were achieved for 50nm thick silicon nitride $SiN_{1.33}$**,** Table II in [Habermehl, et al., 2005].

In summary, there are deposition techniques for the dielectrics SiO2, Si3N4, SiON that yield breakdown field strengths in the range 1.2 volts/nm. We consider these dielectrics for the coatings on the upper and lower chambers of the micropump. Consequently, for the purposes of this dissertation, the ratio of maximum applied voltage to dielectric thickness is set at 1 volt/nm for the breakdown field strength of the dielectric coatings on the surfaces of the micropump chamber:

$$\frac{Maximum\ voltage\ across\ dielectric}{Thickness\ of\ \ dielectric\ layer} = \frac{1\ volt}{nm}$$

For example, if the dielectric thickness is 200nm, the applied voltage is limited to a maximum of 200 volts. If the dielectric thickness is 50nm, the applied voltage is limited to a maximum of 50 volts.

The relative permittivity for the dielectrics - silicon dioxide (**SiO_2**), silicon nitride (Si_3N_4), and silicon oxynitride (SiON) – have posted values between 3.9 for SiO_2

to **7.5** for Si_3N_4. For the purposes of this dissertation, we consider relative permittivity values as given in the following Table 2.1.

Table 2.1. Relative Permittivity of Dielectrics

	Silicon Dioxide (SiO2)	Silicon Oxynitride (SiON)	Silicon Nitride (Si3N4)
Relative Permittivity	3.9	5	6.5-7.5

Using the parallel plate model, Fig. 2.8, we derive an expression for the pressure on the plate due to electrostatics that attracts it towards the surface of the dielectric for an applied voltage ***V*** at the electrode.

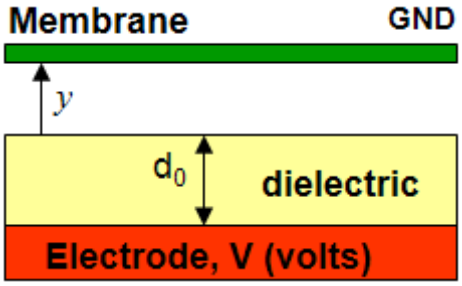

Fig. 2.8 Electrostatic forces provide electro-zipper pressure on plate

The electrostatic energy of the parallel plate system is given by $E = 0.5CV^2$ where ***C*** is the total capacitance and satisfies

$$\frac{1}{C} = \frac{1}{C_{air}} + \frac{1}{C_{dielectric}};\ C_{air} = \frac{\varepsilon_0 \varepsilon_a A}{y}; C_{dielectric} = \frac{\varepsilon_0 \varepsilon_d A}{d_0} \tag{2.1}$$

where ***A*** is the plate area, ε_0 is the permittivity of free space (i.e., $\varepsilon_0 = 8.85 \times 10^{-12} F/m$), ε_a is the relative permittivity of air, ε_d is the relative permittivity of the dielectric, ***x*** is the distance between the plate and the dielectric, and d_0 is the thickness of the dielectric.

The force of attraction is the partial derivative of the energy ***E*** with respect to ***y***. The pressure of attraction ***p***(***y***) on the plate is the force divided by the area ***A***.

$$p(y) = \frac{\partial}{\partial y}\left(E / A\right) = 0.5V^2 \frac{\partial}{\partial y}\left(\frac{C}{A}\right) \tag{2.2}$$

Carrying out the partial derivative with respect to ***y*** gives:

$$p\left(y\right) = -0.5\varepsilon_0\varepsilon_a \frac{(\lambda V)^2}{\left[1+\lambda y\right]^2} \text{ where } \lambda = \frac{\varepsilon_d}{\varepsilon_a d_0}; \tag{2.3}$$

The maximum pressure is obtained at ***x***=0:

$$p_{\max} = 0.5\varepsilon_0\varepsilon_a(\lambda V)^2; \tag{2.4}$$

In terms of the maximum pressure $p_{\max}$, the pressure of attraction ***p***(***y***) is given by

$$p\left(y\right) = -\frac{p_{\max}}{\left[1+\lambda y\right]^2}; \tag{2.5}$$

Since the pump chamber height (i.e., 20 microns) is small in comparison to the plate length or width (i.e., several mm), the parallel plate pressure ***p***(***y***) is a good approximation for the pressure acting on the plate, Fig. 2.9a, referred to herein as the electro-zipper pressure:

$$p_{electrozipper}\left(y\right) \cong -\frac{p_{\max}}{\left[1+\lambda y\right]^2}; \tag{2.6}$$

For the special case where ***V/d₀*** = 1volt/nm, $p_{\max}$ satisfies

$$p_{\max} = 0.5\varepsilon_0\varepsilon_a(\varepsilon_d / \varepsilon_a)^2\left(V / d_0\right)^2 = \varepsilon_a(\varepsilon_d / \varepsilon_a)^2\left(10^9 V / m\right)^2\left(0.5*8.85\times10^{-12} F / m\right);$$

$$p_{\max} = \varepsilon_a(\varepsilon_d / \varepsilon_a)^2\left(4.425\times10^6 Pa\right) = \varepsilon_a(\varepsilon_d / \varepsilon_a)^2 43.67\ atm; \tag{2.7}$$

where 101,325 ***Pa*** = 1.0 atm. This indicates that an enormous amount of pressure can be applied at the area where the plate and dielectric layer come together, see Fig. 2.9.

Table 2.2. Maximum Electro-zipper Pressure at Surface Junction of Plate and Dielectric Layer

Dielectric Material	Air $\varepsilon_d = 1$	Silicon Dioxide (SiO2) $\varepsilon_d = 3.9$	**Silicon Oxynitride (SiON)** $\varepsilon_d = 5$	Silicon Nitride (Si3N4) $\varepsilon_d = 6.5$
$p_{\max}$ @1 *volt / nm*	***44 atm***	***664 atm***	***1,092 atm***	***1,845 atm***

The electro-zipper pressure $p(y)$ depends on the distance ***y*** that separates the plate from the surface of the dielectric layer.

$$p(y) = -\frac{p_{\max}}{\left[1+\lambda y\right]^2}; \tag{2.9}$$

The factor $1/\left[1+\lambda y\right]^2$ decreases rapidly as the distance x extends out to a distance equal to the thickness $\boldsymbol{d_0}$ of the dielectric layer. This factor is plotted in Figs. 2.9a, b, c for various dielectrics. As an example of the rapid decrease, the electro-zipper pressure for an SiO2 dielectric layer would decrease to about 11.5% of its maximum value when the distance ***x*** is one-half the thickness of the dielectric (i.e., ratio $\boldsymbol{y/d_0}$=0.5) and would be about 4% when the distance ***y*** is equal to the thickness of the dielectric (i.e., ratio $\boldsymbol{y/d_0}$=1).

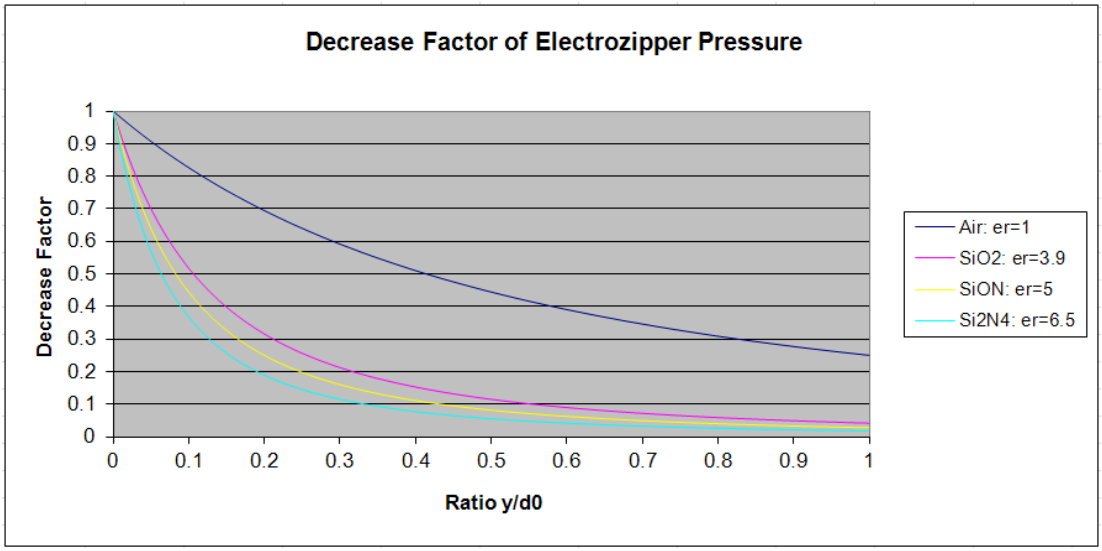

Fig. 2.9a. Electro-zipper pressure factor decreases rapidly as the distance ***y*** increases to one thickness of the dielectric.

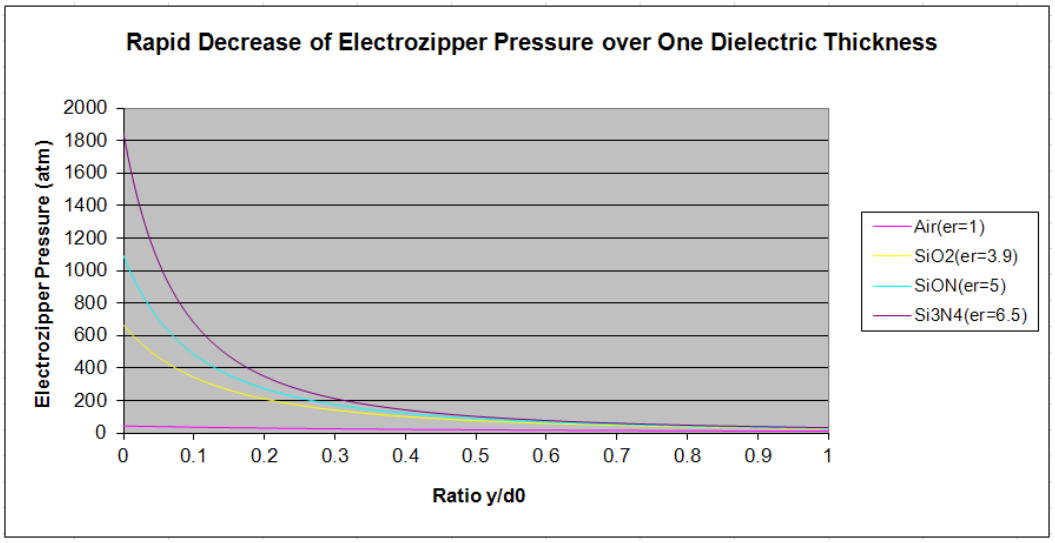

Fig. 2.9b. Electro-zipper pressure decreases rapidly as the distance ***y*** increases to one thickness of the dielectric.

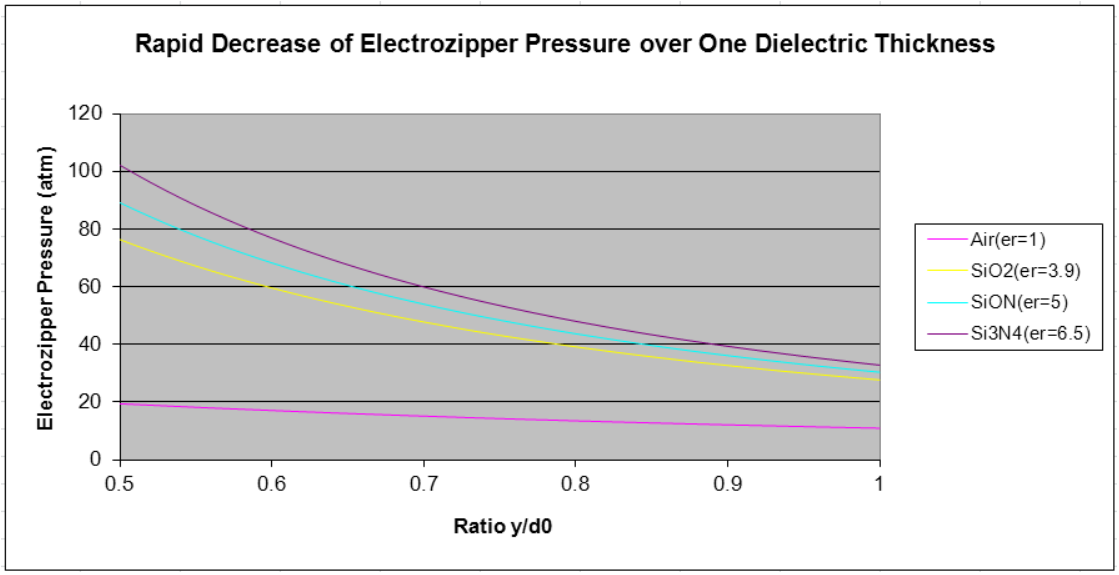

Fig. 2.9c. Electro-zipper pressure decreases rapidly as the distance ***y*** increases from 0.5 to one thickness of the dielectric.

For the case of an ideal (i.e., simple bending and linear deflections less than half the thickness) fixed (i.e., clamped) circular plate or plate of radius ***a*** that is pressurized on one side by pressure $\boldsymbol{p_0}$, the deflection $\delta(r)$ at radius r is given by

$$\delta(r) = \delta_{\max}\left(1-\left(\frac{r}{a}\right)^2\right)^2 \quad where\ a \geq r \geq 0 \tag{2.10}$$

where $\delta_{\max}$ depends on the pressure $\boldsymbol{p_0}$, material properties of the plate geometric properties and is given by:

$$\delta_{\max} = \frac{p_0 a^4}{64D};\ D = \frac{Et^3}{12\left(1-\nu^2\right)} \tag{2.11}$$

where *a* is the radius of the circular plate *t* is the plate thickness, E is Young's modulus, and *v* is Poisson's ratio. In terms of the deflection $y = \delta(r)$, the pressure of attraction ***p***(***r***) as a function of the radius ***r*** is given by

$$p(r) = -\frac{p_{\max}}{\left[1+\lambda\delta_{\max}\left(1-\left(\frac{r}{a}\right)^2\right)^2\right]^2}; \tag{2.12}$$

Let $x=a-r$. In terms of x, we can write

$$\lambda\delta_{\max}\left(1-\left(\frac{r}{a}\right)^2\right)^2 = \frac{\varepsilon_a}{\varepsilon_d}\frac{t}{d_0}\frac{3p_0}{4E}\frac{a^2}{t^2}\frac{x^2}{t^2}\left(1-\nu^2\right)\left(1-\frac{x}{2a}\right)^2 \tag{2.13}$$

For illustration purposes, we consider the ratios

$$\frac{t}{d_0} = 50;\ \ \frac{p_0}{E} = \frac{1}{1,600,000};\ \ \frac{a}{t} = 100;\ \ \nu = 0.23;\ \ 0 \le \frac{x}{t} \le 2 \tag{2.14}$$

In terms of these ratios, we have

$$\lambda\delta_{\max}\left(1-\left(\frac{r}{a}\right)^2\right)^2 = \frac{\varepsilon_a}{\varepsilon_d}\frac{15}{64}\frac{x^2}{t^2}\left(1-\nu^2\right)\left(1-\frac{x}{200t}\right)^2 \tag{2.15}$$

The following electro-pressure ratio is plotted in Fig. 2.8.4 over the range $0 \le \frac{x}{t} \le 2$:

$$\frac{p(x)}{p_{\max}} = -\frac{1}{\left[1+\frac{\varepsilon_a}{\varepsilon_d}\frac{15}{64}\frac{x^2}{t^2}\left(1-\nu^2\right)\left(1-\frac{x}{200t}\right)^2\right]^2}; \qquad (2.16)$$

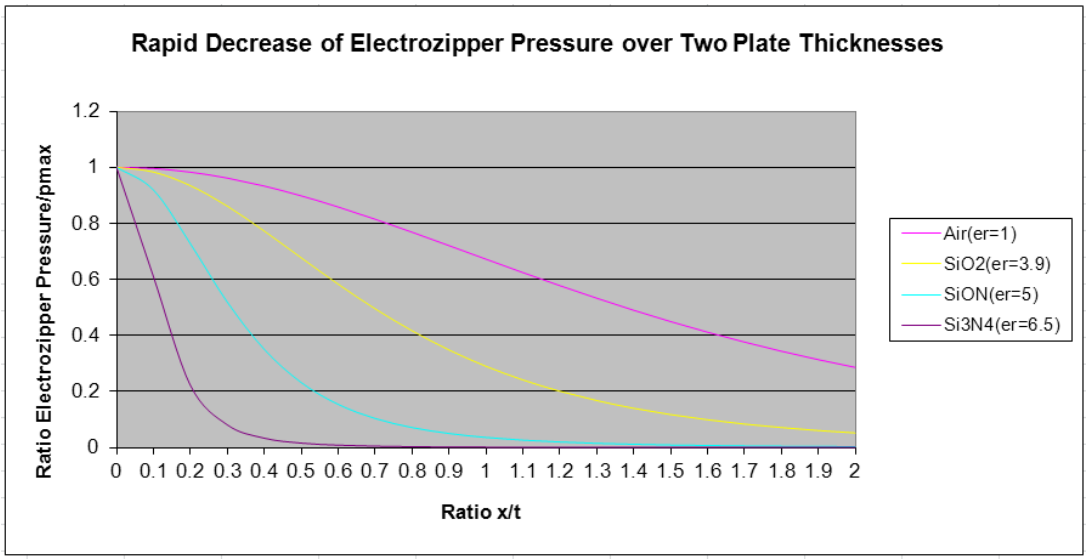

Fig. 2.10 Electro-zipper pressure decreases rapidly as the distance ***x*** increases to two thicknesses of the plate thickness ***t***.

Figs. 2.9 and 2.10 illustrate that electro-zipper pressure is significant only over distances comparable to dielectric thickness in the y deflection direction and to plate thickness in the *x* radial direction.

Therefore, the pressure is high at the edge but quickly diminish as long it moves away of the edges.

For more realistic cases (i.e., bending, stretching, nonlinear deflections), 3D simulations are run to obtain a more accurate relationship between radius point $\boldsymbol{r}$ and deflection $\boldsymbol{y} = \delta(r)$ for use in the electro-zipper pressure equation $p(y)$.

CHAPTER 3

FEM SIMULATION AND MODEL VALIDATION OF NONLINEAR LARGE DISPLACEMENT THIN PLATE

3.1 Non linear large deflection of rectangular plates.

The fundamental concept behind the design of this micro pump is the solution of the non-linear stretching and bending of thin plate for large displacement. Classical plate theory is applied when the deflection is less than 1/5 of the thicknesses [Chia 1980] [Reddy 2004] of the plate and the relationship between the load and deflection is linear, it assumes that the middle plane does not develop tensile stresses.

However when the deflection of the plate is larger than 1/5 of the thicknesses, the middle plane of the plate develops stresses than support part of the load and therefore increase the load capacity of the plate. The nonlinear theory for large displacement is also applicable if the magnitude of deflection is smaller than the lateral dimension of the plate. Plates with large deflection can be seen as a plate that carry bending and stretches stresses.

The governing partial differential equations for the non-linear plate were derived by von Kármán in 1910 [Szilard 1974]. The von Kármán equations are coupled non-linear partial differential equation of fourth order. These equations are very complex and finding an exact solution is a formidable task and very rare. Researchers use

indirect analytical methods to find a few solutions under certain cases. These indirect methods which are analytical approximations can be classified as: double Fourier series, generalized Fourier series, perturbation techniques, Galerkin's method, Ritz method, finite difference techniques as well as finite element methods [Chia, 1973].

Need to be solved in designing a micropump based on deflection of the plate as a moving part for pumping the fluid, the non-linear, coupled partial differential equation for large deflection problem. The Finite element method is required to solve the non-linear von Kármán governing equations for large displacement. In order to trust in the results for the multi-physics simulation, first of all, it needs to validate the solution of the governing equation.

The validation is investigated under clamped edges condition and for square plate with Poisson ratio υ=0.316 as the previous analytical solution stated by [Sundara Raja, Levy, 1942, Yamaki, 1961] and uniformly distributed pressure. The geometry is described by Fig. 3.0.

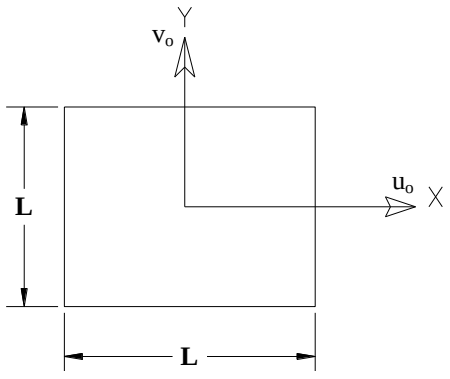

Fig. 3.0. Geometry of square plate with clamped edges

3.2 Von Kármán equations for Non-Linear Rectangular Plate.

The governing coupled non-linear partial differential equation that treat large displacement in plate structures were developed by von Kármán in 1910, and they are:

$$D\nabla^4 w(x,y) = p + h\left(\frac{\partial^2 w}{\partial x^2}\frac{\partial^2 F}{\partial y^2} + \frac{\partial^2 w}{\partial y^2}\frac{\partial^2 F}{\partial x^2} - 2\frac{\partial^2 w}{\partial x \partial y}\frac{\partial^2 F}{\partial x \partial y}\right) \tag{3.1}$$

$$\frac{1}{E}\nabla^4 F(x,y) = \left(\left(\frac{\partial^2 w}{\partial x \partial y}\right)^2 - \frac{\partial^2 w}{\partial x^2}\frac{\partial^2 w}{\partial y^2}\right) \tag{3.2}$$

the nonlinear biharmonic is:

$$\nabla^4 w(x,y) = \frac{\partial^4 w}{\partial x^4} + 2\frac{\partial^4 w}{\partial x^2 \partial y^2} + \frac{\partial^4 w}{\partial x^4} \tag{3.3}$$

Where:

w = Deflection of the plate in z direction.

P = Load pressure (uniformly distributed pressure).

h = Thickness of the plate.

E = Young's modulus of the material of the plate

D = Flexural rigidity of plate.

F = Stress Function (Airy Stress Function)

The mid-plane stresses are:

$$\sigma_x = \frac{\partial^2 F}{\partial y^2} \quad , \quad \sigma_y = \frac{\partial^2 F}{\partial x^2} \quad , \quad \tau_{xy} = -\frac{\partial^2 F}{\partial x \partial y} \tag{3.4}$$

Clamped edges: boundary conditions.

i) At x = ±L/2; u = 0, w = 0,

$$\frac{\partial w}{\partial x} = 0 \tag{3.5}$$

ii) At y = ±L/2; v = 0, w = 0,

$$\frac{\partial w}{\partial y} = 0 \tag{3.6}$$

The solution, based on an approximation with double series by K. T. Sundara Raja and Matin Naqvi, are presented here as a analytical model reference and the FEM solution obtained is agreement with the analytical-approximation solution presented by [levy, 1942, Yamaki, Way, Chia 1973] under same conditions.

A classical and linear solution is shown in Fig. 3.1 [Boresi & Schmidt 1978] with the non-linear theory case as comparison with the Finite element result obtained by the software simulations.

3.3 Finite Element Method with CFD-ACE© Software.

The stress module for the Finite element is activated with non-linear solid shell brick elements and the Boundary condition are chosen to be fixed at $x = \pm L/2$ and $y = \pm L/2$.

The solid shell brick element are more accurate than the standard elements (triangle, hexahedrals, etc). Beside, a second order elements can be used, if this is necessary, however simulations results show the same results for second order element and they obtained the same result as the shell elements, however the memory and computational time requirements are increased by factor of 3 using second order elements.

The plate analysis is carry out on square plate with L=2,000 microns, thickness of 1.5 microns, uniform load-pressure, clamped edges, and isotropic material with Young's Modulus of $1.6x10^{+11}$ N/m^2 and Poisson ratio υ =0.316.

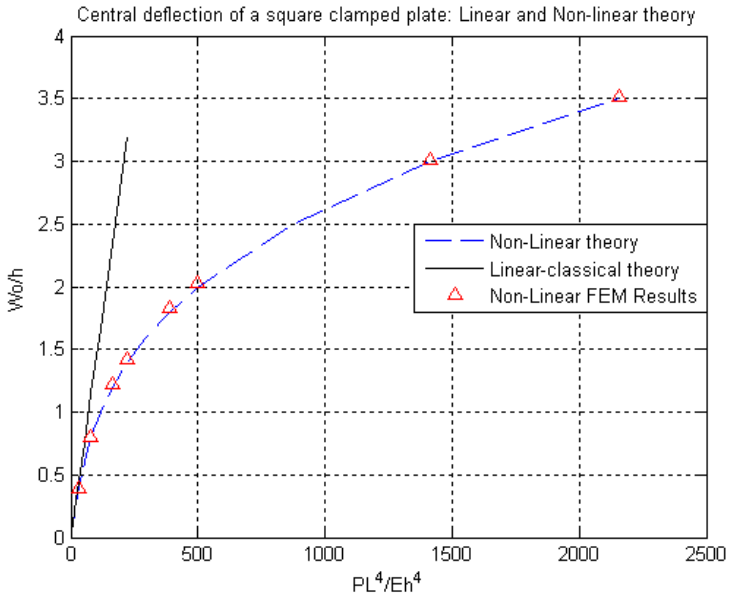

Fig. 3.1. Central deflection of a clamped square plate: Linear, Non-Linear and FEM results for $PL^4/Eh^4 \rightarrow$[0 - 2158]

Validation results on Fig. 3.1 and Fig. 3.2 show that, the non-linear solid shell brick elements has the same results with the non-linear analytical approximation by K.T. Sundara Raja. Several authors [Levy (1942), Yamaki (1961)] have approximate and close solutions for the square and clamped plate as Sundara Raja.

Fig. 3.1, show the simulation result for different values of parameter PL^4/Eh^4 in the moderately large deflection are in agreement with these values and reproduce and match the non-linear theory of the large plate displacement.

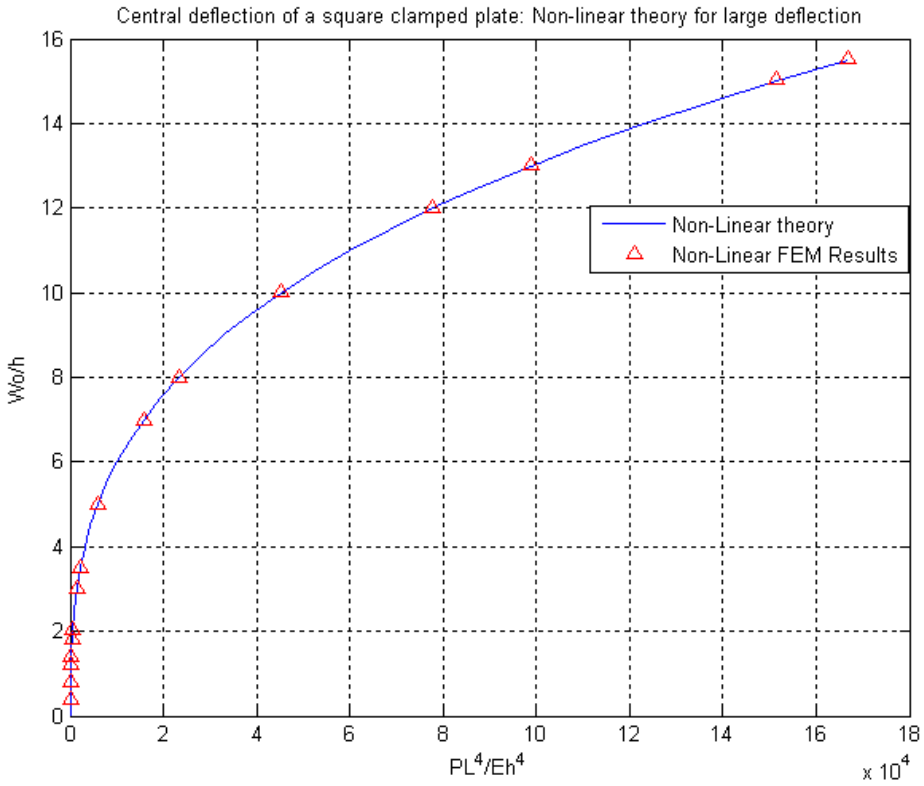

Fig. 3.2. Central deflection of a clamped square plate: Non-Linear and FEM results for large displacements.

The maximum large deflection in this case is around 20 microns and it can be seen that FEM simulation result match very well the non-linear theory, Fig. 3.2 show the entire range from 0 to 23 microns, corresponding to w_o/h [0 - 15.3].

Particular cases of the simulation can be seen in Fig. 3.3 and Fig. 3.4 for different values of $PL^4/(Eh^4)$=[31 - 166,885] which correspond to pressure [1.6 – 8449] N/m^2, plate with thickness of h =1.5 microns.

The simulation using finite element method with CFD-ACE stress module has good agreement with the non-linear theory solution of the von Kármán equations. As we said before, the FEM needs to solve the plate stress function satisfactory which is the foundation of this work in order to guarantee reliable result with the coupling with fluids and the electrostatic field, under moving boundaries feature. These multi-physics coupling fields can be seen as the pressure/force from these fields is applied to the plate surface in order to solve the stresses.

3.4 CFD ACE Model for non-linear large deflection problem.

The simulation model is based on a square plate whose material is structural polysilicon and whose square dimension is 2000 microns with a thickness of h=1.5 microns. The material properties of polysilicon are given in Table 3.4.1.

Table 3.4.1 Material properties for structural polysilicon.

Mechanical Properties	Polysilicon (Structural)
Young's Modulus (N/m^2) :	$1.6 \times 10^{+011}$
Modulus of Rigidity (N/m^2) :	$77.2 \times 10^{+09}$
Ultimate strength tension (N/m^2) :	$1.55 \times 10^{+09}$
Coefficient of Thermal Expansion (1/ºC) :	2.5×10^{-06}
Poisson's Ratio :	0.23
Density (Kg/m^3) :	2,331

Because of the symmetry of this model, only a quarter of model was used for modeling the membrane. The elements chosen to mesh the entire volume were chosen to be solid-shell-hexahedral-brick type, first order with 8 noded-hexahedral.

However simulation with second order hexahedral were perfomed to compare the result, the second order brick element, become a 20 noded hexahedral, it just the solver will added a node in the middle of the edge and these simulation require more memory and computational power to perform well, and they obtained the same results as first order solid-shell hexahedral elements.

Therefore, in order to model a membrane with a dimension 2000microns x 2000 microns and high of 1.5 microns, only a quarter model is necessary due to the symmetry

advantage, only a square footprint of 1000 microns and high of 1.5 microns was developed, the number of grid points was chose to be 51 on the long edges and for the high edge it was 7 grid points. Therefore, as results; 1 Volume (Polysilicone membrane) structured meshing, with 15000 total cells hexahedral-solid-shellelement and 18207 nodes.

The simulation converged at 10 iteration with a residual criterion value for displacement of $1x10^{-04}$, 100 iteration for shared displacement were chosen and for the stress solver it was chosen to run 100 non-linear iteration under "calculated loads first" scheme with a criterion residual value of convergence of $1x10^{-09}$. Once it calculated the force, it will update the displacement and repeat again the cycle and this process took 566.95 seconds for each simulation. Moving grid deformation feature was chosen in order to simulate the deformation on the membrane.

As a result of modeling with FEM a total volume is 1, six total boundaries conditions were applied, total of nodes are 18207, total hexahedral (solid-shell-bricks type elements) cells are 15000, structured meshing grid. Steady analysis condition and the time accuracy is Euler first order for this model.

A summarize from the simulation result is following:

"Initialization of solver for solving FEM module
Total number of FEM Nodes : 18207
Maximum number of DOF per node : 3
Total number of FEM Equations : 54621
Total number of FEM Volume elements : 15000
Number of FEM Boundary face elements and nodes (free) : 2500 2601
Number of FEM Boundary face elements and nodes (fix Displacement) : 1200 1400
Number of FEM Boundary face elements and nodes (Load) : 2500 2601
Total number of FEM Boundary face elements : 6200 "
"Summary of 3D Grid Data
Total No. of nodes = 18207
No. of quad faces = 48100
Total No. of faces = 48100
No. of hexa cells = 15000
Total No. of cells = 15000 "
Problem converged to specified criterion (1.00E-04) in 10 iterations.

CPU Time at the end of = 1 time steps.
End of Output Elapsed Time= 5.669531E+02 Delta-time= 5.650781E+02"

3.5 Set up boundary conditions

For the plate model the boundaries condition are provided, due to the symmetry, two are chosen to be symmetry, and two boundaries to be fixed (clamped), the top surface is assigned to be free and the bottom surface is exposed to uniform constant pressure. Equations 3.5 and 3.6 are provided.

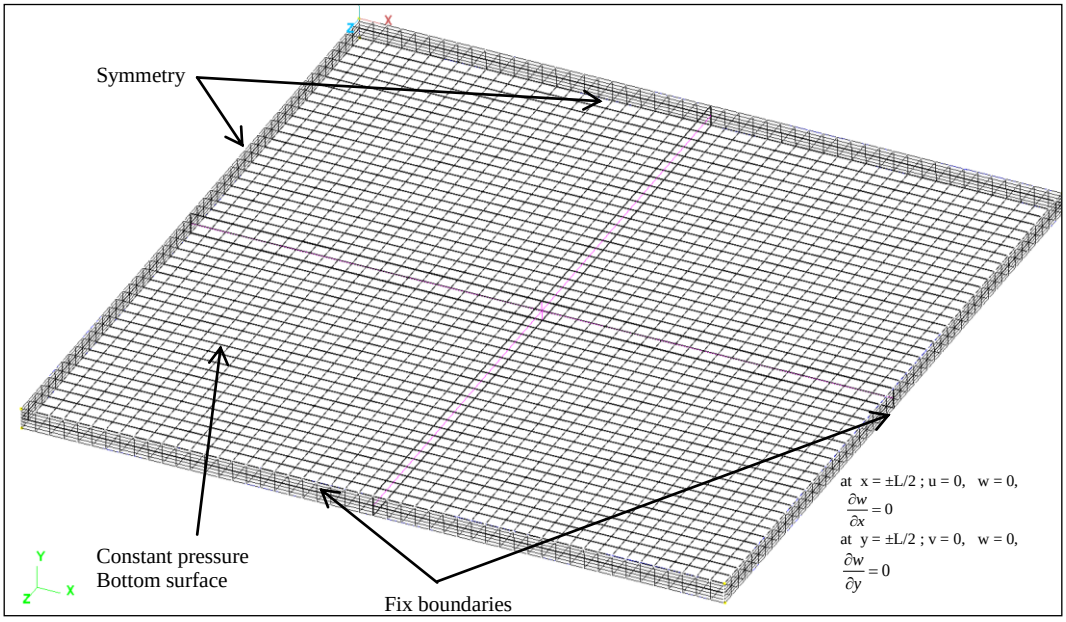

Fig. 3.3 Boundaries conditions applied to symetric ¼ square plate.

The Fig. 3.4 and Fig. 3.5 shows the simulation results for each simulation with pressure [1.6 – 8449] N/m^2, plate with thickness of h =1.5 microns. This results were summarize and presented on Fig. 3.2, showing completed agreement with the analytical solution provide by K.T. Sundara Raja and [Levy (1942), Yamaki (1961)]

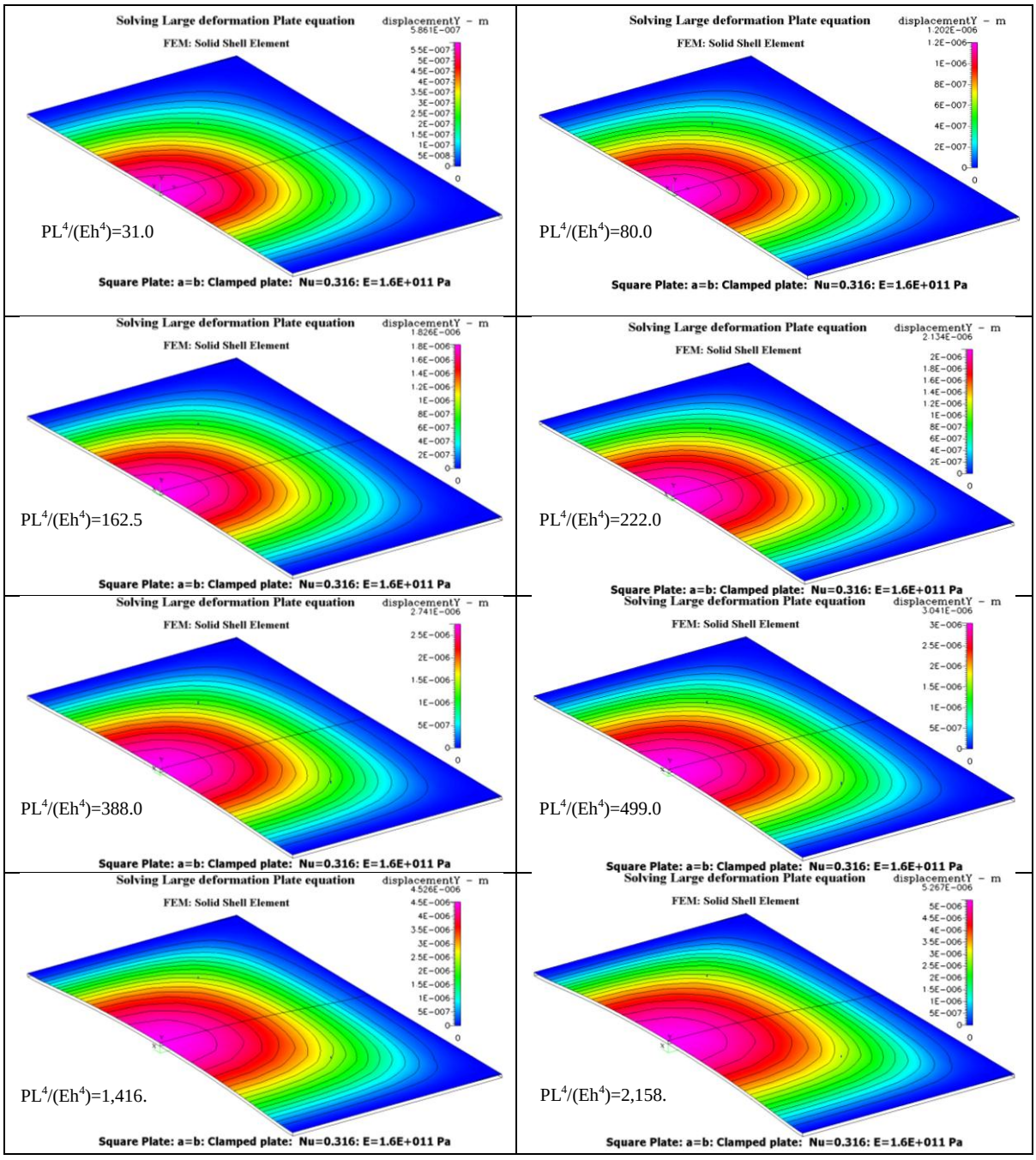

Fig. 3.4 Results; Large displacements for square plate with clamped edge.
$PL^4/(Eh^4)$=[31-2,158]

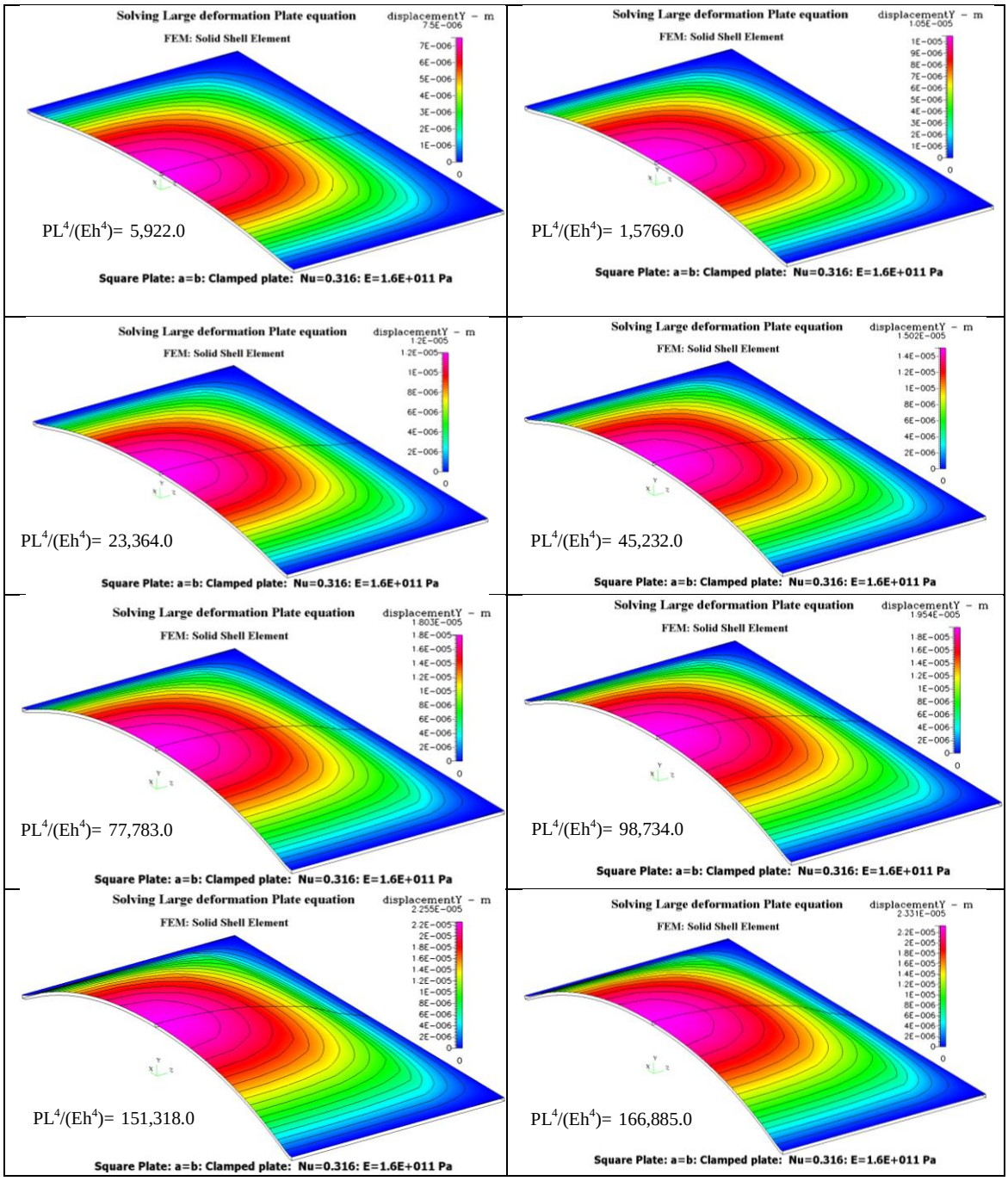

Fig. 3.5 Results Large displacements for square plate with clamped edge. $PL^4/(Eh^4)$ = [5,922-166,885]

CHAPTER 4

MATHEMATICAL MODELING AND NUMERICAL SIMULATION INTAKE POWER STROKE OF MICROPUMP

4.1 Overview

The mathematical model and simulation of the 2D intake power stroke for the micropump will be described in this chapter. The intake power stroke of this micro-pump is based on electrostatic actuation and it will be analyzed under quasi-static condition, the mathematical model proposed is based on continuum solid mechanics, the inertial effect of the plate have been neglected and this model.

The analytical proposed mathematical model will be compared and validated with the Mutiphysics CFD-ACE+© Software. The Finite Volume approach is adopted due to the conservation energy and mass laws. The analysis has been done under 2D modeling and simulation for the basic principle of the micro-pump during the intake stroke stage. Different physics parameters and geometric dimensions have been using to target the design rules for the positive displacement micropump. Complete and exhaustive parameter sensitivity analysis will be described in order to show how the performance is targeting the design rules required for micropumps. For the simulation a full nonlinear fluid - structure and electrostatic coupling effect has been used under mutiphysics simulation to capture the realistic behavior of this micro device. The simplified mathematical model proposed is based on quasi-static condition, to reveal what are the physics parameters involved to performance regarding with the design rules.

This chapter begins with the geometry description of the electrostatic micropump during the intake power stroke and the relevant physics parameters involved during the process. The 2D simulation model and the physics parameters used in this work are described next. A simplified and reduced quasi-static mathematical model is then proposed to capture the behavior of the main parameters involved in the simulation to match those design which they will be acceptable for the requirements of this dissertation. The main goal is finding the suitable candidates to achieve large differential pressure of 1 atm (101,325 KPa).

Geometry Modeling of the Intake Power Stroke

A 3D CAD model of the micropump is presented in Fig. 4.1 part a, and part b. It shows the geometry and the main parts of the design; on the top of the curved electrodes there is a groove for venting the air out when the plate is going up and it moves the above air fluid out against to atmospherically pressure, exhausting the air out.

At the same time the plate moves up, it creates an expansion chamber underneath which is filled with fluid (air) during this motion. Therefore, the intake power stroke energy has to overcome the air resistance fluid viscosity, the stretching and bending of the plate structure and the residual stresses applied on the plate.

A 2D CAD simplified model can be extracted and it is presented in Fig. 4.1 part c. It shows a plate which has thickness ***t*** range from 2 micron to 10 microns, and total length of 4000 microns. The total length is divided in three sections of 2000 microns each; these sections are separated by a thin dielectric layer. Fig. 4.1 part d, it shows the same model but scale up 5 times for a sake of clearly the internal curved chamber above the

plate; The material chosen for the plate was Polysilicon and the maximum height of the circular chamber above the plate is 20 microns, and the maximum surface area available due to the integrated circuit footprint is 4000 microns. However for future additional design it can be increased if needed. For this design study, the maximum area available is 4mm x 2mm. That is usually the footprint for fabrication that for instance, Sandia National Laboratory used to mass production MEMS devices.

For the 2D micropump simulation and modeling one of the sections, it will be considered and analyzed; it has a surface area of 2mm x 2mm with 20 microns height. The other two sections have the same surface area and they will have the same motion just in sequence to squeeze the air fluid from inlet to outlet ports.

The curved Chamber above the plate is constructed with a new Dry etching process developed recently in Sandia National Lab. The curved chambers are wired up to electrical connectors in order to applied voltage and create the electrical field to attract the plate which is connected to the ground all the time. There are dielectric material layer on both side of the plate; the thickness of the dielectric material it has been chosen to be 200nm thin, because of the maximum break voltage allowed.

A previous table on chapter 2.0, table 2.9 shows the dielectric material and its dielectric permittivity properties used for the simulation. The two dielectric layers are placed fix on the curved chamber's surface and on the silicon substrate underneath of the plate; this design feature simplifies the mutiphysics FVM-FEM simulation.

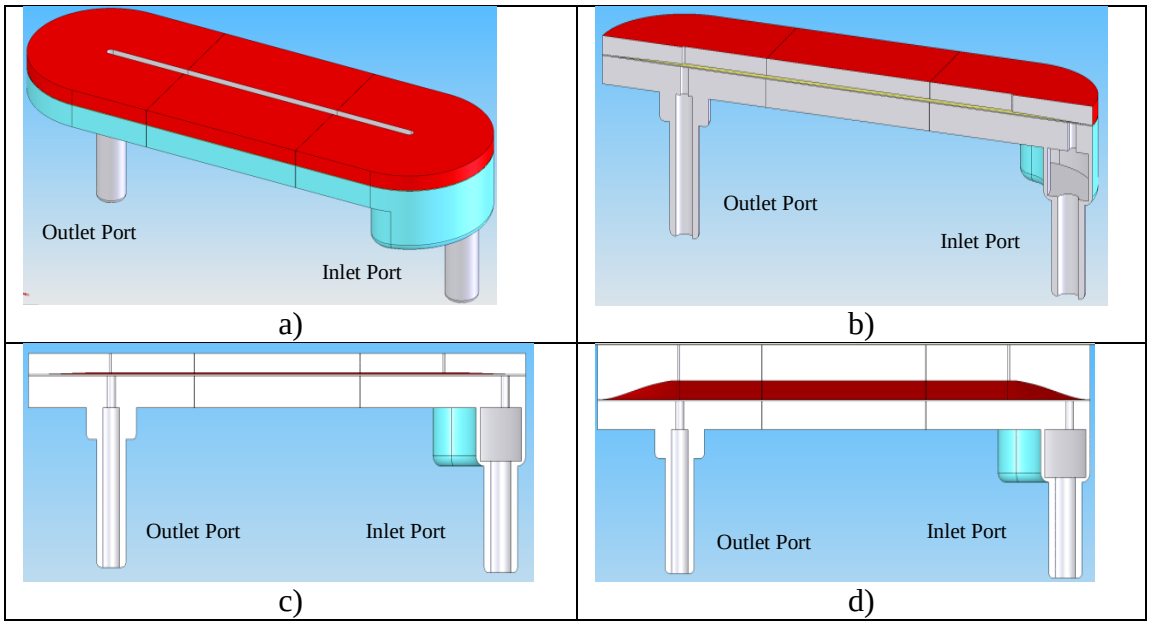

Fig. 4.1 a) 3D CAD Model of the Electrostatic micropump. b) Section Cut View. c) Front cut view y d) 2D Chamber scale up 5 times in Z direction.

The curved chamber above the plate is constructed with a new Dry Etching process developed recently in Sandia national Lab.

4.3The Physics Parameters for Power Intake Stroke Simulation

Several geometry and physics parameters were considered to analysis in order to create a region of possible candidates to performance well. The variables considered on this study are mentioned on table 4.1. This table shows that the analysis was done on the maximum footprint area available of 4mm x2mmx20 μm. However, for the 2D study, the length of 2mm and the height was taken for simulation and the analytical result. The curved chamber model was to be chosen as a quadratic model, due to fabrication process it can be done as well as favor the natural shape for plate deformations under external pressure.

Table 4.1 Design Parameter used for sizing the micropump for the intake stroke.

Foot-print: design (2D)	Dielectric material and thickness	Thickness of plate	Residual Stresses RSxx[MPa]	Max Applied Voltages [V]
2mmx20μm Curved Chamber Shape: quadratic model	SiO2 (e_{SiO2} 3.9) d_o [200]nm Air (e_{air} 1) d_o [5nm-20 μm]	2 μm	200	100
		4 μm	400	125
		4 μm	400	150
		8 μm	800	175
		10 μm	1000	200

4.4. The Mathematical Model for the Power Intake Stroke.

The Fig. 4.2 shows a cross section of the 2D micropump, where the bottom layer is actually the Silicon Substrate (Wafer), and a thin layer of 200nm has been deposited in between the Polysilicon plate and the bottom and upper curved conductor.

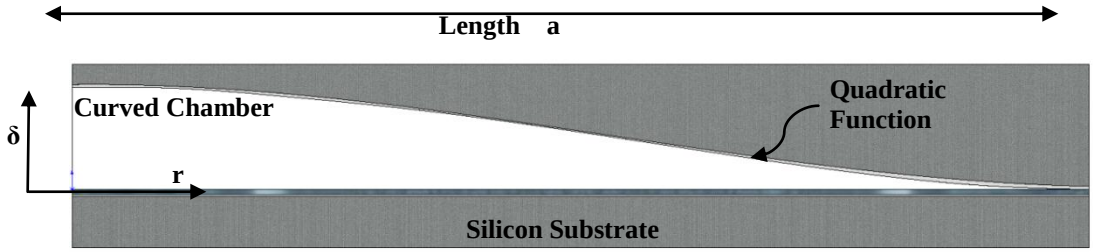

Fig. 4.2. 2D Half Profile of curved chamber and Dioxide Silicon (SiO_2) layer and silicon substrate (5 times scale up in Z direction)

Fig. 4.3 shows a detailed zooming region on the clamped edge side to expose the dielectric deposition of the 200nm dioxide layer (SiO2) which isolates the plate conductor from the upper and lower electrodes.

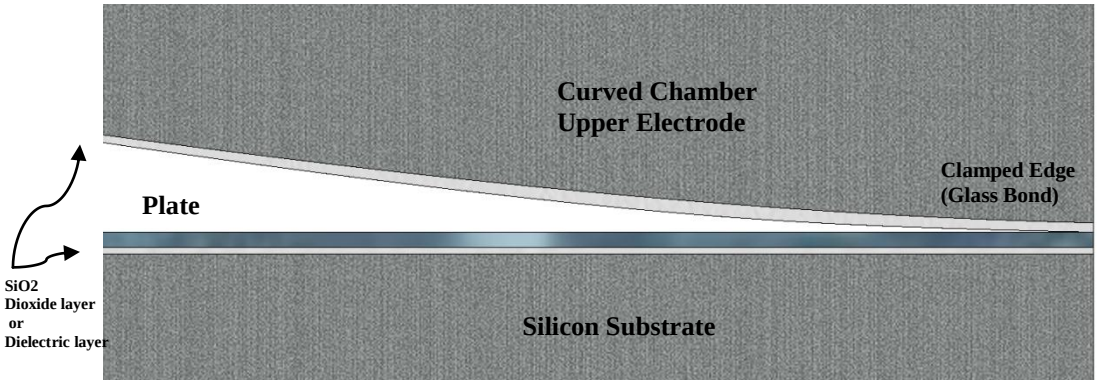

Fig. 4.3. Clamped Edge detail for the 2D micropump

4.5 The working Mechanism for Intake Power Stroke

The working mechanism on the intake power stroke is due to the electrostatic forces created by the applied differential voltage between the upper electrode and the thin plate; it creates a force that is inversely proportional to the separation distance from the two conductors. The Electrostatic forces create an attracted moment that pulls up the thin plate against the dielectric wall, which causes stretching and bending simultaneously on the thin plate.

The electric energy applied to the upper electrode has to balance the deformation energy on the stretching part of the plate and the bending moment on the plate as well. Besides, it is considered that the thin plate has residual tension stress build up due to fabrication process, which it is make hard to pull up the thin plate. And that residual stresses can be adjusted as needed it upon the fabrication temperature and release.

As shown in Fig. 4.4, it is considered the intake cycle of the electro-zipper based micro-pump, where the geometry parameters are highlight. The plate electro-zips up along the surface of the upper chamber and will stop at the point $\boldsymbol{a}$ where the tensile stresses σ in the plate balance the electrostatic forces that are attracting the plate against to the chamber walls. Therefore, the main objective is to determine the maximum

tensile residual stresses σ that a plate can have and still completely open up on the intake cycle.

The following aspects are noted:

(1) The bending stresses are zero where the plate is straight along the chamber wall (i.e., to the right before point "***a***" and to the left after point "***b***"). That is, the resulting moments at points "***a***" and "***b***" are zero. At the point "***a***", the moment due to tensile stresses must balance the moment due to electrostatic forces. At the point "b", the moment due to tensile stresses must balance the moment due to electrostatic forces. As a note the bending moment on the plate after point "***b***" is actually close to zero, there is a very large curvature due to stiffness of the plate, however the axial tension stress are dominant and on the half point of the plate where the slope it is also zero the tension force is $F=\sigma\tau$.

(2) The maximum bending stress σ_B in the plate occurs between points "***a***" and "***b***" and depends on bending stresses created by the electrostatics forces and the opposing forces due to the tensile stresses in the plate.

(3) The tensile stresses are the sum of the residual stresses in the plate plus the stresses due to tensile strain in the plate.

(4) At the point "***a***", the force perpendicular to the chamber surface due to tensile stresses must be less than that due to electrostatics.

(5) The maximum tensile stresses that can be supported by a plate electro-zippering all the way up the wall is determined at the point along the wall that has the greatest slope (i.e., angle ϕ) with the horizontal.

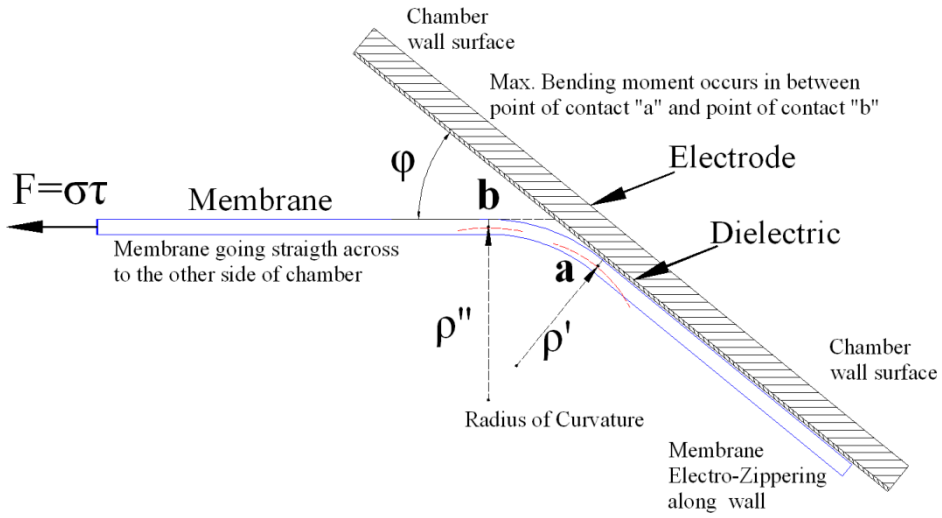

Fig. 4.4 Model of the Power Intake cycle, electro-zippering pump.

4.6 Shape of Chamber and Point of Maximum Slope

The shape of the curved chamber above the polysilicon plate was considered to be a quadratic function due to realistic shape and also for fabrication purposes. Therefore, the relationship between the curved upper chamber of radius a with the deflection profile ***δ(r)*** at radius ***r*** is given by quadratic equation 4.1. The Fig. 4.5 shows the plate and a particular interest point where the plate was found to stop just before to reach the maximum slope.

$$\delta(r) = \delta_{max}\left[1 - \left(\frac{r}{a}\right)^2\right]^2, where\ a \geq r \geq 0 \qquad (4.1)$$

where

δ(r) is the height of the chamber (microns).

δ_{max} is the maximum height, 20 microns for the analysis at ***r = 0.***

a is the maximum radius of the pump, 1000 microns.

δ_{max} is the maximum deflection at the center of the chamber.

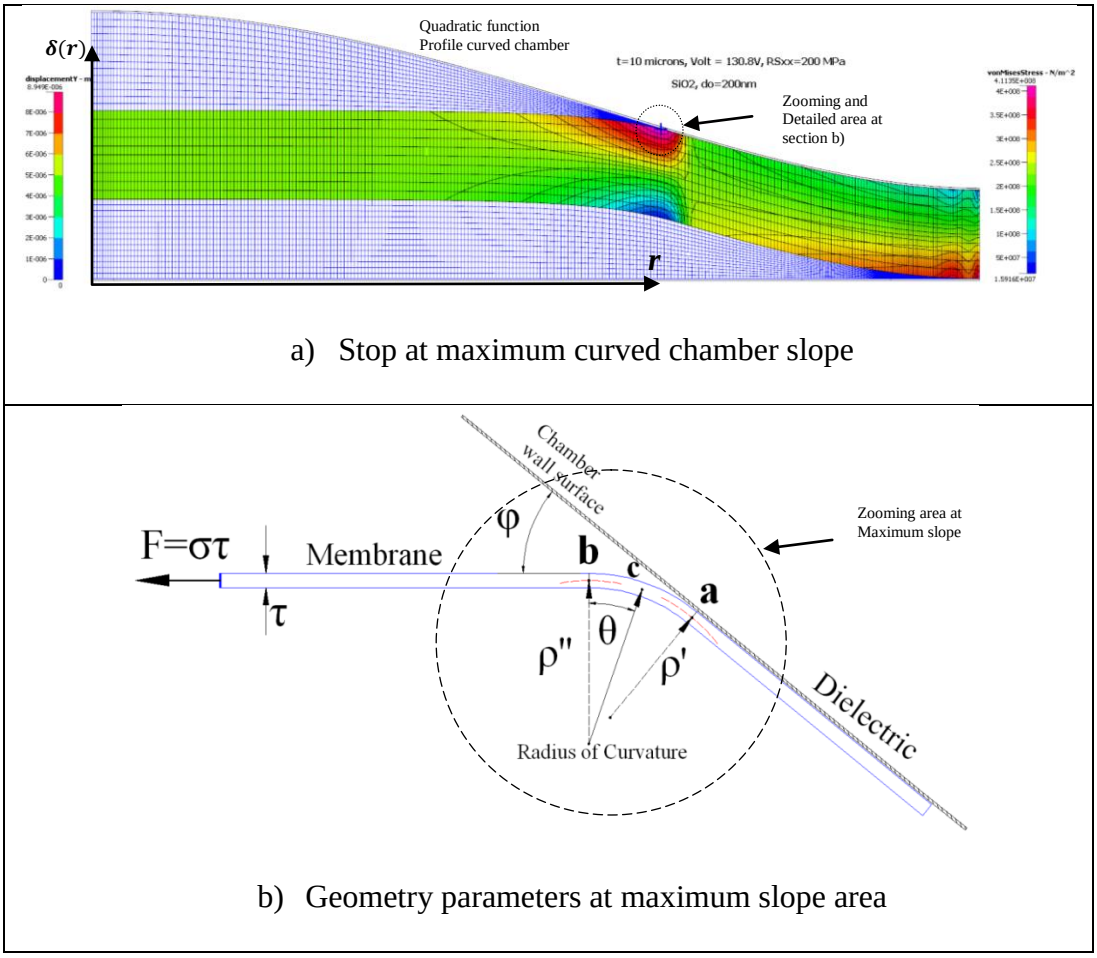

a) Stop at maximum curved chamber slope

b) Geometry parameters at maximum slope area

Fig. 4.5 Maximum slope point on the Power Intake cycle, electro-zippering pump; a) Maximum slope stop, b) Geometry parameters at maximum slope area

For this study the maximum deflection is limited to 20 microns height. The derivative $\frac{d\delta(r)}{dr}$ of the equation 4.1 is the slope of the chamber at a given radius $\boldsymbol{r}$ and it is given by equation (4.2).

$$\frac{d\delta(r)}{dr} = 4\frac{\delta_{max}}{a}\left[\left(\frac{r}{a}\right)^3 - \frac{r}{a}\right] \tag{4.2}$$

It is shown below that the maximum tensile stress $\boldsymbol{\sigma}$ that is sustainable on the intake cycle is determined to be close to the point of maximum slope. The maximum slope of

the chamber is determined at the point ***r**** for which the 2nd derivative of the deflection is equal to zero. The 2nd derivative of the deflection is given by equation (4.3).

$$\frac{d^2\delta(r)}{dr^2} = 4\frac{\delta_{max}}{a}\left[3\left(\frac{r}{a}\right)^2 - \frac{1}{a}\right] \tag{4.3}$$

Setting this equation (4.3) to zero and solving for ***r**** gives

$$\frac{d^2\delta(r)}{dr^2} = 0 \quad \therefore \quad \left(\frac{r^*}{a}\right)^2 = \frac{1}{3} \quad or \quad \frac{r^*}{a} = \pm\frac{1}{\sqrt{3}} \tag{4.4}$$

The maximum slope is given by taking the absolute value of the equation (4.2); it is given by

$$\frac{d\delta(r^*)}{dr} = \pm\frac{\delta_{max}}{a}\left[\frac{8\sqrt{3}}{9}\right] \tag{4.5}$$

For the case that $\delta_{max} = 20$ microns and a $= 1000$ microns, the maximum slope angle θ^* is given by equation (4.4).

$$\boldsymbol{\theta}^* = tan^{-1}\left(\frac{\delta_{max}}{a}\left[\frac{8\sqrt{3}}{9}\right]\right) = tan^{-1}(0.0308) = 0.0308\, radians. \tag{4.4}$$

Therefore, the maximum slope $\boldsymbol{\theta}^*$ which is about 1.74 degrees occurs at $\boldsymbol{r}^* = \pm\frac{1}{\sqrt{3}}a$ which is $\boldsymbol{r}^* = \pm 577.35$ microns.

4.7 Distributive Load on Curved Arc between "a" and "b" Due to Tensile Stresses.

Consider a plate being raised up on the intake cycle such that at some slope $\emptyset$, between $0 \leq \emptyset \leq \theta^*$ the forces due to the electrostatics just balance the tensile stresses in the plate at the point "***a***" as was shown in Fig. 4.4. The plate curves away from the chamber wall at point "***a***", curving toward the point "***b***" at which the plate becomes close to be horizontal and extends across to other side of the chamber. For the derivation in this section, the radius of curvature $\boldsymbol{\rho}$ along the curved portion of the

plate from point "***a***" to point "***b***" is assumed to variable, so it is assumed that it will a point where is minimum curvature $\boldsymbol{\rho'}$ which means high stresses combined $(M_c + T_c)$ and it will be the critical point of analysis. The tensile stresses $\boldsymbol{\sigma}$ in the horizontal section of the plate (e.g., point "***b***") are assuming to be constant and are an unknown in the problem, it assumed that at the half of the length at ***r=0***. Where the slope is zero only tensile stresses survives$\boldsymbol{\sigma}$.

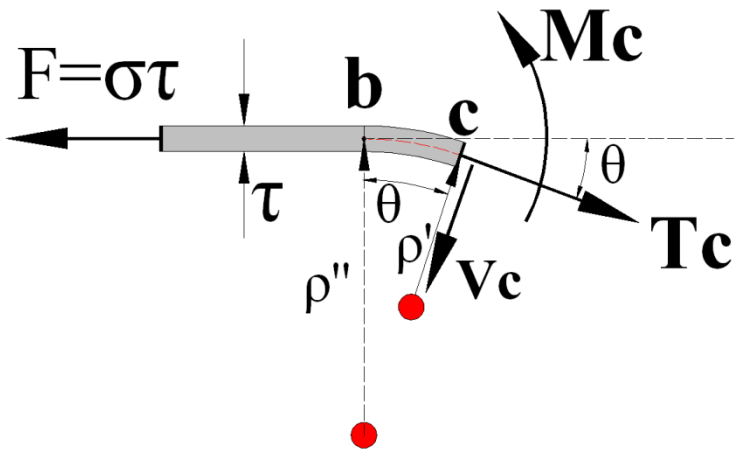

Fig. 4.6 Critical point of analysis with the smallest radius of curvature $\boldsymbol{\rho'}$

The constant $\boldsymbol{\sigma}$ is to be determined by the condition of equilibrium between the tensile and electrostatic forces acting on the plate. The tensile force $\boldsymbol{F}$ per "unit dimension into the plane of the paper" at the point "***b***" is given by $\boldsymbol{F = \sigma\tau}$ where $\boldsymbol{\tau}$ is the thickness of the plate.

4.8Large deflection mathematical analysis intake power stroke model

For plate analysis, if the deflection is greater than the thickness of the plate, the use of large deflection theory has to apply in order to account for simultaneous effects of

bending and stretching [Rudolph Szilard 2004]. However using a simplified 2 D static model for the plate analysis, it can be applied the reduced Von Karman governing differential equation as follow en equation 5.1, this equation is usually for thin plate that has bending stresses as well stretching stresses due to the external pressure and initial small curvature. [Ancel C. Ugural 1991]

$$D\nabla^4 w(x) = Pe(x) + T_x \frac{\partial^2 w}{\partial x^2} + T_y \frac{\partial^2 w}{\partial y^2} + 2T_{xy} \frac{\partial^2 w}{\partial x \partial y} \qquad (4.7)$$

Where:

$w(x)$: is deflexion respect to *x.*

Pe(x) : is the electrostatic pressure due to applied differential voltage.

Tx : is the tension due to residual stresses on the polysilicon plate in x direction.

Ty : is the tension due to residual stresses on the polysilicon plate in y direction.

Txy : is the shear force per unit distance on x and y plane due to residual stresses on the polysilicon plate.

D : is the flexural rigidity of the plate.

For the reduced model only 2 D model will be analysis, therefore, the equation 4.7 becomes the equation (4.8) as governing differential equation for this problem.

$$D\nabla^4 w(x) = Pe(x) + T_x \frac{\partial^2 w}{\partial x^2} \qquad (4.7)$$

The following equations, (4.8) through (4.10), from solid mechanics represent the deflection, shear forces and moment been applied over the plate due to the external pressure, [Timoshenko & Young 1948, Ansel C Ugural 1999].

$$D\frac{d^2w(x)}{dx^2} = M(x) = D\left(\frac{1}{\rho}\right) \tag{4.8}$$

$$D\frac{d^3w(x)}{dx^3} = -\frac{dM(x)}{dx} = -V(x) \tag{4.9}$$

$$D\frac{d^4w(x)}{dx^4} = -\frac{dV(x)}{dx} = w(x) \tag{4.10}$$

Therefore, we can rewrite equation (4.7) as a set of two first order equations using the state space matrix notation in equation (4.11). We let $T_x = T$.

$$\dot{\mathbf{Z}} = [\boldsymbol{A}][\mathbf{z}] + [\mathbf{B}][\mathbf{u}] \tag{4.11}$$

The two first order equation obtained using the state variable vector $\mathbf{z} = [M(x)\ \ V(x)]^T$ and equation (4.8) are described by equation (4.12) and equation (4.13)

$$\frac{dV(x)}{dx} = Pe(x) + T\frac{\partial^2 w}{\partial x^2} = Pe(x) + \frac{T}{D}M(x) \tag{4.12}$$

$$\frac{dM(x)}{dx} = V(x) \tag{4.13}$$

Therefore, in a state space representation they become equation (4.14) as follow:

$$\begin{bmatrix} \frac{dM(x)}{dx} \\ \frac{dV(x)}{dx} \end{bmatrix} = \begin{bmatrix} 0 & 1 \\ \frac{T}{D} & 0 \end{bmatrix}\begin{bmatrix} M(x) \\ V(x) \end{bmatrix} + \begin{bmatrix} 0 \\ 1 \end{bmatrix} Pe(x) \tag{4.14}$$

Letting $\lambda = \sqrt{\frac{T}{D}}$, equation (4.14) becomes equation (4.15).

$$\begin{bmatrix} \frac{dM(x)}{dx} \\ \frac{dV(x)}{dx} \end{bmatrix} = \lambda\begin{bmatrix} 0 & \frac{1}{\lambda} \\ \lambda & 0 \end{bmatrix}\begin{bmatrix} M(x) \\ V(x) \end{bmatrix} + \begin{bmatrix} 0 \\ 1 \end{bmatrix} Pe(x) \tag{4.15}$$

Rewriting equation (4.15) in state space notation, we get

$$\boldsymbol{Z}(x) = \begin{bmatrix} \boldsymbol{Z_1}(\boldsymbol{x}) \\ \boldsymbol{Z_2}(\boldsymbol{x}) \end{bmatrix} = \begin{bmatrix} M(x) \\ V(x) \end{bmatrix}, \quad [\boldsymbol{A}] = \begin{bmatrix} 0 & \frac{1}{\lambda} \\ \lambda & 0 \end{bmatrix} \text{ and } [\boldsymbol{B}] = \begin{bmatrix} 0 \\ 1 \end{bmatrix}$$

Equation (4.15) is the state space equation for the intake stroke and the boundary conditions (BC) are described by equation (4.17).

State space notation $$\begin{bmatrix} \dot{\boldsymbol{Z}}_1 \\ \dot{\boldsymbol{Z}}_2 \end{bmatrix} = \lambda \boldsymbol{A}\boldsymbol{Z}(x) + \boldsymbol{B}Pe(x) \tag{4.14}$$

Boundary conditions (B.C.) $$\begin{bmatrix} \boldsymbol{Z}_1(\boldsymbol{0}) \\ \boldsymbol{Z}_2(\boldsymbol{x_c = L/2}) \end{bmatrix} = \begin{bmatrix} Mo \\ 0 \end{bmatrix} \tag{4.17}$$

The solution has two parts :

a) $0 \leq x \leq x_1$ where x_1 is defined by the quadratic model approximation.

b) $x_1 \leq x \leq (x_c = L/2)$

The solution of the state space equation has the following form.

$$e^{-\boldsymbol{A}\lambda x} \ \boldsymbol{Z}(\boldsymbol{x}) = \boldsymbol{Z}(\boldsymbol{0}) + \int_{x=0}^{x} e^{-\boldsymbol{A}\lambda\omega} \begin{bmatrix} \boldsymbol{0} \\ \boldsymbol{1} \end{bmatrix} Pe(\omega)d\omega \tag{4.18}$$

Solving for $e^{\boldsymbol{A}\lambda x}$ and $e^{-\boldsymbol{A}\lambda x}$ we get equations (4.19) and (4.20)

$$e^{\boldsymbol{A}\lambda x} = \begin{bmatrix} \cosh(\lambda x) & \frac{\sinh(\lambda x)}{\lambda} \\ \lambda\sinh(\lambda x) & \cosh(\lambda x) \end{bmatrix} \tag{4.19}$$

$$e^{-\boldsymbol{A}\lambda x} = \begin{bmatrix} \cosh(\lambda x) & -\frac{\sinh(\lambda x)}{\lambda} \\ -\lambda\sinh(\lambda x) & \cosh(\lambda x) \end{bmatrix} \tag{4.20}$$

The quadratic model for the electrostatic pressure $P_e(x)$ has the form describe by equation (4.21).

$$Pe(\omega) = P_{e\_max}\left[1 - \frac{\omega}{x_1}\right]^2 = P_{e\_max}[1 - y]^2 \tag{4.21}$$

Let $y = \frac{\omega}{x_1}$ and $dy = \frac{d\omega}{x_1}$ then $d\omega = x_1 dy$

So equation (4.18) becomes equation (4.22)

$$e^{-\boldsymbol{A}\lambda x}\ \ \boldsymbol{Z}(\boldsymbol{x}) = \boldsymbol{Z}(\boldsymbol{0}) + P_{e\_max}\, x_1 \int_{x=0}^{x} e^{-\boldsymbol{A}\lambda x_1 y} \begin{bmatrix}\boldsymbol{0}\\ \boldsymbol{1}\end{bmatrix} [1-y]^2 dy \qquad (4.22)$$

Carrying out the solution of this equation for $0 \le x \le x_1$, equation 4.23 becomes

$$e^{-\boldsymbol{A}\lambda x}\ \begin{bmatrix}M(x)\\ V(x)\end{bmatrix} = \begin{bmatrix}M(0)\\ V(0)\end{bmatrix} + P_{e\_max}\, x_1 \left[e^{-\boldsymbol{A}\lambda x} \begin{bmatrix}f_1(x)\\ f_2(x)\end{bmatrix} - \begin{bmatrix}f_1(0)\\ f_2(0)\end{bmatrix}\right] \qquad (4.23)$$

Let $\beta = \lambda x_1$ and use the expression $\boldsymbol{A}\begin{bmatrix}\boldsymbol{0}\\ \boldsymbol{1}\end{bmatrix} = \frac{1}{\lambda}\begin{bmatrix}1\\ 0\end{bmatrix}$ in obtaining $f_1(x)$ and $f_2(x)$ as defined by equation (4.24).

$$\begin{bmatrix}f_1(x)\\ f_2(x)\end{bmatrix} = \begin{bmatrix} -\frac{1}{\lambda}\left[\frac{\left(1-\frac{x}{x_1}\right)^2}{\beta} + \frac{2}{\beta^3}\right] \\ \frac{2\left(1-\frac{x}{x_1}\right)}{\beta^2} \end{bmatrix} \qquad (4.24)$$

Note that equation (4.24) evaluated at $x = 0$ yields equation (4.25)

$$\begin{bmatrix}f_1(0)\\ f_2(0)\end{bmatrix} = \begin{bmatrix} -\frac{1}{\lambda\beta}\left[1 + \frac{2}{\beta^3}\right] \\ \frac{2}{\beta^2} \end{bmatrix} \qquad (4.25)$$

Equation (4.24) evaluated at $x = x_1$ yields expression (4.26)

$$\begin{bmatrix}f_1(x_1)\\ f_2(x_1)\end{bmatrix} = \begin{bmatrix} -\frac{2}{\lambda\beta^3} \\ 0 \end{bmatrix} \qquad 4.26)$$

Define

$$\begin{bmatrix}M(x)\\ V(x)\end{bmatrix} = P_{e\_max}\, x_1 \left[e^{-\boldsymbol{A}\lambda x} \begin{bmatrix}f_1(x)\\ f_2(x)\end{bmatrix} - \begin{bmatrix}f_1(0)\\ f_2(0)\end{bmatrix}\right] \qquad (4.27)$$

The solution can be written as

$$e^{-\boldsymbol{A}\lambda x}\ \begin{bmatrix}M(x)\\ V(x)\end{bmatrix} = \begin{bmatrix}M(0)\\ V(0)\end{bmatrix} + \begin{bmatrix}M_1(x)\\ V_1(x)\end{bmatrix} \qquad (4.28)$$

We find the particular solution at : $x = x_1$.

$$\begin{bmatrix} M_1(x_1) \\ V_1(x_1) \end{bmatrix} = P_{e\_max}\, x_1 \left[e^{-\boldsymbol{A}\lambda x_1} \begin{bmatrix} f_1(x_1) \\ f_2(x_1) \end{bmatrix} - \begin{bmatrix} f_1(0) \\ f_2(0) \end{bmatrix} \right] \tag{4.29}$$

$$\begin{bmatrix} M(x) \\ V(x) \end{bmatrix} = e^{\boldsymbol{A}\lambda x} \begin{bmatrix} M(0) + M_1(x) \\ V(0) + V_1(x) \end{bmatrix} \tag{4.30}$$

The solutions on the intervals a) $0 \le x \le x_1$ and b) $x_1 \le x \le x_c$ are obtained by applying the BC $V(x_c) = 0$.

The solution on the interval a) $0 \le x \le x_1$ is given by

$$\begin{bmatrix} M_1(x) \\ V_1(x) \end{bmatrix} = P_{e\_max}\, x_1 \left[\begin{bmatrix} f_1(x)cosh(\lambda x) - \frac{f_2(x)}{\lambda} sinh(\lambda x) \\ -f_1(x)\lambda sinh(\lambda x) + f_2(x)cosh(\lambda x) \end{bmatrix} - \begin{bmatrix} f_1(0) \\ f_2(0) \end{bmatrix} \right] \tag{4.31}$$

$$M_1(x_1) = P_{e\_max}\, x_1 \left[f_1(x_1)cosh(\lambda x_1) - \frac{f_2(x x_1)}{\lambda} sinh(\lambda x_1) - f_1(0) \right] \tag{4.32}$$

$$V_1(x) = P_{e\_max}\, x_1 [-f_1(x_1)\lambda sinh(\lambda x_1) + f_2(x_1)cosh(\lambda x_1) - f_2(0)] \tag{4.33}$$

The solution on the interval b) $x_1 \le x \le x_c$ is given by

$$M(x) = [M_0 + M_1(x_1)]cosh(\lambda x) + \left[\frac{V_0 + V_1(x_1)}{\lambda} \right] sinh(\lambda x) \tag{4.34}$$

$$V(x) = [M_0 + M_1(x_1)]\lambda sinh(\lambda x) + [V_0 + V_1(x_1)]sinh(\lambda x) \tag{4.35}$$

We apply the boundary conditions $V(x_c) = 0$ at $x = x_c$.

$$0 = [M_0 + M_1(x_1)]\lambda sinh(\lambda x) + [V_0 + V_1(x_1)]sinh(\lambda x) \tag{4.34}$$

$$[V_0 + V_1(x_1)] = -[M_0 + M_1(x_1)]\lambda tanh(\lambda x_c) \tag{4.37}$$

$$[V_0] = -V_1(x_1) - [M_0 + M_1(x_1)]\lambda tanh(\lambda x_c) \tag{4.38}$$

The solution for V_0 is given by (4.38).

The solution of the interval $0 \le x \le x_1$ satisfies

$$M(x) = [M_0 + M_1(x_1)]cosh(\lambda x) + \left[\frac{V_0 + V_1(x_1)}{\lambda} \right] sinh(\lambda x) \tag{4.39}$$

$$V(x) = [M_0 + M_1(x_1)]\lambda sinh(\lambda x) + [V_0 + V_1(x_1)]sinh(\lambda x) \qquad (4.40)$$

The 2D plate has symmetry around the y-axis. The maximum chordlength is 2000 microns. The radius r varies from zero at the center to $r_{max} = a = 1000$ microns. The maximun heigth at the center is 20 microns. We see that $y_{max} = 20$ microns. The thickness of the plate is t micron; in the study, *t* takes on the values 2, 4, 6, 8 and 10 microns.

The function for the curved upper electrode chamber shape was chosen to be the 4th order form as given in equation (4.41).

$$\delta_{chamber}(r) = \delta_{max}\left(1 - \left[\frac{r}{a}\right]^2\right)^2 \qquad (4.41)$$

where $0 \leq r \leq a, \quad \delta_{max} = 20$ microns with $a = 1000$ microns.

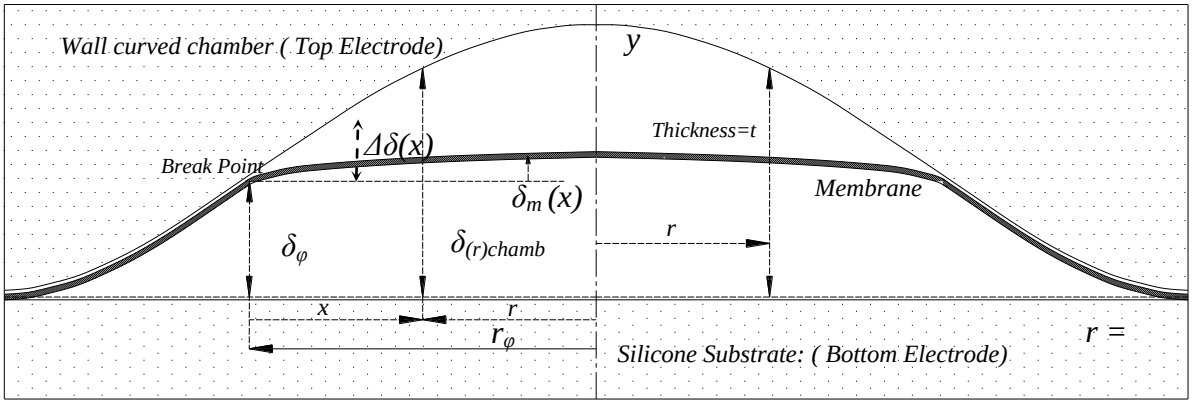

Fig. 4.7 A 2D Curved chamber with geometry parameters for the electrostaic quadratic model

Fig. 4.7 shows the 2D curved Chamber with plate during the intake stroke moving up the chamber wall; the plate has thickness $\boldsymbol{t}$ with total length of $\boldsymbol{L}$ =2000 microns.

The follwing notation has to be used for this math derivation of the electrostic model.

Where $\boldsymbol{r_\varphi}$: is the radius at break point.

$\boldsymbol{x}$: is the distance measure from break point.

$\boldsymbol{\delta_\emptyset}$: is the height of the chamber at break point.

$\boldsymbol{\delta_r}$: is the height of the chamber at $\boldsymbol{x}$

$\boldsymbol{\delta_m(x)}$: is the deflection of the plate with respect to the break point: $\boldsymbol{x} = 0$

$\Delta\boldsymbol{\delta(x)}$ **:** is the distance from the plate to chamber wall.

Therefore the relation equation obtained from these geometry relationship are describe in equation (4.42):

$$r_\varphi = x + r \ , \quad then: \quad r = r_\varphi - x \tag{4.42}$$

Taking the derivative, we get $\frac{dr}{dx} = -1$ where $\boldsymbol{x}$ is measure from the break point with $x = 0\ at\ r = r_{\varphi}$. The distance from the plate to the wall chamber can be express by the equation (4.43).

$$\Delta\delta(x) = \delta_{chamber}(r) - \delta_{(\emptyset)} - \delta_m(x) = cx^2 \tag{4.43}$$

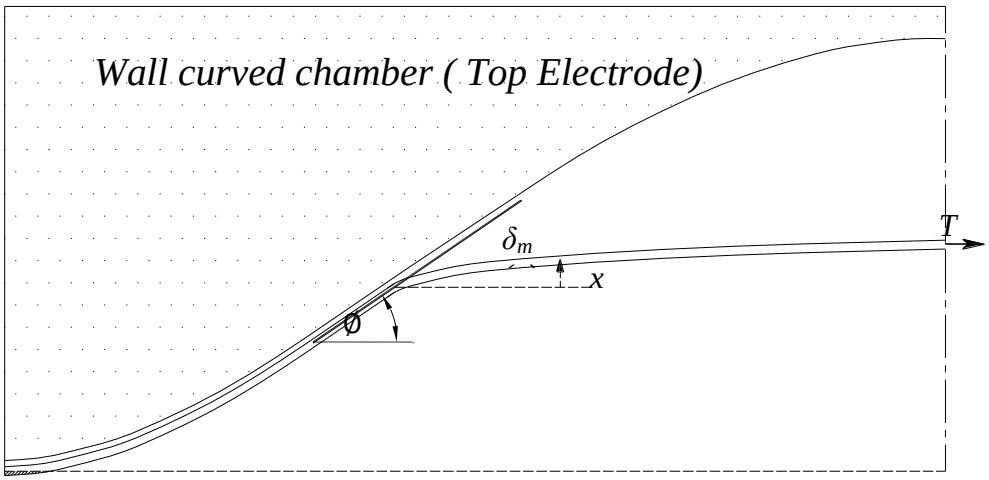

Fig. 4.8 An approximate deflection model of the plate.

Fig. 4.8 shows a geometric model for deflection of the plate. From the $\delta_m(x)$ approximation we get equation (4.44).

$$\frac{M(x)}{D} = \theta(x)\sqrt{\frac{T}{D}} \tag{4.44}$$

From solid mechanics, [Ugural Ansel C 1999], equation (4.45) holds.

$$\frac{M(x)}{D} = \frac{d\theta(x)}{dx} \tag{4.45}$$

Substituting equation (4.45) into equation (4.44), we get

$$\frac{d\theta(x)}{dx} = \theta(x)\sqrt{\frac{T}{D}} \tag{4.44}$$

This first order differential equation (4.44) has a solution of the form (4.47).

$$\theta(x) = \emptyset e^{-\sqrt{\frac{T}{D}}} \quad ; \quad with \ \emptyset = \ \theta(0) \tag{4.47}$$

The slope of the plate is defined by equation (4.48).

$$\frac{d\delta m(x)}{dx} = \theta(x) \tag{4.48}$$

It has the boundary condition $\delta m(0) = 0$.

The combination of equation (4.47) and (4.48) yield equation (4.49).

$$\delta m(x) = \frac{\emptyset}{\sqrt{\frac{T}{D}}}\left(1 - e^{-\sqrt{\frac{T}{D}}x}\right) \tag{4.49}$$

Using a Taylor series expansion and approximating the result up to the quadratic term, equation (4.49) has the approximation given by equation (4.50).

$$\delta m(x) = \emptyset x - \frac{\emptyset}{2}\sqrt{\frac{T}{D}}x^2 \tag{4.50}$$

Electrostatic model equation is equation (4.51).

$$P_e(x) = \frac{P_{e\_max}}{\left[1+\left(\frac{\varepsilon_d \, gap}{\varepsilon_a \, d_0}\right)\right]^2} = \frac{1}{\left[1+\frac{\frac{\varepsilon_d}{\varepsilon_a \, d_0}\Delta\delta(x)}{1+\frac{\varepsilon_d gap}{\varepsilon_0 d_0}}\right]^2} \tag{4.51}$$

$$\Delta\delta(x) = a\emptyset\left[\frac{\left(3{R_0}^2-1\right)}{2R_0\left(1-{R_0}^2\right)} + \frac{1}{2}a\sqrt{\frac{T}{D}}\right]\left[\frac{x}{a}\right]^2 \tag{4.52}$$

wherein $R_0 = {}^{r_\emptyset}/_{a}$. Therefore, with the above approximate, we get equation (4.53).

$$\Delta\delta(x) = k[x]^2 \tag{4.53}$$

where

$$k = a\emptyset\left[\frac{\left(3{R_0}^2-1\right)}{2R_0\left(1-{R_0}^2\right)} + \frac{1}{2}a\sqrt{\frac{T}{D}}\right]\left[\frac{1}{a}\right]^2 \tag{4.54}$$

The equation of electrostatic pressure is approximated by equation (4.55).

$$P_e(x) = \tilde{P}_{e\_max} \frac{1}{[1+kx^2]} \tag{4.55}$$

$$\Delta\delta(x) = \delta_{chamber}(r) - \delta_{(\emptyset)} - \delta_m(x) \tag{4.54}$$

where the geometry relationship are given by

$$r_\varphi = x + r \tag{4.57}$$

$$r = r_\emptyset - x \tag{4.58}$$

$$\frac{r}{a} = \frac{r_\emptyset}{a} - \frac{x}{a} = R - \frac{x}{a} \tag{4.59}$$

$$\delta_{chamber}(r) = \delta_{max}\left[1 - \left(\frac{r}{a}\right)^2\right]^2 \tag{4.60}$$

$$\delta_{(\emptyset)} = r_\emptyset$$

Slope at the break point is given by

$$\emptyset = \frac{d\delta(r)}{dx} = \left(\frac{dr}{dx}\right)\frac{d\delta(r)}{dr}\Big]_{r=r_\emptyset} \tag{4.61}$$

Since $\frac{dr}{dx} = -1$, the slope satisfies $\emptyset = -\frac{d\delta(r)}{dx}$.

Note that the following equation is satisfied.

$$\frac{d\delta(r)}{dx} = -\delta_{max}\frac{4}{a}\left(\frac{r}{a}\right)\left[1 - \left(\frac{r}{a}\right)^2\right] \tag{4.62}$$

The slope at the break point where $r = r_\emptyset$ satisfies

$$\emptyset = \delta_{max}\frac{4}{a}\left(\frac{r_\emptyset}{a}\right)\left[1 - \left(\frac{r_\emptyset}{a}\right)^2\right] \tag{4.63}$$

Using the definition $R = \left(\frac{r_\emptyset}{a}\right)$, δ_{max} satisfies the expression (4.44).

$$\delta_{max} = \frac{a\emptyset}{4R[1-R^2]} \tag{4.64}$$

$$\delta(x) = \delta_{max}\left[1 - \left(R - \frac{x}{a}\right)^2\right]^2 \tag{4.65}$$

Expanding equation (4.65) using a Taylor series expansion, we get

$$\delta(0) = \delta_{max}[1 - R^2]^2 \tag{4.67}$$

$$\delta(x) = \delta(0) + \left[\frac{d\delta(0)}{dx}\right]x + \left[\frac{d^2\delta(0)}{dx^2}\right]\frac{x^2}{2!} + \left[\frac{d^3\delta(0)}{dx^3}\right]\frac{x^3}{3!} + \left[\frac{d^4\delta(0)}{dx^4}\right]\frac{x^4}{4!} \tag{4.68}$$

Define $y = \frac{x}{a}$. We get the following expression.

$$\frac{d\delta(x)}{dx} = \delta_{max}\frac{4}{a}[1 - (R - y)^2](R - y) \tag{4.69}$$

The slope at the $x = 0$ satisfies

$$\frac{d\delta(0)}{dx} = \delta_{max}\frac{4}{a}[1 - R^2]R = \emptyset \tag{4.70}$$

The second order term satisfies

$$\frac{d^2\delta(x)}{dx^2} = \delta_{max}\left[-\frac{4}{a^2}[1 - 3(R - y)^2]\right] \tag{4.71}$$

$$\frac{d^2\delta(x0)}{dx^2} = \delta_{max}\left[-\frac{4}{a^2}[1 - 3R^2]\right] \tag{4.72}$$

The third order term satisfies

$$\frac{d^3\delta(x)}{dx^3} = \delta_{max}\left[-\frac{24}{a^3}[R - y]\right] \tag{4.73}$$

$$\frac{d^3\delta(0)}{dx^3} = \delta_{max}\left[-\frac{24}{a^3}R\right] \tag{4.74}$$

The fourth order term satisfies

$$\frac{d^4\delta(x)}{dx^4} = \delta_{max}\left[\frac{24}{a^4}\right] \tag{4.75}$$

$$\frac{d^4\delta(0)}{dx^4} = \delta_{max}\left[\frac{24}{a^4}\right] \tag{4.76}$$

Substituting the above expressions into (4.68) we get

$$\delta(x) = \delta(0) + \emptyset x + \delta_{max}[1 - 3R^2]\left(\frac{x}{a}\right)^2 - 4R\delta_{max}\left(\frac{x}{a}\right)^3 + \delta_{max}\left(\frac{x}{a}\right)^4 \tag{4.77}$$

$$\delta(x) - \delta(0) = +\emptyset x + \delta_{max}[1 - 3R^2]\left(\frac{x}{a}\right)^2 - 4R\delta_{max}\left(\frac{x}{a}\right)^3 + \delta_{max}\left(\frac{x}{a}\right)^4 \tag{4.78}$$

Apply approximation, keeping only up to the quadratic terms.

$$\delta(x) - \delta(0) \cong \emptyset x + \delta_{max}[1 - 3R^2]\left(\frac{x}{a}\right)^2 \tag{4.79}$$

Recall that the displacement of the beam is given by equations (4.49) and (4.50).

$$\delta m(x) = \frac{\emptyset}{2}\sqrt{\frac{T}{D}}x^2 \tag{4.80}$$

In summary we have the following equations.

$$\Delta\delta(x) = \delta(x) - \delta(0) - \delta m(x) \tag{4.81}$$

$$\Delta\delta(x) = 2\delta_{max}[3R^2 - 1]\left(\frac{x}{a}\right)^2 + \frac{\emptyset}{2}\sqrt{\frac{T}{D}}x^2 \tag{4.82}$$

$$\Delta\delta(x) = \frac{2a\emptyset}{4R[1-R^2]}[3R^2 - 1]\left(\frac{x}{a}\right)^2 + \frac{\emptyset}{2}\sqrt{\frac{T}{D}}x^2 \tag{4.83}$$

$$\Delta\delta(x) = a\emptyset\left[\frac{3R^2-1}{2R(1-R^2)} + \frac{1}{2}a\sqrt{\frac{T}{D}}\right]\left(\frac{x}{a}\right)^2 \tag{4.83}$$

The approximation $\Delta\delta(x) = kx^2$ was derived above. The following equations hold.

$$c = \emptyset\left[\frac{1}{a}\frac{3R^2-1}{2R(1-R^2)} + \frac{1}{2}\sqrt{\frac{T}{D}}\right] \tag{4.84}$$

The electrostatic force model satisfies

$$P_e(x) = \frac{\tilde{P}_{e\_max}}{[1+kx^2]^2} \tag{4.85}$$

where

$$k = \frac{\frac{\varepsilon_d}{\varepsilon_a d_0}c}{\left[1+\left(\frac{\varepsilon_d\, gap}{\varepsilon_a\, d_0}\right)\right]} \tag{4.86}$$

In order to analytically integrate equations that contain the electrostatic force, we need to make another approximation so that the electrostatic force model is quadratic. That approximation in the electrostatic model satisfies

$$\frac{1}{[1+kx^2]^2} = \left[1 - \frac{x}{x_1}\right]\left[1 - \frac{x}{x_1}\right] \tag{4.87}$$

where $x_1 = \frac{3}{\sqrt{k}}$ Therefore, the final model for electrostatic pressure is satisfies the quadratic model in equation (4.88).

$$P_e(x) = \tilde{P}_{e\_max}\left[1 - \frac{x}{x_1}\right]^2 \tag{4.88}$$

4.9 Setting Up the Simulation 2D Model for the Power Intake.

4.10 Overview.

The multi-physics software tools and description of the multi-domain fields for the model are introduced here. Next, a 2D model of the micropump simulation is introduce, simulation with sensitivity analysis for the parameters involved are shown as a results, as well as the optimized candidates. The simulation and the geometry parameters are constant for a particular and maximum dimension available at the start of the simulations.

A 2D structures grid geometry model was written in Python programming language under CDF-GEOM© Multiphysics Software. The model boundaries conditions and material properties as well as physics domain was set up using CFD ACE© software, due to symmetry only half of the model was needed to build the simulation model. Fig. 5.4 shows only half the model. A program was created in Python where variables can be changed in order to construct a new model with different thicknesses on the thin plate. The upper dielectric wall has a thicknesses of 200 nm with artificial air gap of 5nm in order to leave room to accommodate the fluid volume when is moving up against the dielectric wall. The artificial air gap is created to avoid a negative volume once the plate moves up against the upper wall. Structural grid quad cells were created to get better and faster convergence compare with unstructured grids.

A 2D model is proposed for performing the multiphysics simulations; the objective is to determine the physical parameter involved and how they affect the performance of the model and to provide insight into obtaining the best performing candidates that are

suitable with respect to the design requirement describe in the chapter 1. Therefore, we seek to optimize the micropump designs regarding the requirements associated with the main objective of the simulations.

Finding what physical parameters are involved and which ones are important to recreate the physics for the simulation is the key for the success to capture the real physics, without losing any significant behavior.

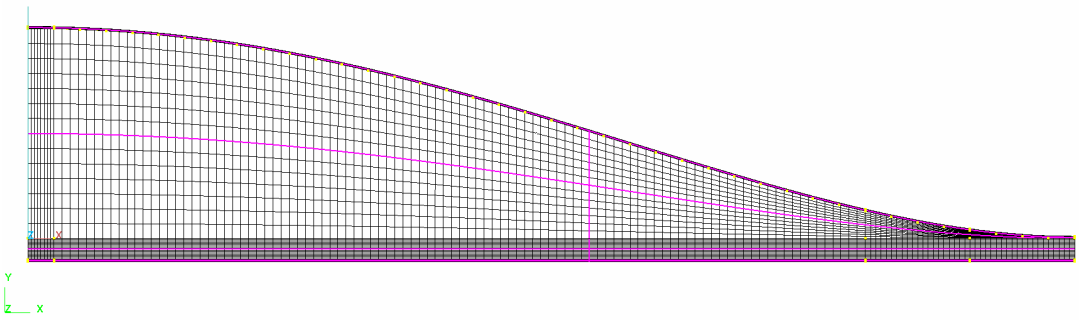

Fig. 4.9 Structured Geometry grid domain of simulation for a symmetry 2D Electrostatic-Fluid-Structure Interaction

The zoomed in view of the edge area shown in Fig. 4.10 shows the thickness of the thin plate, the air gap of 5nm and the 200nm dielectric material layer on the upper side as well as the bottom side.

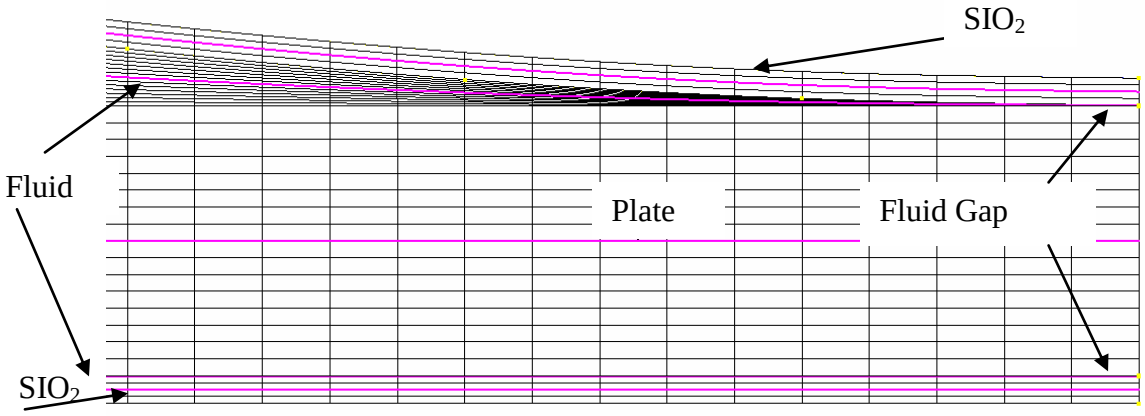

Fig. 4.10 Structured Geometry grid domain on the clamped edge of micropump

4.11 Model Parameters for 2D Model

The 2D model geometries and dimension were created in agreement with the surface micromachining SUMMiT V process (Sandia National Laboratory). The maximum footprint dimension to pack in a single chip for the baseline is taken to be 6mm by 2mm with a suitable chamber height being 20 μm for the plate to open up as the maximum height on the intake stroke. This was taken as the on-chip module size for the baseline design. Creating a chamber with a high of 20 μm is the subject of fabrication and is beyond the scope of this dissertation work. Fig. 4.1 shows an example of a cylindrical curve envisioned for the chamber geometry.

Three of the variables for the 2D model are the thickness of the plate, the differential voltage applied to the micro-pump, and the differential pressure on the plate. The thickness of the silicon dioxide insulation layer is chosen to be 0.2 μm in the baseline design. The 20 μm chamber height is chosen for the baseline design. Width and length dimensions of the baseline micropump chamber geometry are 2mm and 6mm, respectively. Adding additional degrees of freedom to the model would make the multiphysics simulation work computationally prohibitive in getting solutions to the complex multiphysics model. It is tradeoff between getting enough simulation results to determine a suitable micropump to meet performance requirements and to execute simulations having reasonable computational times expended on a complex and heavy simulation model while finding good micropump candidates that perform well.

4.12 Multi-physics Fields and Tools

Fluid, structure and electrical fields are coupled in this multiphysics simulation model; the Euler-Lagrange technique for moving grids is the feature to recreate the model dynamics. This model uses the finite element method for solving stress fields (structural field) and fluid mechanics (non-linear Navier-Stoke equations); it uses the finite volume method to solve for the field of the electrostatics. The multi-physics model can be solved with multi-physics software tools available; examples include CDF-ACE Plus, ANSYS Multiphysics, COMSOL, MEMCAD, Algor, etc.

4.13 2D Micropump Geometry Model Set Up.

The 2D simplify geometry of the micro-pump is elaborate on CFD-GEOM tools under scripting Python program. The length (x-axis), the height (y-axis), and the insulation gap layer dimensions are applied to the geometry of the simulation model as constant parameter values. One parametric value used in the 2D simulations is the thickness of the plate, ranging from 2μm to 4μm; these values came after several simulation were performed. Another parametric value is the differential voltage applied to the micropump electrodes ranging from 150 volts to 325 volts. Another parametric value is the differential pressure ranging from 4895 Pa to 41348 Pa (i.e., 1 psi to 4 psi). These parameters values are shown in Table 4.2.

A preliminary 3D simplified CAD design was constructed using the dimension described above. The 3D compact unit model is constructed using the square footprint 2000 μm x 2000 μm and the maximum height dimension 20 μm for the top curve electrode. The 2000 μm dimension is 1/3 of the total 6000 μm length taken for the on-

chip footprint. Figs. 4.11a and 4.11b show these dimensions. From the 3D basic pumping unit, we extract the 2D model for simulations, as shown in Fig. 4.11c which shows the reduced geometry established for 2D CAE model.

Table 4.2 Variable and constant parameter for 2D simulations.

	Design Variable Parameters			Design Constant Parameters		
Simulation Parameters	Thickness {t} [µm]	Voltage {V} [volt]	Diff Pressure G {ΔP} [N/m^2]	Length {L} [µm]	High {h} µm	Gap {gap } [nm]
Simulation values	[2, 4, 6, 8, 10]	[100-200]	[0-101325]	2000	20	5

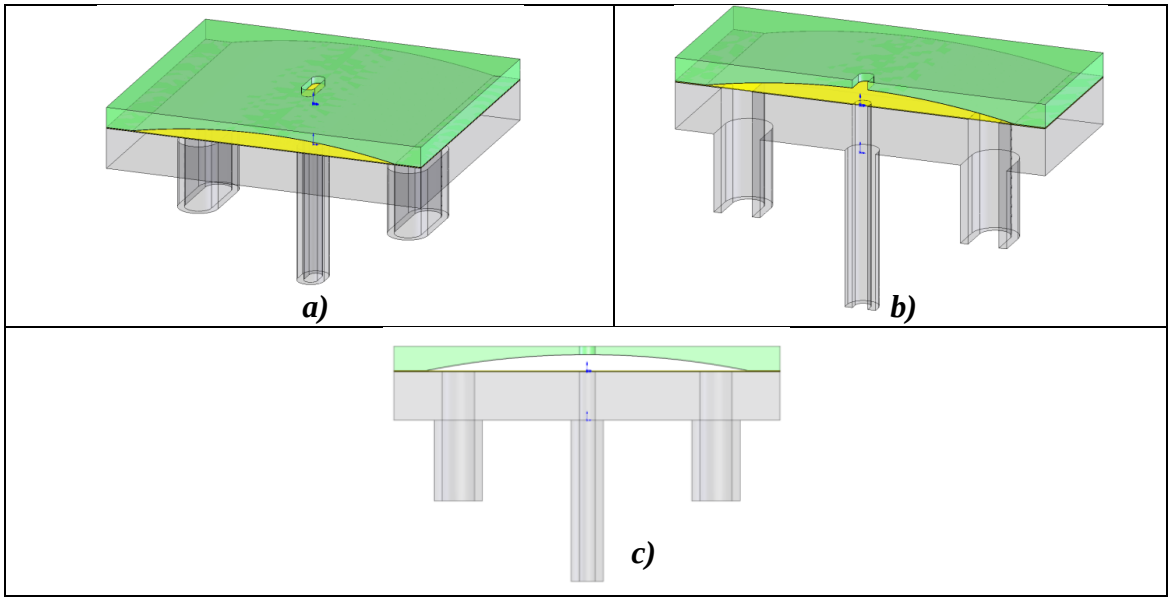

Fig. 4.11. CAD models for the micropump. a) Preliminary 3D compact design micropump, b) 3D cut view compact micropump y c) 2D transversal extracted micropump for modeling and meshing.

The meshing model, elaborate with CFD ACE-Geometry module software, is presented in Fig. 4.12 where it shows the length, high, insulation thickness (gap), input and output ports for the gas (air), meshing with finite elements for the areas for fluids, solid material, and boundaries. Fig. 4.12 is a scale up 10 times in the y direction for the

purpose of viewing. The 2D CAD meshing model is a simplify model of the 2D CAE extracted model; the sensitivity analysis studied in this model considers just the variables involved in performance in order to find the relationship between the variables described in Table 4.1.

The external dimension for the 2D Model are h and L where: h stand for the chamber height of 20 μm plus the thickness of the plate, the dielectric insulation layer of 0.2 μm, and the length 1000 μm of the symmetric one half of micropump.

Using the symmetry feature of this model, respect to the y-axis, only one half of the 2D micropump model needs to be analyzed. The one half 2D multiphysics meshing model will have several boundaries conditions: one clamped end, one symmetric axis for the entire 2D model; furthermore, it covers the fluid above and below the plate, the external 5 boundary surfaces of the electrodes on the top and the bottom walls, two more boundaries for the inlet and the outlet ports (both assigned with constant pressure), and finally two boundaries for the fluid-structure interactions between the plate and the surrounding fluid media (assigned with implicit pressure-load interactions) as well as the third interaction (electrical potential for a plate "Ground" volts and the electrode as +V volts). Two additional external boundaries will be walls for the fluid. These external and internal important boundaries are described in Fig. 4.12 and Table 4.2.

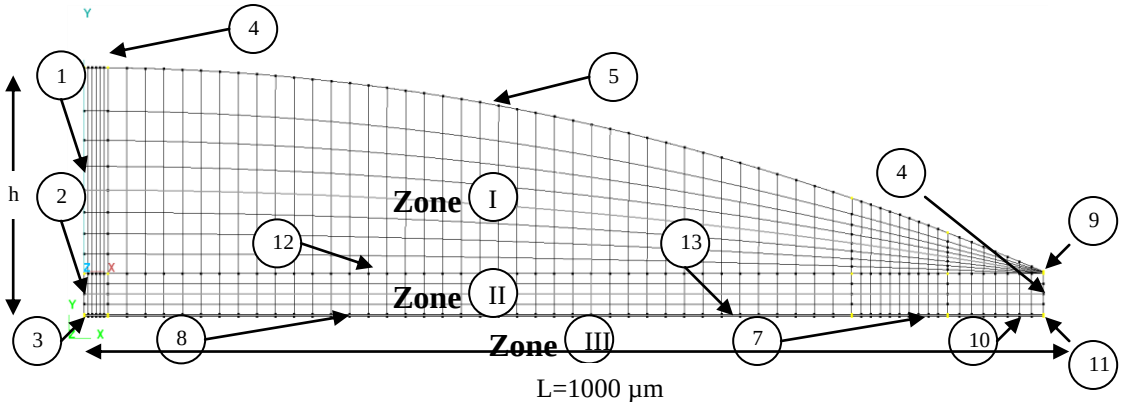

Fig. 4.12 General dimensions, boundaries conditions and 2D meshing micropump model.

Three main zones are shown in Fig. 4.12; these zones are involved in this new micro device physics. Zone II is the structural plate surrounding by the fluid which are zone I and zone III. Air is the fluid simulated. The plate material properties are from structural polysilicon. This 2D model problem is comprised of coupled interactions of fluid, structural, and electrostatic fields; the whole model involves moving boundaries and grid deformations. Table 4.3 points out the boundaries applied to 2D case model of Fig. 4.12.

Table 4.3 Boundaries conditions applied to the 2D model micropump

External/internal Boundary conditions	Contour domain	Zone	Volume conditions
Symmetry	1,2,3	I, II,II	Fluid and Solid
Rigid Clamped end	4	II	Solid
External wall	5, 8,9,10,11	I,II	Fluid
Input/Outlet flow Constant pressure	4 ,7	I,II	Fluid
Internal interface	12,13	1&2, 2&3	Fluid-solid interface

.

Scripting Python program was used to create the variable parameters, geometry and the meshing with description of the volume, boundary conditions. Structured meshing was used on all surfaces; the moving grid deformation feature requires that the mesh to be

structured to perform in a consistent way, using the structured geometry. Unstructured meshing is not available to use with moving boundaries feature.

In scripting the Python program, a number of grid points are selected to be applied on each external counter domain; this is a tradeoff set up. The rule of thumb is the minimal number of grid points required without sacrificing convergence on the residual values for the physicals parameter, like pressure, velocity vector fields, electrical field, FEM contact, stresses, density, viscosity, and grid motion. The process has to be used with caution. If very few grid points are used, and therefore, few structured mesh are built, the solution may occur in a short time and result in very poor convergence and an unrealistic sense of physics. On the other hands, if a very large number of grid points are chosen to discretize in order to have a large number of finite elements, and therefore improve the convergence, the required computational power and time will be prohibited. The chosen number of grids is a tradeoff. Balance has to be maintained between convergence and time required to complete the simulation. All of the parameters need to convergence in order to get a good data results from the simulation. For example, the criterion for the nonlinear stress convergence is 10^{-10} and for the shared interaction it is 10^{-04}.

4.14 2D Modeling Physics and 2D Equations on CFD-ACE.

Once the geometry and meshing is completed, the solver module from CFD ACE Solver GUI is called to set up the computational simulation run. Table 4.4 shows a list with the major and important features to be used in the multiphysics simulations. During this phase of setting up, the type of field domains chosen are Flow, Stress,

Electrostatic field, grid deformation, time dependence, and the time scheme. For stress, first order enhanced elements are chosen for this nonlinear shell; for the electrostatic field, a finite volume method is chosen. Next, volume conditions and material property values are assigned to the 2D zone created from the Geometry and meshing setting up phase. Specific values for the boundaries condition are in accordance with the parametric values for each simulation assigned to the external boundaries. Next, initial conditions are assigned for each zone and material in the model; the solver set up is made to select the number of iteration and convergence criteria for nonlinear stresses. For the coupled parameters, a spatial differential scheme is selected; a type of solver is selected for each major parameter. The numbers of iterations with the desired convergence criteria values and the relaxation values are chosen to help convergence. Finally, the set of output values are specified at each iteration step of the simulation to handle transient behaviors.

Table 4.4 Selecting the mutiphysics domain

Application Mode	2D	3D
Fluid Dynamics		
Full Navier-Stoke Equation	√	√
Structural Mechanics:		
Plane stress	√	
Plane strain	√	
3D Solid		√
Electromagnetic		
Electrostatic	√	√

4.15 Fluid Mechanics Module.

The governing equation for the flow is the full Navier-Stoke Equation which implies a conservation of mass, and the time rate is always equal of the forces on the fluid [CFD-ACE] the software solve this set of nonlinear equation in iterative process. In order to capture the squeezing dominant effect a compressible gas "Air" was chosen as a test fluid, [Wang & Chen, 2000].

4.16 Stress Module.

The stress module uses the theory provided by [Zienkiewics, 1971] with finite element method. This well known theory solves the structural mechanics equations. The software has the capability to coupling the stress module with electric module and flow under moving boundaries conditions. The stress module calculates the stresses and displacement of each node belonging to the elements.

4.17 Electrical Module in CFD-ACE

The governing equation to solve for this particular problem is the electrostatics equation with dielectrics and conductor materials. Electrical potential is used to calculate the electrical field, capacitance, pressure-forces. There are two methods; Finite Volume Method (FVM) and Boundary Element Method (BEM) for solving Poisson's equations, [CFD-ACE-2008]. The Finite Volume Method was chosen to performance the simulations. The electrostatics module calculates the electrostatic pressure, and this in turn is used by the stress module to calculate the forces and displacements. The electrostatics module is governed by Gauss' Law. Detailed information is found on the [CFD-ACE 2008 manual].

4.18 Moving Boundaries Grid Deformations Module.

This module is coupled with the stress module in order to study fluids structure interactions as well as electrostatic pressures. The Grid Deformation module can also work in conjunction with the stress module and the flow module to perform a Fluid Structure interaction simulation. Typically the stress module will control the deformation in solid regions, and Grid deformation module will control the grid deformations in the fluid regions.

The Grid deformation Module has two ways to controls the grid deformation; automatic remeshing and when we have very complex grid deformation problems, its need to use a user defined remeshing. The auto-remeshing means that the Grid Deformation Module (GDM) will automatically remesh the interiors of the structured grid volume conditions since their boundaries are moving. The remeshing scheme feature uses a standard transfinite interpolation (TFI) scheme to determine the interior node distribution based on the motion of the boundaries nodes. This scheme can be applied only to structured regions, therefore the fluid regions must be created using structured grids; Each region must have one volume condition; it cannot be applied to composited blocks [CFD-ACE 2008 manuals]. When the auto-remeshing method is used, only structured quad, hex grid types are supported with the commercial software. The moving grid re-meshing algorithm uses the linear TFI (Standard Transfinite Interpolation) method.

The motion of internal grid points (i,j) is calculated based on the motions defined at edges through the 2D remeshing.

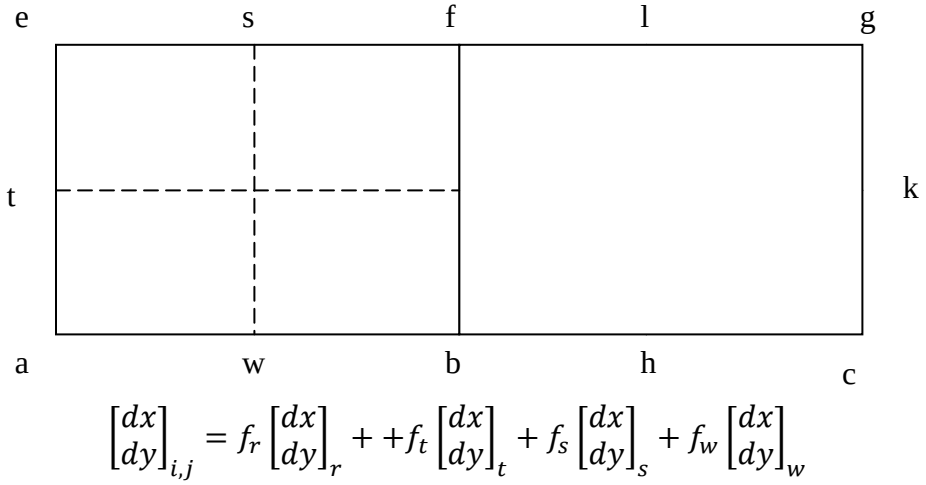

Fig. 4.13. Standard transfinite interpolation (TFI) scheme.

Where, dx and dy are displacements, function f is a linear interpolation function that is defined by the ratio of the edge length. Sometimes, if the geometry has edges that are extremely non-linear and complex, the re-meshing may not work.

Consider the particular case of 10 microns; see Figure 4.13. The fluid above the plate, has an edge ***a*** that was divided with 15 points, this edge is 20 microns in height so that dy_n=1.4289 microns. On the opposite side, it has the same number of points (structured domain), but the height is only 5 nm; the edge ***d*** has dy_n=0.357nm. The edge ***a***, interface between plate and fluid has been divided by 151 points. Also the quadratic function edge ***c*** has 151 points. Next, the structured mesh is created, and the TFI is activated on these structured zones. Once the stress module is activated on the plate zone, two loops of iterations are performed. The inner loop is used by the stress module, and the loads are applied based on the plate's electrical potential; 100 non-linear iterations with a frequency of 10 to the coupling with the flow are performed. Once this inner loop of iteration ends, the external loop of 200 times is run for coupling flow and electrostatics field; the new displacements are calculated until convergence.

The time durations of 1E-07 seconds is chosen for the transient Euler time accuracy. An air gap of 5nm between fluid zone and the dielectric material was chosen to accommodate the meshing of the fluid and therefore simulate the contact force between the plate and electrode as it acts against the dielectric material. If we use too small air gaps to simulate the hard contact between these two surfaces, the grid deformation will fail. Since roughness of the surface is not perfect at this dimension, it is a conservative design to have 5nm air gap with dielectric relative permittivity of 1 rather than the dielectric relative permittivity 3.9 of silicon dioxide. The inertial relaxation for moving boundaries was chosen to be 0.2, allowing the deformation to be elastic of the fluid grid under the TFI scheme as well as the 0.5 inertial relaxations for FEM contact.

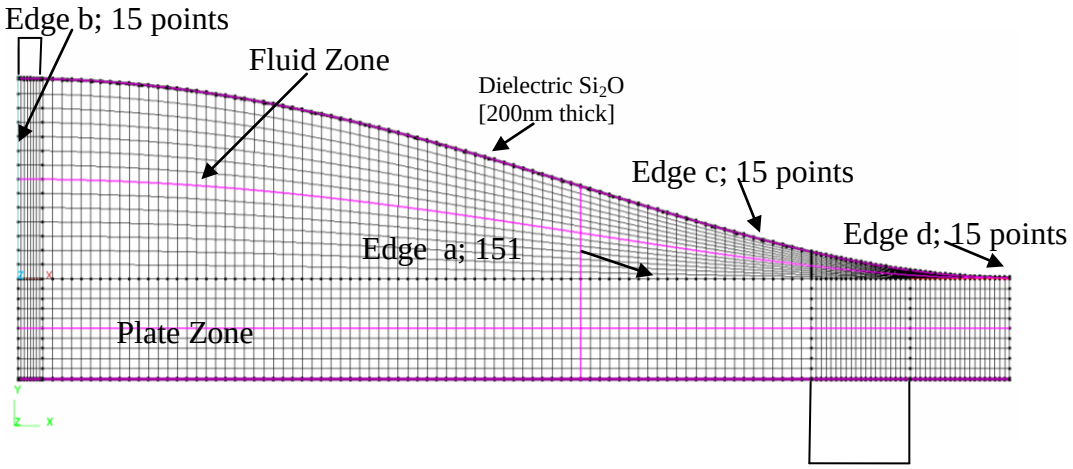

Fig. 4.14. Structured Meshing to allow use standard transfinite interpolation (TFI) scheme.

When the plate is fully against the upper wall, there will be a film of fluid trapped between the plate and the dielectric surface with a separation of 5nm.

4.19 Setting Up the 2D Model of Micropump.

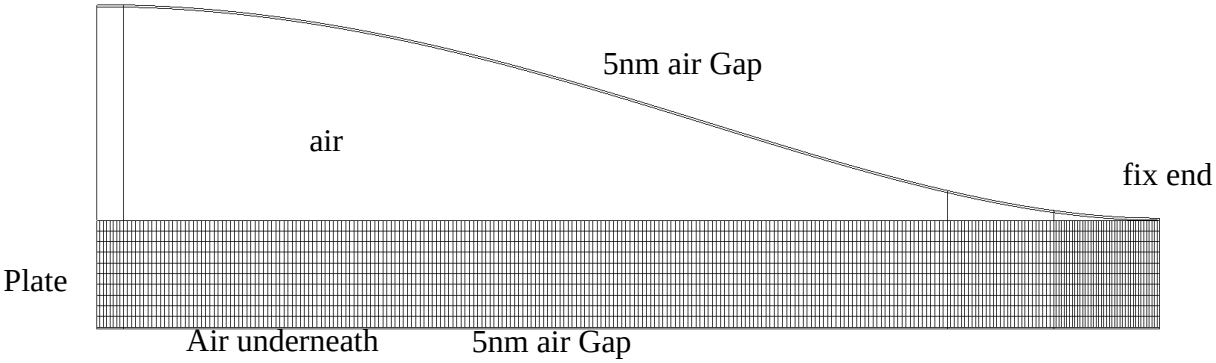

Fig. 4.15. Boundary conditions for plate

Half symmetry 2D micropump chamber was set up on CFD ACE+ software. There are several steps that have to be done in order to run a simulation. Seven steps in average have to be performed to prepare the simulation.

Step 1: Once the structured meshing is done on CFD GEOM, the saved model has to be open on the CFD solver in order to set up the multiphysics parameters. The following modules have to be activated: Flow, Stress, Grid Deformation and Electrostatic modules. For the flow module, the reference pressure was chosen as 101325 Pa and for the time dependence transient, the time steps of 1E-06 seconds as Euler time accuracy are chosen. For the stress module, Nonlinear Analysis was chosen due to the large deformation of the plate; first order element was chosen for fast and stable scheme and for nonlinear geometry and contact analysis. For the Grid Deformation, chosen was the auto remesh with transfinite interpolation. And, for the Electrostatic module, chosen was Electrostatic using the Finite Volume method for solver type.

Step 2: Define the control volume properties for each material involved on the simulation. Table 4.5 shows the material properties chosen for set up the simulation.

Material	Density rho[Kg/m^3]	Viscosity [Kg/m-s]	Material Type	Young's module [N/m^2]	Poisson's ratio	Thermal exp [1/K]	Electrical Conductivity/resistivity	Relative permittivity	Space charge
Polysilicone	2331	-	Linear/isotropic material	160E09	0.23	2.5E-06	Isotropic/conductor	1	0
Air	1.204	3.47E-06	-	-	-	-	Isotropic/1E-09 1/ohm	1	0
SiON	-	-	Linear/isotropic material	200E09	0.3	-	Isotropic/dielectric	3.9	0

Table 4.5 Volume control setting modes: material properties.

Step 3: Boundaries conditions for Plate.

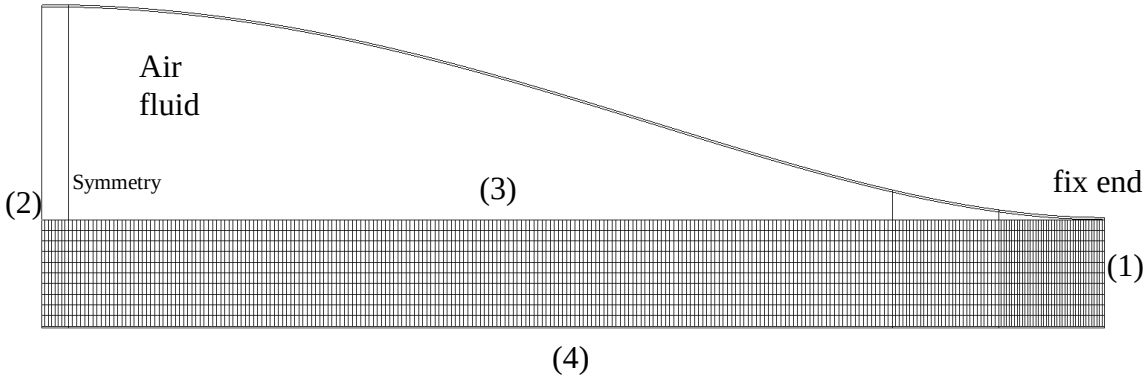

Fig. 4.16 Boundary conditions for micropump poly-silicon plate.

Fig. 4.16 shows the boundary condition for (1) fix-fix end, for the BC (2) Symmetry. For the BC (3) and (4) which are free to move and have contact analysis, an air gap of 5nm simulates the physical hard contact against to the dielectric material. If the air gap is reduced much below 5nm, the simulation will fail due to moving grid conditions and will reach elements with zero volume elements. The surfaces of the plate will have implicit applied pressure from the fluid interactions. For electrostatic properties, the plate is set to ground, 0 volts.

Step 5: Boundaries condition for the fluid.

For both fluids on the top and bottom of the plate, in order to activate the fluid structure and electrostatic interactions between the fluid, the electrodes and the plate, the boundaries condition have to be paired for both.

(5)
Output port

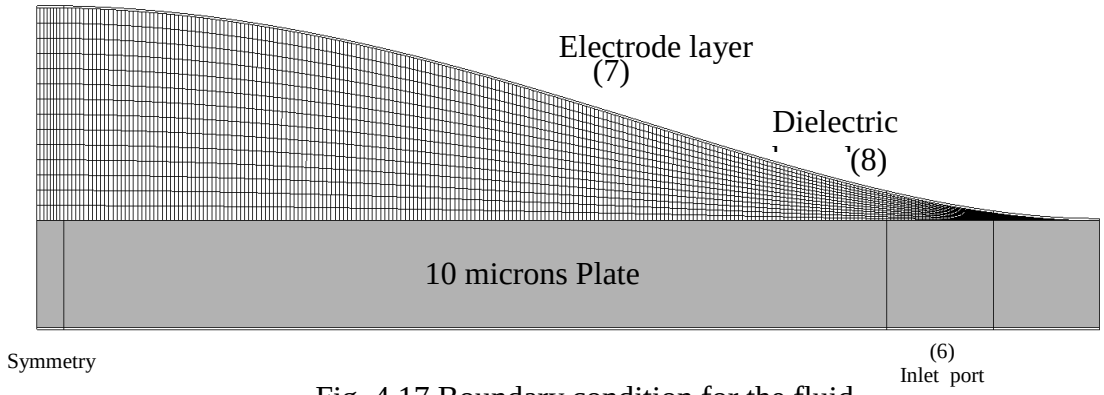

Fig. 4.17 Boundary condition for the fluid.

Fig. 4.17 shows, for the outlet (5) and inlet (6) ports, a fluid air is chosen to be open to the atmosphere and it shows that residual stresses are applied to the plate. On the top of the dielectric material (8) the simulation voltage is applied. The thickness of the dielectric material is d_0=200nm. The top surface of the plate has to match the dielectric boundary with the same contact force name as the air gap of 5 nm in order to accommodate the grid deformation; the same has to be done on the bottom surface of the plate with the fluid underneath with the dielectric contact force name pair. Therefore, voltage is applied on the top electrode if we want to perform the inlet stroke where the micropump sucks air from the bottom inlet port and exhaust air at the vent port. The left edge boundary is chosen to be symmetric for all the elements. Basically the micropump is mirrored in order to simulate half of the 2D micropump and save a large amount of computational time. Fig. 4.18 shows a 10 microns thick plate with residual stresses of 300MPa moving up, sucking air and squeezing out air from the curved chamber. A vector field of the fluid is formed as long the plate is going up, showing the direction of the fluid inside chambers, and showing how the plate is squeezing out the fluid through the outlet port and sucking air from the inlet port.

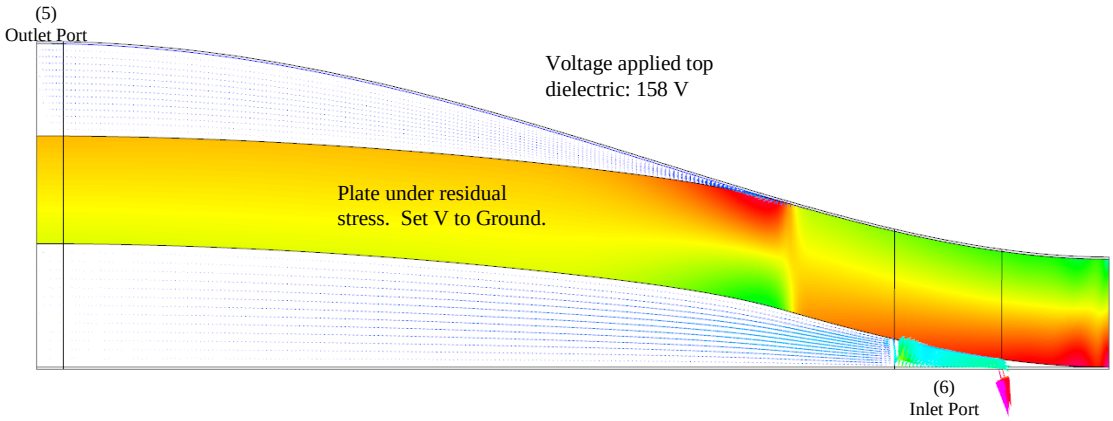

Fig. 4.18. 10μm plate, moving up under fluid structure and electrostatic interaction simulation.

Step 4: Set up the initial condition for all the material. Most of them start from rest but residual stresses are applied to the plate (tension residual stresses).

Step 5: Set up the solver: for the velocity of the fluid, the Upwind scheme is chosen; the number of interaction is set to 100 with convergence criterion of 0.0001. For the stress module nonlinear iterations, 100 steps were chosen. For the coupling where the scheme of calculation is first load-based and later displacement-based, the frequency is set to 5.

Step 6: Set up the output option to visualize under CFD View, it has to check the parameters need to review once the simulation is perform.

Step 7: Run the simulation, submit to the solver and check the convergence and residual variables, they must drop to lower levels, usually 1E-06. It will indicate that the simulation is converging to a stable solution.

4.20 Simulation Results for Power Intake Stroke

These simulations results for power intake stroke were performed under steady state analysis of parametric study for the 2 D cross-section of the 2 mm plate length; due to

the symmetry, only half of the model was necessary for simulation and analysis. Therefore symmetric boundary conditions have been applied to the fluid, structure and electrostatic field coupling problem.

Several cases have been analyzed in this study. The main goal is to determine which of the micropump candidate late sizes have a potential to handle large residual stresses on the plate as well as bending stresses combined when the thickness on plate is varied with different applied voltages (maximum available is 200V). The applied voltage must avoid the dielectric breakdown voltage (1 volt/nm is maximum), as explained in Chapter 2. For the studies herein, 200nm of silicon dioxide (SiO_2) is selected as the dielectric material thickness. Silicon dioxide (SiO_2) has a relative dielectric permittivity of 3.9.

Different plate thickness cases have been performed: cases from [2 μm, 4 μm, 4 μm, 8 μm, and 10 μm] with different residual stresses applied to each case from [200 MPa, 400 MPa, 500 MPa, 400 MPa, 800 MPa, 1000 MPa up to 1200 MPA] at different levels of applied voltages. Voltages from 40 V through 200 V are applied. For the cases presented, the minimum applied voltage is determined that is needed to lift up the thin plate, during the intake stroke. The plate is lifted up to the point where all forces are in equilibrium. At that particular point which is close to the maximum slope occurred, the analytical model is validated by its ability to predict the same results as provided by the multiphysics simulations for all cases considered (different plate thicknesses, residual stresses, and applied voltages). The analytical model developed in the Section 4.4 section is shown to be validated by how well it matched the simulation results. Therefore, analytical model is useful to predict with and to design micro-pump

based on electro zippering mechanics. Therefore, the physics of the electrozippering mechanism approach that has been developed here will be validated with numerical Mutiphysics FEM simulations.

Results from intake power stroke simulations conducted by the multiphysics Software CFD-ACE + are shown to compare well with the results of analytical model for all the cases.

Case study 1) Plate with 10 microns thicknesses to raise up 20microns, while the initial condition on residual stresses was constant from [200, 400 , 500 , 400 800 and 1000] MPa, and varies the voltage until found the maximum critical voltage that led the plate goes up 20 microns full intake stroke, for instance it was found that thickness of 10 microns plate with initial residual stresses of 200 MPa, it is found that 131 volt applied to the electrode on the top of the curved chamber was the maximum critical voltage to hold the plate in an unstable condition (Pull-up) before to jump up to open 100% intake stroke. The data then was extracted form that very particular and interest situation, and then the residual stresses were increase and repeat the process to find the critical voltage and their plate location. This study also provide insight about how the plate behaves when is lifting up due to the electrostatic force to create the intake power stroke while is moving up. We find the maximum residual stress that the micropump can handle while keeping the voltage as low as possible below the maximum allowable voltage due to dielectric breakdown safety voltage of 200 Volts (for the case of do=200nm); recall that the dielectric SiO_2 has permittivity 3.9 and that we have an air gap of 5nm. The results are shown in Figs. 4.20.1 through Fig. 4.20.28. Studies for case 1, the plate thickness is

10 microns; for case 2, it is 8 microns; for case 3, it is 6 microns; for case 4, it is 4 microns; and for case 5 it is 2microns.

Table 4.6 Simulation Results for Intake Stroke

t	*RS*	*V*	*SigT*	*SigB*	*SigVM*
um	MPa	Volts	MPa	MPa	MPa
10	500	199	513.4	285.5	794.03
10	400	179	413.5	240.5	670.2
10	200	130.8	214.7	198.4	411.35
8	600	195	615.3	301.9	912.5
8	400	160.5	415.4	257.6	669.2
8	200	116	214.4	192.4	405.2
6	200	100.5	216.5	188.7	404.07
6	400	139	415.6	244.8	658.05
6	600	169	615.3	285.3	895.55
6	800	195	971.8	320.4	1292.2
4	200	82	216.1	174.8	390.18
4	400	114	416.6	225.9	640.38
4	600	138.5	615.5	258.5	871.39
4	800	160	817.1	285	1098.6
4	1000	178.5	1016.2	309.3	1320.7
4	1200	195.5	1216.7	331.1	1542.4
2	200	58.5	217.21	147.9	364.8
2	400	81.3	416.96	184.5	601.22
2	600	99	616.55	210.3	826.45
2	800	114	816.19	228.2	1043.8
2	1000	127.5	1017.3	242.6	1259.2
2	1200	139.5	1216.7	252.2	1468.01
2	1400	150.5	1416.4	259.5	1674.81
2	1600	161	1616.9	266.9	1882.6
2	1800	170.5	1816	271.2	2085.84
2	2000	180	2016.9	278.4	2293.85
2	2200	188.5	2216	280.2	2494.53
2	2400	197	2416.3	284.7	2698.5

Results: Case 1.1. 10 µm, Rsxx=500MPa, Voltage = 199 V (Critical) Well refine meshing model. 10 µm thickness: 200Volts, Rsxx=500MPa, do=200nm (Si02) 3.9 air gap of 5nm.

Ymax_plate = 8.049 µm, σt= 513.4MPa (44.27%) y σb= 285.5MPa(35.73%):Von Mises= 794.03MPa < Suy
Volumen displacement = 12.02E-03 mm3/mm (54.34%)
rmax_B=449 µm, radius(break-up)=474µm, rho =2.479 mm (minimum curvature) at max bending area

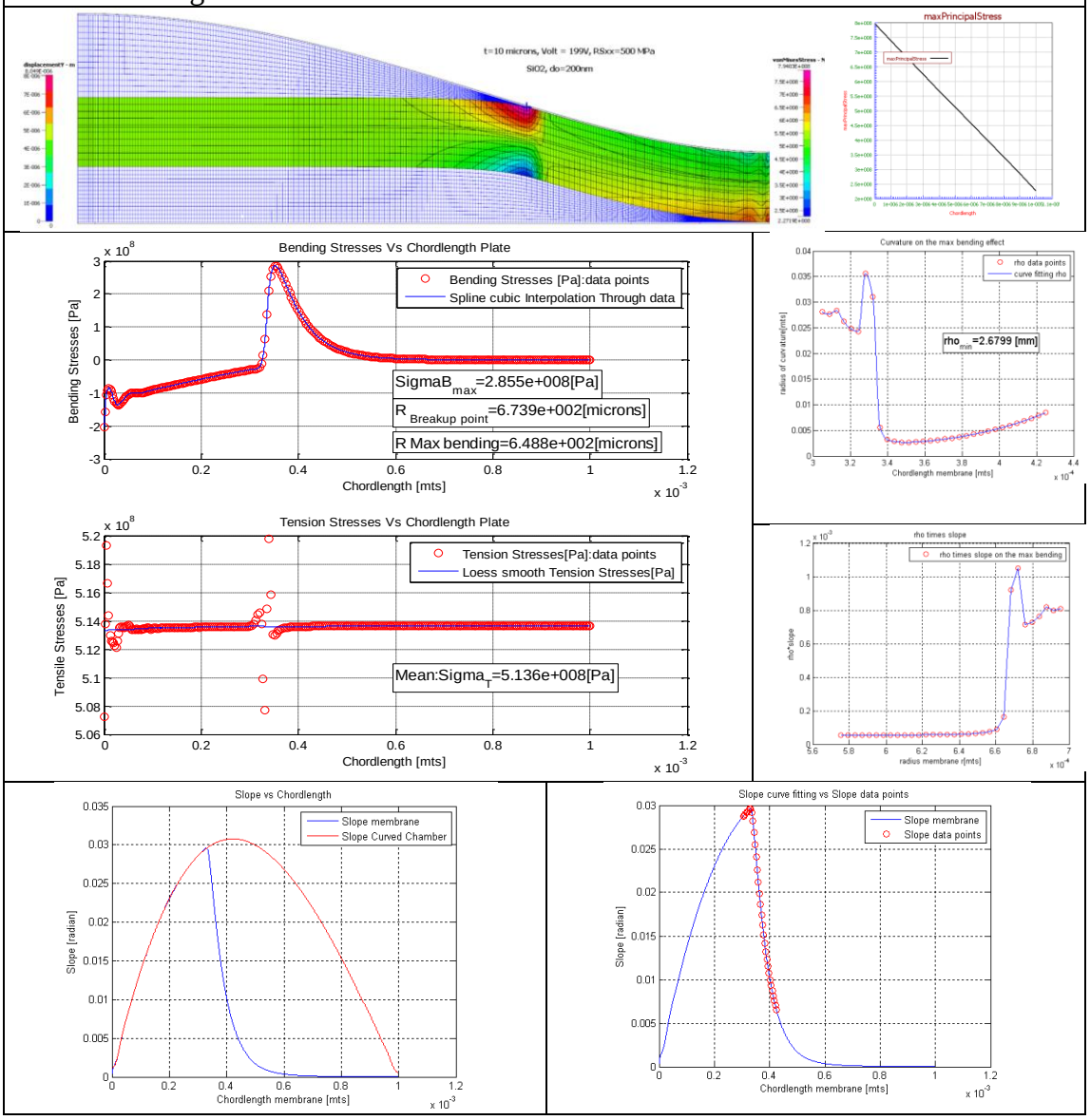

Fig. 4.20.1. Summary results for 10 µm thickness of the plate with Rsxx=500MPa applied Voltage 199 V. $Si0_2$ do=200nm. Critical Voltage found is 199V

Results: Case 1.2. 10 µm thickness: Residual stress set to 400 MPa.
10 µm thickness: 179 Volts, RSxx=400MPa, do=200nm (Si02) 3.9 air gap of 5nm.

Ymax_plate = 8.109 µm. σt= 413.5MPa (41.35%) and σb= 240.5 MPa (38.45%), Von Mises= 670.2MPa < Suy: Volumen displacement =12.08 E-03 mm3/mm (50.40%)
rmax_B 448.8 µm, radius(Break_up) = 477.4 µm , rho = 2.95 mm (minimum curvature) at max bending area.

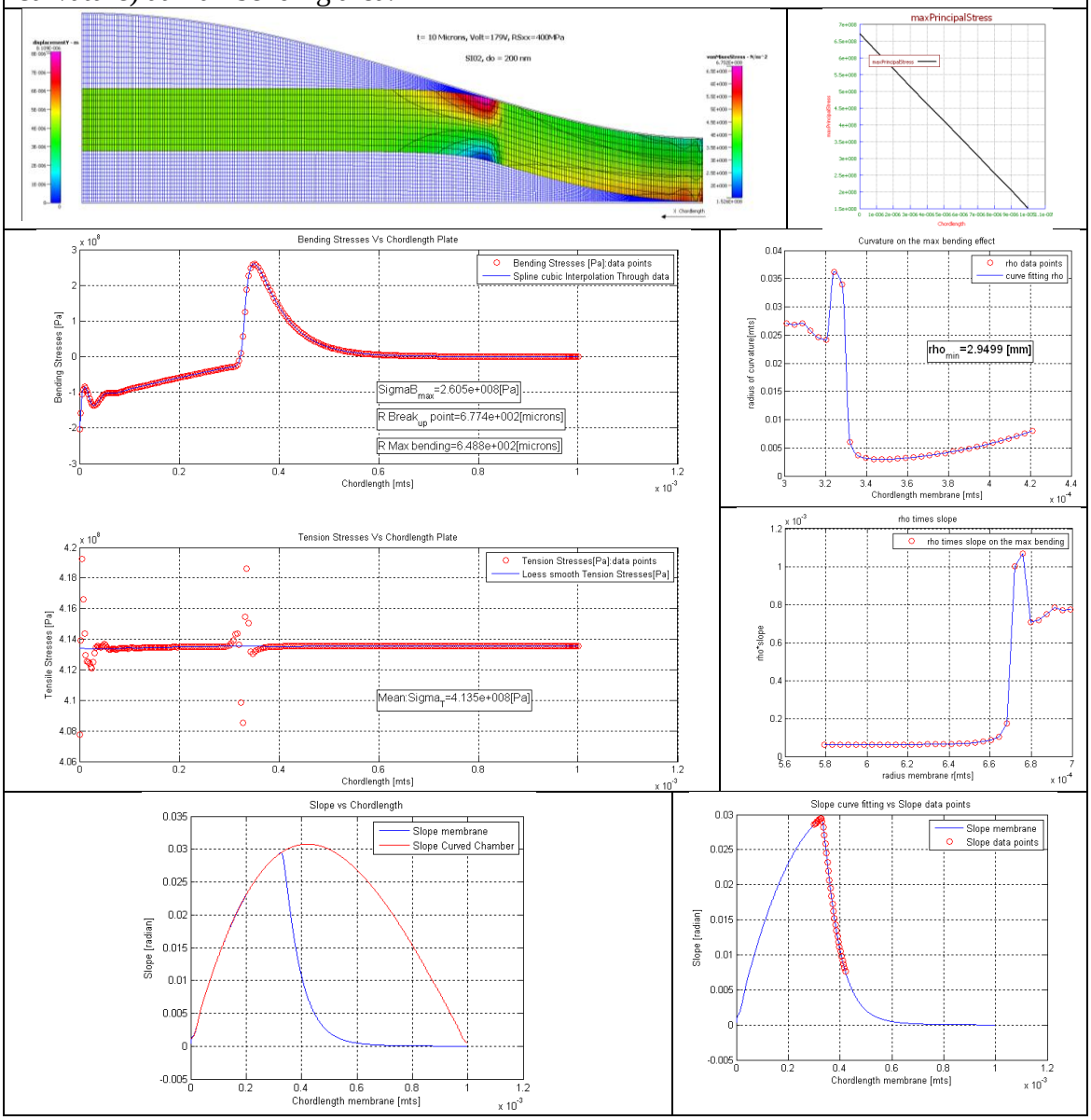

Fig. No. 4.20.2 Summary results for 10 µm thickness of the plate with Rsxx 400MPa applied Voltage 179 V. $Si0_2$ do=200nm ,Critical Voltage found is 179Volts

Results: Case 1.3. 10 µm thickness, Residual stress set to RSxx=200MPa,
10 µm thickness, Voltage = 130.8 V (Critical) do=200nm (Si02) 3.9 air gap of 5nm.

Ymax_plate = 8.949 µm. σt= 214.7 (51.95%) y σb= 198.4MPa(48.05%): Von Mises= 411.35MPa < Suy
Volumen displacement = 12.02E-03 mm3/mm (54.34%)
rmax_B=441.1 µm, radius(break-up)= 472 µm, rho =3.94 mm

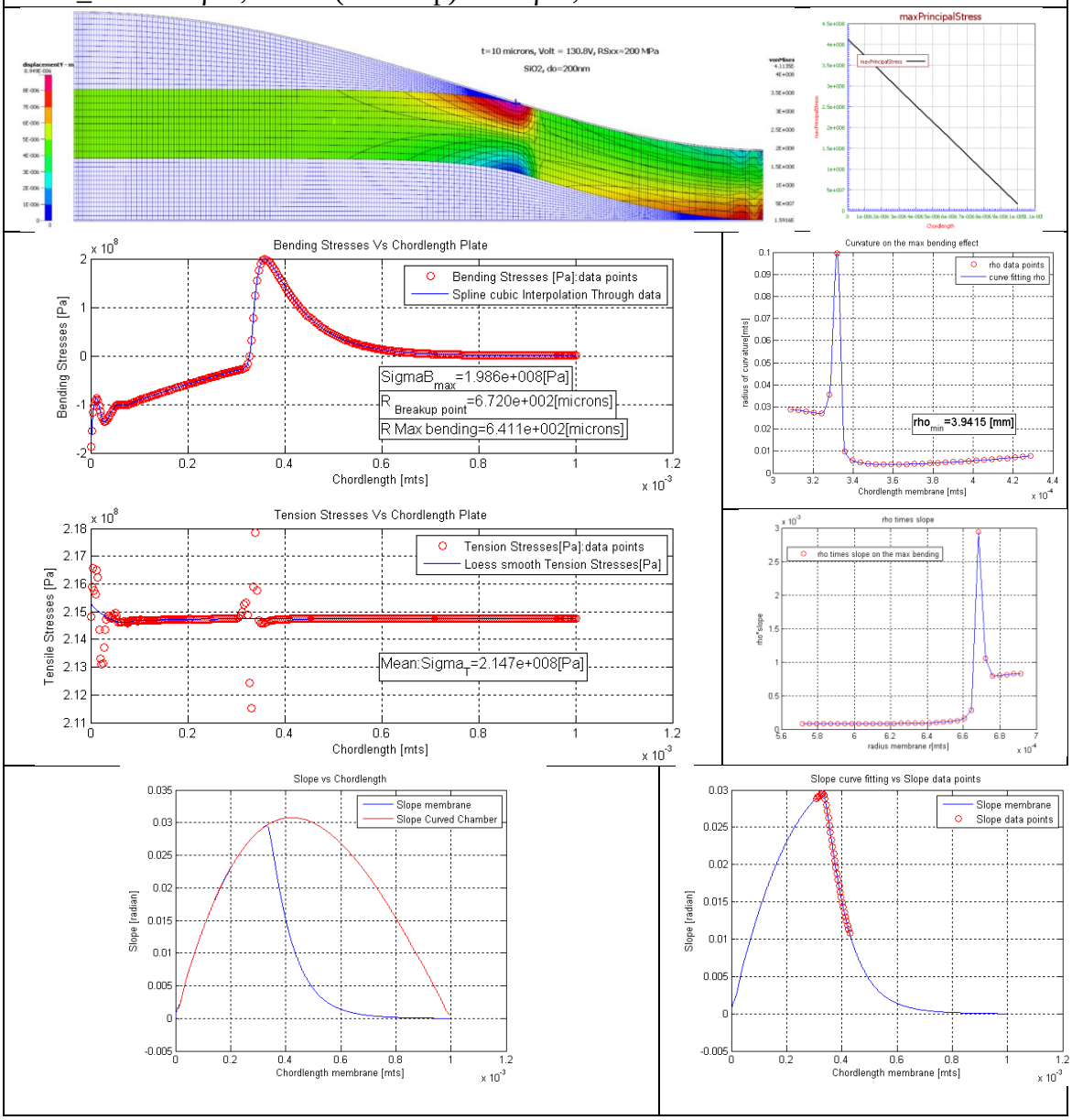

Fig. No. 4.20.3 Summary results for 10 µm thickness of the plate with Rsxx 200MPa applied 130.8 V. Critical Voltage found is 130.8Volts

Results: case 2.1. 8 µm thickness: Residual stress set to 600 MPa.
8 µm thickness: 195 Volts, RSxx=600MPa, do=200nm (Si02) 3.9 air gap of 5nm.

$Y_{max\_membrane}$ = 8.59 µm. σt= 615.3 MPa (67.08%) and σb=301.9 MPa (32.92%), Von Mises= 912.5MPa < Suy: Volumen displacement =12.71 E-03 mm^3/mm (59.55%) $r_{(Max\ bending)}$=617.8 µm, $radius_{(Break\_up)}$ =642.8 µm , rho = 2.02 mm (minimum curvature) at max bending area.

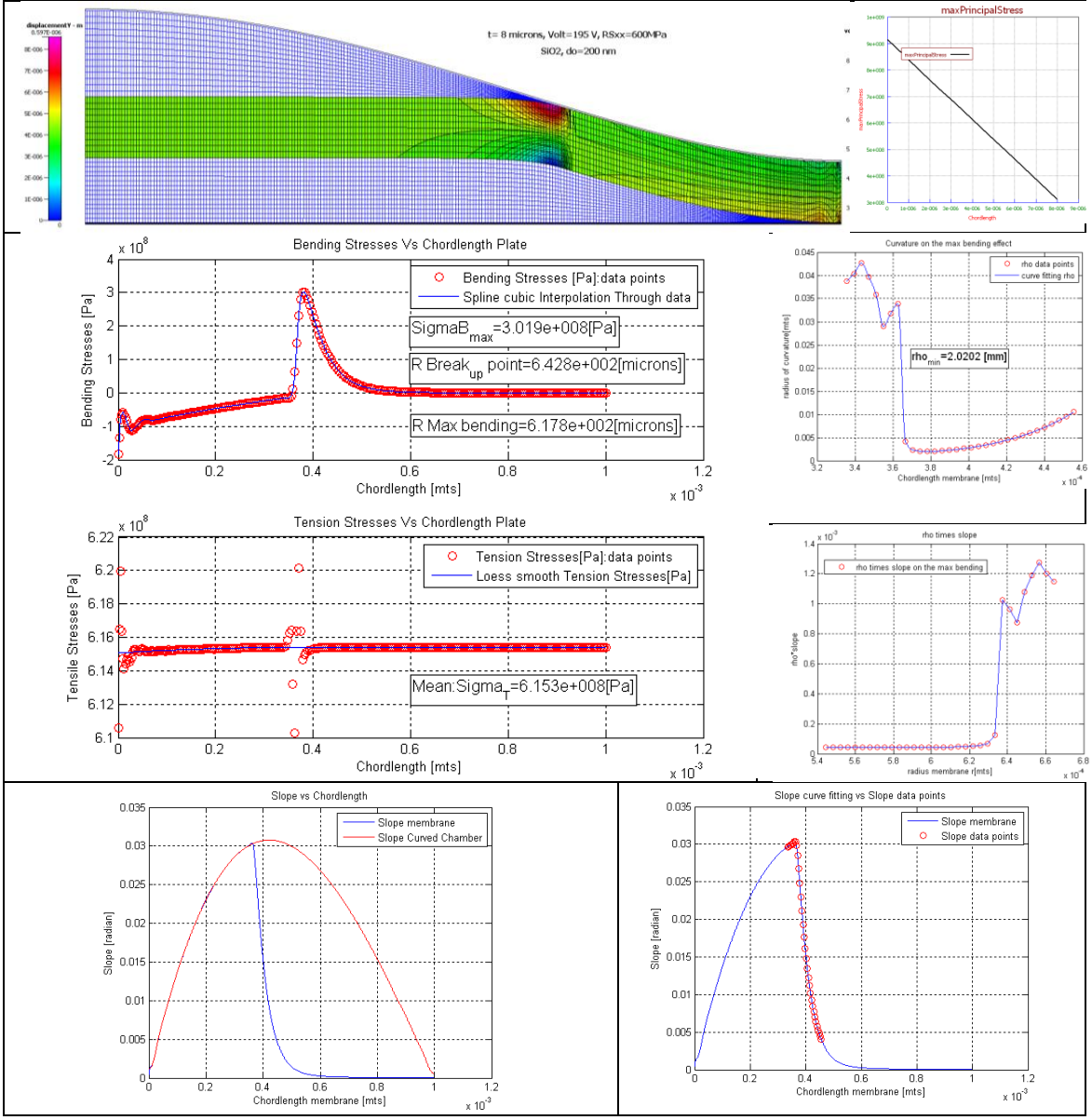

Fig 4.20.4 Summary results for 8 µm thickness of the plate with RSxx 600MPa applied 195V. Critical Voltage found is 195Volts.

Results: Case 2.2. 8 µm thickness: Residual stress set to 400 MPa.
8 µm thickness: 160.5 Volts, RSxx=400MPa, do=200nm (Si02) 3.9 air gap of 5nm.

$Y_{max\_membrane}$ = 8.747µm. σt= 415.4 MPa (61.72%) and σb= 257.6MPa (32.28%), Von Mises= 669.2MPa < Suy:
Volumen displacement =12.87 E-03 mm^3/mm (60.32%)
$r_{(Max\ bending)}$= 621.7µm, $radius_{(Break\_up)}$= 646.0µm , rho = 2.405 mm (minimum curvature) at max bending area.

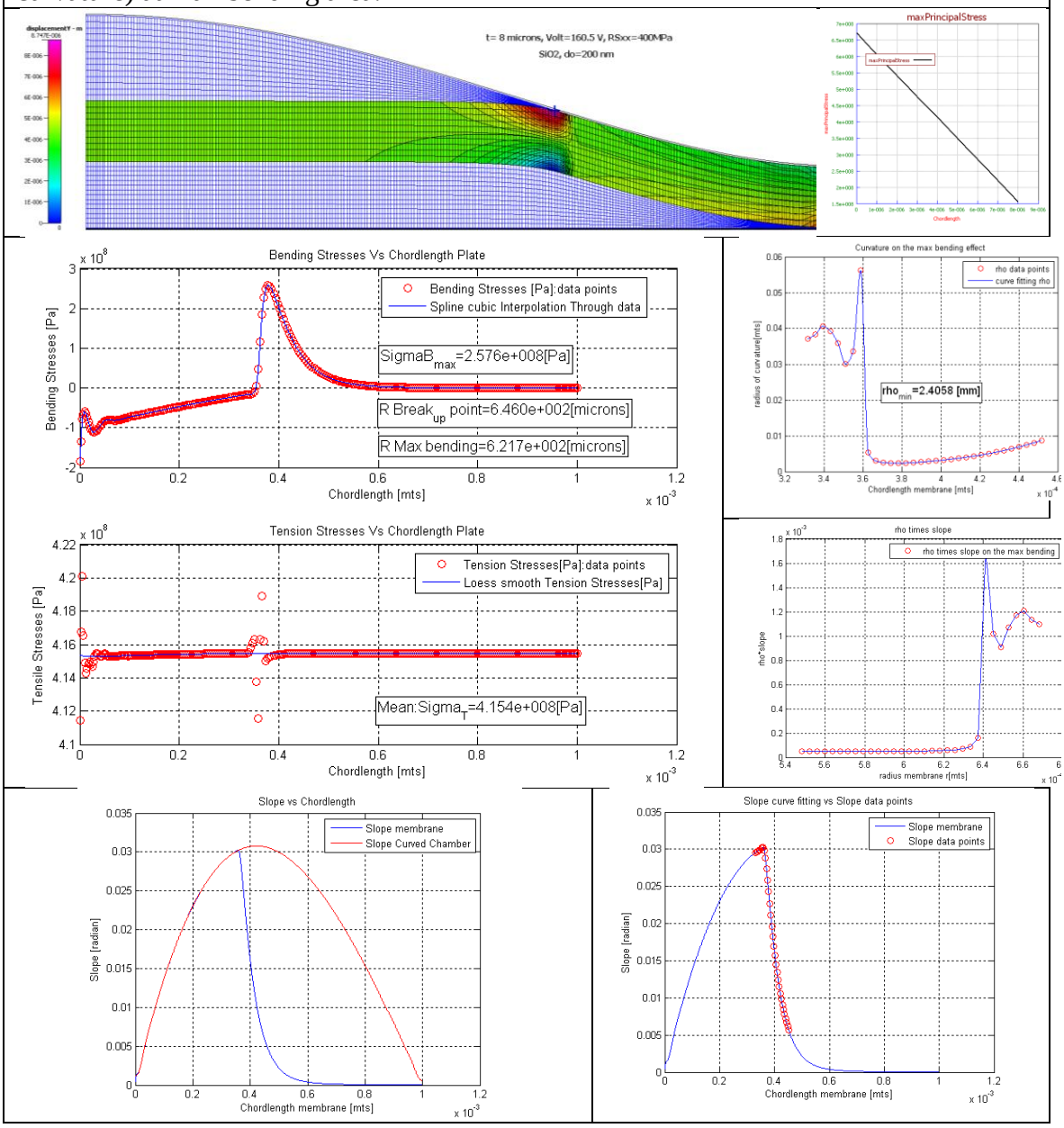

Fig. 4.20.5. Summary results for 8 µm thickness of the plate with RSxx 400MPa applied 160.5V. Critical Voltage found is 160.5Volts.

Results: Case 2.3. 8 µm thickness: Residual stress set to 200 MPa.
8 µm thickness: 116 Volts, RSxx=200MPa, do=200nm (Si02) 3.9 air gap of 5nm.

$Y_{max\_membrane}$ = 8.60 µm. σt= 214.4MPa (52.70%) and σb= 192.4MPa (47.30%), Von Mises= 405.5MPa < Suy: Volumen displacement =12.64 E-03 mm^3/mm (59.25%) $r_{(Max\ bending)}$=637.2µm, $radius_{(Break\_up)}$=667.4µm , rho = 3.25mm (minimum curvature) at max bending area.

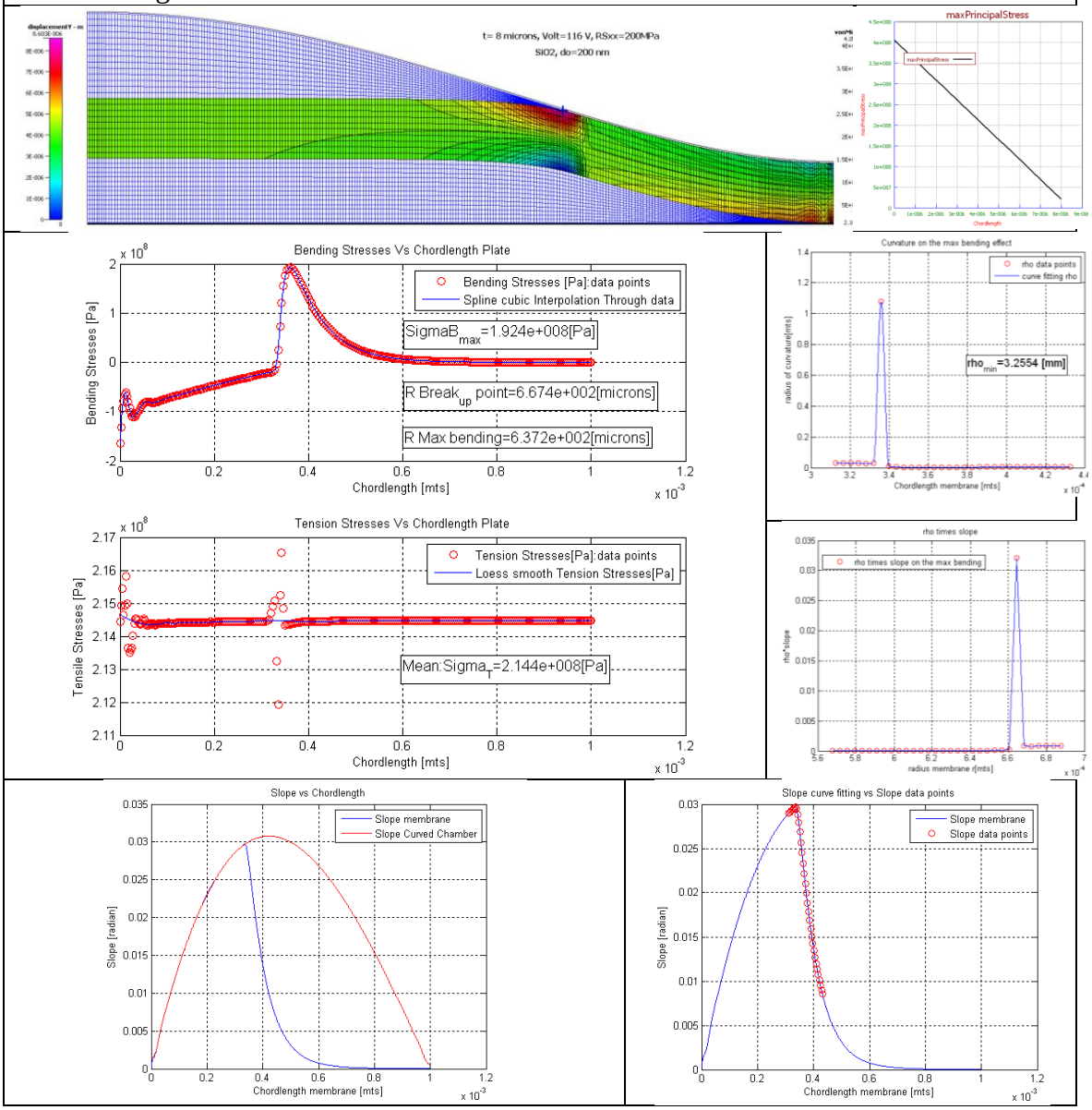

Fig. 4.20.6. Summary results for 8 µm thickness of the plate with RSxx 200MPa applied 116 V. Critical Voltage found is 116Volts.

Results: case 3.1. 6µm thickness: Residual stress set to 200 MPa.
6µm thickness: 100.5 Volts, RSxx=200MPa, do=200nm (Si02) 3.9 air gap of 5nm.

$Y_{max\_membrane}$ = 9.218µm. σt=216.5MPa (53.43%) and σb=188.7MPa (46.57%),Von Mises=404.07MPa < Suy:
Volume displacement =13.40E-03 mm^3/mm (62.82%)
$radius_{(Break\_up)}$ = 629.1µm , $r_{(Max\ bending)}$=606.2µm, rho = 2.50mm (minimum curvature) at max bending area.

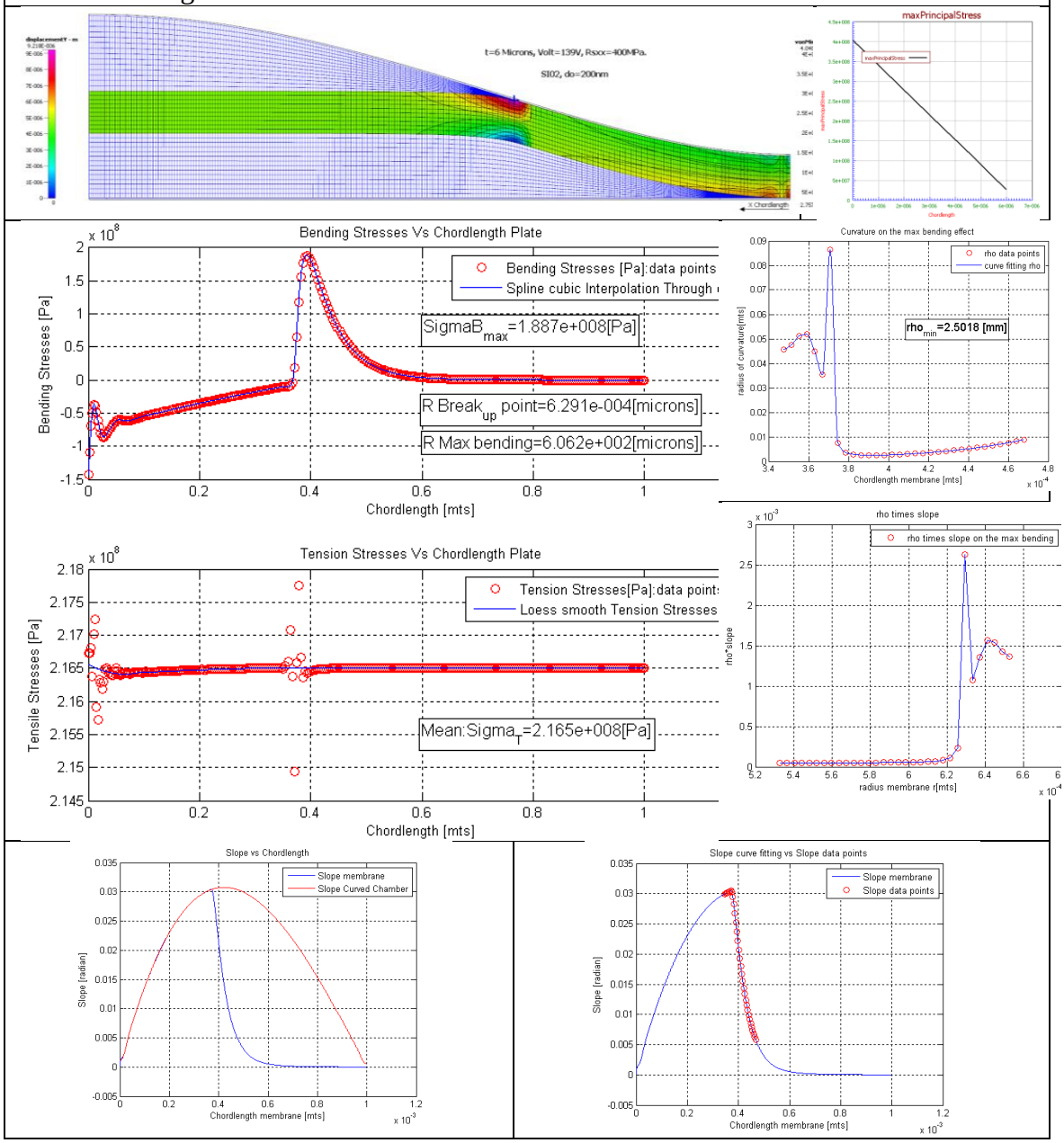

Fig. 4.20.7. Summary results for 6 µm thickness of plate with RSxx 200MPa applied 100.5V. Critical Voltage found is 100.5Volts.

Results: Case 3.2. 6µm thickness: Residual stress set to 400 MPa.
6µm thickness: 139 Volts, RSxx=400MPa, do=200nm (Si02) 3.9 air gap of 5nm.

$Y_{max\_membrane}$ =8.649µm. σt=415.6MPa (62.93%) and σb=244.8MPa (37.07%),Von Mises=658.05MPa < Suy:
Volume displacement =12.78E-03 mm^3/mm (59.92%)
$radius_{(Break\_up)}$ =633.20µm , $r_{(Max\ bending)}$=614.0µm, rho =1.907mm (minimum curvature) at max bending area.

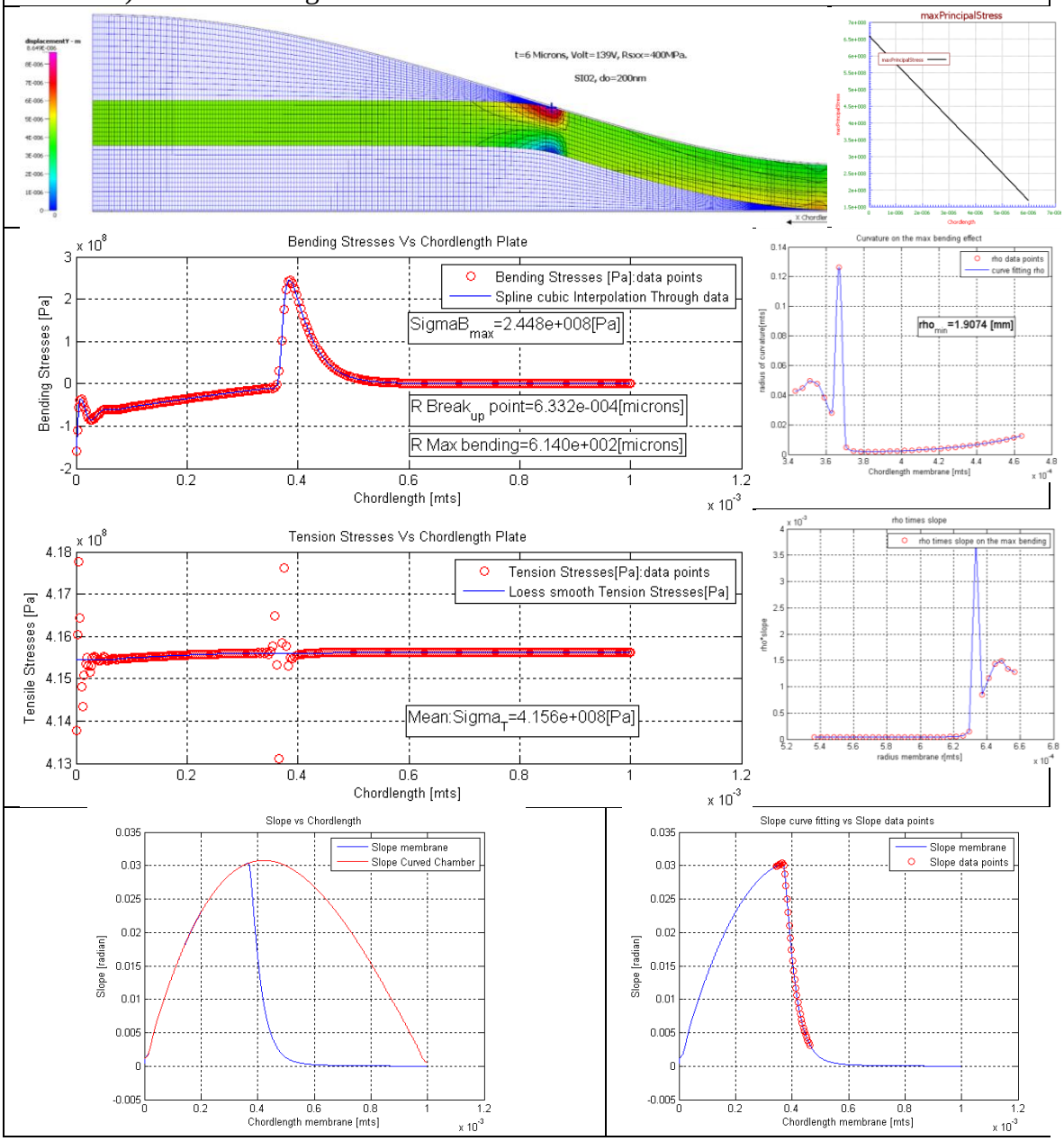

Fig. 4.20.8. Summary results for 6 µm thickness of plate with RSxx 400MPa applied 139V. Critical Voltage found is 139Volts.

Results:Case 3.3. 6µm thickness: Residual stress set to 600 MPa.
6µm thickness: 169 Volts, RSxx=600MPa, do=200nm (Si02) 3.9 air gap of 5nm.

$Y_{max\_membrane}$ =8.44µm. σt=615.30MPa (%) and σb=285.3MPa (%),Von Mises=895.55MPa < Suy:
Volume displacement =12.55E-03 mm^3/mm (58.82%)
$radius_{(Break\_up)}$ =633.3µm , $r_{(Max\ bending)}$=617.8µm, rho =1.614mm (minimum curvature) at max bending area.

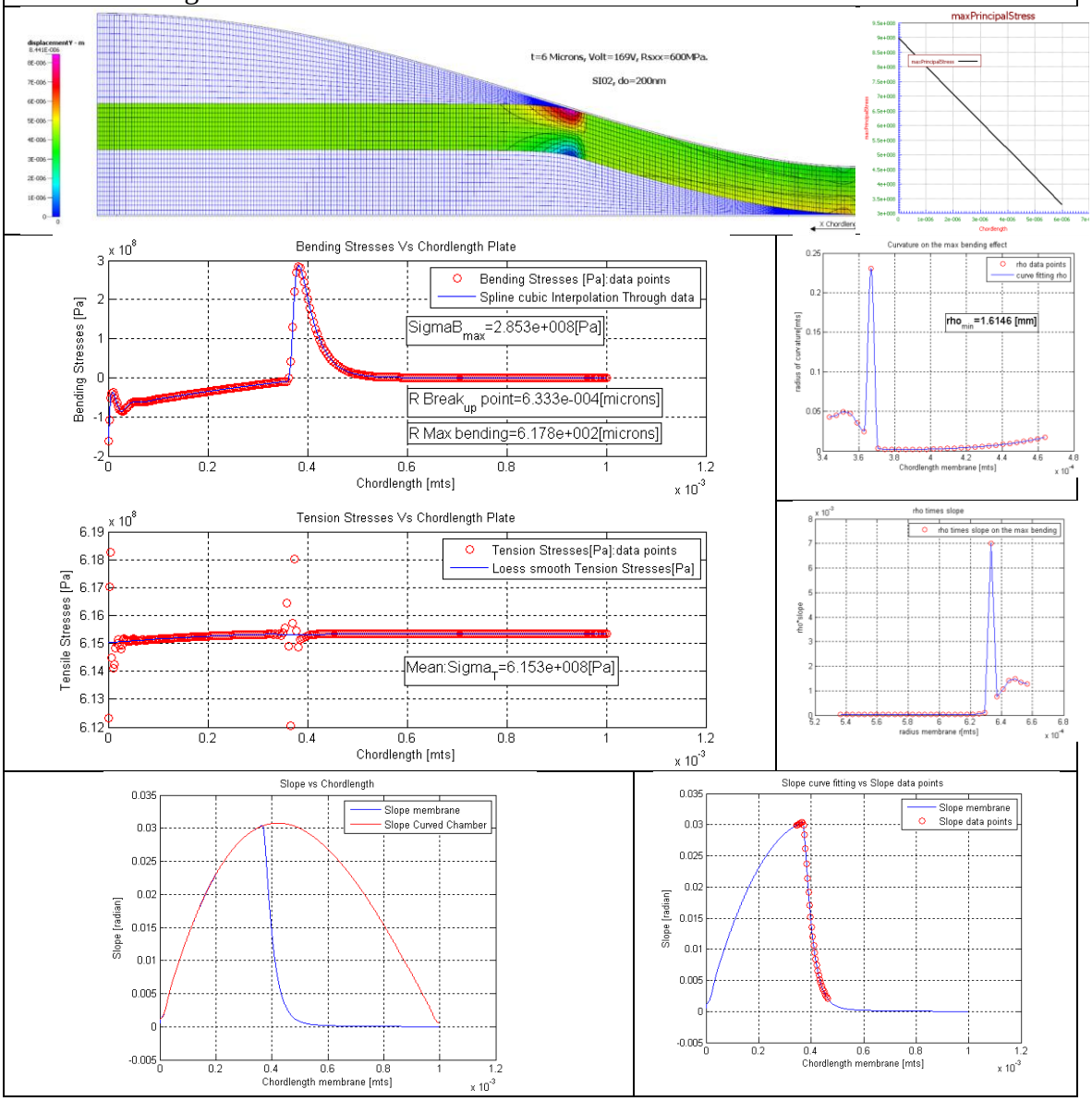

Fig. 4.20.9. Summary results for 6 µm thickness of plate and RSxx 600MPa applied 169V. Critical Voltage found is 169Volts.

Results: case 3.4. 6µm thickness: Residual stress set to 800 MPa.
6µm thickness: 195 Volts, RSxx=800MPa, do=200nm (Si02) 3.9 air gap of 5nm.

$Y_{max\_membrane}$ =8.91µm. σt=971.8MPa (%) and σb=320.4MPa (28.17%),Von Mises=1292.2MPa < Suy:
Volume displacement =13.11E-03 mm^3/mm (61.46%)
$radius_{(Break\_up)}$ =614.1µm , $r_{(Max\ bending)}$=598.5µm, rho =1.437mm (minimum curvature) at max bending area.

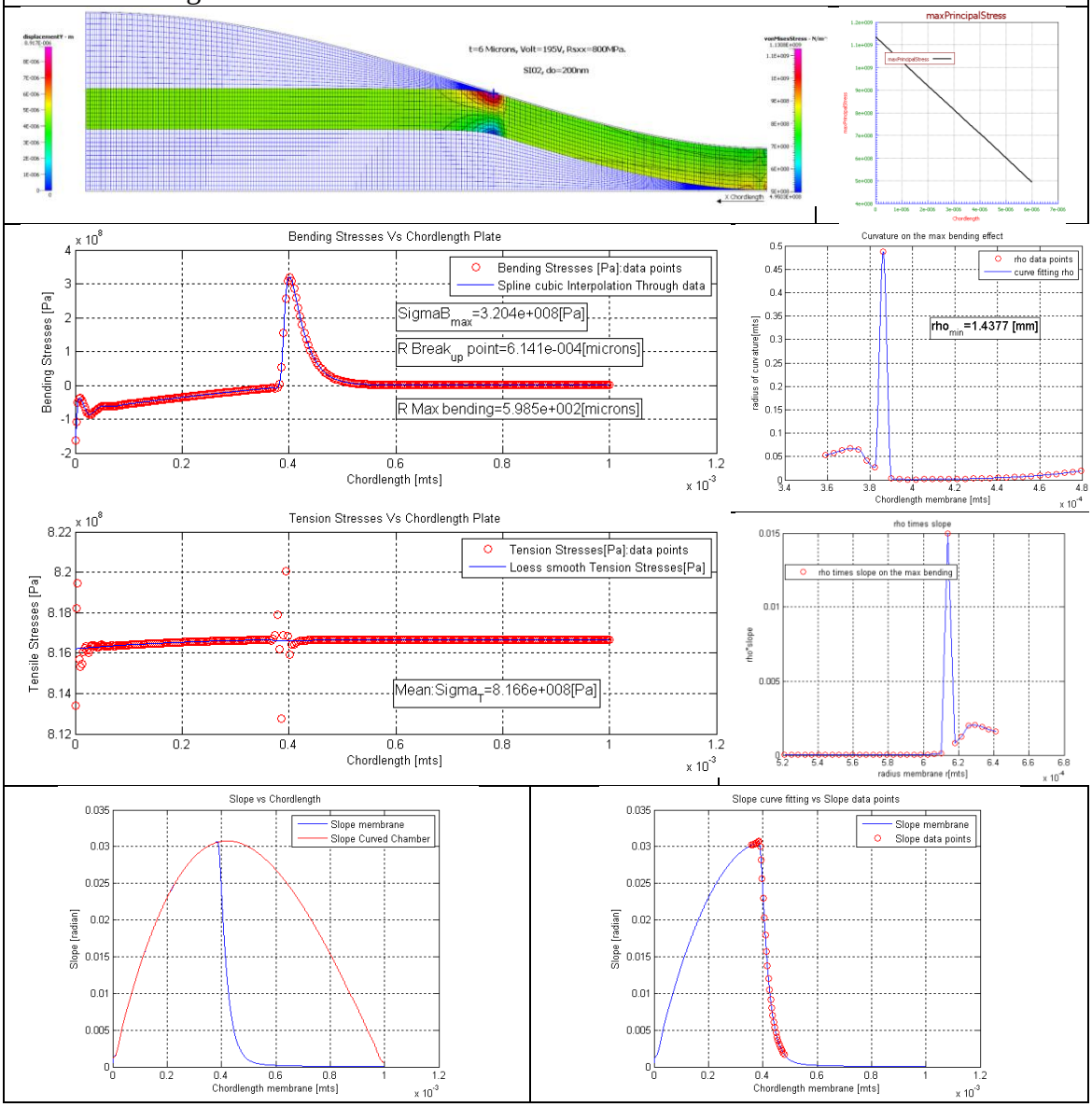

Fig. 4.20.10 Summary results for 6 µm thickness of plate with RSxx 800MPa applied 195V. Critical Voltage found is 195Volts.

Results: Case 4.1. 4µm thickness: Residual stress set to 200 MPa.
4µm thickness: 82 Volts, RSxx=200MPa, do=200nm (Si02) 3.9 air gap of 5nm.

$Y_{max\_membrane}$ = 8.84µm. σt=216.10MPa (55.29%) and σb=174.8MPa (44.71%),Von Mises=390.18MPa < Suy:
Volume displacement =13.01E-03 mm^3/mm (61.01%)
$radius_{(Break\_up)}$ = 624.9µm , $r_{(Max\ bending)}$=606.2µm, rho =1.803mm (minimum curvature) at max bending area.

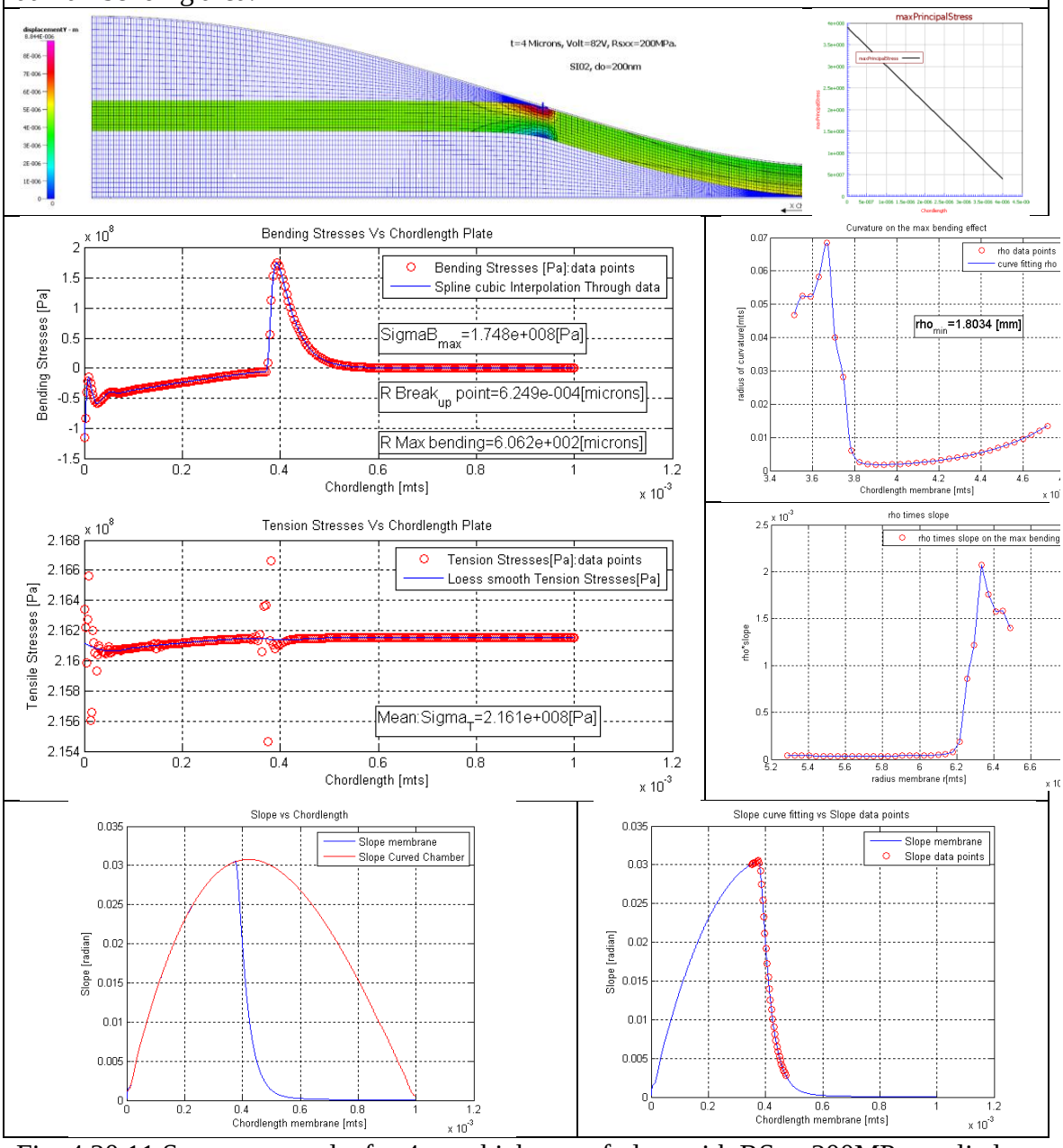

Fig. 4.20.11 Summary results for 4 µm thickness of plate with RSxx 200MPa applied 82V. Critical Voltage found is 82Volts.

Results: case 4.2. 4µm thickness: Residual stress set to 400 MPa.
114 Volts, RSxx=400MPa, do=200nm ($Si0_2$) permittivity 3.9 air gap of 5nm.

$Y_{max\_membrane}$ =8.90 µm. σt=416.6MPa (64.84%) and σb=225.9MPa (35.16%),Von Mises=640.38MPa < Suy:
Volume displacement =13.10E-03 mm^3/mm (61.41%)
$radius_{(Break\_up)}$ = µm , $r_{(Max\ bending)}$=µm, rho = mm (minimum curvature) at max bending area.

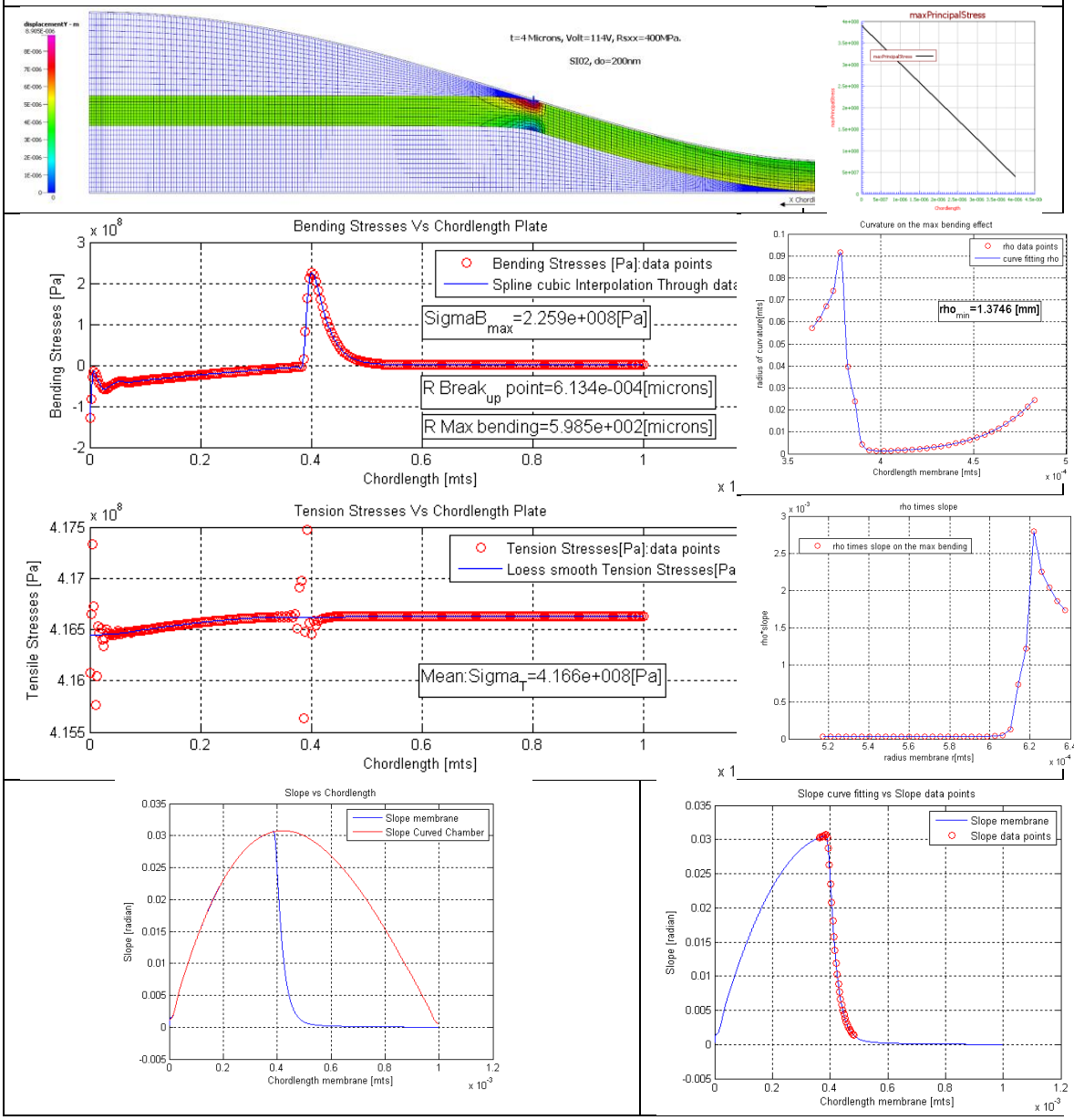

Fig. 4.20.12. Summary results for 4 µm thickness of plate with RSxx=400MPa applied 114V. Critical Voltage found is 114Volts.

Results: Case 4.3. 4µm thickness: Residual stress set to 600 MPa.
4µm thickness: 138.5 Volts, RSxx=600MPa, do=200nm (Si02) 3.9 air gap of 5nm.

$Y_{max\_membrane}$ = 8.40µm. σt=615.5MPa (70.42%) and σb=258.5Pa (29.57%),Von Mises=871.39MPa < Suy:
Volume displacement =12.52E-03 mm^3/mm (58.67%)
$radius_{(Break\_up)}$ =625.0µm , $r_{(Max\ bending)}$=610.1µm, rho = 1.2 mm (minimum curvature) at max bending area.

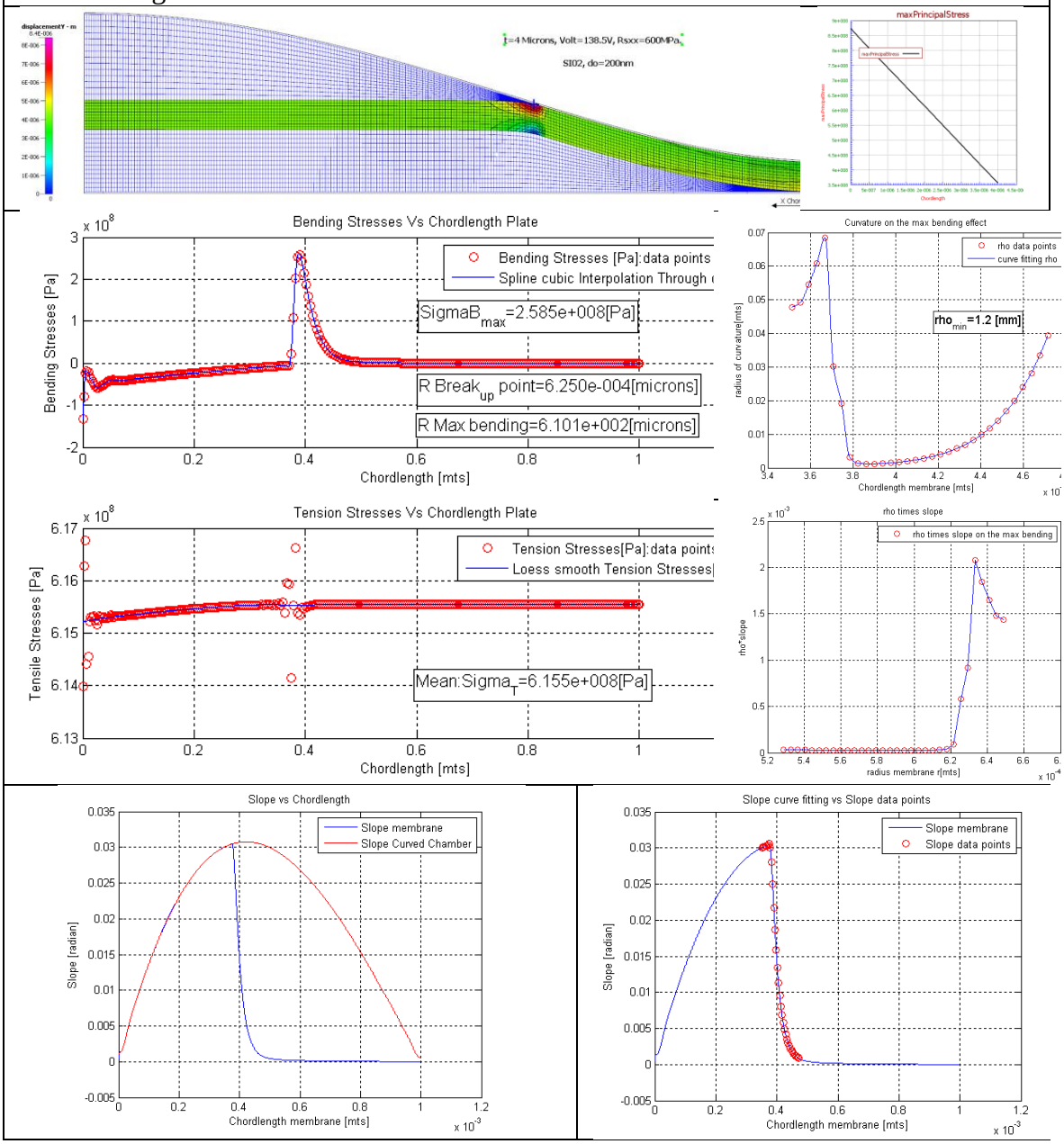

Fig. 4.20.13. Summary results for 4 µm thickness of plate with RSxx 600MPa applied 138.5V. Critical Voltage found is 138.5Volts.

Results: Case 4.4. 4µm thickness: Residual stress set to 800 MPa.
4µm thickness: 160 Volts, RSxx=800MPa, do=200nm (Si02) 3.9 air gap of 5nm.

$Y_{max\_membrane}$ = 9.038µm. σt=817.1MPa (74.15%) and σb=285.0MPa (25.85%),Von Mises=1098.6MPa < Suy:
Volume displacement =13.26E-03 mm^3/mm (62.16%)
$radius_{(Break\_up)}$ = 601.8µm , $r_{(Max\ bending)}$=590.7µm, rho = 1.059 mm (minimum curvature) at max bending area.

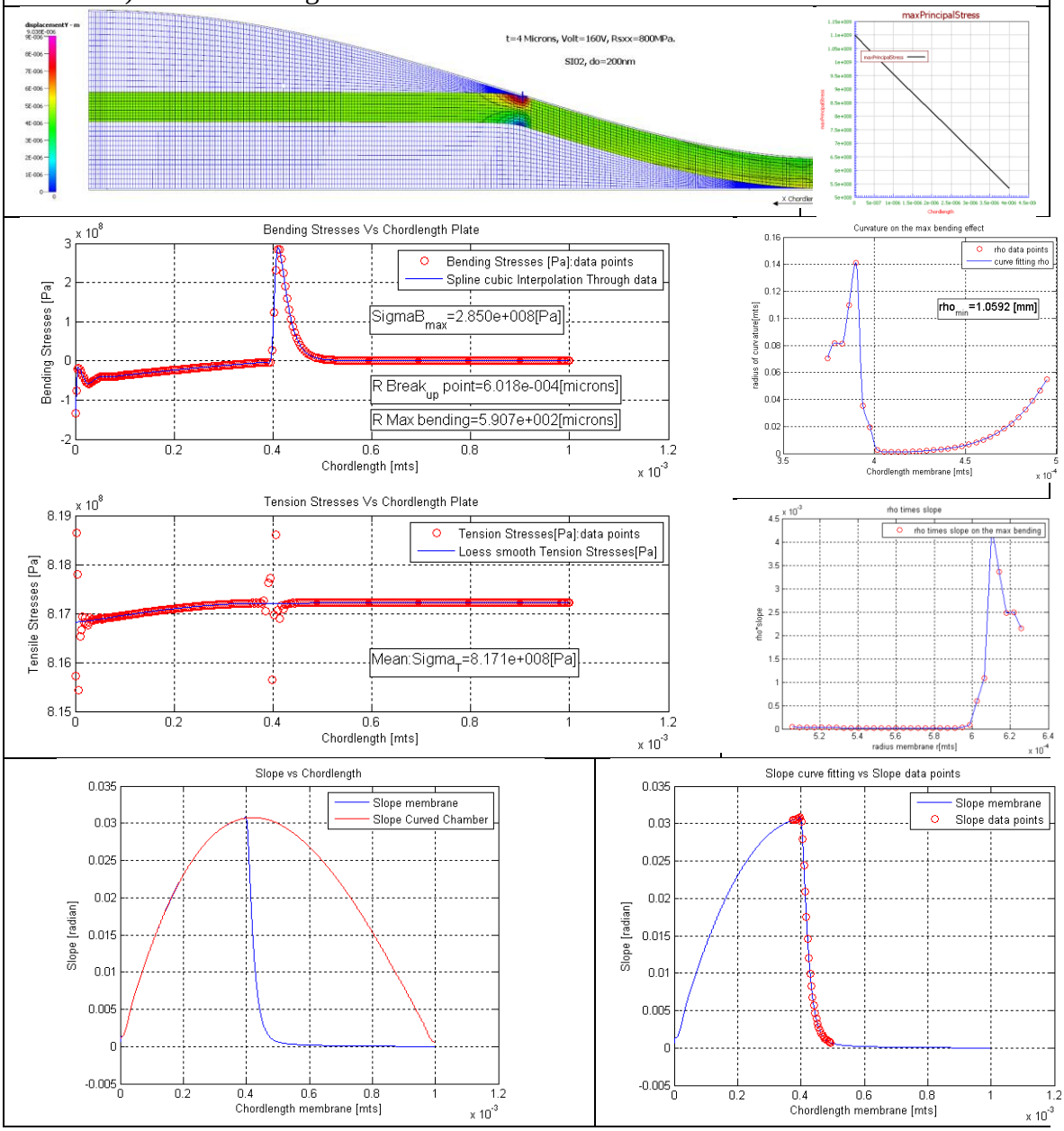

Fig. 4.20.14. Summary results for 4 µm thickness of plate with RSxx 800MPa applied 160V. Critical Voltage found is 160Volts.

Results: Case 4.5. 4µm thickness: Residual stress set to 1000 MPa.
4µm thickness: 178.5Volts, RSxx=1000MPa, do=200nm (Si02) 3.9 air gap of 5nm.

$Y_{max\_membrane}$ = 8.62µm. σt=1016.2MPa (76.66%) and σb=309.3MPa (23.34%),Von Mises=1320.7MPa < Suy:
Volume displacement =12.78E-03 mm^3/mm (59.90%)
$radius_{(Break\_up)}$ = 613.4µm , $r_{(Max\ bending)}$=602.3µm, rho = 0.974mm (minimum curvature) at max bending area.

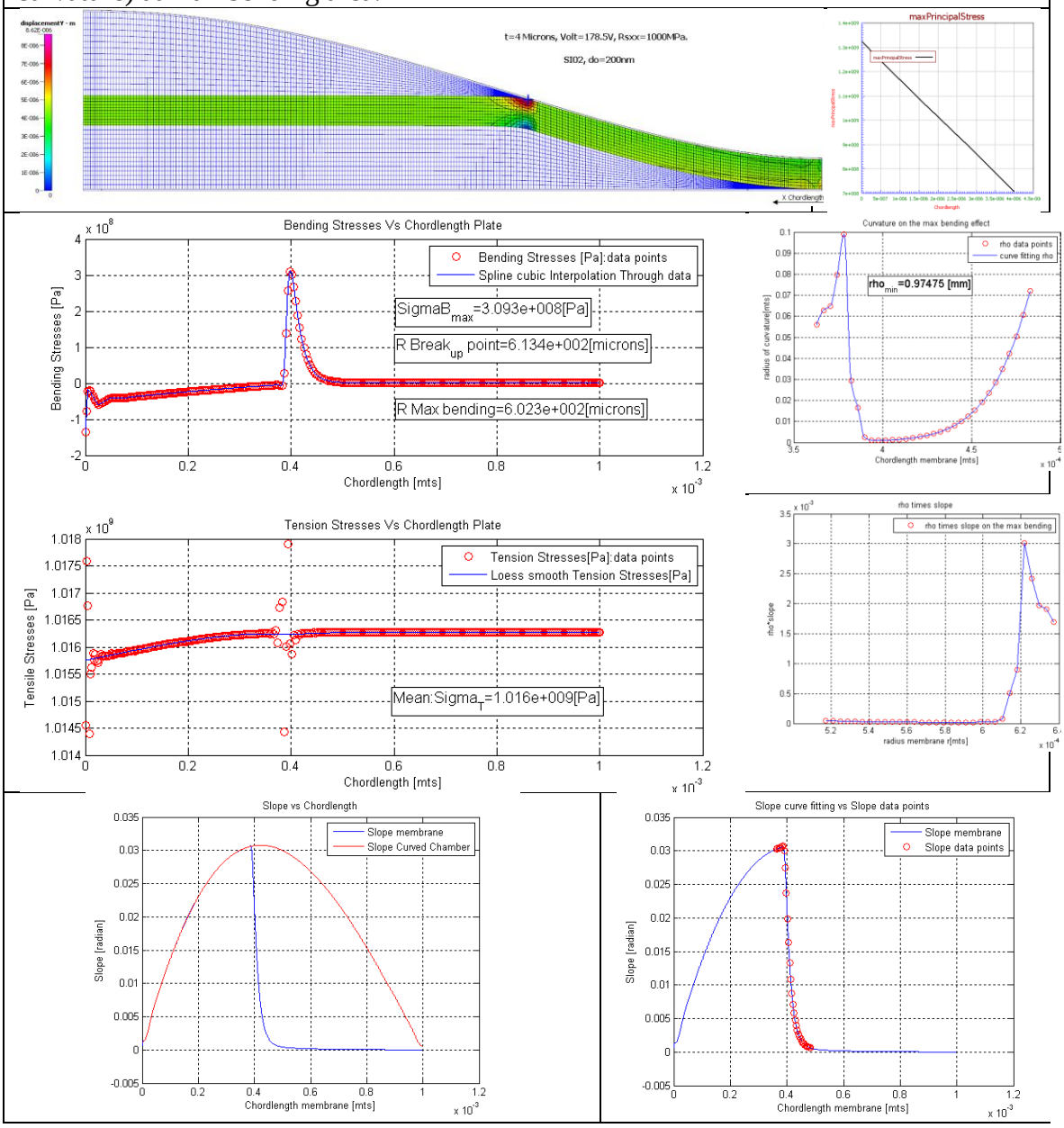

Fig. 4.20.15. Summary results for 4 µm thickness of plate with RSxx 1000MPa applied 178.5V. Critical Voltage found is 178.5Volts.

Results: Case 4.6. 4µm thickness: Residual stress set to 1200 MPa.
4µm thickness: 195.5Volts, RSxx=1200MPa, do=200nm (Si02) 3.9 air gap of 5nm.

$Y_{max\_membrane}$ = 8.81µm. σt=1216.7MPa (78.60%) and σb=331.1MPa (21.40%),Von Mises=1542.4MPa > Suy:
Volume displacement =13.00E-03 mm^3/mm (60.91%)
$radius_{(Break\_up)}$ =605.8 µm , $r_{(Max\ bending)}$=594.6µm, rho = 0.9118mm (minimum curvature) at max bending area.

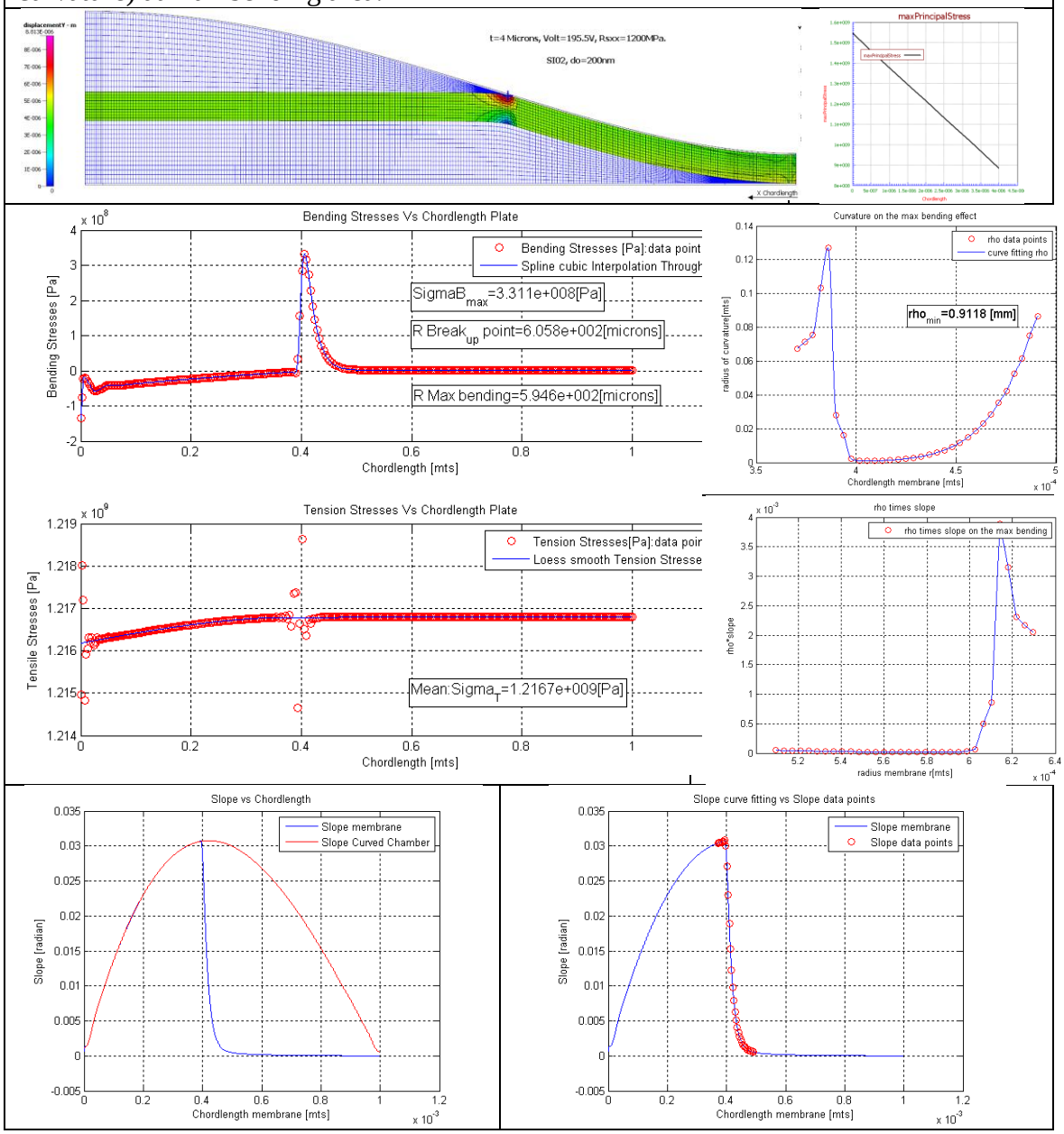

Fig. 4.20.16 Summary results for 4 µm thickness of plate with RSxx 1200MPa applied 195.5V. Critical Voltage found is 195.5Volts.

Results: Case 5.1. 2µm thickness: Residual stress set to 200 MPa.
2µm thickness: 58.5 Volts, RSxx=200MPa, do=200nm (Si02) 3.9 air gap of 5nm.

$Y_{max\_membrane}$ = 9.06µm. σt=217.21MPa (59.49%) and σb=147.9MPa (40.51%),Von Mises=364.8MPa < Suy:
Volume displacement =13.29E-03 mm^3/mm (62.29%)
$radius_{(Break\_up)}$ =601.5µm , $r_{(Max\ bending)}$=586.8µm, rho =1.059mm (minimum curvature) at max bending area.

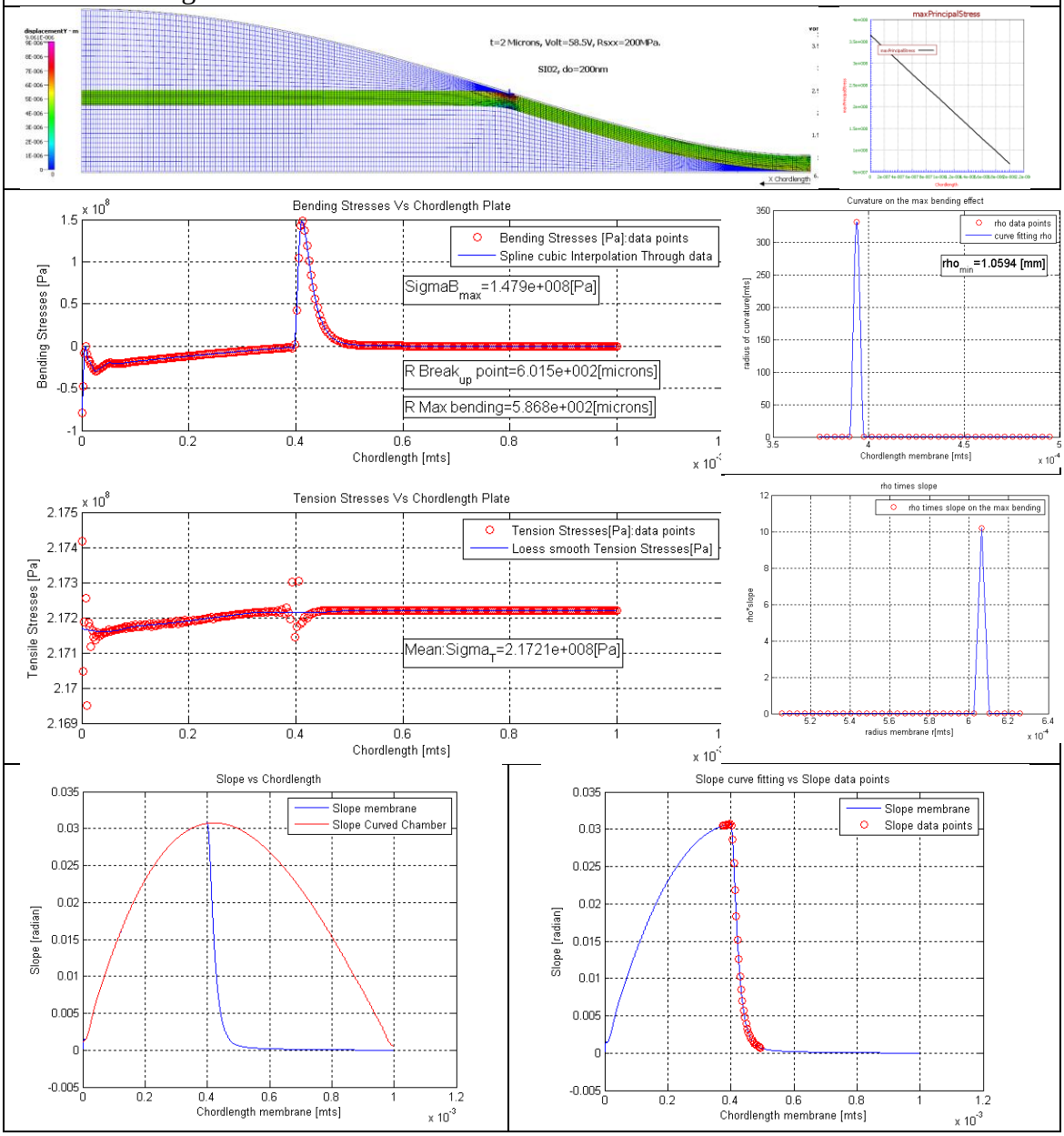

Fig. 4.20.17. Summary results for 2 µm thickness of plate with RSxx 200MPa applied 58.5V. Critical Voltage found is 58.5Volts.

Results: Case 5.2. 2µm thickness: Residual stress set to 400 MPa.
2µm thickness: 81.3Volts, RSxx=400MPa, do=200nm (Si02) 3.9 air gap of 5nm.

$Y_{max\_membrane}$ =8.904µm. σt=416.96MPa (69.33%) and σb=184.5MPa (30.67%),Von Mises=601.22MPa < Suy:
Volume displacement =13.11E-03 mm^3/mm (61.46%)
$radius_{(Break\_up)}$ =601.15µm , $r_{(Max\ bending)}$=590.7µm, rho = 0.824mm (minimum curvature) at max bending area.

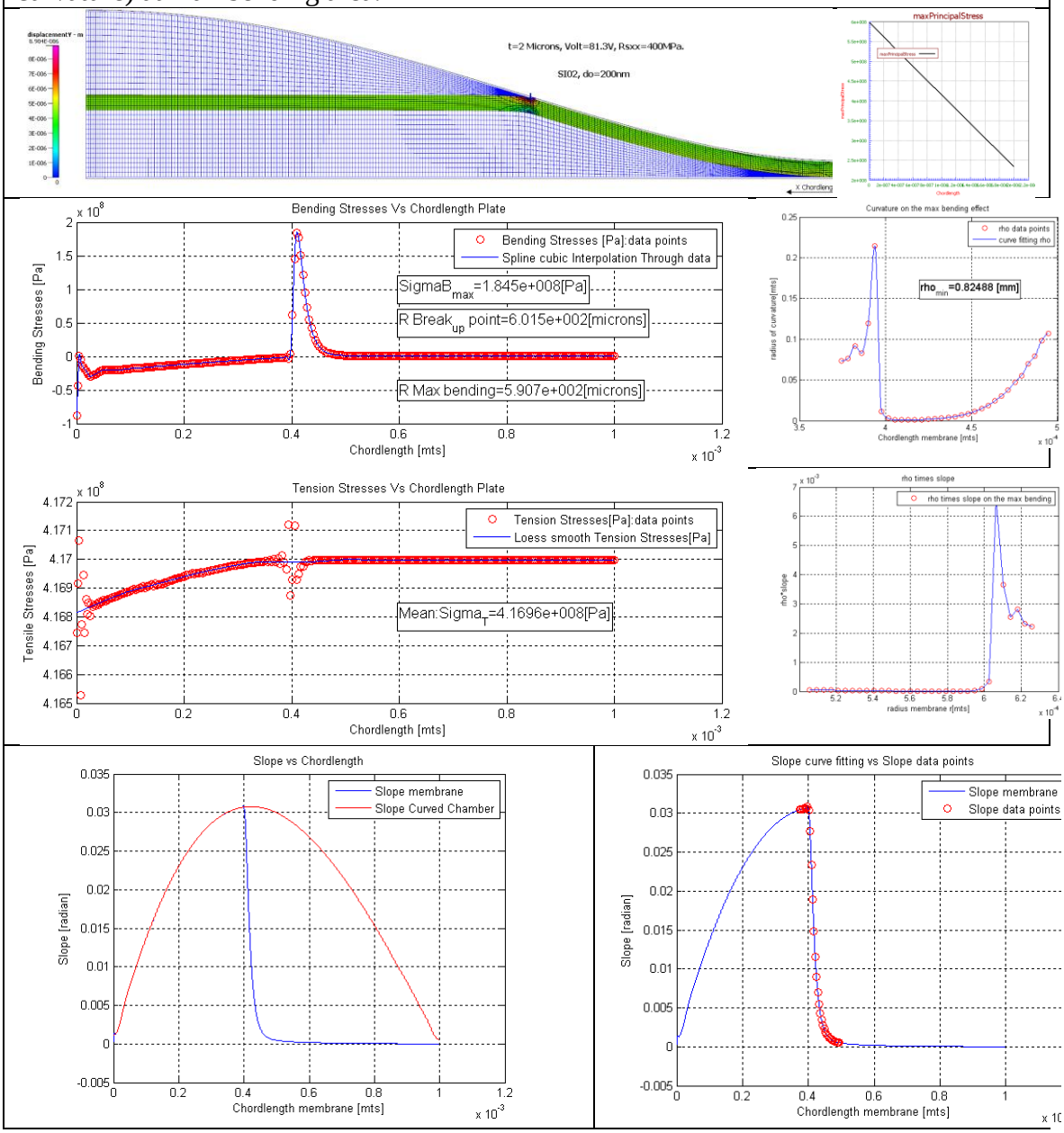

Fig. 4.20.18. Summary results for 2µm thickness of plate with RSxx 400MPa applied 81.3V. Critical Voltage found is 81.3Volts

Results: Case 5.3. 2µm thickness: Residual stress set to 600 MPa.
2µm thickness: 99Volts, RSxx=600MPa, do=200nm (Si02) 3.9 air gap of 5nm.

$Y_{max\_membrane}$ =8.71µm. σt=616.55MPa (74.56%) and σb=210.3MPa (25.44%),Von Mises=826.45MPa < Suy:
Volume displacement =12.89E-03 mm^3/mm (60.40%)
$radius_{(Break\_up)}$ =605.4µm , $r_{(Max\ bending)}$=594.6µm, rho =0.723mm (minimum curvature) at max bending area.

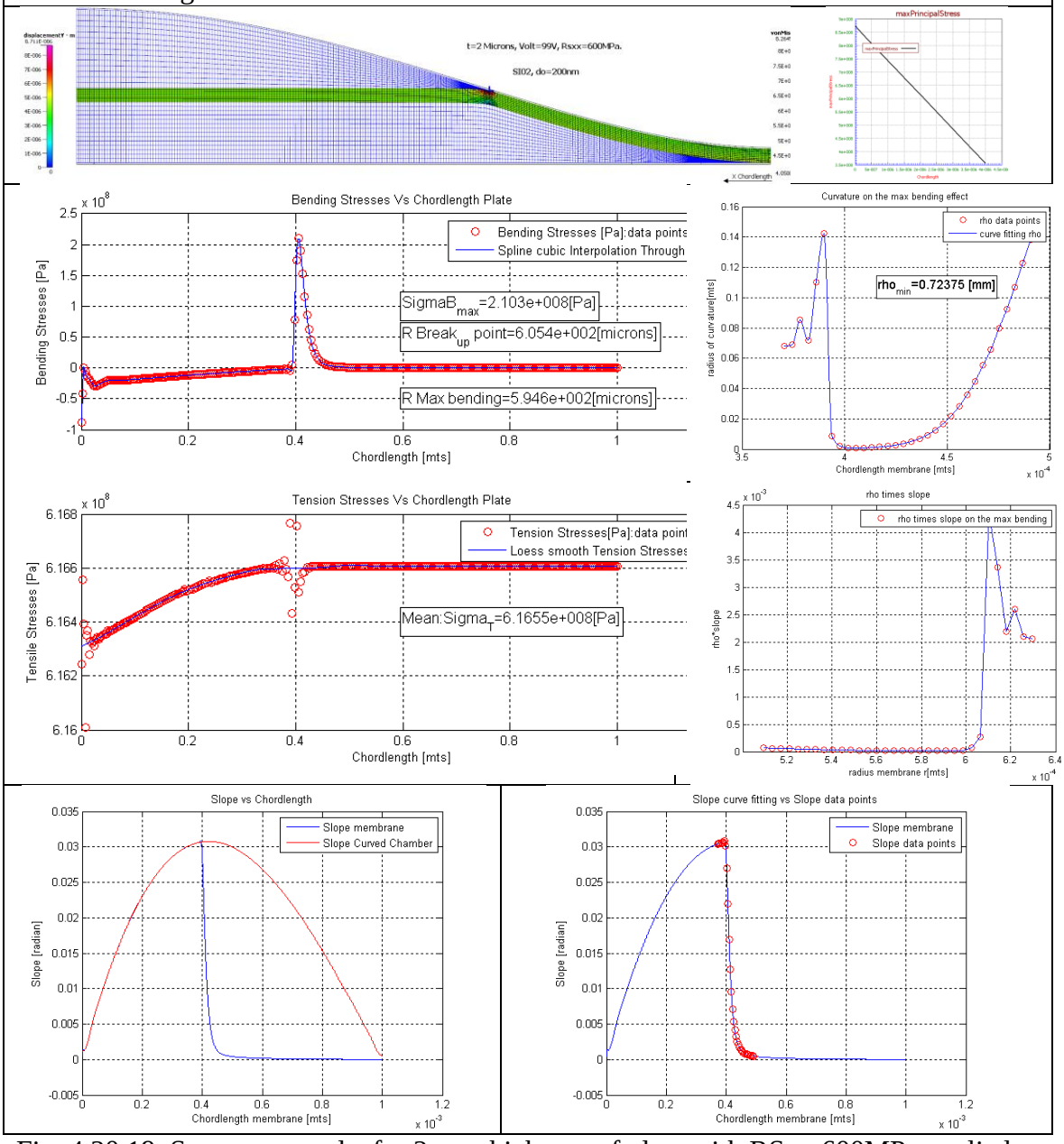

Fig. 4.20.19. Summary results for 2 µm thickness of plate with RSxx 600MPa applied 99V. Critical Voltage found is 99Volts.

Results: Case 5.4. 2µm thickness: Residual stress set to 800 MPa.
2µm thickness: 114Volts, RSxx=800MPa, do=200nm (Si02) 3.9 air gap of 5nm.

$Y_{max\_membrane}$ =8.549µm. σt=816.19MPa (78.14%) and σb=228.2MPa (21.86%),Von Mises=1043.8MPa < Suy:
Volume displacement =12.70E-03 mm^3/mm (59.53%)
$radius_{(Break\_up)}$ =609.3µm , $r_{(Max\ bending)}$=598.5µm, rho =0.666mm (minimum curvature) at max bending area.

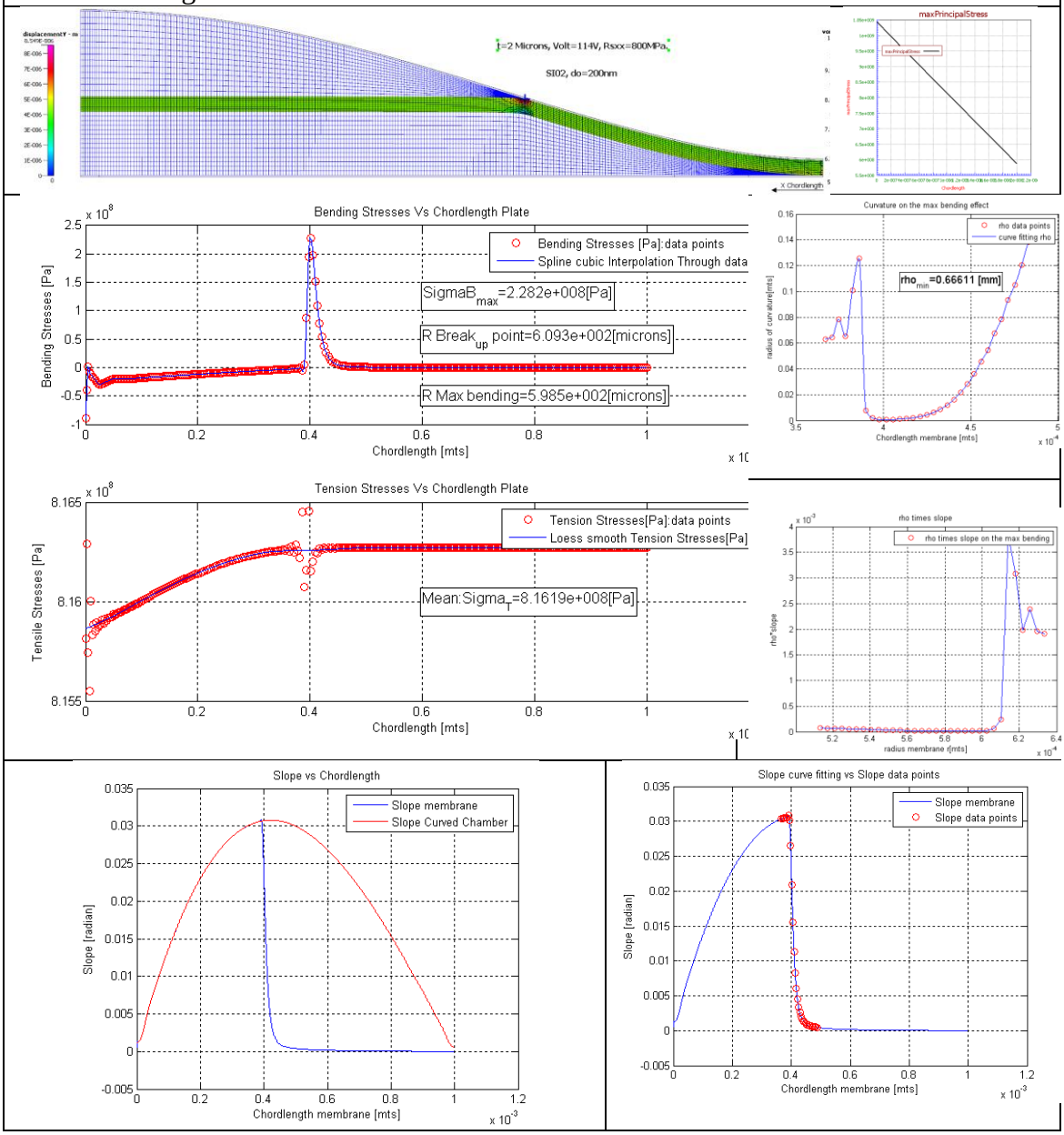

Fig. 4.20.20 Summary results for 2 µm thickness of plate with RSxx 800MPa applied 114V. Critical Voltage is 114Volts

Results: case 5.5. 2µm thickness: Residual stress set to 1000 MPa.
2µm thickness: 127.5Volts, RSxx=1000MPa, do=200nm (Si02) 3.9 air gap of 5nm.

$Y_{max\_membrane}$ =8.549µm. σt=1017.3MPa (70.75%) and σb=242.6MPa (19.25%),Von Mises=1259.2MPa < Suy:
Volume displacement =12.70E-03 mm^3/mm (59.53%)
$radius_{(Break\_up)}$ =593.8µm , $r_{(Max\ bending)}$=583.0µm, rho =0.6264mm (minimum curvature) at max bending area.

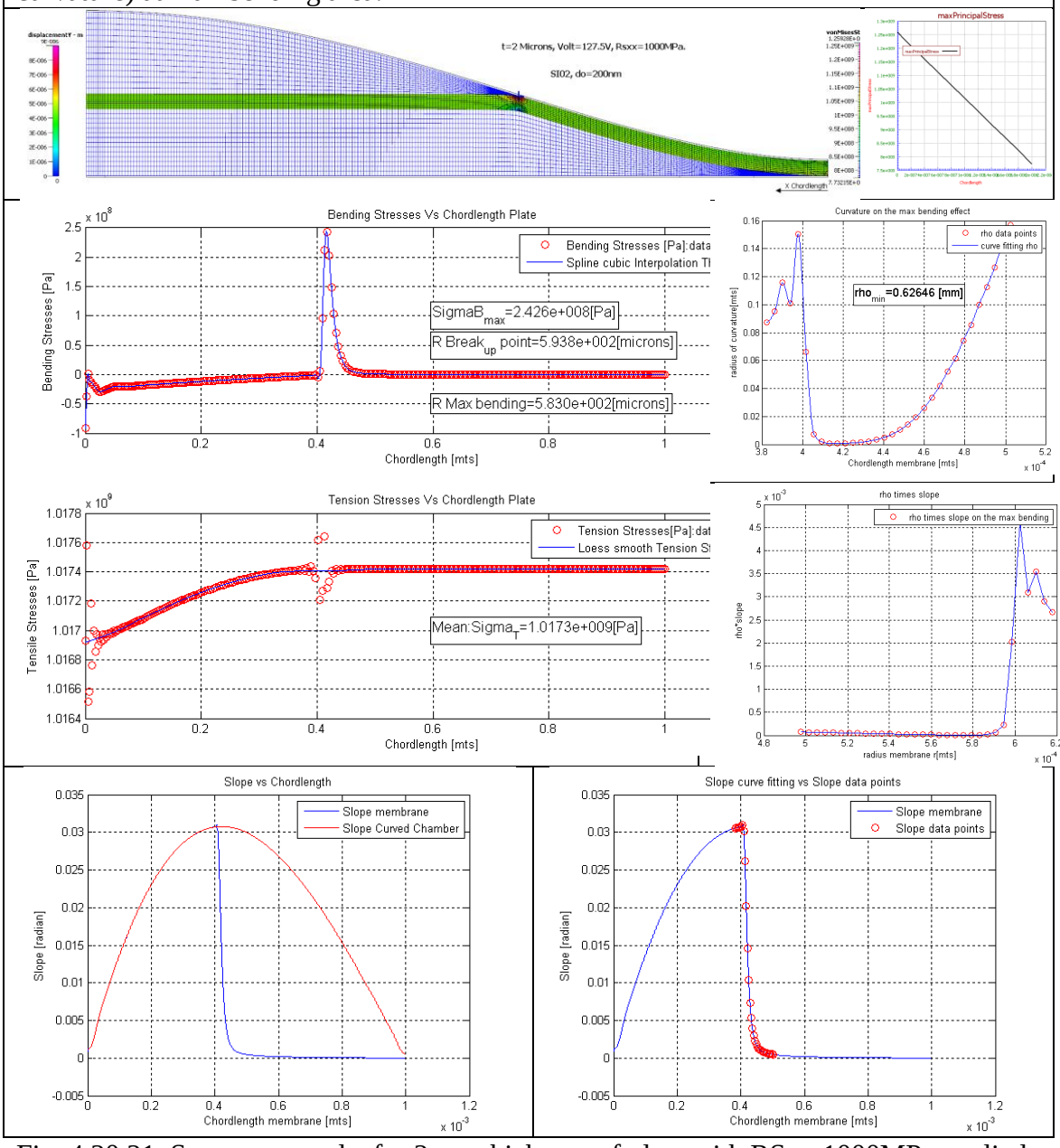

Fig. 4.20.21. Summary results for 2 µm thickness of plate with RSxx 1000MPa applied 125V. Critical Voltage found is 125Volts.

Results: Case 5.6. 2µm thickness: Residual stress set to 1200 MPa.
2µm thickness: 139.5Volts, RSxx=1200MPa, do=200nm (Si02) 3.9 air gap of 5nm.

$Y_{max\_membrane}$ =8.735µm. σt=1216.7MPa (82.84%) and σb=252.2MPa (17.16%),Von Mises=1468.01MPa < Suy:
Volume displacement =12.92E-03 mm^3/mm (60.56%)
$radius_{(Break\_up)}$ =601.5µm , $r_{(Max\ bending)}$=590.7µm, rho =0.6044mm (minimum curvature) at max bending area.

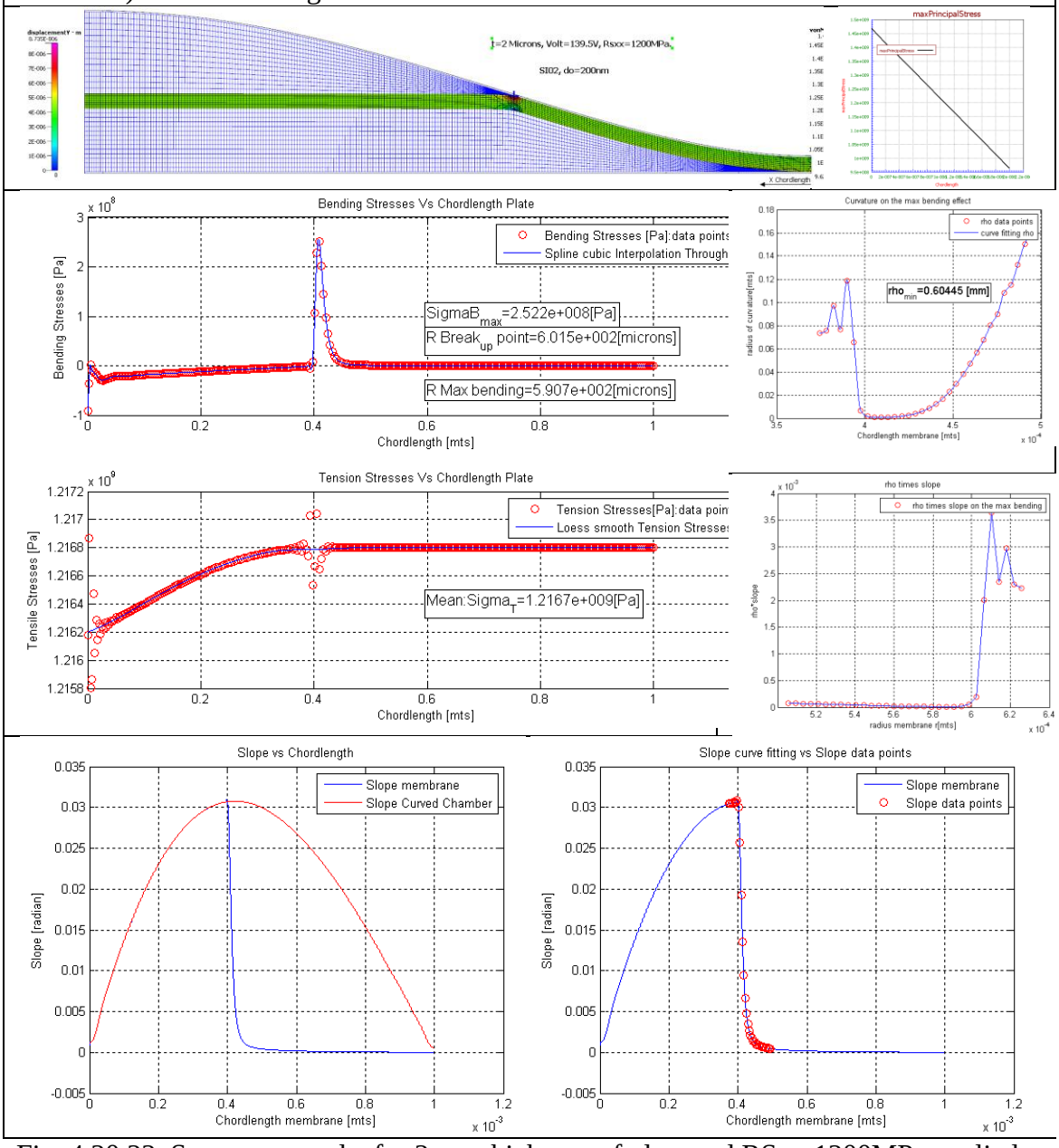

Fig. 4.20.22. Summary results for 2 µm thickness of plate and RSxx 1200MPa applied 139.5V. Critical Voltage found is 139.5Volts.

Results: Case 5.7. 2µm thickness: Residual stress set to 1400 MPa.
2µm thickness: 150.5Volts, RSxx=1400MPa, do=200nm (Si02) 3.9 air gap of 5nm.

$Y_{max\_membrane}$ =8.596µm. σt=1416.4MPa (84.51%) and σb=259.5MPa (14.49%),Von Mises=1674.81MPa > Suy:
Volume displacement =12.76E-03 mm^3/mm (59.80%)
$radius_{(Break\_up)}$ =605.4µm , $r_{(Max\ bending)}$=594.6µm, rho =0.5681mm (minimum curvature) at max bending area.

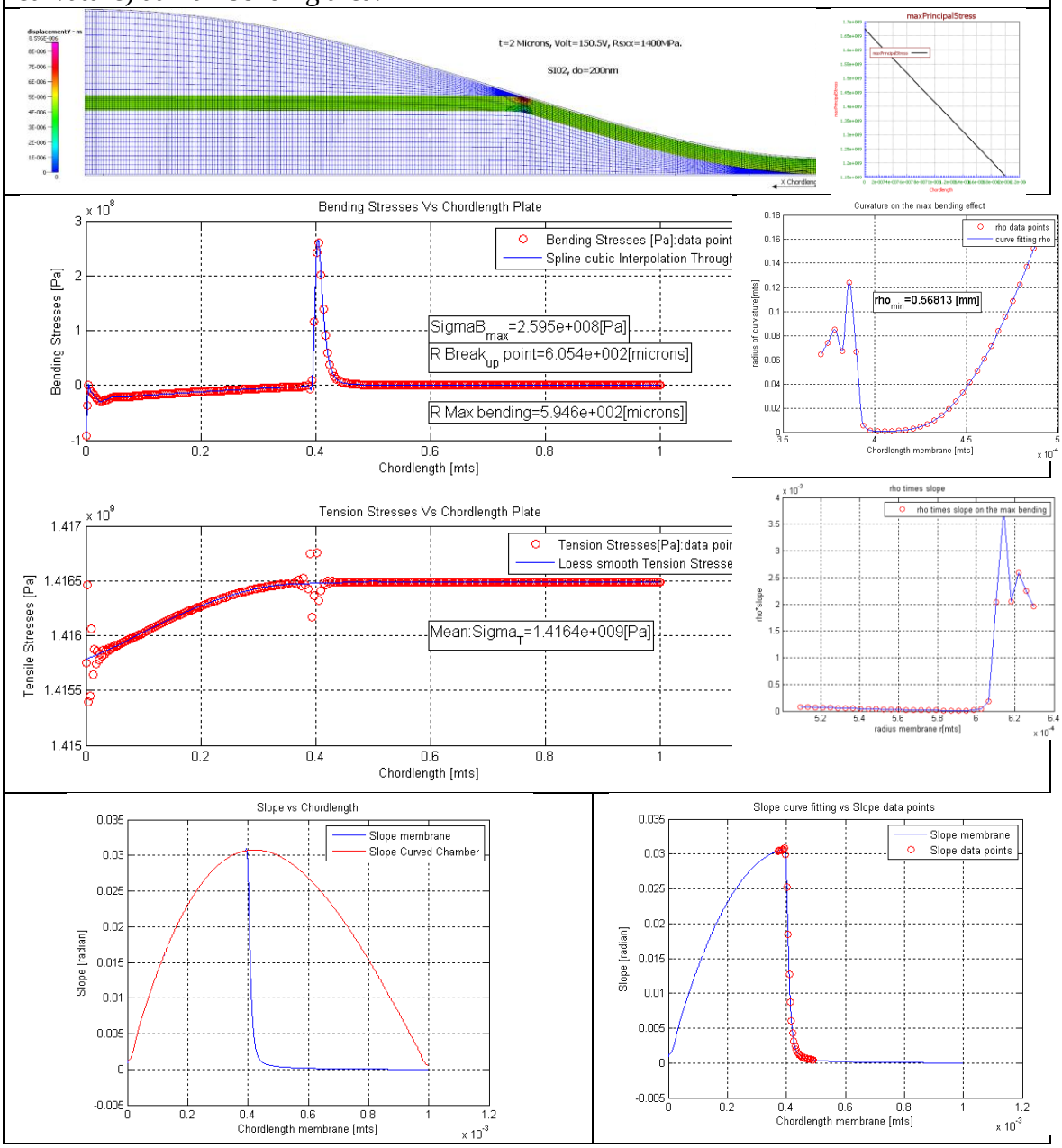

Fig. 4.20.23 Summary results for 2 µm thickness of plate with RSxx 1400MPa applied 150.5V. Critical Voltage is 150.5Volts.

Results: Case 5.8. 2µm thickness: Residual stress set to 1600 MPa.
2µm thickness: 161Volts, RSxx=1600MPa, do=200nm (Si02) 3.9 air gap of 5nm.

$Y_{max\_membrane}$ =8.82µm. σt=1616.9MPa (85.84%) and σb=266.9MPa (14.16%),Von Mises=1882.6MPa > Suy:
Volume displacement =13.02E-03 mm^3/mm (61.04%)
$radius_{(Break\_up)}$ =597.7µm , $r_{(Max\ bending)}$=586.8µm, rho =0.5407mm (minimum curvature) at max bending area.

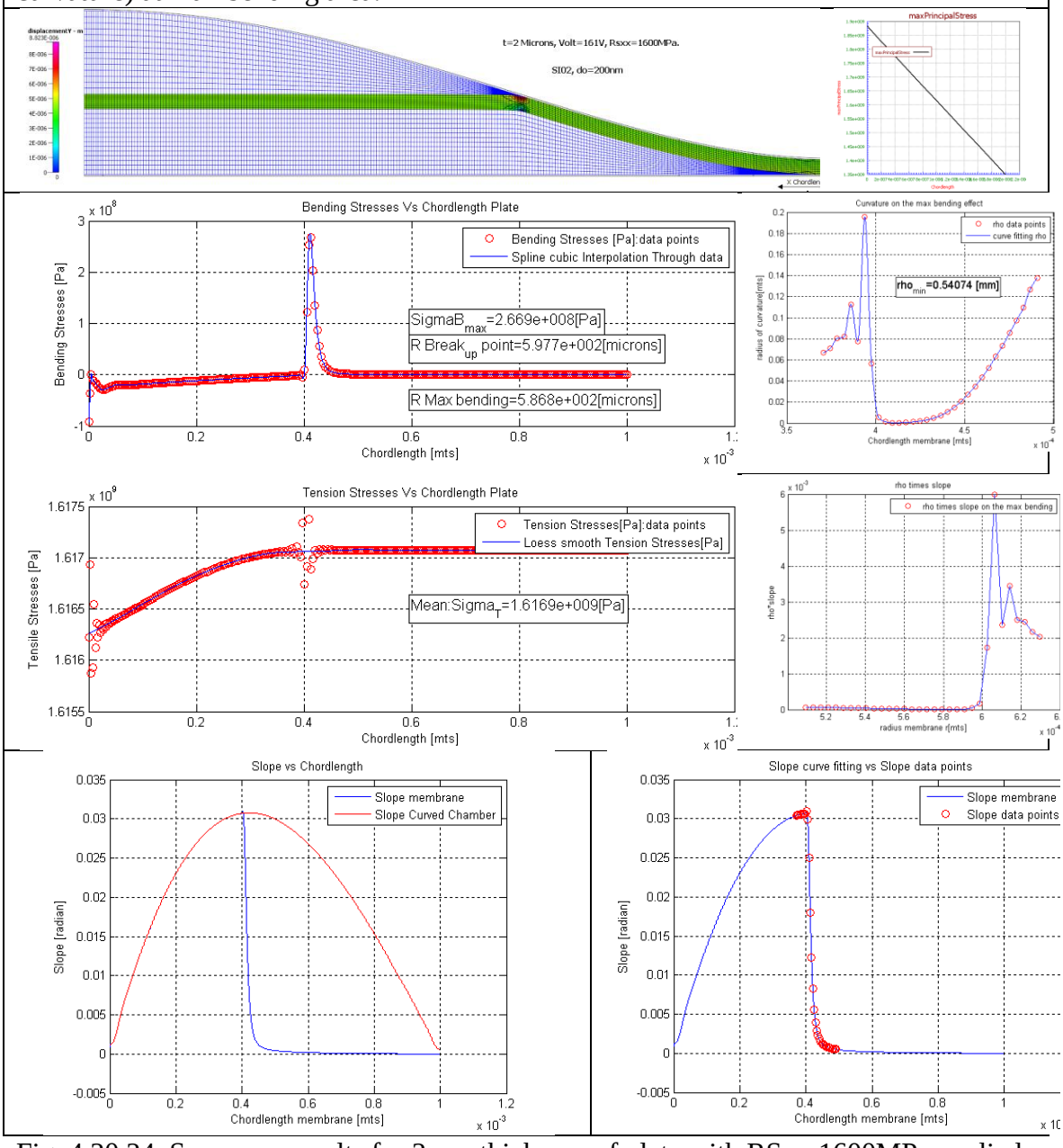

Fig. 4.20.24. Summary results for 2 µm thickness of plate with RSxx 1600MPa applied 161V. Critical Voltage found is 161Volts

Results: case 5.9. 2µm thickness: Residual stress set to 1800 MPa.
2µm thickness: 170.5Volts, RSxx=1800MPa, do=200nm (Si02) 3.9 air gap of 5nm.

$Y_{max\_membrane}$ =8.452µm. σt=1816.0MPa (87.01%) and σb=271.2MPa (12.99%),Von Mises=2085.84MPa > Suy:
Volume displacement =12.59E-03 mm^3/mm (59.00%)
$radius_{(Break\_up)}$ =609.3µm , $r_{(Max\ bending)}$=598.5µm, rho =0.5183mm (minimum curvature) at max bending area.

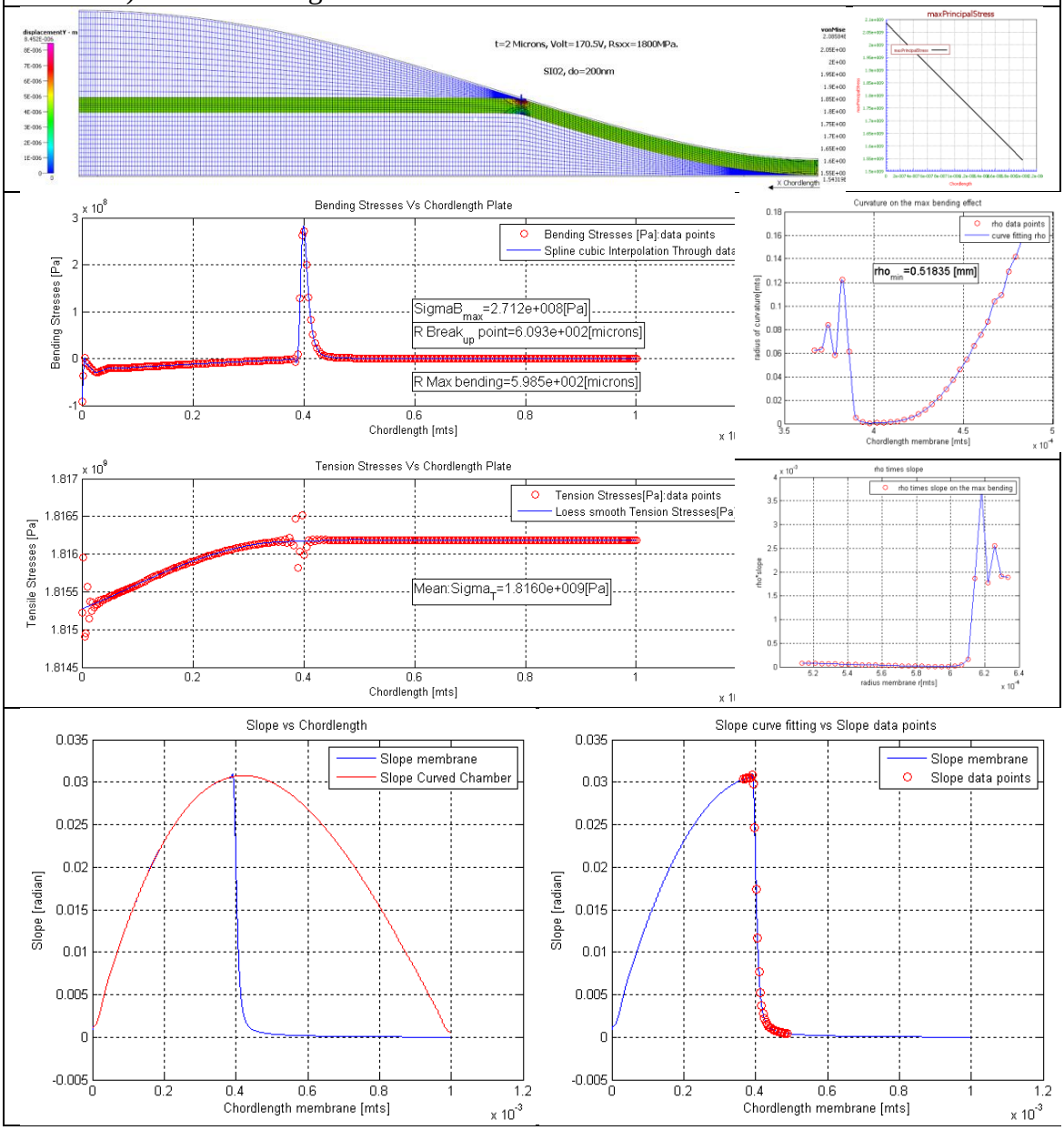

Fig. 4.20.25. Summary results for 2 µm thickness of plate with RSxx 1800MPa applied 170.5V. Critical Voltage is 170.5Volts.

Results: Case 5.10. 2µm thickness: Residual stress set to 2000 MPa.
2µm thickness: 180Volts, RSxx=2000MPa, do=200nm (Si02) 3.9 air gap of 5nm.

$Y_{max\_membrane}$ =8.805µm. σt=2016.9MPa (87.88%) and σb=278.4MPa (12.12%),Von Mises=2293.85MPa > Suy:
Volume displacement =13.00E-03 mm^3/mm (60.94%)
$radius_{(Break\_up)}$ =597.7µm , $r_{(Max\ bending)}$=586.8µm, rho =0.501mm (minimum curvature) at max bending area.

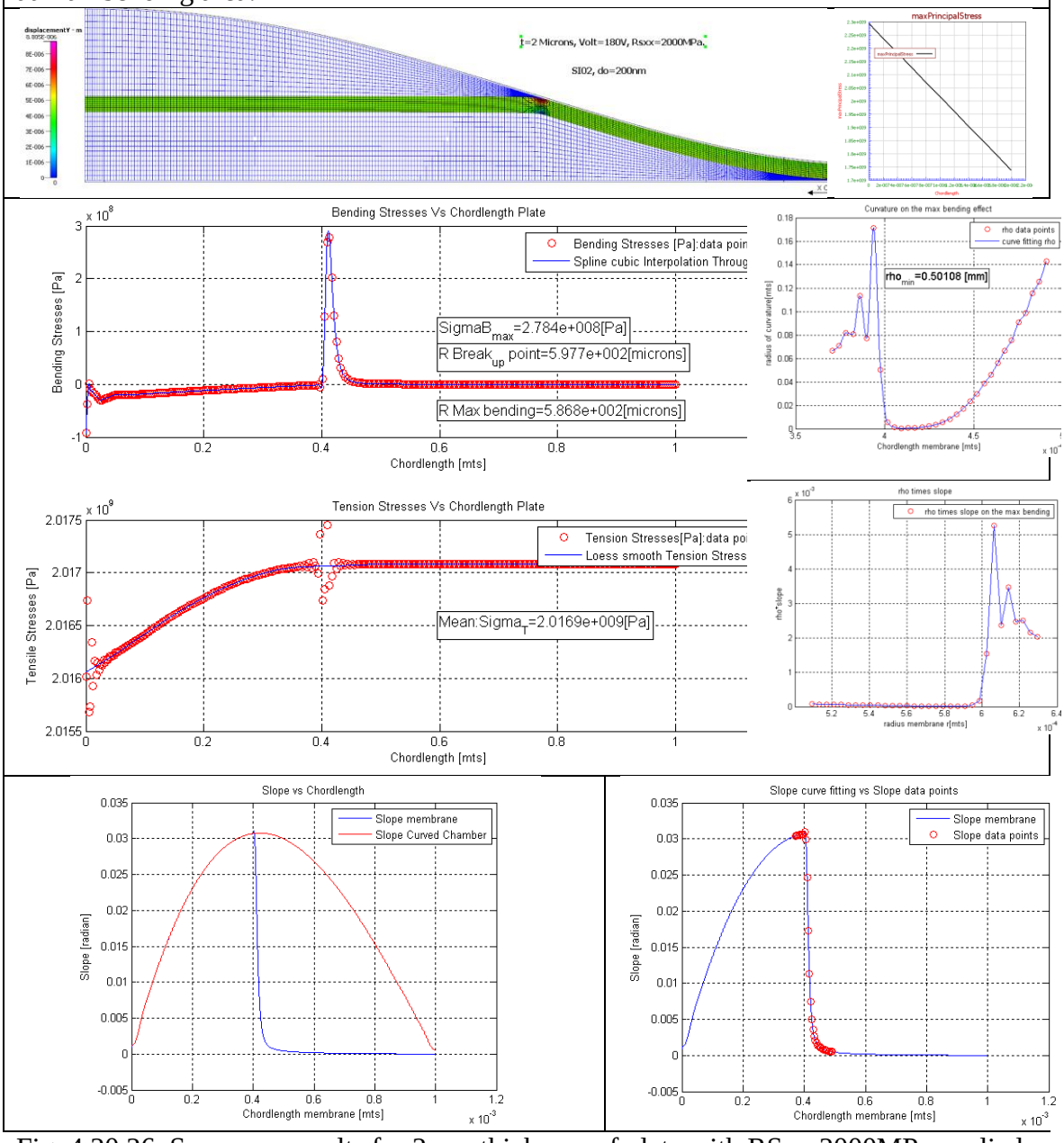

Fig. 4.20.26. Summary results for 2 µm thickness of plate with RSxx 2000MPa applied 180V. Critical Voltage found is 180Volts.

Results: Case 5.11. 2µm thickness: Residual stress set to 2200 MPa.
2µm thickness: 188.5Volts, RSxx=2200MPa, do=200nm (Si02) 3.9 air gap of 5nm.

$Y_{max\_membrane}$ =8.43µm. σt=2216.0MPa (88.77%) and σb=280.2MPa (11.23%),Von Mises=2494.53MPa > Suy:
Volume displacement =12.57E-03 mm^3/mm (58.90%)
$radius_{(Break\_up)}$ =609.3µm , $r_{(Max\ bending)}$=598.5µm, rho =0.4845mm (minimum curvature) at max bending area.

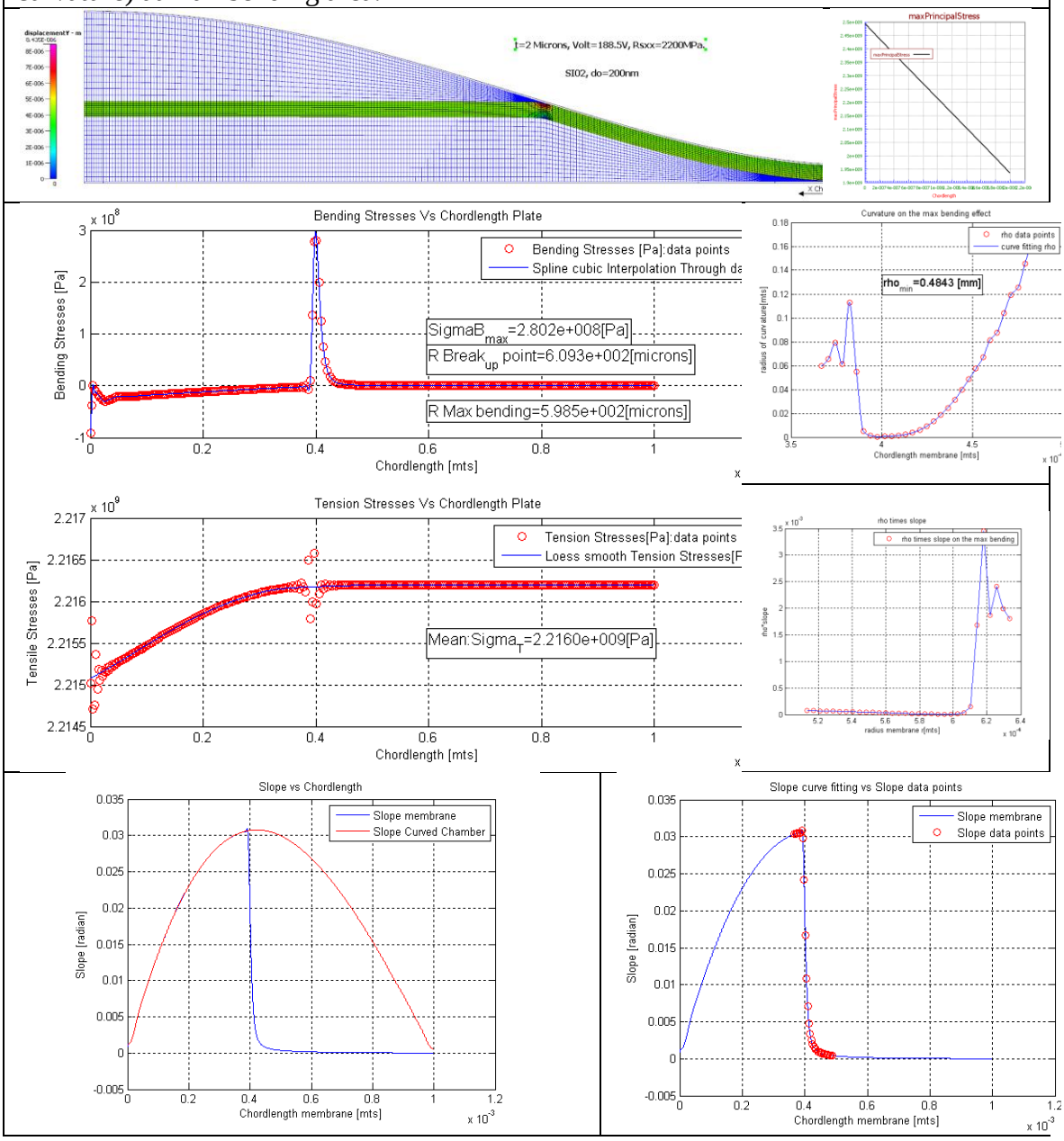

Fig. 4.20.27. Summary results for 2 µm thickness of plate with RSxx 2200MPa applied 188.5V. Critical Voltage is 188.5Volts.

Results: Case 5.12. 2µm thickness: Residual stress set to 2400 MPa.
2µm thickness: 197Volts, RSxx=2400MPa, do=200nm (Si02) 3.9 air gap of 5nm.

$Y_{max\_membrane}$ =8.54µm. σt=2416.3MPa (89.45%) and σb=284.7MPa (10.55%),Von Mises2698.5MPa > Suy:
Volume displacement =12.70E-03 mm^3/mm (59.53%)
$radius_{(Break\_up)}$ =605.4µm , $r_{(Max\ bending)}$=598.5µm, rho =0.4699mm (minimum curvature) at max bending area.

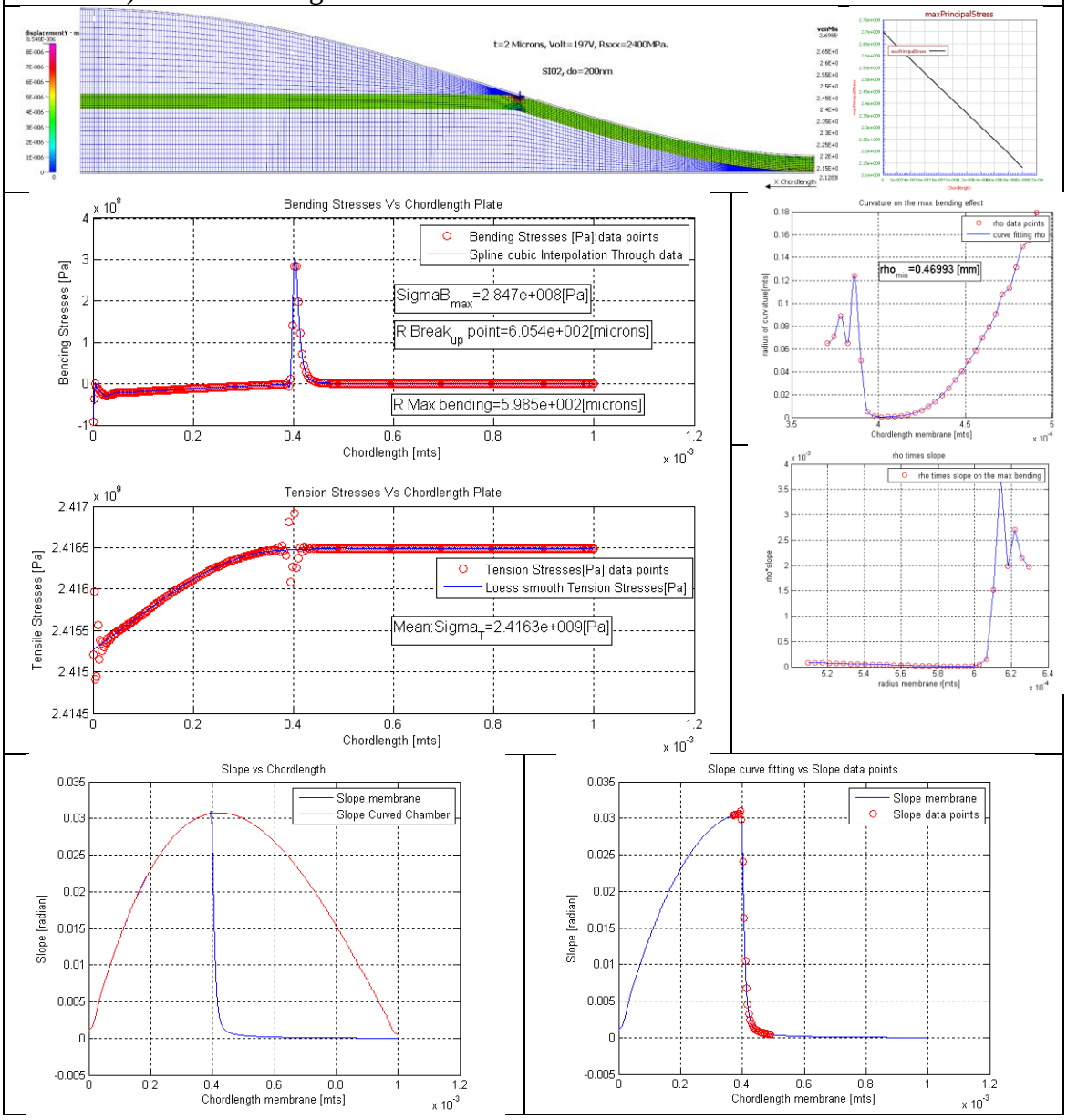

Fig. 4.20.28. Summary results for 2 µm thickness of plate with RSxx 2400MPa applied 197V. Critical Voltage is 197Volts

4.21 Fatigue Aspects of Polysilicon and Its Use in Micropump Design

In this section, we examine the fatigue characteristics of the micropump baseline design. The alternating and mean stresses for fatigue purposes result from the intake stroke and are calculated as follows. Consider the simulation results for the intake stroke, Table 4.6. The mean of the bending stresses (i.e., half of SigB) is added to the residual stresses SigT to obtain Sig-Mean as given in Table 4.21.1. Alternating stresses come from the other half of SigB; they are presented as Sig-Alt. in Table 4.21.1.

Table 4.21.1 Alternating and mean stresses for maximum voltage cases (i.e., 200 volts) of the plate thicknesses 2, 4, 6, 8, and 10 microns

t	RS	*V*	*SigT*	*SigB*	*SigVM*	*Sig-Alt*	*Sig-Mean*
um	MPa	Volts	MPa	MPa	MPa	MPa	MPa
10	500	199	513.4	285.5	794.03	142.75	656.15
8	600	195	615.3	301.9	912.5	150.95	766.25
6	800	195	971.8	320.4	1292.2	160.2	1132
4	1200	195.5	1216.7	331.1	1542.4	165.55	1382.25
2	2400	197	2416.3	284.7	2698.5	142.35	2558.65

Experimental investigations into the fracture strength and fatigue of polysilicon show that polysilicon has good fatigue characteristics. The experimental results from [Kapels, et al, 2000], covering out to 1 million cycles, are presented in Fig. 4.21.1 as "Ref. Data" with extrapolations shown out to 1 trillion cycles. Note that for each increase in cycles by a factor of 10, the fracture stresses decrease by 160 MPa.

In this dissertation, we have taken, as a conservative value, the ultimate strength of polysilicon to be 1550 MPa which is that used by Sandia National Labs for their SUMMiT V^{TM} process. Extrapolating the "Ref. Data", Fig. 4.21.1, back to 1 cycle gives 3250 MPa as the ultimate strength for the polysilicon considered in [Kapels, et al, 2000]. Using the ratio 1550/3250, we scale the data given in Fig. 4.21.1 from 3250

MPa to the conservative value 1550 MPa for the ultimate strength of polysilicon as utilized in this dissertation; Fig. 4.21.2 contains the scaled data.

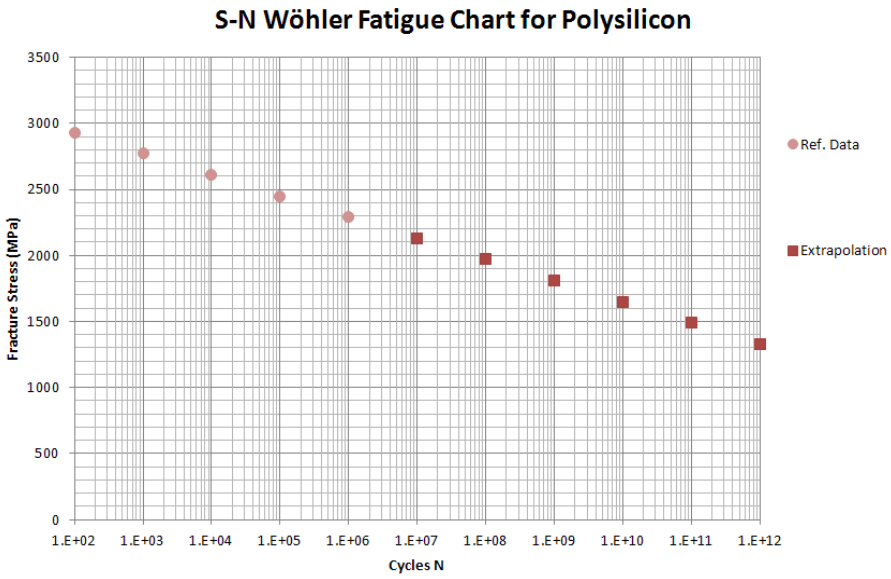

Fig. 4.21.1 S-N Wohler fatigue chart for polysilicon based on 3250 MPa ultimate strength of polysilicon.

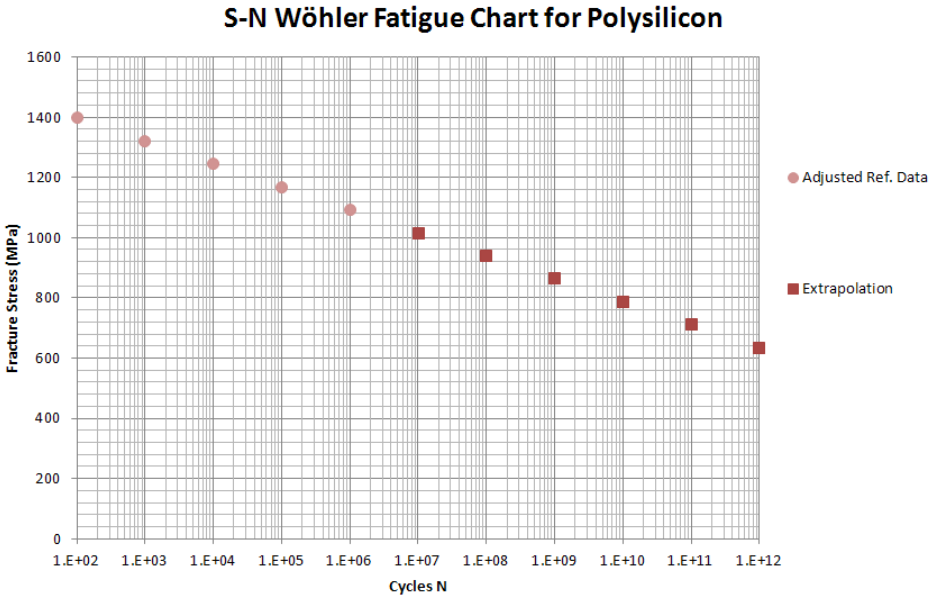

Fig. 4.21.2 S-N Wohler fatigue chart for polysilicon, scaled to conservative 1550 MPa ultimate strength of polysilicon.

Using the S-N data in Fig. 4.21.2, a constant-life fatigue diagram is constructed in Fig. 4.12.3 with Goodman lines for 10^6, 10^9, and 10^{12} cycles. In addition, we see from the constant-life fatigue diagram, Fig. 4.21.3, that the 10 micron plate thickness offers better fatigue characteristics over that of the thinner plate thicknesses 2-8 microns. Fatigue quality decreases with plate thickness.

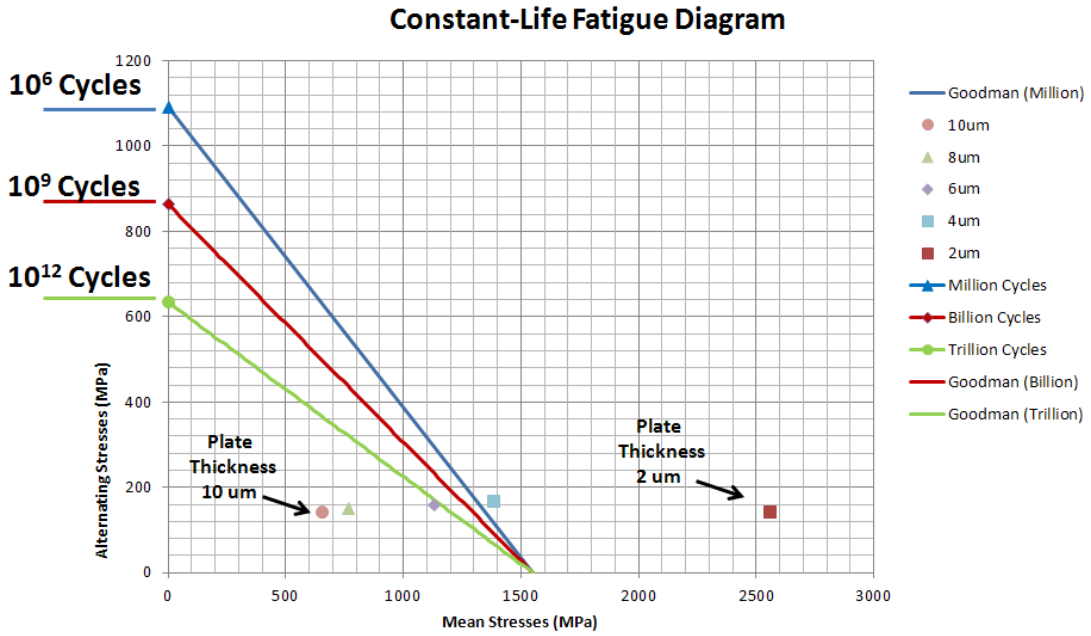

Fig. 4.21.3 Constant-Life fatigue diagram for 10^6, 10^9, and 10^{12} cycles.

CHAPTER 5

QUADRATIC ELECTROSTATIC DISTRIBUTIVE FORCE MODEL FOR INTAKE STROKE

We seek an electrostatic distributive force model for the intake stroke with which the 4^{th} order reduced von Kármán governing differential equations can be analytically integrated. In this chapter, we derive a quadratic electrostatic distributive force model for the intake stroke that can be used in the next chapter in carrying out the integration.

During the intake stroke, the plate forms one electrode and the chamber wall forms a second electrode. When a voltage differential is placed across the electrodes, an electrostatic distributive force of attraction is developed on the plate which depends, in particular, on point-wise distances between the plate and the chamber wall. Such a distance model depends on chamber geometry and plate deflection. A model for plate deflection is derived in Section 5.1. In Section 5.2, plate deflection is approximated near the junction where the plate departs from the chamber wall. Since electrostatic forces decay rapidly at points away from that junction due to large increases in distance, plate deflection is only needed in the vicinity of that junction. Taking into account chamber geometry, an approximation model with lowest order term is derived in Section 5.3 for the distance between the plate and the chamber wall. In Section 5.4, parallel plate theory is used in deriving an electrostatic distributive force model. Since that model is not conducive for analytical integration, a quadratic approximation to the

electrostatic distributive force model is derived in Section 5.5 that is conducive for analytical integration.

5.1 Deflection Curve for Plate under Tension

We determine the deflection curve *w(r)* for a plate in tension *T* that has the boundary conditions (5.1a-e) at the walls, Fig. 5.1.1 The boundary conditions (5.1a-e) are achieved by appropriate moment $\boldsymbol{M_0}$ and force $\boldsymbol{F_0}$.

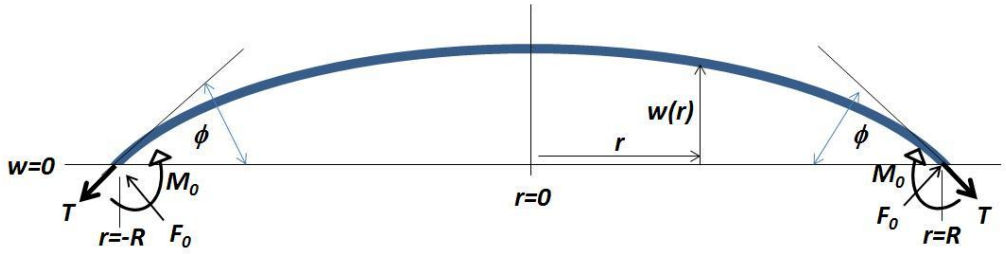

Figure . 5.1.1 Deflection curve for plate.

$$\frac{dw}{dr}(r) = 0 \text{ at } r = 0 \qquad (5.1.1a)$$

$$\frac{dw}{dr}(r) = \phi \text{ at } r = -R \qquad (5.1.1b)$$

$$\frac{dw}{dr}(r) = -\phi \text{ at } r = R \qquad (5.1.1c)$$

$$w(r) = 0 \text{ at } r = -R \qquad (5.1.1d)$$

$$w(r) = 0 \text{ at } r = R \qquad (5.1.1e)$$

The use of large deflection theory is required in order to account for simultaneous effects of bending and stretching [Rudolph Szilard 2004]. This covers the case where the deflection is greater than the thickness of the plate. However, using a simplified 2 D static model for the plate analysis, the reduced Von Karman governing differential equation suffices, [Ancel C. Ugural 1991].

$$D\frac{d^4w}{dr^4} = T\frac{d^2w}{dr^2} \qquad (5.1.2)$$

where D is the flexural rigidity of the plate.

We define λ as

$$\lambda = \sqrt{\frac{T}{D}} \tag{5.1.3}$$

The solution *w(r)* of (5.2) that satisfies boundary conditions (5.1.1a-e) is easily derived as

$$w(r) = \frac{-\phi}{\lambda}\frac{\left[\cosh(\lambda r) - \cosh(\lambda R)\right]}{\sinh(\lambda R)} \tag{5.1.4}$$

Consider the moment *M(r)* defined by equation 5.1.5

$$M(r) = D\frac{d^2 w}{dr^2} \tag{5.1.5}$$

$$M(r) = -D\lambda\phi\frac{\cosh(\lambda r)}{\sinh(\lambda R)} \tag{5.1.6}$$

$$M(-R) = M(R) = -D\lambda\phi\frac{\cosh(\lambda R)}{\sinh(\lambda R)} \tag{5.1.7}$$

The moment $\boldsymbol{M_0}$ satisfies

$$M_0 = -M(-R) = D\lambda\phi\frac{\cosh(\lambda R)}{\sinh(\lambda R)} \tag{5.1.8}$$

The force $\boldsymbol{F_0}$ satisfies

$$F_0 = T\tan(\phi) \tag{5.1.9}$$

The slope $\theta(r)$ is defined by

$$\theta(r) = \frac{dw}{dr} = -\phi \frac{\left[\sinh(\lambda r)\right]}{\sinh(\lambda R)} \tag{5.1.10}$$

from which we get

$$\theta(-R) = \phi \tag{5.1.11a}$$

$$\theta(R) = -\phi \tag{5.1.11b}$$

$$\theta(0) = 0 \tag{5.1.11c}$$

The moment at $r=0$ satisfies

$$M(0) = -\frac{D\lambda\phi}{\sinh(\lambda R)} \tag{5.1.12}$$

The shear force $v(r)$ is defined by

$$v(r) = D\frac{dM}{dr} = D\frac{d^3w}{dr^3} = -D\lambda^2\phi\frac{\sinh(\lambda r)}{\sinh(\lambda R)} = -T\phi\frac{\sinh(\lambda r)}{\sinh(\lambda R)} \tag{5.1.13}$$

from which we obtain

$$v(-R) = T\phi \tag{5.1.14a}$$

$$v(R) = -T\phi \tag{5.1.14b}$$

$$v(0) = 0 \tag{5.1.14c}$$

Note that the shear force in (5.1.14a) is approximately the force $\boldsymbol{F_0}$ in (5.1.9).

From (5.1.4), we see that the maximum displacement $w_{\max}$ occurs at *r=0* and is given by

$$w_{\max} = w(0) = \frac{\phi}{\lambda}\frac{\left[\cosh(\lambda R)-1\right]}{\sinh(\lambda R)} \tag{5.1.15}$$

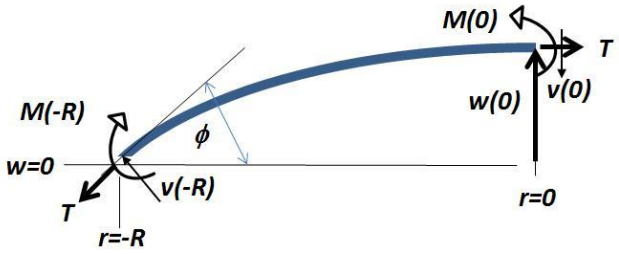

Fig. 5.1.2. Free body diagram with cuts at *r=-R* and *r=0*.

Consider free body diagram Fig. 5.1.2. Taking moments at *r=-R*, we see that the following moment balance must hold since $v(0) = 0$.

$$-M(-R) + M(0) - Tw_{\max} = 0 \tag{5.1.16}$$

Substituting in values from (5.1.7), (5.1.12) and (5.1.15), we see that (5.1.16) is identically satisfied since $D\lambda^2 = T$.

$$D\lambda\phi\frac{\cosh(\lambda R)}{\sinh(\lambda R)} - \frac{D\lambda\phi}{\sinh(\lambda R)} - T\frac{\phi}{\lambda}\frac{\left[\cosh(\lambda R)-1\right]}{\sinh(\lambda R)} = 0 \tag{5.1.17}$$

5.2 Approximation of Plate Deflection near Junction with Chamber Wall

We consider deflection of plate near the boundary *r=-R*. Define the state *x* as

$$x = r + R \tag{5.2.1}$$

Eq. (5.1.4) in terms of *x* is given by

$$w(x) = \frac{-\phi}{\lambda}\left[\coth(\lambda R)\left[\cosh(\lambda x) - 1\right] - \sinh(\lambda x)\right] \tag{5.2.2a}$$

Or, equivalently,

$$w(x) = \frac{-\phi}{\lambda}\coth(\lambda R)\left[\cosh(\lambda x) - 1 - \sinh(\lambda x) + \sinh(\lambda x)\left[1 - \tanh(\lambda R)\right]\right] \tag{5.2.2b}$$

$$w(x) = \frac{-\phi}{\lambda}\coth(\lambda R)\left[\left(e^{-\lambda x} - 1\right) + \sinh(\lambda x)\left[1 - \tanh(\lambda R)\right]\right] \tag{5.2.2c}$$

We observe that the following series (5.2.3a,b) hold.

$$\left(e^{-\lambda x} - 1\right) = \left(\frac{\lambda x}{1!} - \frac{(\lambda x)^2}{2!} + \frac{(\lambda x)^3}{3!}\ldots\right),\ (\lambda x)^2 < \infty \tag{5.2.3a}$$

$$\sinh(\lambda x) = \left(\frac{\lambda x}{1!} + \frac{(\lambda x)^3}{3!} + \frac{(\lambda x)^5}{5!} + \frac{(\lambda x)^7}{7!}\ldots\right),\ (\lambda x)^2 < \infty \tag{5.2.3b}$$

We note that if $\lambda R = 3$, then $\coth(\lambda R) = 1.005$ and $1 - \tanh(\lambda R) = 0.005$; and, that if $\lambda R = 6$, then $\coth(\lambda R) = 1.00001$ and $1 - \tanh(\lambda R) = 0.00001$. In Chapter 7, the values of $\lambda R = \lambda r_\phi$ are between 8.25 and 125.6. Therein, several plate thicknesses *t*=2, 4, 6, 8 and 10 microns are treated. For plate thickness *t*=10 microns, the values of λr_ϕ for the cases treated are between 8.25 and 12.76; for plate thickness *t*=8 microns, the values of λr_ϕ for the cases treated are between 10.25 and 16.65; for plate thickness *t*=6 microns, the values of λr_ϕ for the cases treated are between 13 and 24.64; for plate

thickness t=4 microns, the values of λr_ϕ for the cases treated are between 19.38 and 44.55; for plate thickness t=2 microns, the values of λr_ϕ for the cases treated are between 37.4 and 125.57. Consequently, for $\lambda R \geq 6$ and for small λx, the solution (5.2.2) can be approximated well by

$$w(x) \cong \frac{\phi}{\lambda}\left(1 - e^{-\lambda x}\right), \text{ small } x\lambda \geq 0 \tag{5.2.4a}$$

In series form, the approximation of $w(x)$ is given by

$$w(x) \cong \frac{\phi}{\lambda}\left(\frac{\lambda x}{1!} - \frac{(\lambda x)^2}{2!} + \frac{(\lambda x)^3}{3!}...\right), \text{ small } x\lambda \geq 0 \tag{5.2.4b}$$

This series (5.2.4b) will be utilized below in deriving a model for the electrostatic distributive forces acting on the plate. That is, the electrostatic distributive forces acting on the plate depend on plate deflection (5.2.4b). Electrostatic distributive forces cannot be determined without an estimate of plate deflection. Approximation (5.2.4b) provides what we need.

5.3 Distance Between Plate and Chamber Wall on Intake Stroke

In this section, we derive an approximation for the distance between the plate and the chamber wall, Fig. 5.3.1.

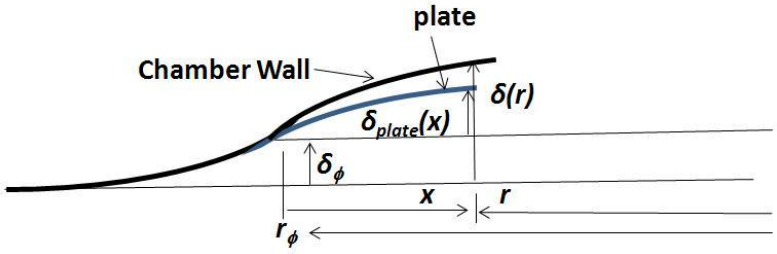

Fig. 5.3.1 Plate geometry with respect to chamber wall.

We are interested in the vertical distance $\Delta\delta(x)$ from the plate to the chamber wall. From Fig. 5.3.1, we see that this distance is given by

$$\Delta\delta(x) = \delta(r) - \delta_{\phi} - \delta_{plate}(x) \tag{5.3.1}$$

where *δ(r)* is the distance of the chamber wall above the floor and is given by the equation

$$\delta(r) = \delta_{\max}\left[1 - \left(\frac{r}{a}\right)^2\right]^2, \quad -a \le r \le a \tag{5.3.2}$$

$\delta_{\max}$, the maximum height of the chamber above the valley floor, occurs in the center of the chamber at the radius $r = 0$. The radius a is the radius of the chamber at the point where the chamber attaches itself to the valley floor. As shown in Fig. 5.3.1, the plate departs from the chamber wall at some radius r_{ϕ}. ϕ is the tangent angle of the chamber wall at the radius r_{ϕ}. For a given radius r_{ϕ} the tangent angle ϕ satisfies

$$\phi = \frac{4\delta_{\max}}{a}\frac{r_{\phi}}{a}\left[1 - \left(\frac{r_{\phi}}{a}\right)^2\right] \tag{5.3.3}$$

For convenience, we make the definition

$$R_{\phi} = \frac{r_{\phi}}{a} \tag{5.3.4}$$

Using (5.3.3) and (5.3.4), we find

$$a\phi = 4\delta_{\max}R_{\phi}\left[1 - \left(R_{\phi}\right)^2\right] \tag{5.3.5}$$

From this we determine the relationship that $\delta_{\max}$ has with ϕ and R_ϕ:

$$\delta_{\max} = \frac{a\phi}{4R_\phi\left[1-\left(R_\phi\right)^2\right]} \tag{5.3.6}$$

We define the variable *x* as the distance

$$x = r_\phi - r \tag{5.3.7}$$

The distance *δ(r)* at radius *r* as given by (5.3.2) can be expanded in terms of *x* and is given by

$$\delta(x) = \delta(r) = \delta_\phi + a\phi\left(\frac{x}{a}\right) + \delta_{\max} 2\left[3R_\phi^2 - 1\right]\left(\frac{x}{a}\right)^2 - \delta_{\max} 4R_\phi\left(\frac{x}{a}\right)^3 + \delta_{\max}\left(\frac{x}{a}\right)^4,\ 0 \le x \tag{5.3.8}$$

Using (5.3.6), this can be rewritten as

$$\delta(x) - \delta_\phi = Term1\left(\frac{x}{a}\right) + Term2\left(\frac{x}{a}\right)^2 - Term3\left(\frac{x}{a}\right)^3 + Term4\left(\frac{x}{a}\right)^4 \tag{5.3.7}$$

where

$$Term1 = a\phi \tag{5.3.8a}$$

$$Term2 = a\phi\frac{\left[3R_\phi^2 - 1\right]}{2R_\phi\left[1-\left(R_\phi\right)^2\right]} \tag{5.3.8b}$$

$$Term3 = -a\phi\frac{R_\phi}{R_\phi\left[1-\left(R_\phi\right)^2\right]} \tag{5.3.8c}$$

$$Term4 = a\phi \frac{1}{4R_\phi \left[1-\left(R_\phi\right)^2\right]} \tag{5.3.8d}$$

From (5.2.4b) in the previous section

$$\delta_{plate}(x) = w(x) \cong \frac{\phi}{\lambda}\left(\frac{\lambda x}{1!} - \frac{(\lambda x)^2}{2!} + \frac{(\lambda x)^3}{3!}...\right) \tag{5.3.9a}$$

This can be rewritten as

$$\delta_{plate}(x) = w(x) \cong a\phi\left(\frac{x}{a}\right) - \frac{1}{2}a\phi(a\lambda)\left(\frac{x}{a}\right)^2 + \frac{1}{6}a\phi(a\lambda)^2\left(\frac{x}{a}\right)^3 - \frac{1}{24}a\phi(a\lambda)^3\left(\frac{x}{a}\right)^4 + ... \tag{5.3.9b}$$

Substituting (5.3.7) and (5.3.9b) into (5.3.1), we get the approximation

$$\Delta\delta(x) = C_2\left(\frac{x}{a}\right)^2 + C_3\left(\frac{x}{a}\right)^3 + C_4\left(\frac{x}{a}\right)^4 + ... \tag{5.3.11}$$

where

$$C_2 = \frac{1}{2}a\phi\left[\frac{\left[3R_\phi^2 - 1\right]}{R_\phi\left[1-\left(R_\phi\right)^2\right]} + a\lambda\right] \tag{5.3.12a}$$

$$C_3 = -\frac{1}{3}a\phi\left[\frac{3}{\left[1-\left(R_\phi\right)^2\right]} + \frac{(a\lambda)^2}{2}\right] \tag{5.3.12b}$$

$$C_4 = \frac{1}{4} a\phi \left[\frac{1}{R_\phi \left[1 - \left(R_\phi \right)^2 \right]} + \frac{\left(a\lambda \right)^3}{6} \right] \tag{5.3.12c}$$

For analytical modeling purposes in this work, we further approximate $\Delta\delta(x)$ by keeping only the lowest order term:

$$\Delta\delta(x) \cong C_2 \left(\frac{x}{a} \right)^2 \tag{5.3.13}$$

For purposes to be later, we note that the following derivatives hold

$$\frac{d\delta(r_\phi)}{dr} = \phi = \frac{4\delta_{\max}}{a} \frac{r_\phi}{a} \left[1 - \left(\frac{r_\phi}{a} \right)^2 \right] \tag{5.3.14}$$

$$\frac{d^2\delta(r_\phi)}{dr^2} = \frac{4\delta_{\max}}{a^2} \left[\frac{3r_\phi^2}{a^2} - 1 \right] \tag{5.3.15}$$

5.4 Electrostatic Distributive Force Model on Intake Stroke

In this section, we develop an electrostatic distributive force model for the intake stroke. where *d* is the distance between parallel plates.

$$p\left(d \right) = \frac{p_0}{\left[1 + \frac{\varepsilon_d d}{\varepsilon_a d_0} \right]^2} \tag{5.4.1}$$

where p_0 is given by

$$p_0 = 0.5\varepsilon_0\varepsilon_a\left(\frac{\varepsilon_d V}{\varepsilon_a d_0}\right)^2 \tag{5.4.2}$$

In the above parallel plate model, ε_0 is the permittivity of free space, ε_d is the relative permittivity of the dielectric, ε_a is the relative permittivity of air, d_0 is the thickness of the dielectric, and *V* is the voltage differential between the plates.

We model the distance *d* in the case of the plate/chamber geometry as

$$d = gap + \Delta\delta(x) \tag{5.4.3}$$

where *gap* is a spacer distance between the actual boundary of the chamber wall and the assumed boundary of the chamber wall used in simulations and where $\Delta\delta(x)$ is given by (5.3.1). In the simulations, *gap* is taken to be about 5nm. We make the following definition.

$$\alpha_0 = \frac{\varepsilon_d}{\varepsilon_a d_0} \tag{5.4.4}$$

Using (5.4.3) and (5.4.4), we can rewrite (5.4.1) as

$$p(x) = \frac{p_{e-\max}}{\left[1 + \frac{\alpha_0\Delta\delta(x)}{1+\alpha_0 gap}\right]^2} \tag{5.4.5}$$

where

$$p_{e-\max} = \frac{0.5\varepsilon_0\varepsilon_a}{1+\alpha_0 gap}(\alpha_0 V)^2 \tag{5.4.6}$$

We make the following definition.

$$\alpha_1 = \frac{\alpha_0}{1+\alpha_0 gap} \tag{5.4.7}$$

Using (5.4.7), (5.4.5) can be rewritten as

$$p(x) = \frac{p_{e-\max}}{\left[1 + \alpha_1 \Delta\delta(x)\right]^2} \tag{5.4.8}$$

Substituting (5.3.13) into (5.4.8) gives the electrostatic distributive force model for the intake stroke, in its lowest order approximation, as a function of x^2 as follows.

$$p(x) = \frac{p_{e-\max}}{\left[1 + kx^2\right]^2} \tag{5.4.9}$$

where the constant k is defined as

$$k = \frac{\alpha_1 C_2}{a^2} \tag{5.4.10}$$

Substituting (5.3.12a) into (5.4.10) we get

$$k = \phi \frac{\alpha_1 a}{2a^2} \left[\frac{\left[3R_\phi^2 - 1\right]}{R_\phi \left[1 - \left(R_\phi\right)^2\right]} + a\lambda \right] \tag{5.4.11}$$

The electrostatic distributive force model for the intake stroke as given by the lowest order approximation (5.4.9) depends on the parameters: a, the radius of the plate; T, the tension in the plate; D, the flexural rigidity of the plate; ϕ, the tangent angle at the point where the plate leaves the chamber wall; r_ϕ, the radius of the plate portion that has not been electro-zipped up the side of the chamber wall; ε_0, the permittivity of free space; ε_d, the relative permittivity of the dielectric; ε_a, the relative permittivity of air; d_0, the thickness of the dielectric layer; V, the voltage differential between the plate electrode and the chamber wall electrode; and *gap*, a 5nm spacer between the actual boundary of the chamber wall and the assumed boundary of the chamber wall used in simulations.

5.5 Quadratic Model for Electrostatic Distributive Force on Intake Stroke

The model (5.4.9) is not conducive in deriving closed form analytical solutions when it is used together with the 4th order differential equations such as the reduced Von Karman equation (5.1.2). On the other hand, a quadratic model of distributive forces is conducive. For that purpose, we consider now a quadratic model of the distributive forces acting on the plate at the wall junction during the intake stroke

$$p(x) = p_{e-\max}\left[1-\frac{x}{x_1}\right]^2,\ 0 \le x \le x_1 \text{ and } p(x) = 0,\ x \ge x_1 \tag{5.5.1}$$

in which the constant x_1 is to be determined so that (5.5.1) provides the same change in slope angle as (5.4.9) does when each is applied as the distributive force load *q(x)* to a simple cantilever beam, Fig. 5.5.1.

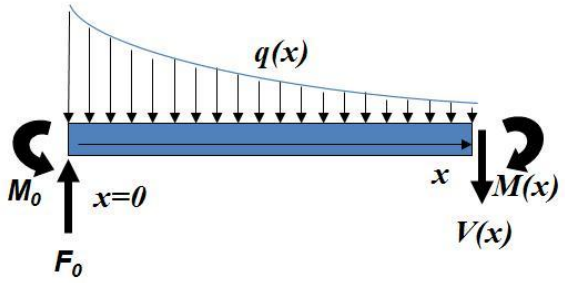

Fig. 5.5.1. Distributive forces *q(x)* acting on cantilever beam

The force F_0 and moment M_0 at the clamped end (i.e., $x=0$) are given by

$$F_0 = \int_0^\infty q(x)\,dx \tag{5.5.2}$$

$$M_0 = \int_0^\infty xq(x)\,dx \tag{5.5.3}$$

For convenience, we make definitions for the force $F_0(x)$ and moment $M_0(x)$ that account for the distributive loads only out to the point x:

$$F_0(x) = \int_0^x q(x)\,dx \tag{5.5.4}$$

$$M_0(x) = \int_0^x xq(x)\,dx \tag{5.5.5}$$

The moment $M(x)$, Fig. 5.5.1, satisfies

$$M(x) = -M_0 + x\left[F_0 - F_0(x)\right] + M_0(x) \tag{5.5.6}$$

We start first with the distributive load model (5.4.9):

$$\frac{q(x)}{p_{e-\max}} = \frac{1}{\left[1+kx^2\right]^2} \tag{5.5.7}$$

Carrying out the integrations (5.5.2) –(5.5.5) using (5.5.7), $M(x)$ satisfies

$$\frac{2kM(x)}{p_{e-\max}} = -\frac{1}{\left[1+kx^2\right]} + \sqrt{k}x\left[\frac{\pi}{2} - \left[\frac{\sqrt{k}x}{\left[1+kx^2\right]} + \tan^{-1}\left(\sqrt{k}x\right)\right]\right] \tag{5.5.8}$$

We integrate (5.5.8) to get the slope change $\Delta\theta$

$$\frac{2kD\Delta\theta}{p_{e-\max}} = \int_0^\infty \left[-\frac{1}{\left[1+kx^2\right]} + \sqrt{k}x\left[\frac{\pi}{2} - \left[\frac{\sqrt{k}x}{\left[1+kx^2\right]} + \tan^{-1}\left(\sqrt{k}x\right)\right]\right]\right] dx \tag{5.5.9}$$

where D is the flexural rigidity of the plate. The integration of (5.5.9) yields the slope change for (5.5.7).

$$\frac{\Delta\theta}{p_{e-\max}} = -\frac{\pi}{8k\sqrt{k}D} \tag{5.5.10}$$

Next, we determine the slope change using the quadratic distributive load model (5.5.1):

$$\frac{q(x)}{p_{e-\max}} = \left[1 - \frac{x}{x_1}\right]^2, \ 0 \le x \le x_1 \text{ and } q(x) = 0, \ x \ge x_1 \tag{5.5.11}$$

Carrying out the integrations (5.5.2) –(5.5.5) using (5.5.11), *M(x)* satisfies

$$\frac{M(x)}{p_{e-\max}} = x_1^2 \left[-\left[\frac{\left(1-\frac{x}{x_1}\right)^3}{3} - \frac{\left(1-\frac{x}{x_1}\right)^4}{4} \right] + \frac{x}{x_1}\frac{\left(1-\frac{x}{x_1}\right)^3}{3} \right], \ 0 \le x \le x_1 \text{ and } M(x) = 0, \ x \ge x_1 \tag{5.5.12}$$

We integrate (5.5.12) to get the slope change $\Delta\theta$ for the quadratic model (5.5.11)

$$\frac{D\Delta\theta}{p_{e-\max}} = \int_0^{x_1} \left[x_1^2 \left[-\left[\frac{\left(1-\frac{x}{x_1}\right)^3}{3} - \frac{\left(1-\frac{x}{x_1}\right)^4}{4} \right] + \frac{x}{x_1}\frac{\left(1-\frac{x}{x_1}\right)^3}{3} \right] \right] dx \tag{5.5.13}$$

where D is the flexural rigidity of the plate. The integration of (5.5.13) yields the slope change for the quadratic model (5.5.11).

$$\frac{\Delta\theta}{p_{e-\max}} = -\frac{x_1^3}{60D} \tag{5.5.14}$$

Equating the slope changes for the two models determines the constant x_1 as a function of *k*.

$$x_1 = \frac{1}{\sqrt{k}}\left(\frac{15\pi}{2}\right)^{1/3} = \sqrt{\frac{8.22}{k}} \tag{5.5.15}$$

The electrostatic distributive forces acting on the plate at the wall junction during the intake stroke has the quadratic model approximation (5.5.1) where the constant x_1 is given by (5.5.15).

5.6 Summary: Quadratic Electrostatic Distributive Force on Intake Stroke

In summary, the quadratic electrostatic distributive force model derived above is given by

$$p(x) = p_{e-\max}\left[1-\frac{x}{x_1}\right]^2,\ 0 \le x \le x_1 \text{ and } p(x) = 0,\ x \ge x_1 \tag{5.6.1}$$

where

$$k = \phi\frac{\alpha_1 a}{2a^2}\left[\frac{\left[3R_\phi^2 - 1\right]}{R_\phi\left[1-\left(R_\phi\right)^2\right]} + a\lambda\right] \tag{5.6.2a}$$

$$x_1 = \sqrt{\frac{8.22}{k}} \tag{5.6.2b}$$

$$\alpha_0 = \frac{\varepsilon_d}{\varepsilon_a d_0} \tag{5.6.2c}$$

$$\alpha_1 = \frac{\alpha_0}{1+\alpha_0 gap} \tag{5.6.2d}$$

$$\lambda = \sqrt{\frac{T}{D}} \tag{5.6.2e}$$

$$R_\phi = \frac{r_\phi}{a} \tag{5.6.2f}$$

This model (5.6.1) is utilized in the 4th order reduced von Kármán governing differential equations in deriving analytical solutions for the intake stroke. That is, while the model

(5.4.9), due to its particular nonlinear form, is not conducive, the quadratic model (5.5.1) is conducive in deriving closed form analytical solutions to the 4^{th} order differential equations.

$$D\frac{d^4w}{dx^4} = T\frac{d^2w}{dx^2} + p(x) \tag{5.6.3}$$

CHAPTER 6

ANALYTICAL DEFLECTION MODEL FOR INTAKE POWER STROKE

6.1 Large deflection mathematical analysis intake power stroke model

We consider the deflection of a plate as shown in Fig. 6.1.1. Electrostatic forces p(x) (e.g., Eq. 5.6.1) attract the plate to the chamber wall, causing the plate to adhear to the chamber wall up to a break point. The location of the break point depends on how much voltage potential is applied between the plate electrode and the chamber wall electrode. The break point moves up the wall as the voltage potential increases. We assume symmetric geometry and plate conditions. The horizontal distance between break points from chamber left side to chamber right side is defined to be $2 * x_c$ where x_c is the horizontal distance from a break point to the center of the chamber.

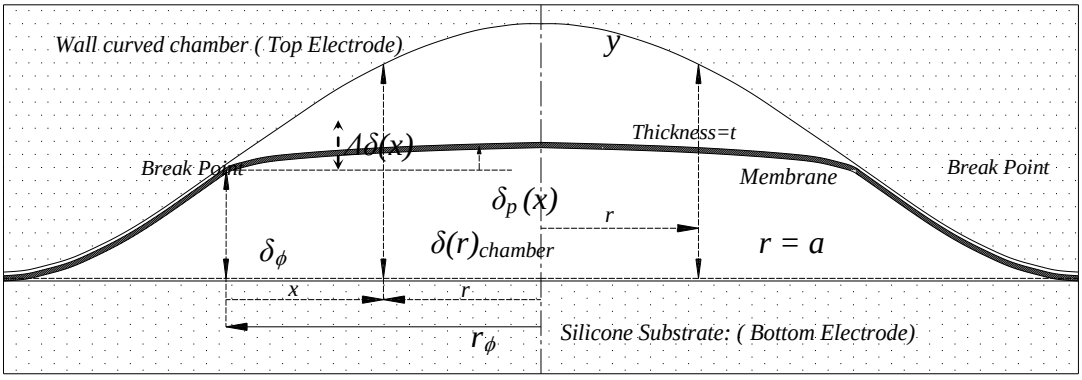

Fig. 6.1.1 Geometry of 2D Curved chamber with parameters

For plate analysis, if the deflection is greater than the thickness of the plate, the use of large deflection theory has to apply in order to account for simultaneous effects of

bending and stretching [Rudolph Szilard 2004]. Various references (e.g., Timoshenko & Young 1968, Ansel C Ugural 1999) provide treatment of the deflection, shear forces and moment for applied external pressure over a plate. However using a simplified 2 D static model for the plate analysis, it can be applied the reduced Von Karman governing differential equation as follow en equation 5.1, this equation is usually for thin plate that has bending stresses as well stretching stresses due to the external pressure and initial small curvature. [Ancel C. Ugural 1991]

$$D\frac{d^4w}{dx^4} = T\frac{d^2w}{dx^2} + p(x) \tag{6.1.1}$$

Where $w(x)$ deflection respect to x is, $p(x)$ is the electrostatic pressure on the plate due to applied differential voltage across the electrodes, T is the tension due to residual stresses in the plate, and D is the flexural rigidity of the plate. The electrostatic forces p(x) are assumed to have the quadratic form (5.6.1) and are assumed to be symmetric at both break points on the leftside and the rightside. The state x is zero at the break point and increases to the maximum $x = x_c$ as one moves toward the center of the chamber. We make the following definitions

$$M(x) = D\frac{d^2w}{dx^2} \tag{6.1.2}$$

$$V(x) = \frac{dM(x)}{dx} = D\frac{d^3w}{dx^3} \tag{6.1.3}$$

For boundary conditions we assume that $M(0)$ satisfies (6.1.2) at the break point and we assume that, due to symmetry, $V(x_c) = 0$ holds at the center of the plate.

$$M(0) = D\frac{d^2\delta(r)}{dr^2} = D\frac{4\delta_{\max}}{a^2}\left[\frac{3r_\phi^2}{a^2} - 1\right] \tag{6.1.4}$$

$$V(x_c) = 0 \tag{6.1.5}$$

Since the plate follows the curvature of the chamber wall up to the break point, boundary condition (6.1.4) is the condition that the plate holds the same curvature as the chamber wall at the break point. Since the chamber geometry and the distributive forces acting across the plate are symmetric with respect to the radius r, condition (6.1.5) is the condition that the shear force is zero at the center of the chamber.

6.2 Linear State Space Equation

Using definitions (6.1.2) and (6.1.3), we can rewrite (6.1.1) in the second order form

$$\frac{dM(x)}{dx} = V(x) \tag{6.2.1a}$$

$$\frac{dV(x)}{dx} = \lambda^2 M(x) + p(x) \tag{6.2.1b}$$

Where

$$\lambda = \sqrt{\frac{T}{D}} \tag{6.2.2}$$

In state space matrix form, we can rewrite (6.2.1) as follows

$$\begin{bmatrix} \dfrac{dM(x)}{dx} \\ \dfrac{dV(x)}{dx} \end{bmatrix} = \lambda \begin{bmatrix} 0 & 1/\lambda \\ \lambda & 0 \end{bmatrix} \begin{bmatrix} M(x) \\ V(x) \end{bmatrix} + \begin{bmatrix} 0 \\ 1 \end{bmatrix} p(x) \tag{6.2.3}$$

By defining the state variable Z as the vector

$$Z = \begin{bmatrix} M(x) \\ V(x) \end{bmatrix} \tag{6.2.4}$$

Eq. (6.2.3) has the standard state space matric form which is linear in state Z and input u.

$$\frac{dZ}{dx} = \lambda AZ + Bu \tag{6.2.5}$$

Where

$$A = \begin{bmatrix} 0 & 1/\lambda \\ \lambda & 0 \end{bmatrix} \tag{6.2.6a}$$

$$B = \begin{bmatrix} 0 \\ 1 \end{bmatrix} \tag{6.2.6b}$$

$$u = p(x) \tag{6.2.6c}$$

The following matrix exponentials, which are used below, are easily derived.

$$e^{A\lambda x} = \begin{bmatrix} \cosh(\lambda x) & [\sinh(\lambda x)]/\lambda \\ \lambda \sinh(\lambda x) & \cosh(\lambda x) \end{bmatrix} \tag{6.2.7a}$$

$$e^{-A\lambda x} = \begin{bmatrix} \cosh(\lambda x) & -[\sinh(\lambda x)]/\lambda \\ -\lambda \sinh(\lambda x) & \cosh(\lambda x) \end{bmatrix} \tag{6.2.7b}$$

6.3 Solution for the interval $0 \le x \le x_1$

The unique solution to (6.2.5) satisfies

$$e^{-A\lambda x} Z(x) = Z(0) + \int_0^x e^{-A\lambda \bar{x}} Bp(\bar{x}) d\bar{x}, 0 \le x \le x_1 \tag{6.3.1}$$

Where $\bar{x}$ is the integration variable and $p(\bar{x})$ is given by

$$p(\bar{x}) = p_{e-\max} \left[1 - \frac{\bar{x}}{x_1} \right]^2, \ 0 \le \bar{x} \le x_1 \text{ and } p(\bar{x}) = 0, \ \bar{x} \ge x_1 \tag{6.3.2}$$

With the change in the integration variable

$$y = \frac{\bar{x}}{x_1} \tag{6.3.3}$$

We can rewrite (6.3.1) as

$$e^{-A\lambda x} Z(x) = Z(0) + p_{e-\max} x_1 \int_0^y e^{-A\lambda x_1 y} \begin{bmatrix} 0 \\ 1 \end{bmatrix} [1-y]^2 \, dy, 0 \le y \le 1 \tag{6.3.4}$$

Integrating (6.3.4) yields

$$e^{-A\lambda x} Z(x) = Z(0) + p_{e-\max} x_1 \left[e^{-A\lambda x} \begin{bmatrix} f_1(x) \\ f_2(x) \end{bmatrix} - \begin{bmatrix} f_1(0) \\ f_2(0) \end{bmatrix} \right], 0 \le x \le x_1 \tag{6.3.5}$$

Where

$$f_1(x) = -\frac{1}{\lambda}\left[\frac{\left[1-\frac{x}{x_1}\right]^2}{(\lambda x_1)} + \frac{2}{(\lambda x_1)^3}\right] \tag{6.3.6a}$$

$$f_2(x) = \frac{2\left[1-\frac{x}{x_1}\right]}{(\lambda x_1)^2} \tag{6.3.6b}$$

$$f_1(0) = -\frac{1}{\lambda(\lambda x_1)}\left[1+\frac{2}{(\lambda x_1)^2}\right] \tag{6.3.7a}$$

$$f_2(0) = \frac{2}{(\lambda x_1)^2} \tag{6.3.7b}$$

Note that

$$f_1(x_1) = -\frac{1}{\lambda}\left[\frac{2}{(\lambda x_1)^3}\right] \tag{6.3.8a}$$

$$f_2(x_1) = 0 \tag{6.3.8b}$$

We make the following definition

$$\begin{bmatrix} M_1(x) \\ V_1(x) \end{bmatrix} = p_{e-\max} x_1 \left[e^{-A\lambda x} \begin{bmatrix} f_1(x) \\ f_2(x) \end{bmatrix} - \begin{bmatrix} f_1(0) \\ f_2(0) \end{bmatrix} \right], 0 \le x \le x_1 \tag{6.3.9}$$

Substituting (6.2.7b) into (6.3.9) gives

$$\begin{bmatrix} M_1(x) \\ V_1(x) \end{bmatrix} = p_{e-\max} x_1 \left[\begin{bmatrix} \cosh(\lambda x) & -[\sinh(\lambda x)]/\lambda \\ -\lambda \sinh(\lambda x) & \cosh(\lambda x) \end{bmatrix} \begin{bmatrix} f_1(x) \\ f_2(x) \end{bmatrix} - \begin{bmatrix} f_1(0) \\ f_2(0) \end{bmatrix} \right], 0 \le x \le x_1$$

(6.3.10)

That is,

$$M_1(x) = p_{e-\max} x_1 \left[f_1(x) \cosh(\lambda x) - f_2(x) [\sinh(\lambda x)]/\lambda - f_1(0) \right], 0 \le x \le x_1$$

(6.3.11a)

$$V_1(x) = p_{e-\max} x_1 \left[-\lambda f_1(x) \sinh(\lambda x) + f_2(x) \cosh(\lambda x) - f_2(0) \right], 0 \le x \le x_1$$

(6.3.11b)

At $x = x_1$, these have the values

$$M_1(x_1) = p_{e-\max} x_1 \left[f_1(x_1) \cosh(\lambda x_1) - f_2(x_1) [\sinh(\lambda x_1)]/\lambda - f_1(0) \right] \qquad (6.3.12a)$$

$$V_1(x_1) = p_{e-\max} x_1 \left[-\lambda f_1(x_1) \sinh(\lambda x_1) + f_2(x_1) \cosh(\lambda x_1) - f_2(0) \right] \qquad (6.3.12b)$$

We can rewrite (6.3.5) as

$$e^{-A\lambda x} \begin{bmatrix} M(x) \\ V(x) \end{bmatrix} = \begin{bmatrix} M(0) \\ V(0) \end{bmatrix} + \begin{bmatrix} M_1(x) \\ V_1(x) \end{bmatrix}, 0 \le x \le x_1 \qquad (6.3.13)$$

From this, we get the solution for $0 \le x \le x_1$,

$$\begin{bmatrix} M(x) \\ V(x) \end{bmatrix} = e^{A\lambda x} \left(\begin{bmatrix} M(0) \\ V(0) \end{bmatrix} + \begin{bmatrix} M_1(x) \\ V_1(x) \end{bmatrix} \right), 0 \le x \le x_1 \qquad (6.3.14)$$

Or, equivalently,

$$\begin{bmatrix} M(x) \\ V(x) \end{bmatrix} = \begin{bmatrix} \cosh(\lambda x) & [\sinh(\lambda x)]/\lambda \\ \lambda \sinh(\lambda x) & \cosh(\lambda x) \end{bmatrix} \left(\begin{bmatrix} M(0) \\ V(0) \end{bmatrix} + \begin{bmatrix} M_1(x) \\ V_1(x) \end{bmatrix} \right), 0 \le x \le x_1 \quad (6.3.15)$$

$$M(x) = [M(0) + M_1(x)]\cosh(\lambda x) + [V(0) + V_1(x)][\sinh(\lambda x)]/\lambda, 0 \le x \le x_1$$

(6.3.16a)

$$V(x) = [M(0) + M_1(x)]\lambda \sinh(\lambda x) + [V(0) + V_1(x)]\cosh(\lambda x), 0 \le x \le x_1$$

(6.3.16b)

At $x = x_1$, we have the values

$$M(x_1) = [M(0) + M_1(x_1)]\cosh(\lambda x_1) + [V(0) + V_1(x_1)][\sinh(\lambda x_1)]/\lambda \quad (6.3.17a)$$

$$V(x_1) = [M(0) + M_1(x_1)]\lambda \sinh(\lambda x_1) + [V(0) + V_1(x_1)]\cosh(\lambda x_1) \quad (6.3.17b)$$

From the above equations, one can derive the following expression for $M(x)$

$$\mathrm{M(x)} = \mathrm{p_{e-max} x_1 xf_1(x)} + [\mathrm{M(0)} - \mathrm{p_{e-max} x_1 xf_1(x0)}]\cosh(\lambda \mathrm{x}) + \mathrm{V(0)} - \mathrm{p_{e-max} x_1 xf_2(x0)}]\frac{\sinh(\lambda \mathrm{x})}{\lambda}, \quad 0 \le \mathrm{x} \le \mathrm{x_1} \quad (6.3.18)$$

6.4 Solution for the interval $x_1 \le x \le x_c$

Since

$$p(x) = 0, \; x \ge x_1 \quad (6.4.1)$$

We have the solution for $x_1 \le x \le x_c$,

$$\begin{bmatrix} M(x) \\ V(x) \end{bmatrix} = e^{A\lambda x}\left(\begin{bmatrix} M(0) \\ V(0) \end{bmatrix} + \begin{bmatrix} M_1(x_1) \\ V_1(x_1) \end{bmatrix}\right), x_1 \le x \le x_c \tag{6.4.2}$$

Or, equivalently,

$$\begin{bmatrix} M(x) \\ V(x) \end{bmatrix} = \begin{bmatrix} \cosh(\lambda x) & [\sinh(\lambda x)]/\lambda \\ \lambda\sinh(\lambda x) & \cosh(\lambda x) \end{bmatrix}\left(\begin{bmatrix} M(0) \\ V(0) \end{bmatrix} + \begin{bmatrix} M_1(x_1) \\ V_1(x_1) \end{bmatrix}\right), x_1 \le x \le x_c$$

(6.4.3)

$$M(x) = \left[M(0) + M_1(x_1)\right]\cosh(\lambda x) + \left[V(0) + V_1(x_1)\right]\left[\sinh(\lambda x)\right]/\lambda, x_1 \le x \le x_c$$

(6.4.4a)

$$V(x) = \left[M(0) + M_1(x_1)\right]\lambda\sinh(\lambda x) + \left[V(0) + V_1(x_1)\right]\cosh(\lambda x), x_1 \le x \le x_c$$

(6.4.4b)

At $x = x_c$, we have the values

$$M(x_c) = \left[M(0) + M_1(x_1)\right]\cosh(\lambda x_c) + \left[V(0) + V_1(x_1)\right]\left[\sinh(\lambda x_c)\right]/\lambda, x_1 \le x_c$$

(6.4.5a)

$$V(x_c) = \left[M(0) + M_1(x_1)\right]\lambda\sinh(\lambda x_c) + \left[V(0) + V_1(x_1)\right]\cosh(\lambda x_c), x_1 \le x_c$$

(6.4.5b)

Next, we apply boundary conditions. At $x = x_c$, the center of the chamber, we have the boundary condition

$$V(x_c) = 0 \tag{6.4.6}$$

Utilizing the boundary condition (6.4.6) in (6.4.5b) gives

$$0 = \left[M(0) + M_1(x_1) \right] \lambda \sinh(\lambda x_c) + \left[V(0) + V_1(x_1) \right] \cosh(\lambda x_c) \tag{6.4.7a}$$

$$V(0) = -V_1(x_1) - \left[M(0) + M_1(x_1) \right] \lambda \tanh(\lambda x_c) \tag{6.4.7b}$$

$$M(x_c) = -\frac{\left[V(0) + V_1(x_1) \right]}{\lambda \sinh(\lambda x_c)}, x_1 \le x_c \tag{6.4.8a}$$

$$M(x_c) = \frac{\left[M(0) + M_1(x_1) \right]}{\cosh(\lambda x_c)}, x_1 \le x_c \tag{6.4.8b}$$

6.5 Summary of Solution Equations For Intake Power

We summarize the equations needed in computing the solutions $M(x)$ and $V(x)$, $0 \le x \le x_c$.

$$\lambda = \sqrt{\frac{T}{D}} \tag{6.2.2}$$

$$f_1(0) = -\frac{1}{\lambda(\lambda x_1)} \left[1 + \frac{2}{(\lambda x_1)^2} \right] \tag{6.3.7a}$$

$$f_2(0) = \frac{2}{(\lambda x_1)^2} \tag{6.3.7b}$$

$$f_1(x_1) = -\frac{1}{\lambda} \left[\frac{2}{(\lambda x_1)^3} \right] \tag{6.3.8a}$$

$$f_2(x_1) = 0 \tag{6.3.8b}$$

$$M_1(x_1) = p_{e-\max} x_1 \left[f_1(x_1)\cosh(\lambda x_1) - f_2(x_1)\left[\sinh(\lambda x_1)\right]/\lambda - f_1(0)\right] \tag{6.3.12a}$$

$$V_1(x_1) = p_{e-\max} x_1 \left[-\lambda f_1(x_1)\sinh(\lambda x_1) + f_2(x_1)\cosh(\lambda x_1) - f_2(0)\right] \tag{6.3.12b}$$

$$M(0) = D\frac{4\delta_{\max}}{a^2}\left[\frac{3r_\phi^2}{a^2} - 1\right] \tag{6.1.4}$$

$$V(0) = -V_1(x_1) - \left[M(0) + M_1(x_1)\right]\lambda\tanh(\lambda x_c) \tag{6.4.7b}$$

$$f_1(x) = -\frac{1}{\lambda}\left[\frac{\left[1-\frac{x}{x_1}\right]^2}{(\lambda x_1)} + \frac{2}{(\lambda x_1)^3}\right] \tag{6.3.6a}$$

$$f_2(x) = \frac{2\left[1-\frac{x}{x_1}\right]}{(\lambda x_1)^2} \tag{6.3.6b}$$

$$M_1(x) = p_{e-\max} x_1 \left[f_1(x)\cosh(\lambda x) - f_2(x)\left[\sinh(\lambda x)\right]/\lambda - f_1(0)\right], 0 \le x \le x_1 \tag{6.3.11a}$$

$$V_1(x) = p_{e-\max} x_1 \left[-\lambda f_1(x)\sinh(\lambda x) + f_2(x)\cosh(\lambda x) - f_2(0)\right], 0 \le x \le x_1 \tag{6.3.11b}$$

$$M(x) = \left[M(0) + M_1(x)\right]\cosh(\lambda x) + \left[V(0) + V_1(x)\right]\left[\sinh(\lambda x)\right]/\lambda, 0 \le x \le x_1$$

(6.3.16a)

$$V(x) = \left[M(0) + M_1(x)\right]\lambda\sinh(\lambda x) + \left[V(0) + V_1(x)\right]\cosh(\lambda x), 0 \le x \le x_1 \tag{6.3.16b}$$

$$M(x) = p_{e-max} x_1 x f_1(x) + [M(0) - p_{e-max} x_1 x f_1(x0)] \cosh(\lambda x) + V(0) - p_{e-max} x_1 x f_2(x0)] \frac{\sinh(\lambda x)}{\lambda}, \quad 0 \le x \le x_1 \quad (6.3.18)$$

$$M(x) = \left[M(0) + M_1(x_1)\right] \cosh(\lambda x) + \left[V(0) + V_1(x_1)\right] \left[\sinh(\lambda x)\right] / \lambda, x_1 \le x \le x_c$$

(6.4.4a)

$$V(x) = \left[M(0) + M_1(x_1)\right] \lambda \sinh(\lambda x) + \left[V(0) + V_1(x_1)\right] \cosh(\lambda x), x_1 \le x \le x_c \quad (6.4.4b)$$

$$M(x_c) = -\frac{\left[V(0) + V_1(x_1)\right]}{\lambda \sinh(\lambda x_c)}, x_1 \le x_c \quad (6.4.8a)$$

$$M(x_c) = \frac{\left[M(0) + M_1(x_1)\right]}{\cosh(\lambda x_c)}, x_1 \le x_c \quad (6.4.8b)$$

CHAPTER 7

COMPARE ANALYTICAL AND SIMULATION RESULTS FOR INTAKE POWER STROKE

In this chapter, we compare bending stress σ_B results obtained from simulation with those generated using the analytical model developed in the previous two chapters. The following parameters are held constant in this comparison. Here, we use the standard symbol μm for the unit of microns where the prefix μ is 10^{-6}. The radius of the chamber at the point where the chamber attaches itself to the valley floor is $a = 1000\ \mu m$. The maximum height of the chamber at the center of the chamber is $\delta_{\max} = 20\mu m$. Young's modulus is taken as $E = 160GPa$ and Poisson's ratio as $\upsilon = 0.23$. The permittivity of free space is $\varepsilon_0 = 8.85 \times 10^{-12}$ F/m; the relative permittivity of the dielectric is $\varepsilon_d = 3.9$; the relative permittivity of air is $\varepsilon_a = 1$; the thickness of the dielectric is $d_0 = 200nm$; and the spacer distance between the actual boundary of the chamber wall and the assumed boundary of the chamber wall used in simulation is $gap = 3\mu m$. For convenience, these parameters are listed in Table 7.0.1.

Table 7.0.1. Parameters held constant in Comparison

$a\ (\mu m)$	$\delta_{\max}(\mu m)$	$d_0(nm)$	$gap(\mu m)$
1000	20	200	5
$E(GPa)$	υ	ε_d	ε_a
160	0.23	3.9	1

The quadratic model parameter $x_1 = \sqrt{8.22}/\sqrt{k}$ was derived in Chapter 5. In the next section, we make comparisons using the slightly larger value $x_1 = \sqrt{8.70}/\sqrt{k}$. It turns out that the slightly larger value has a better fit with the maximum bending moment of the simulations for all cases considered and that the former model with 8.22 results in a maximum bending moment that is about 4-5% less than that given by simulation. In the first case considered in Section 7.1, we show comparisons using both. Then, for the rest of the comparisons in this chapter, we use the model having the slightly larger value, $x_1 = \sqrt{8.70}/\sqrt{k}$. Furthermore, the comparisons for the cases with thicknesses $2,4,6,8\mu m$ are carried out using an offset in plotting the analytically calculated bending stresses as well as without any offset. That is, those plots are also shifted an offset to the right and then compared with simulated. For example, cases with thicknesses $8\mu m$ are shifted $2\mu m$ in offset to the right; cases with thicknesses $2\mu m$ are shifted $5\mu m$ in offset to the right.

The equation for bending stress σ_B is given by (7.0.1) where $M(x)$ comes from (6.3.16a) or (6.4.4a) and where *t* is the plate thickness.

$$\sigma_B(x) = 6\frac{M(x)}{t^2} \tag{7.0.1}$$

The tension *T* is computed by multiplying plate thickness *t* times tension stresses σ_T.

$$T = \sigma_T * \mathrm{t} \tag{7.0.2}$$

The flexural rigidity of the plate is given by

$$D = \frac{EI}{b\left(1-\upsilon^2\right)} = \frac{Et^3}{12\left(1-\upsilon^2\right)} \tag{7.0.3}$$

where b is the width of the plate and I is the moment of inertia of the cross-section is given by

$$I = \frac{bt^3}{12} \tag{7.0.3}$$

7.1 Comparison of Results for Plate Thickness 10 Microns

For the plate thickness $10\mu m$, we consider four (4) cases given in Table 7.1.1. The flexural rigidity for this plate thickness is D=14.08 $N\text{-}\mu m$.

Table 7.1.1. Conditions for plate thickness $t = 10\mu m$

Case	Plate Thickness t (μm)	Tension Stresses σ_T (MPa)	Tension T (N/m)	Voltage V (volts)	$\lambda = \sqrt{\frac{T}{D}}$ ($1/\mu m$)	Radius r_ϕ (μm)	$r_\phi\sqrt{\frac{T}{D}}$	Slope Angle ϕ (rad.)	$p_{e-\max}$ (MPa)
1	10	513.60	5136	199	0.0191003	668.2219	12.76	0.02958777	59.4712
2	10	414.20	4142	179	0.0171527	672.1	11.53	0.02948008	48.1179
3	10	314.4	3144	157	0.0149441	664.34	9.93	0.02969069	37.0169
4	10	214.7	2147	130.8	0.0123494	668.2195	8.25	0.02958784	25.6931

First, we consider case 1 which has a tension T= 5,136 N/m and an applied voltage V= 199 volts. For this case, the plate electrozips up the chamber wall, from the starting radius r=1000μm to the radius r=668.22μm at which point the plate breaks away from the chamber wall. The resulting analytically calculated bending stresses σ_B are compared against simulation values in Fig. 7.1.1a,b using the two models of x_1, one with the 8.22 factor and the other with factor 8.70. The quantities associated with the analytical calculation are given in Tables 7.1.1a,b.

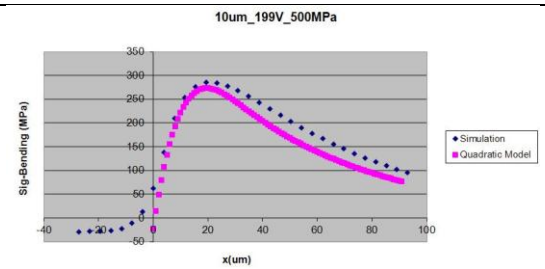

Fig. 7.1.1a. σ_B comparison with $x_1 = \sqrt{8.22}/\sqrt{k}$ $\mathbf{10}\mu m$

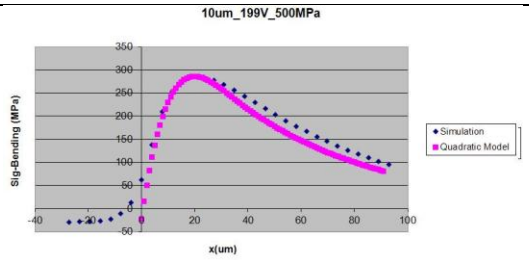

Fig. 7.1.1b. σ_B Comparison with $x_1 = \sqrt{8.70}/\sqrt{k}$ $\mathbf{10}\mu m$

Table 7.1.1a. Quantities with $x_1 = \sqrt{8.22}/\sqrt{k}$

$1/\sqrt{k}$ (μm)	$f_1(0)$	$f_2(0)$ (μm)	$f_1(x_1)$	$f_2(x_1)$ (μm)
13.54	-323.6	3.60	-253.3	0
x_1 (μm)	$V(0)$ (N/m)	$M(0)$ (μN)	$V_1(x_1)$ (N/m)	$M_1(x_1)$ (μN)
39	-655.5	382.4	794.9	-7678.8

Table 7.1.1b. Quantities with $x_1 = \sqrt{8.70}/\sqrt{k}$

$1/\sqrt{k}$ (μm)	$f_1(0)$	$f_2(0)$ (μm)	$f_1(x_1)$	$f_2(x_1)$ (μm)
13.54	-303.3	3.43	-234.8	0
x_1 (μm)	$V(0)$ (N/m)	$M(0)$ (μN)	$V_1(x_1)$ (N/m)	$M_1(x_1)$ (μN)
40	-669.3	382.4	816.4	-8085.4

In Fig. 7.1.1a, the analytically calculated value for the maximum bending stresses is about 4-5% less than that from the simulation. The difference between the two maximum bending stresses in Fig. 7.1.1b is less than 1%. Since this trend was observed in all cases treated in this chapter, we use the quadratic model $x_1 = \sqrt{8.70}/\sqrt{k}$ throughout the rest of this chapter.

Next, we consider case 2 which has a tension T= 4,142 N/m and an applied voltage V= 179 volts. For this case, the plate electrozips up the chamber wall, from the starting radius r=1000μm to the radius r=672.1μm at which point the plate breaks away from the chamber wall. The resulting analytically calculated bending stresses σ_B are compared against simulation values in Fig. 7.1.2 using the model of x_1 with factor 8.70. The quantities associated with the analytical calculation are given in Tables 7.1.2.

Table 7.1.2. .**10**μm Case 2, Quantities with $x_1 = \sqrt{8.70}/\sqrt{k}$

$1/\sqrt{k}$ (μm)	$f_1(0)$	$f_2(0)$ (μm)	$f_1(x_1)$	$f_2(x_1)$ (μm)
14.257	-392.8	3.85	-311.9	0
x_1 (μm)	$V(0)$ (N/m)	$M(0)$ (μN)	$V_1(x_1)$ (N/m)	$M_1(x_1)$ (μN)
42	-574.8	399.98	691.35	-7196.8

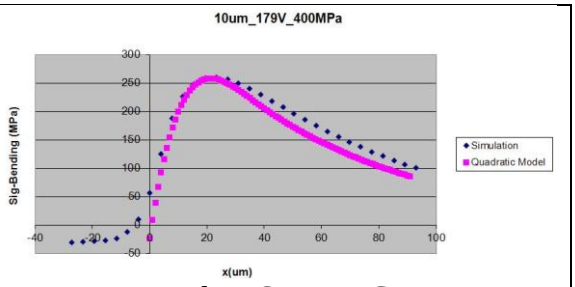

Fig. 7.1.2. Bending Stresses Comparison, **10**μm Case 2

Case 3 has a tension T= 3,144 N/m and an applied voltage V= 157 volts. For this case, the plate electrozips up the chamber wall, from the starting radius r=1000μm to the radius r=664.3μm at which point the plate breaks away from the chamber wall. The resulting analytically calculated bending stresses σ_B are compared against simulation values in Fig. 7.1.3 using the model of x_1 with factor 8.70. The quantities associated with the analytical calculation are given in Tables 7.1.3.

Table 7.1.3. **10**μm Case 3, Quantities with $x_1 = \sqrt{8.70}/\sqrt{k}$

$1/\sqrt{k}$ (μm)	$f_1(0)$	$f_2(0)$ (μm)	$f_1(x_1)$	$f_2(x_1)$ (μm)
15.204	-539.6	4.42	-440.1	0
x_1 (μm)	$V(0)$ (N/m)	$M(0)$ (μN)	$V_1(x_1)$ (N/m)	$M_1(x_1)$ (μN)
45	-478.6	364.97	567.94	-6341.5

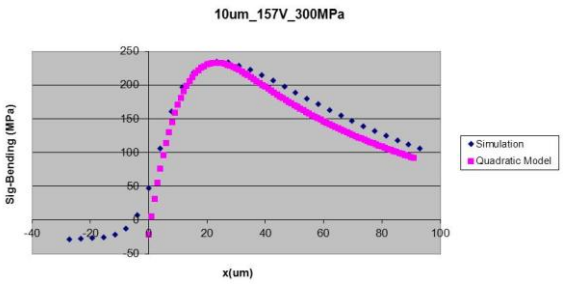

Fig. 7.1.3. Bending Stresses Comparison, **10** μm Case 3

Case 4 has a tension T= 2,147 N/m and an applied voltage V= 130.8 volts. For this case, the plate electrozips up the chamber wall, from the starting radius r=1000μm to

the radius r=668.2μm at which point the plate breaks away from the chamber wall. The resulting analytically calculated bending stresses σ_B are compared against simulation values in Fig. 7.1.4 using the model of x_1 with factor 8.70. The quantities associated with the analytical calculation are given in Tables 7.1.4.

Table 7.1.4. **10**μm Case 4, Quantities with $x_1 = \sqrt{8.70}/\sqrt{k}$

$1/\sqrt{k}$ (μm)	$f_1(0)$	$f_2(0)$ (μm)	$f_1(x_1)$	$f_2(x_1)$ (μm)
16.630	-864.7	5.46	-730.9	0
x_1 (μm)	$V(0)$ (N/m)	$M(0)$ (μN)	$V_1(x_1)$ (N/m)	$M_1(x_1)$ (μN)
49	-367.6	364.97	427.40	-5203.9

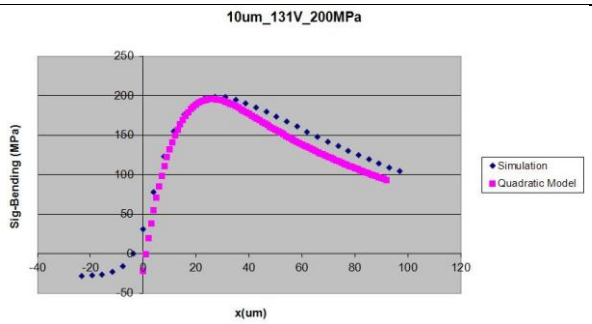

Fig. 7.1.4. Bending Stresses Comparison, 10μm Case 4

7.2 Comparison of Results for Plate Thickness 8 Microns

For the plate thickness $8\mu m$, we consider three (3) cases given in Table 7.2.1. The flexural rigidity for this plate thickness is D=7.21 N-μm. The comparisons for these cases are carried out using a $2\mu m$ offset in plotting the analytically calculated bending stresses as well as without the offset. That is, the plot is also shifted $2\mu m$ to the right and then compared with simulated.

Table 7.2. Conditions for plate thickness $t= 8\mu m$

Case	Plate Thickness t (μm)	Tension Stresses σ_T (MPa)	Tension T (N/m)	Voltage V (volts)	$\lambda = \sqrt{\frac{T}{D}}$ ($1/\mu m$)	Radius r_ϕ (μm)	$r_\phi\sqrt{\frac{T}{D}}$	Slope Angle ϕ (rad.)	$p_{e-\max}$ (MPa)
1	8	615.3	4922.4	195	0.026133	637.2	16.65	0.030278	57.104
2	8	415.4	3323.2	160.5	0.0171527	641.1	13.77	0.02948008	48.1179
3	8	214.4	1715.2	116	0.0149441	664.3	10.25	0.02969069	37.0169

Case 1 has a tension T= 4,922.4 N/m and an applied voltage V= 195 volts. For this case, the plate electrozips up the chamber wall, from the starting radius r=1000μm to the radius r=637.2μm at which point the plate breaks away from the chamber wall. The resulting analytically calculated bending stresses σ_B are compared against simulation values in Fig. 7.2.1a using the model of x_1 with factor 8.70. The quantities associated with the analytical calculation are given in Tables 7.2.1.

Table 7.2.1. **8**μm Case 1, Quantities with $x_1 = \sqrt{8.70}/\sqrt{k}$

$1/\sqrt{k}$ (μm)	$f_1(0)$	$f_2(0)$ (μm)	$f_1(x_1)$	$f_2(x_1)$ (μm)
11.586	-150.3	2.508	-107.49	0
x_1 (μm)	$V(0)$ (N/m)	$M(0)$ (μN)	$V_1(x_1)$ (N/m)	$M_1(x_1)$ (μN)
34.17	-531.02	125.782	676.848	-5706.0

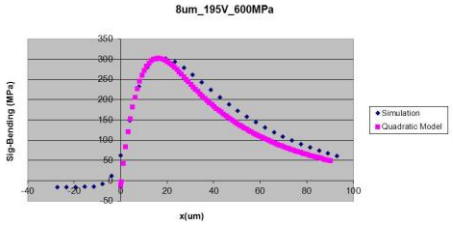

Fig. 7.2.1a. Bending Stresses Comparison, **8**μm Case 1

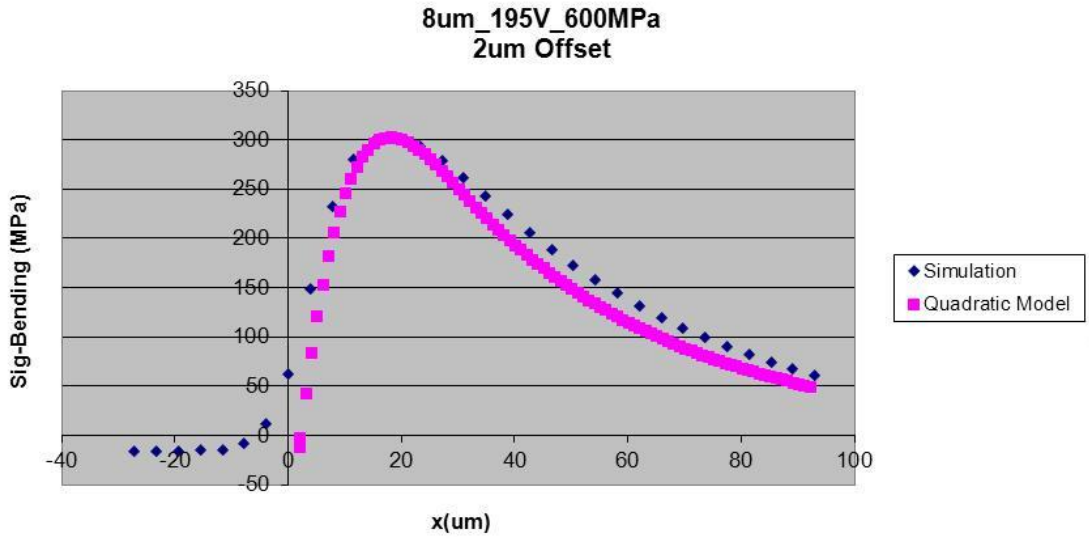

Fig. 7.2.1b. Bending Stresses Comparison, **8**μm ,Case 1, using a 2μm offset.

Case 2 has a tension T= 3,323.2 N/m and an applied voltage V= 160.5 volts. For this case, the plate electrozips up the chamber wall, from the starting radius r=1000μm to the radius r=641.1μm at which point the plate breaks away from the chamber wall. The resulting analytically calculated bending stresses σ_B are compared against simulation values in Fig. 7.2.2a,b using the model of x_1 with factor 8.70. The quantities associated with the analytical calculation are given in Tables 7.2.2.

Table 7.2.2. **8**μm Case 2, Quantities with $x_1 = \sqrt{8.70}/\sqrt{k}$

$1/\sqrt{k}$ (μm)	$f_1(0)$	$f_2(0)$ (μm)	$f_1(x_1)$	$f_2(x_1)$ (μm)
12.755	-234.69	3.068	-177.0	0
x_1 (μm)	$V(0)$ (N/m)	$M(0)$ (μN)	$V_1(x_1)$ (N/m)	$M_1(x_1)$ (μN)
37.6	-403.78	134.351	500.911	-4657.9

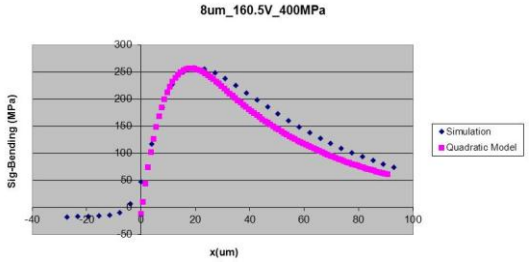

Fig. 7.2.2a. Bending Stresses Comparison, **8**μm ,Case 2

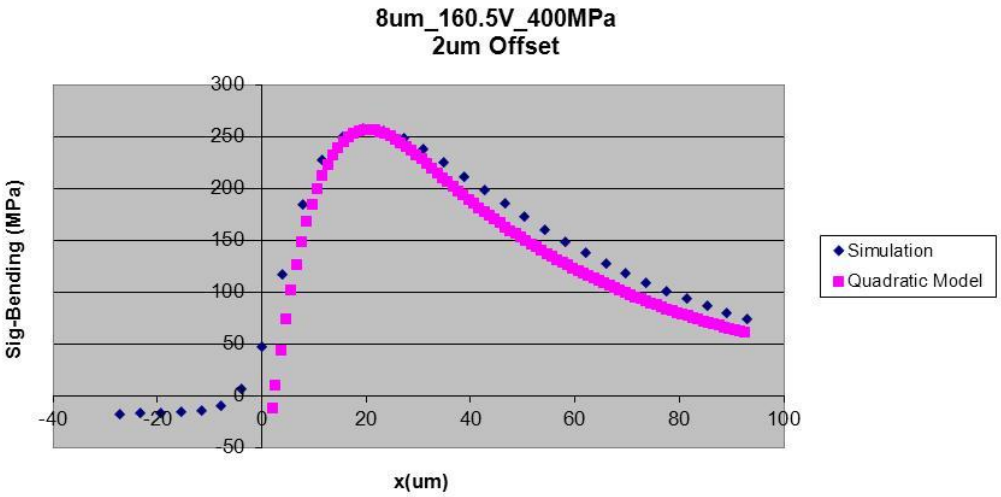

Fig. 7.2.2b. Bending Stresses Comparison, $\mathbf{8}\mu m$, Case 2, using a $2\mu m$ offset.

Case 3 has a tension T= 1,715.2 N/m and an applied voltage V= 116 volts. For this case, the plate electrozips up the chamber wall, from the starting radius r=1000μm to the radius r=664.3μm at which point the plate breaks away from the chamber wall. The resulting analytically calculated bending stresses σ_B are compared against simulation values in Fig. 7.2.3a,b using the model of x_1 with factor 8.70. The quantities associated with the analytical calculation are given in Tables 7.2.3.

Table 7.2.3. $\mathbf{8}\mu m$ Case 3, Quantities with $x_1 = \sqrt{8.70}/\sqrt{k}$

$1/\sqrt{k}$ (μm)	$f_1(0)$	$f_2(0)$ (μm)	$f_1(x_1)$	$f_2(x_1)$ (μm)
14.978	-504.71	4.306	-409.59	0
x_1 (μm)	$V(0)$ (N/m)	$M(0)$ (μN)	$V_1(x_1)$ (N/m)	$M_1(x_1)$ (μN)
44.18	-255.83	177.985	304.58	-3338.2

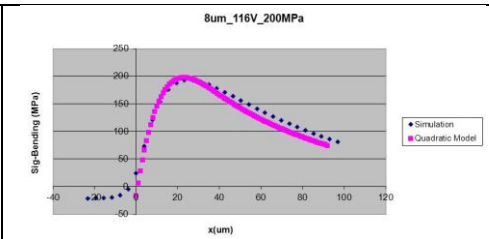

Fig. 7.2.3a. Bending Stresses Comparison, $\mathbf{8}\mu m$,Case 3

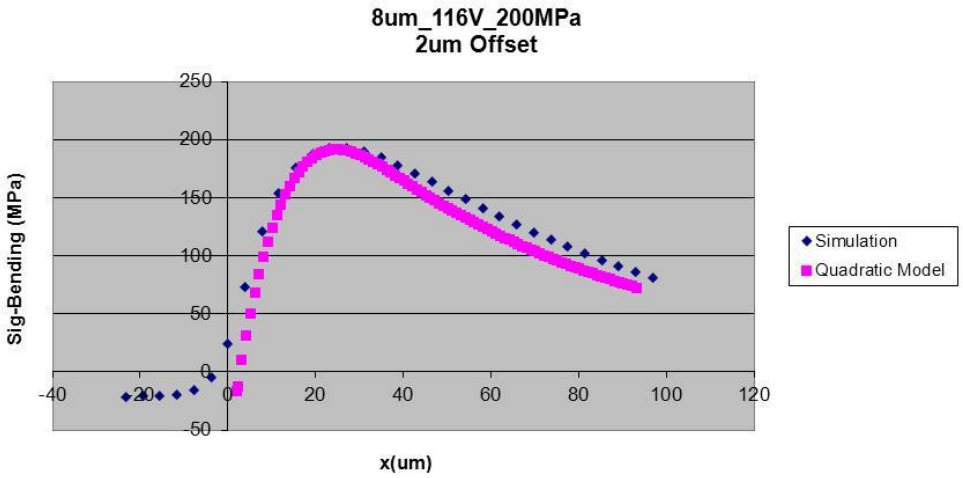

Fig. 7.2.3b. Bending Stresses Comparison, **8**μm , Case 3, using a 2μm offset.

7.3 Comparison of Results for Plate Thickness 6 Microns

For the plate thickness 6μm, we consider four (4) cases given in Table 7.3.1. The flexural rigidity for this plate thickness is D=3.04 N-μm. The comparisons for these cases are carried out utilizing a 3μm offset in plotting the analytically calculated bending stresses as well as without the offset. That is, the plot is also shifted 3μm to the right and then compared with simulated.

Table 7.3. Conditions for plate thickness t= 6μm

Case	Plate Thickness t (μm)	Tension Stresses σ_T (MPa)	Tension T (N/m)	Voltage V (volts)	$\lambda = \sqrt{\frac{T}{D}}$ (1/μm)	Radius r_ϕ (μm)	$r_\phi\sqrt{\frac{T}{D}}$	Slope Angle ϕ (rad.)	$p_{e-\max}$ (MPa)
1	6	816.6	4899.6	195	0.04014	614	24.64	0.03060237	57.1045
2	6	615.3	3691.8	169	0.0348434	633.3	22.07	0.0303436	42.8918
3	6	414.6	2487.6	139	0.0286017	633.3	18.11	0.0303436	29.0155
4	6	216.5	1299	100.5	0.0206683	629.46	13.01	0.03040441	15.1682

Case 1 has a tension T= 4,899.6 N/m and an applied voltage V= 195 volts. For this case, the plate electrozips up the chamber wall, from the starting radius r=1000μm to the radius r=614.μm at which point the plate breaks away from the chamber wall. The resulting analytically calculated bending stresses σ_B are compared against simulation values in Fig. 7.3.1a,b using the model of x_1 with factor 8.70. The quantities associated with the analytical calculation are given in Tables 7.3.1.

Table 7.3.1. **6**μm Case 1, Quantities with $x_1 = \sqrt{8.70}/\sqrt{k}$

$1/\sqrt{k}$ (μm)	$f_1(0)$	$f_2(0)$ (μm)	$f_1(x_1)$	$f_2(x_1)$ (μm)
9.361	-59.61	1.641	-37.04	0
x_1 (μm)	$V(0)$ (N/m)	$M(0)$ (μN)	$V_1(x_1)$ (N/m)	$M_1(x_1)$ (μN)
27.5	-407.12	31.8295	556.291	-3748.2

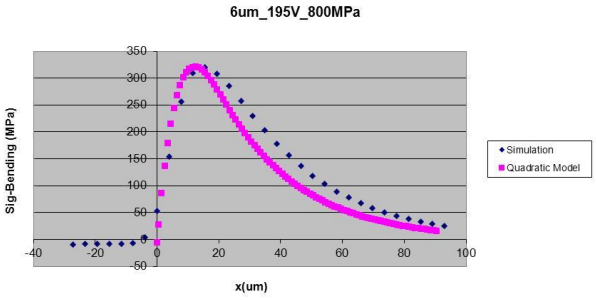

Fig. 7.3.1a. Bending Stresses Comparison, **6**μm Case 1

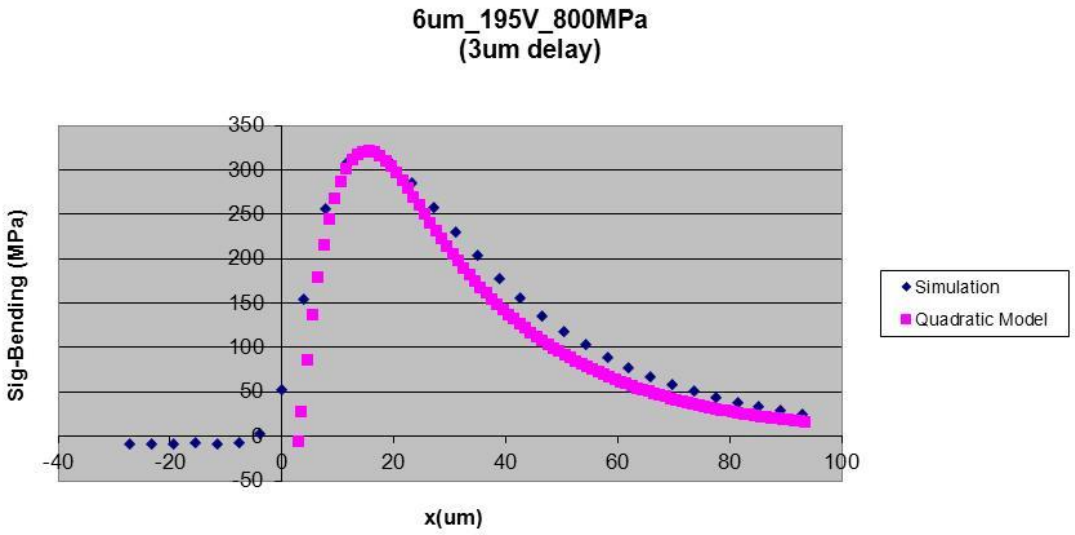

Fig. 7.3.1b. Bending Stresses Comparison, 6μm ,Case 1, using a 3μm offset.

Case 2 has a tension T= 3,691.8 N/m and an applied voltage V= 169 volts. For this case, the plate electrozips up the chamber wall, from the starting radius r=1000μm to the radius r=633.3μm at which point the plate breaks away from the chamber wall. The resulting analytically calculated bending stresses σ_B are compared against simulation values in Fig. 7.3.2a,b using the model of x_1 with factor 8.70. The quantities associated with the analytical calculation are given in Tables 7.3.2.

Table 7.3.2. **6**μm Case 2, Quantities with $x_1 = \sqrt{8.70}/\sqrt{k}$

$1/\sqrt{k}$ (μm)	$f_1(0)$	$f_2(0)$ (μm)	$f_1(x_1)$	$f_2(x_1)$ (μm)
10.056	-80.78	1.8929	-52.854	0
x_1 (μm)	$V(0)$ (N/m)	$M(0)$ (μN)	$V_1(x_1)$ (N/m)	$M_1(x_1)$ (μN)
29.5	-333.946	45.8992	444.619	-3222.2

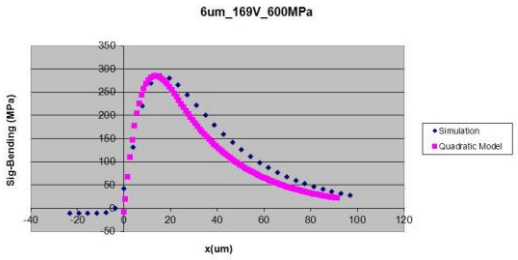

Fig. 7.3.2a. Bending Stresses Comparison, 6μm ,Case 2

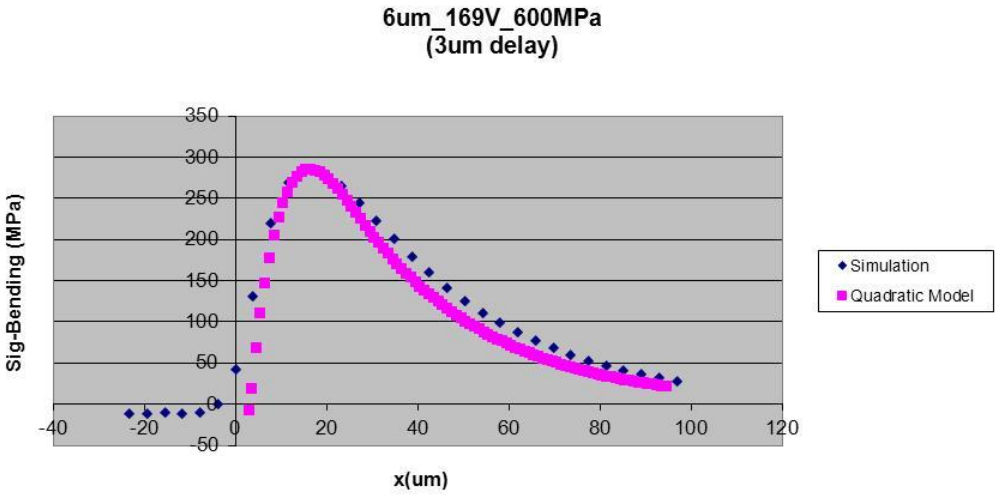

Fig. 7.3.2b. Bending Stresses Comparison, 6μm, Case 2, using a 3μm offset.

Case 3 has a tension T= 2,487.6 N/m and an applied voltage V= 139 volts. For this case, the plate electrozips up the chamber wall, from the starting radius r=1000μm to the radius r=633.3μm at which point the plate breaks away from the chamber wall. The resulting analytically calculated bending stresses σ_B are compared against simulation values in Fig. 7.3.3a,b using the model of x_1 with factor 8.70. The quantities associated with the analytical calculation are given in Tables 7.3.3.

Table 7.3.3. **6**μm Case 3, Quantities with $x_1 = \sqrt{8.70}/\sqrt{k}$

$1/\sqrt{k}$ (μm)	$f_1(0)$	$f_2(0)$ (μm)	$f_1(x_1)$	$f_2(x_1)$ (μm)
11.081	-124.67	2.3146	-87.059	0
x_1 (μm)	$V(0)$ (N/m)	$M(0)$ (μN)	$V_1(x_1)$ (N/m)	$M_1(x_1)$ (μN)
32.5	-254.326	45.8987	328.198	-2628.68

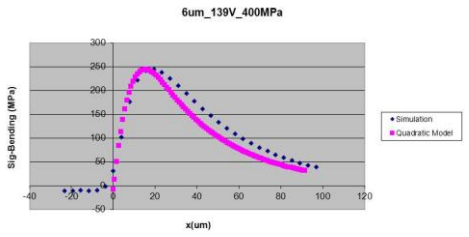

Fig. 7.3.3a. Bending Stresses Comparison, 6μm Case 3

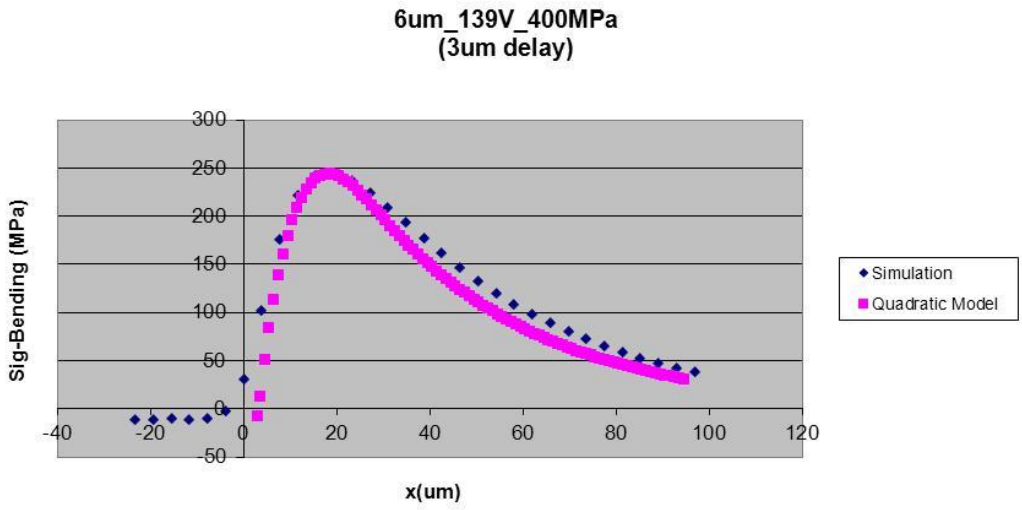

Fig. 7.3.3b. Bending Stresses Comparison, 6μm ,Case 3, using a 3μm offset.

Case 4 has a tension T= 1,299 N/m and an applied voltage V= 100.5 volts. For this case, the plate electrozips up the chamber wall, from the starting radius r=1000μm to the radius r=629.5μm at which point the plate breaks away from the chamber wall. The resulting analytically calculated bending stresses σ_B are compared against simulation values in Fig. 7.3.4a,b using the model of x_1 with factor 8.70. The quantities associated with the analytical calculation are given in Tables 7.3.4.

Table 7.3.4. **6**μm Case 4, Quantities with $x_1 = \sqrt{8.70}/\sqrt{k}$

$1/\sqrt{k}$ (μm)	$f_1(0)$	$f_2(0)$ (μm)	$f_1(x_1)$	$f_2(x_1)$ (μm)
12.989	-256.2	3.1917	-195.078	0
x_1 (μm)	$V(0)$ (N/m)	$M(0)$ (μN)	$V_1(x_1)$ (N/m)	$M_1(x_1)$ (μN)
38.3	-161.548	42.3470	199.805	-1893.3

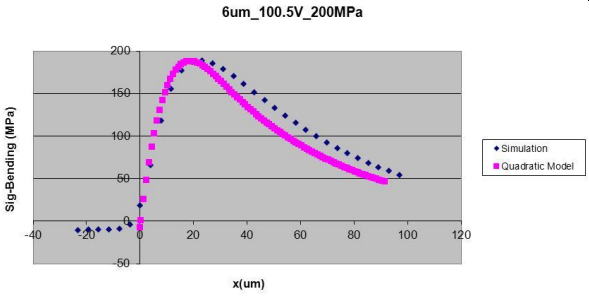

Fig. 7.3.4a. Bending Stresses Comparison, 6μm Case 4

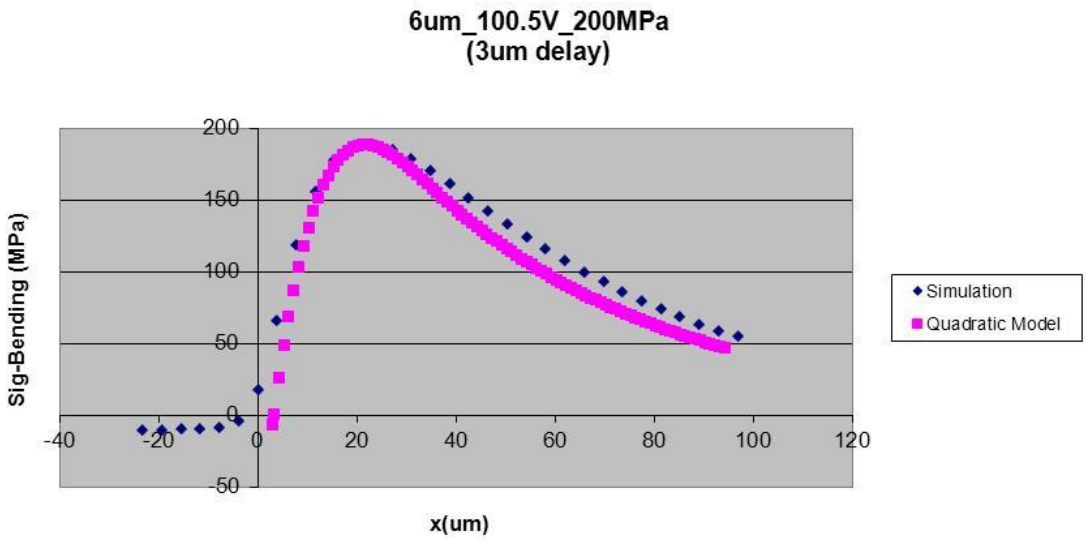

Fig. 7.3.4b. Bending Stresses Comparison, 6μm ,Case 4, using a 3μm offset.

7.4 Comparison of Results for Plate Thickness 4 Microns

For the plate thickness $4\mu m$, we consider six (6) cases given in Table 7.4.1. The flexural rigidity for this plate thickness is $D=0.901\ N\text{-}\mu m$. The comparisons for these cases are carried out using a $4\mu m$ offset in plotting the analytically calculated bending stresses as well as without the offset. That is, the plot is also shifted $4\mu m$ to the right and then compared with simulated.

Table 7.4. Conditions for plate thickness $t= 4\mu m$

Case	Plate Thickness t (μm)	Tension Stresses σ_T (MPa)	Tension T (N/m)	Voltage V (volts)	$\lambda = \sqrt{\frac{T}{D}}$ ($1/\mu m$)	Radius r_ϕ (μm)	$r_\phi\sqrt{\frac{T}{D}}$	Slope Angle ϕ (rad.)	$p_{e-\max}$ (MPa)
1	4	1216.7	4866.8	195.5	0.0734954	606.2	44.55	0.03067469	57.4
2	4	1016.2	4064.8	178.5	0.0671673	614	41.24	0.03060236	47.84
3	4	817.1	3268.4	160	0.0602291	602.3	36.28	0.03070429	38.45
4	4	615.5	2462	138.5	0.052274	625.6	32.70	0.0304606	28.81
5	4	416.6	1666.4	114	0.0430059	614	26.4	0.0306024	19.52
6	4	216.1	864.4	82	0.0309739	625.6	19.38	0.0304606	10.10

Case 1 has a tension $T= 4{,}866.8\ N/m$ and an applied voltage $V= 195.5$ volts. For this case, the plate electrozips up the chamber wall, from the starting radius $r=1000\mu m$ to the radius $r=606.2\mu m$ at which point the plate breaks away from the chamber wall. The resulting analytically calculated bending stresses σ_B are compared against simulation values in Fig. 7.4.1a,b using the model of x_1 with factor 8.70. The quantities associated with the analytical calculation are given in Tables 7.4.1.

Table 7.4.1. $4\mu m$ Case 1, Quantities with $x_1 = \sqrt{8.70}/\sqrt{k}$

$1/\sqrt{k}$ (μm)	$f_1(0)$	$f_2(0)$ (μm)	$f_1(x_1)$	$f_2(x_1)$ (μm)
6.927	-17.825	0.92566	-8.56839	0
x_1 (μm)	$V(0)$ (N/m)	$M(0)$ (μN)	$V_1(x_1)$ (N/m)	$M_1(x_1)$ (μN)
20	-275.507	6.3731	426.181	-2056.50

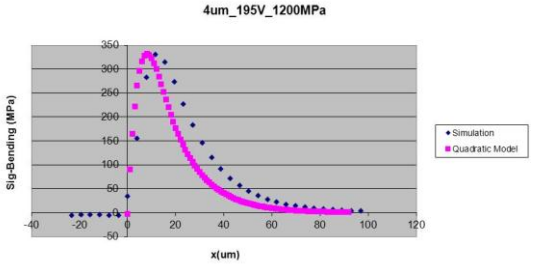

Fig. 7.4.1a. Bending Stresses Comparison, $4\mu m$ Case 1

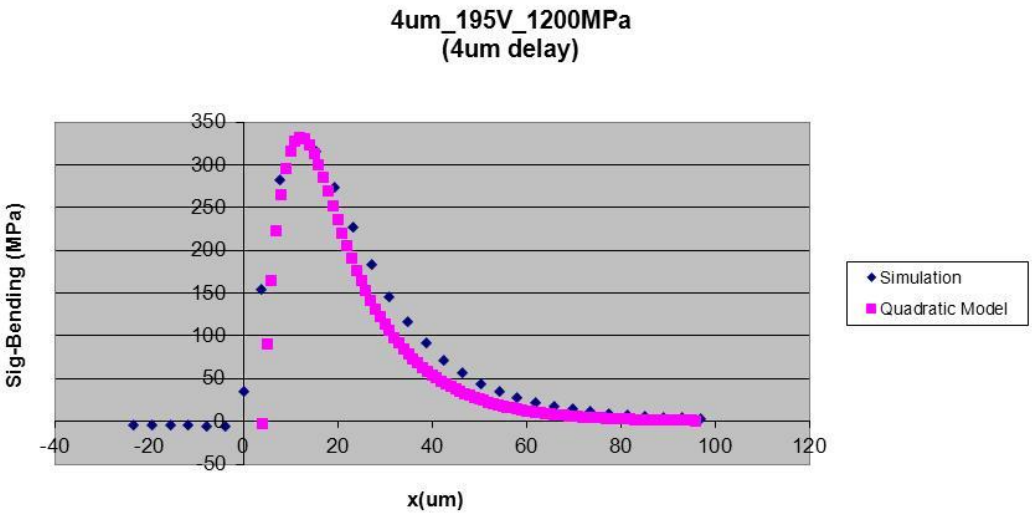

Fig. 7.4.1b. Bending Stresses Comparison, $4\mu m$, Case 1, using a $4\mu m$ offset.

Case 2 has a tension T= 4,064.8 N/m and an applied voltage V= 178.5 volts. For this case, the plate electrozips up the chamber wall, from the starting radius r=1000μm to the radius r=614.0μm at which point the plate breaks away from the chamber wall. The resulting analytically calculated bending stresses σ_B are compared against simulation values in Fig. 7.4.2a,b using the model of x_1 with factor 8.70. The quantities associated with the analytical calculation are given in Tables 7.4.2.

Table 7.4.2. $4\mu m$ Case 2, Quantities with $x_1 = \sqrt{8.70}/\sqrt{k}$

$1/\sqrt{k}$ (μm)	$f_1(0)$	$f_2(0)$ (μm)	$f_1(x_1)$	$f_2(x_1)$ (μm)
7.249	-21.166	1.00525	-10.6106	0
x_1 (μm)	$V(0)$ (N/m)	$M(0)$ (μN)	$V_1(x_1)$ (N/m)	$M_1(x_1)$ (μN)
21	-244.224	8.4055	369.889	-1879.32

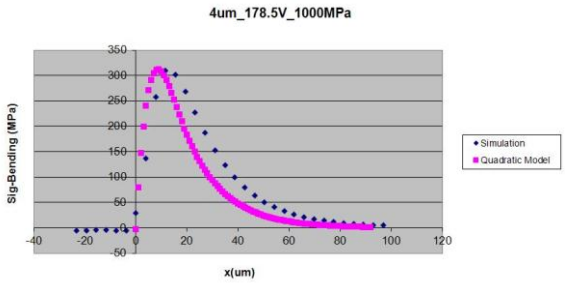

Fig. 7.4.2a. Bending Stresses Comparison, $4\mu m$ Case 2

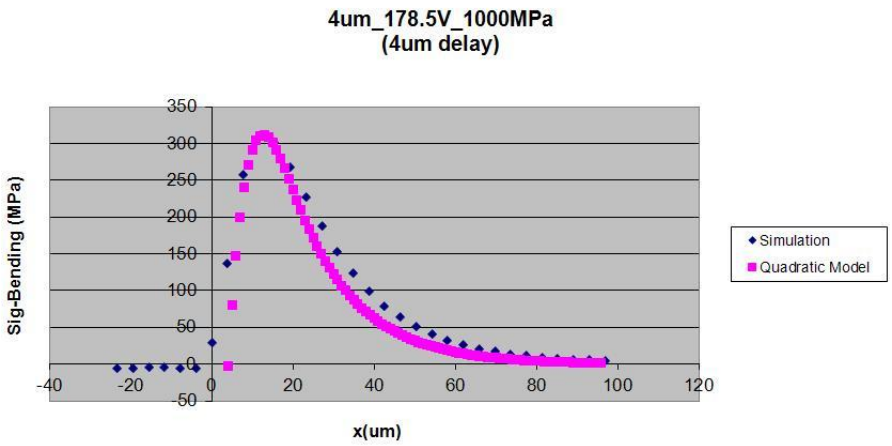

Fig. 7.4.2b. Bending Stresses Comparison, 4μm Case 2, using a 4μm offset.

Case 3 has a tension T= 3,268.4 N/m and an applied voltage V= 160 volts. For this case, the plate electrozips up the chamber wall, from the starting radius r=1000μm to the radius r=602.33μm at which point the plate breaks away from the chamber wall. The resulting analytically calculated bending stresses σ_B are compared against simulation values in Fig. 7.4.3a,b using the model of x_1 with factor 8.70. The quantities associated with the analytical calculation are given in Tables 7.4.3.

Table 7.4.3. 4μm Case 3, Quantities with $x_1 = \sqrt{8.70}/\sqrt{k}$

$1/\sqrt{k}$ (μm)	$f_1(0)$	$f_2(0)$ (μm)	$f_1(x_1)$	$f_2(x_1)$ (μm)
7.647	-25.5951	1.08906	-13.3431	0
x_1 (μm)	$V(0)$ (N/m)	$M(0)$ (μN)	$V_1(x_1)$ (N/m)	$M_1(x_1)$ (μN)
22.5	-212.459	5.36653	316.0016	-1724.51

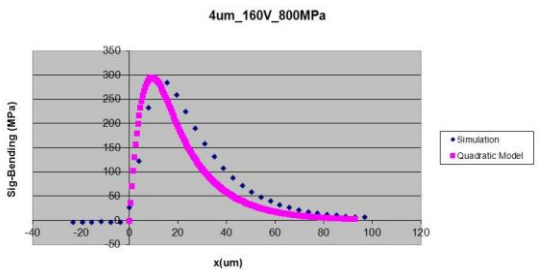

Fig. 7.4.3a. Bending Stresses Comparison, 4μm Case 3

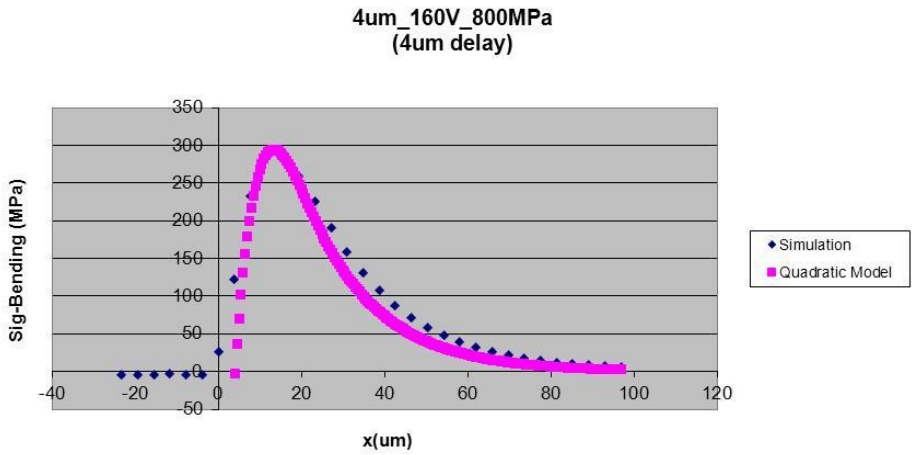

Fig. 7.4.3b. Bending Stresses Comparison, 4μm Case 3, using a 4μm offset.

Case 4 has a tension T= 2,462 N/m and an applied voltage V= 138.5 volts. For this case, the plate electrozips up the chamber wall, from the starting radius r=1000μm to the radius r=625.59μm at which point the plate breaks away from the chamber wall. The resulting analytically calculated bending stresses σ_B are compared against simulation values in Fig. 7.4.4a,b using the model of x_1 with factor 8.70. The quantities associated with the analytical calculation are given in Tables 7.4.4.

Table 7.4.4. 4μm Case 4, Quantities with $x_1 = \sqrt{8.70}/\sqrt{k}$

$1/\sqrt{k}$ (μm)	$f_1(0)$	$f_2(0)$ (μm)	$f_1(x_1)$	$f_2(x_1)$ (μm)
8.221	-34.625	1.2707	-19.3761	0
x_1 (μm)	$V(0)$ (N/m)	$M(0)$ (μN)	$V_1(x_1)$ (N/m)	$M_1(x_1)$ (μN)
24	-173.708	11.5027	249.288	-1457.36

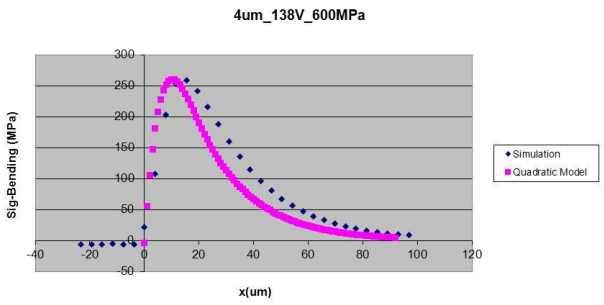

Fig. 7.4.4a. Bending Stresses Comparison, 4μm Case 4

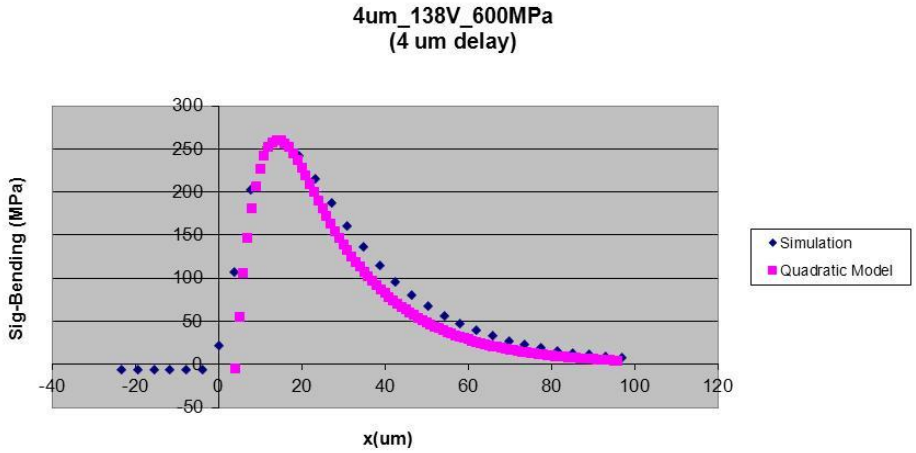

Fig. 7.4.4b. Bending Stresses Comparison, Case 4, using a 4μm offset.

Case 5 has a tension T= 1,666.4 N/m and an applied voltage V= 114 volts. For this case, the plate electrozips up the chamber wall, from the starting radius r=1000μm to the radius r=613.96μm at which point the plate breaks away from the chamber wall. The resulting analytically calculated bending stresses σ_B are compared against simulation values in Fig. 7.4.5a,b using the model of x_1 with factor 8.70. The quantities associated with the analytical calculation are given in Tables 7.4.5.

Table 7.4.5. 4μm Case 5.Quantities with $x_1 = \sqrt{8.70}/\sqrt{k}$

$1/\sqrt{k}$ (μm)	$f_1(0)$	$f_2(0)$ (μm)	$f_1(x_1)$	$f_2(x_1)$ (μm)
9.047	-51.821	1.53986	-31.4181	0
x_1 (μm)	$V(0)$ (N/m)	$M(0)$ (μN)	$V_1(x_1)$ (N/m)	$M_1(x_1)$ (μN)
26.5	-133.013	8.40519	183.947	-1192.76

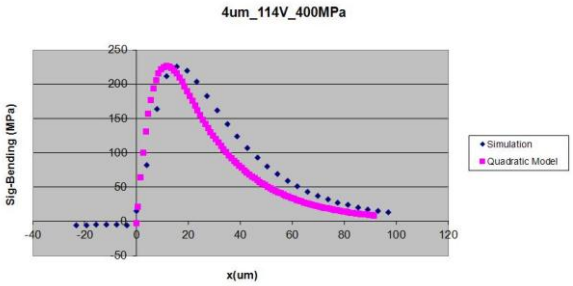

Fig. 7.4.5a. Bending Stresses Comparison, 4μm, Case 5

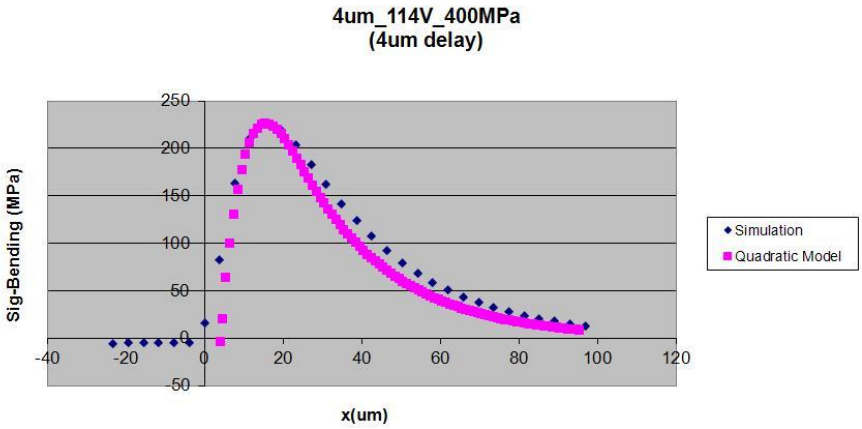

Fig. 7.4.5b. Bending Stresses Comparison, 4μm ,Case 5, using a 4μm offset.

Case 6 has a tension T= 864.4 N/m and an applied voltage V= 82 volts. For this case, the plate electrozips up the chamber wall, from the starting radius r=1000μm to the radius r=625.59μm at which point the plate breaks away from the chamber wall. The resulting analytically calculated bending stresses σ_B are compared against simulation values in Fig. 7.4.6a,b using the model of x_1 with factor 8.70. The quantities associated with the analytical calculation are given in Tables 7.4.6.

Table 7.4.6. 4μm Case 6, Quantities with $x_1 = \sqrt{8.70}/\sqrt{k}$

$1/\sqrt{k}$ (μm)	$f_1(0)$	$f_2(0)$ (μm)	$f_1(x_1)$	$f_2(x_1)$ (μm)
10.649	-102.611	2.10096	-69.5208	0
x_1 (μm)	$V(0)$ (N/m)	$M(0)$ (μN)	$V_1(x_1)$ (N/m)	$M_1(x_1)$ (μN)
31.5	-84.849	11.5023	111.1898	-861.915

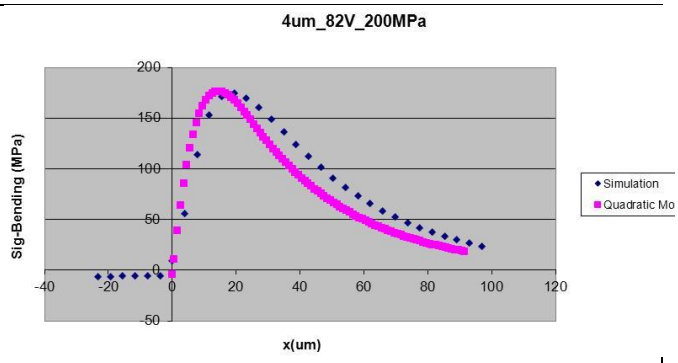

Fig. 7.4.6a. Bending Stresses Comparison, 4μm Case 6

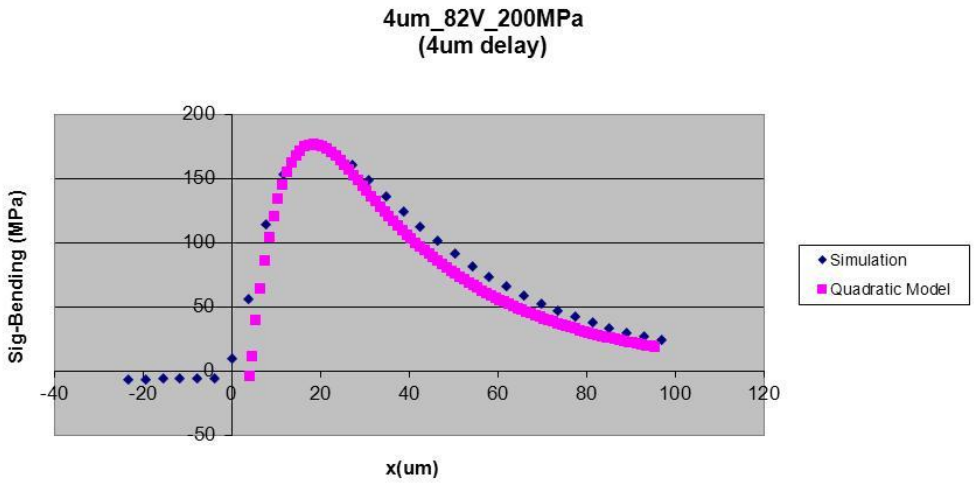

Fig. 7.4.6b. Bending Stresses Comparison, 4μm Case 6, , using a 4μm offset.

7.5 Comparison of Results for Plate Thickness 2 Microns

For the plate thickness $2\mu m$, we consider two (2) cases given in Table 7.5.1. The flexural rigidity for this plate thickness is D=0.1126 N-μm.

Table 7.5. Conditions for plate thickness t= $2\mu m$

Case	Plate Thickness t (μm)	Tension Stresses σT (MPa)	Tension T (N/m)	Voltage V (volts)	$\lambda = \sqrt{\frac{T}{D}}$ (1/μm)	Radius rϕ (μm)	$r_\phi\sqrt{\frac{T}{D}}$	Slope Angle ϕ (rad.)	$p_{e-\max}$ (MPa)
1	2	2416.3	4832.6	197	0.2071447	606.2	125.57	0.03067468	58.2818
2	2	217.21	434.42	58.5	0.0621067	602.33	37.41	0.03070429	5.1394

Case 1 has a tension T= 4,832.6 N/m and an applied voltage V= 197 volts. For this case, the plate electrozips up the chamber wall, from the starting radius r=1000μm to the radius r=606.2μm at which point the plate breaks away from the chamber wall. The resulting analytically calculated bending stresses σ_B are compared against simulation values in Fig. 7.5.1 using the model of x_1 with factor 8.70. The quantities associated with the analytical calculation are given in Tables 7.5.1.

Table 7.5.1 $2\mu m$ Case 1, Quantities with $x_1 = \sqrt{8.70}/\sqrt{k}$

$1/\sqrt{k}$ (μm)	$f_1(0)$	$f_2(0)$ (μm)	$f_1(x_1)$	$f_2(x_1)$ (μm)
4.131	-2.571	0.32368	-0.62862	0
x_1 (μm)	$V(0)$ (N/m)	$M(0)$ (μN)	$V_1(x_1)$ (N/m)	$M_1(x_1)$ (μN)
12	-138.63	0.79668	316.709	-860.47

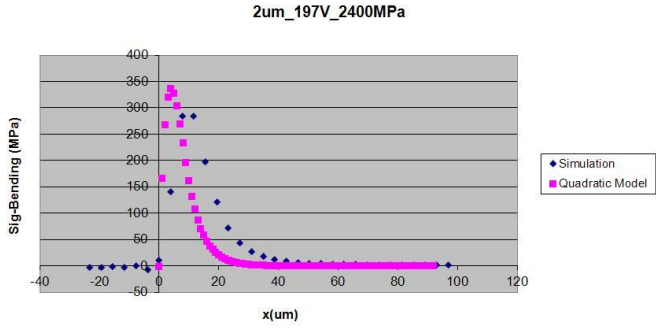

Fig. 7.5.1 Bending Stresses Comparison, $2\mu m$ Case 1

Case 2 has a tension T= 434.42 N/m and an applied voltage V= 58.5 volts. For this case, the plate electrozips up the chamber wall, from the starting radius r=1000μm to the radius r=602.33μm at which point the plate breaks away from the chamber wall. The resulting analytically calculated bending stresses σ_B are compared against simulation values in Fig. 7.5.2 using the model of x_1 with factor 8.70. The quantities associated with the analytical calculation are given in Tables 7.5.2.

Table 7.5.2. 2μm Case 2, Quantities with $x_1 = \sqrt{8.70}/\sqrt{k}$

$1/\sqrt{k}$ (μm)	$f_1(0)$	$f_2(0)$ (μm)	$f_1(x_1)$	$f_2(x$ (μm
7.531	-24.409	1.0713	-12.624	0
x_1 (μm)	$V(0)$ (N/m)	$M(0)$ (μN)	$V_1(x_1)$ (N/m)	$M_1(x$ (μN
22	-27.7067	0.6708	41.3675	-220.(

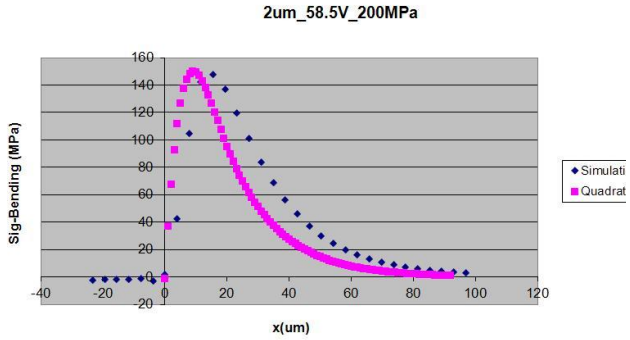

Fig. 7.5.2. Bending Stresses Comparison, 2μm Case 2

For case 1, the analytically calculated curve is plotted in Fig. 7.5.3a using a 5μm shift to the right. For case 2, the analytically calculated curve is plotted in Fig. 7.5.3b using a 5μm shift to the right. That is, the plots are also shifted 5μm to the right and then compared with simulated. From these plots, it is clear that a 5μm shift to right provides a better fit to that of the simulation.

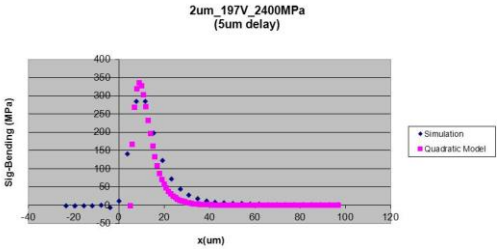

Fig. 7.5.3a. Bending Stresses Comparison, Case 1, with 5μm shift to the right.

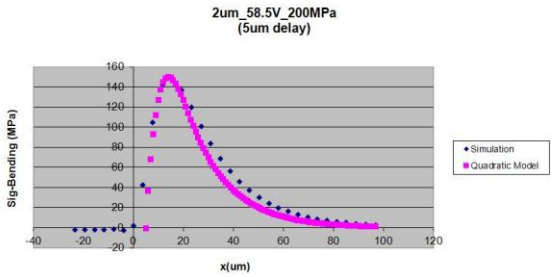

Fig. 7.5.3b. Bending Stresses Comparison, Case 2, with 5μm shift to the right.

7.6 Summary of Comparison Between Analytical and Simulation Results

The comparisons between the analytical method and the simulation was carried out over plate thicknesses 2, 4, 6, 8 and 10μm, tension stresses σ_T between 200 *MPa* and 2,400 *MPa*, and applied voltages between 50 and 200 volts. The results showed that the maximum bending stresses from simulation were computed within about 1% by the analytical method. This was achieved by using the model $x_1 = \sqrt{8.70}/\sqrt{k}$. The differences in the results were about 5% using the model $x_1 = \sqrt{8.22}/\sqrt{k}$ which was derived in Chapter 5. The results showed that there was a small offset between the two locations of the maximum bending stresses. For the thickness 8μm, the offset was 2μm; for the thickness 6μm, the offset was 3μm; for the thickness 4μm, the offset was 4μm; for the thickness 2μm, the offset was 5μm. One of the reason that the offset was necessary is that the simulation was carried out using a soft constraint boundary of several microns so that moving plate boundaries, moving fluids, and changing electrostatics could be accounted for in the simulation.

CHAPTER 8

ESTIMATING VOLTAGES AND BREAKAWAY POINTS FOR INTAKE POWER STROKE

In this chapter, the analytical model is used to estimate the required voltage needed in completely opening up the intake chamber. Simulations showed that as voltage was increased the plate electro-zipped up the side of the chamber wall, but, suddenly, at some breakaway point, the plate would electro-zip all the way open without an increase in voltage. This interesting phenomenon is investigated here in this chapter using the analytical model approach to help understand what the mechanism is that causes it.

8.1 Required Moment at Wall-Plate Junction

Consider the case where the plate has electro-zipped up the chamber wall and breaks away from the chamber wall at the radius r_ϕ, Fig. 5.3.1, in which ϕ is the slope at that point and is given by (5.3.14).

$$\phi = \frac{4\delta_{\max}}{a}\frac{r_\phi}{a}\left[1-\left(\frac{r_\phi}{a}\right)^2\right] \tag{8.1.1}$$

We determine the required moment M_R that is needed to hold the plate against the chamber wall. We can determine M_R as the sum of two components $M_{R-\phi}$ and $M_{R-\kappa}$.

$$M_R = M_{R-\phi} + M_{R-\kappa} \tag{8.1.2}$$

where $M_{R-\phi}$ is the required moment for the case that the chamber wall is assumed to have zero curvature at the radius r_ϕ and $M_{R-\kappa}$ is the additional moment needed to bend the plate from zero curvature into the actual curvature $\kappa = 1/\rho$ of the chamber wall at the radius r_ϕ. This concept is illustrated in Fig. 8.1.1. The couple $M_{R-\kappa}$ pictured on the left hand side of Fig. 8.1.1 generates the curvature of the chamber wall and the moment $M_{R-\phi}$ balances out the moment M(0) and the moment caused by the tension T shown on the right hand side of Fig. 8.1.1. Even though displaced in Fig. 8.1.1 for illustration purposes, the two moments $M_{R-\kappa}$ and $M_{R-\phi}$ occur at exactly the same radius r=-R and, therefore, add to generate the total moment effect that is required.

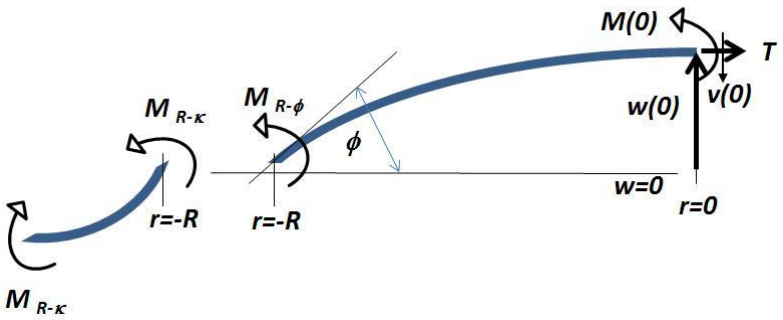

Fig. 8.1.1. Moments at Wall Plate Junction

The horizontal distance x_c from the radius r_ϕ to the center of the chamber is $x_c = r_\phi$. From (5.1.6), we see that for the case of a chamber wall with slope ϕ and zero curvature at the radius r_ϕ, the required moment $M_{R-\phi}$ at the wall-plate junction is given by

$$M_{R-\phi} = D\lambda\phi / \tanh\left(\lambda r_\phi\right) \tag{8.1.3}$$

In the case of the chamber geometry considered herein, the chamber wall has non-zero curvature. From (5.3.14), (5.3.15) and the definition of curvature, the curvature $\kappa = 1/\rho$ at the radius r_ϕ is given by

$$\kappa = \frac{1}{\rho} = \frac{\dfrac{d^2\delta(r_\phi)}{dr^2}}{\left[1+\phi^2\right]^{3/2}} = \frac{\dfrac{4\delta_{\max}}{a^2}\left[\dfrac{3r_\phi^2}{a^2}-1\right]}{\left[1+\phi^2\right]^{3/2}} \tag{8.1.4}$$

The required moment for creating pure curvature $\kappa = 1/\rho$ at the radius r_ϕ is given by

$$M_{R-\kappa} = D/\rho = D\frac{4\delta_{\max}}{a^2}\left[\frac{3r_\phi^2}{a^2}-1\right]/\left[1+\phi^2\right]^{3/2} \tag{8.1.5}$$

The required moment M_R can now be written as

$$M_R = D\lambda\phi/\tanh\left(\lambda r_\phi\right) + D\frac{4\delta_{\max}}{a^2}\left[\frac{3r_\phi^2}{a^2}-1\right]/\left[1+\phi^2\right]^{3/2} \tag{8.1.6}$$

The relationship between the required moment M_R and the required voltage V is given by (5.5.12) with x=0.

$$M_R = p_{e-\max}x_1^2/12 \tag{8.1.7}$$

where $p_{e-\max}$ is given by (5.4.6)

$$p_{e-\max} = \frac{0.5\varepsilon_0\varepsilon_a}{1+\alpha_0 gap}\left(\alpha_0 V\right)^2,\ \alpha_0 = \frac{\varepsilon_d}{\varepsilon_a d_0}; \tag{8.1.8}$$

where we use the value of x_1 is as indicated in the introduction of Chapter 7

$$x_1 = \sqrt{\frac{8.7}{k}} \tag{8.1.9}$$

and where k is given by (5.6.2a)

$$k = \phi \frac{\alpha_1 a}{2a^2} \left[\frac{\left[3R_\phi^2 - 1\right]}{R_\phi \left[1 - \left(R_\phi\right)^2\right]} + a\lambda \right] \tag{8.1.10}$$

The required voltage V can be determined from (8.1.8), making use of (8.1.6) and (8.1.7). By varying the radius r_ϕ toward the center of the chamber in (8.1.6), the breakaway radius r_ϕ is determined as that radius for which the required voltage V reaches a maximum value and then decreases thereafter.

8.2 Estimating Voltages and Breakaway Values for Plate Thickness 10 Microns

For the plate thickness $10\mu m$, we consider the four (4) cases given in Table 8.2.1. The plate thickness and the tension are the quantities used in estimating the maximum voltage needed to complete the full intake cycle (i.e., completely opening up the intake chamber) and the breakaway radius at which point the maximum voltage occurs. Applying the above equations of the analytical model, we obtain the results given in Table 8.2.1 and Fig.s. 8.2.1 – 8.2.4.

Table 8.2.1. Compare voltages and breakaway points for plate thickness $t = 10\mu m$

			Simulation		Analytical Model	
Case	Plate Thickness t (μm)	Tension T (N/m)	Max Voltage V (volts)	Breakaway Radius r_ϕ (μm)	Max Voltage V (volts)	Breakaway Radius r_ϕ (μm)
1	10	5136	199	668.2219	205	632
2	10	4142	179	672.1	190	639
3	10	3144	157	664.34	167	648
4	10	2147	130.8	668.2195	135	664

From Table 8.2.1, we see that the analytical model predicts values within about 5% of those from simulation.

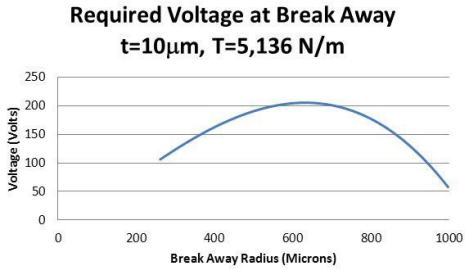

Fig. 8.2.1. Estimated max 205 volts, Case 1

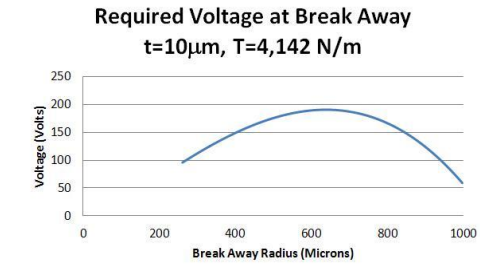

Fig. 8.2.2. Estimated max 190 volts, Case 2

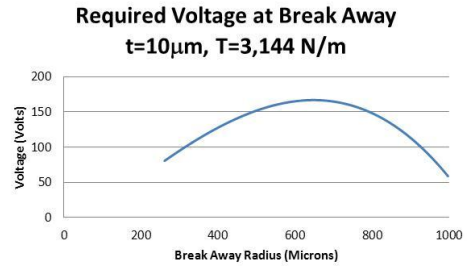

Fig. 8.2.3. Estimated max 167 volts, Case 3

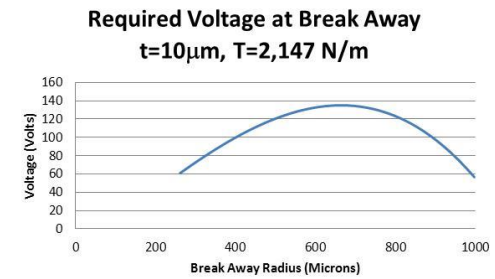

Fig. 8.2.4. Estimated max 135 volts, Case 4

8.3 Estimating Voltages and Breakaway Values for Plate Thickness 8 Microns

For the plate thickness 8μ*m*, we consider the three (3) cases given in Table 8.3.1. The plate thickness and the tension are the quantities used in estimating the maximum voltage needed to complete the full intake cycle (i.e., completely opening up the intake chamber) and the breakaway radius at which point the maximum voltage occurs. Applying the above equations of the analytical model from this chapter, we obtain the results given in Table 8.3.1 and Figs. 8.3.1 – 8.3.3.

Table 8.3.1. Compare voltages and breakaway points for plate thickness $t = 8\mu m$

			Simulation		Analytical Model	
Case	Plate Thickness t (μm)	Tension T (N/m)	Max Voltage V (volts)	Breakaway Radius r_ϕ (μm)	Max Voltage V (volts)	Breakaway Radius r_ϕ (μm)
1	8	4922.4	195	637.2	200	617
2	8	3323.2	160.5	641.1	165	626
3	8	1715.2	116	664.3	120	646

From Table 8.3.1, we see that the analytical model predicts values within about 4% of those from simulation.

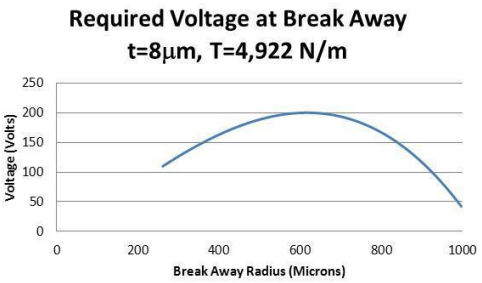

Fig. 8.3.1. Estimated max 200 volts, Case 1

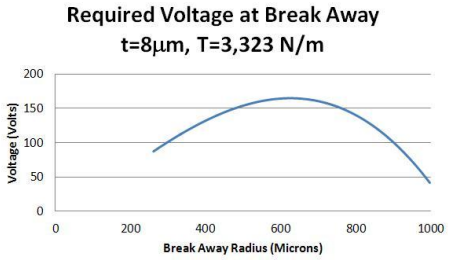

Fig. 8.3.2. Estimated max 165 volts, Case 2

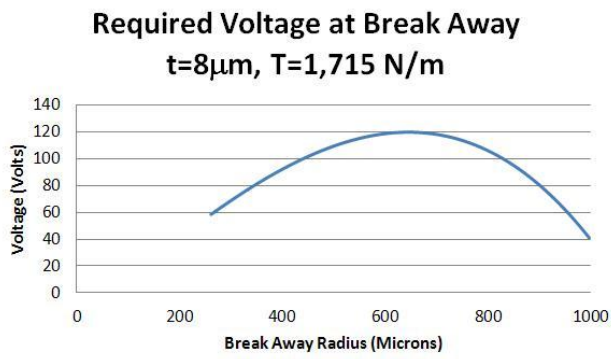

Fig. 8.3.3. Estimated max 120 volts, Case 3

8.4 Estimating Voltages and Breakaway Values for Plate Thickness 6 Microns

For the plate thickness 6μm, we consider the four (4) cases given in Table 8.4.1. The plate thickness and the tension are the quantities used in estimating the maximum voltage needed to complete the full intake cycle (i.e., completely opening up the intake chamber) and the breakaway radius at which point the maximum voltage occurs. Applying the above equations of the analytical model from this chapter, we obtain the results given in Table 8.4.1 and Fig.s. 8.4.1 – 8.4.4.

Table 8.4.1. Compare voltages and breakaway points for plate thickness $t= 6\mu m$

			Simulation		Analytical Model	
Case	Plate Thickness t (μm)	Tension T (N/m)	Max Voltage V (volts)	Breakaway Radius r_ϕ (μm)	Max Voltage V (volts)	Breakaway Radius r_ϕ (μm)
1	6	4899.6	195	614	199	603
2	6	3691.8	169	633.3	173	607
3	6	2487.6	139	633.3	142	613
4	6	1299	100.5	629.46	103	628

From Table 8.4.1, we see that the analytical model predicts values within about 4% of those from simulation.

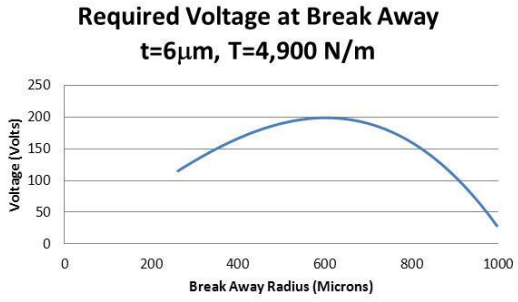

Fig. 8.4.1. Estimated max 199 volts, Case 1

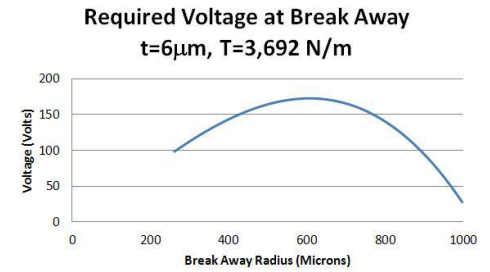

Fig. 8.4.2. Estimated max 173 volts, Case 2

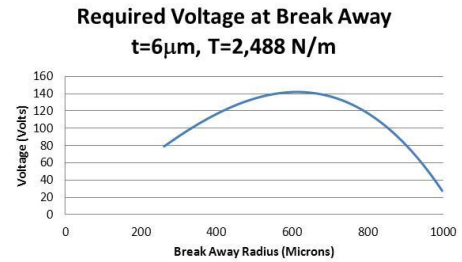

Fig. 8.4.3. Estimated max 142 volts, Case 3

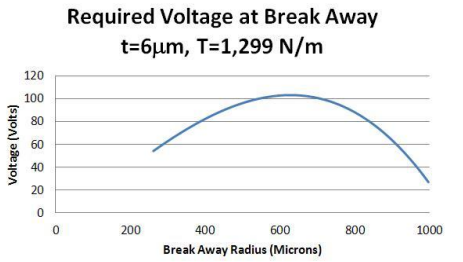

Fig. 8.4.4. Estimated max 103 volts, Case 4

8.5 Estimating Voltages and Breakaway Values for Plate Thickness 4 Microns

For the plate thickness $4\mu m$, we consider the six (6) cases given in Table 8.5.1. The plate thickness and the tension are the quantities used in estimating the maximum voltage needed to complete the full intake cycle (i.e., completely opening up the intake chamber) and the breakaway radius at which point the maximum voltage occurs. Applying the above equations of the analytical model from this chapter, we obtain the results given in Table 8.4.1 and Fig.s. 8.5.1 – 8.5.6.

Table 8.5.1. Compare voltages and breakaway points for plate thickness $t= 4\mu m$

			Simulation		Analytical Model	
Case	Plate Thickness t (μm)	Tension T (N/m)	Max Voltage V (volts)	Breakaway Radius r_ϕ (μm)	Max Voltage V (volts)	Breakaway Radius r_ϕ (μm)
1	4	4866.8	195.5	606.2	198	591
2	4	4064.8	178.5	614	181	592
3	4	3268.4	160	602.3	162	594
4	4	2462	138.5	625.6	141	597
5	4	1666.4	114	614	116	601
6	4	864.4	82	625.6	84	611

From Table 8.5.1, we see that the analytical model predicts values within about 3% of those from simulation.

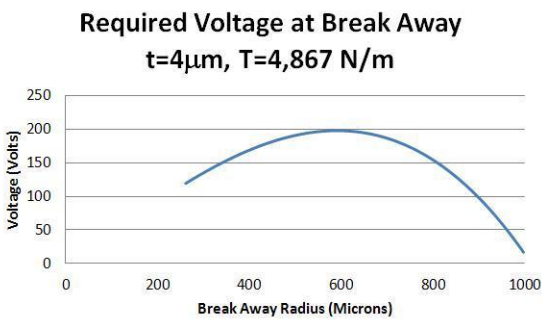

Fig. 8.5.1. Estimated max 198 volts, Case 1

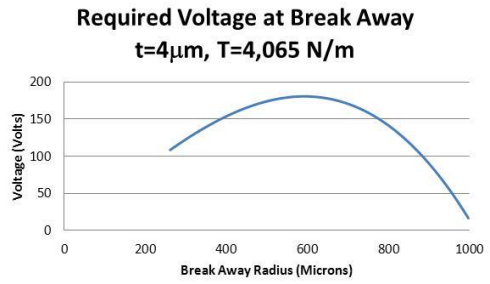

Fig. 8.5.2. Estimated max 181 volts, Case 2

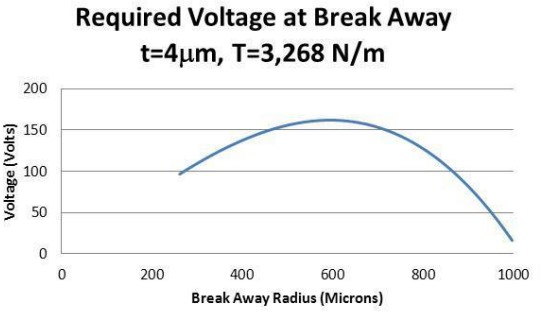

Fig. 8.5.3. Estimated max 162 volts, Case 3

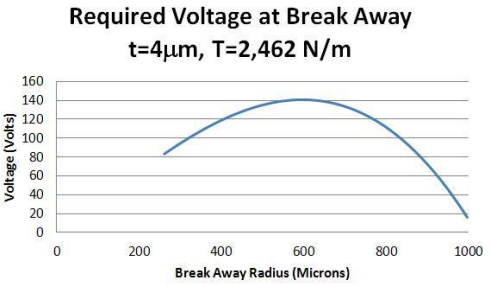

Fig. 8.5.4. Estimated max 141 volts, Case 4

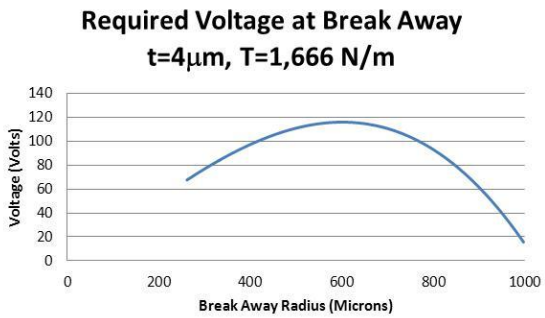

Fig. 8.5.5. Estimated max 116 volts, Case 5

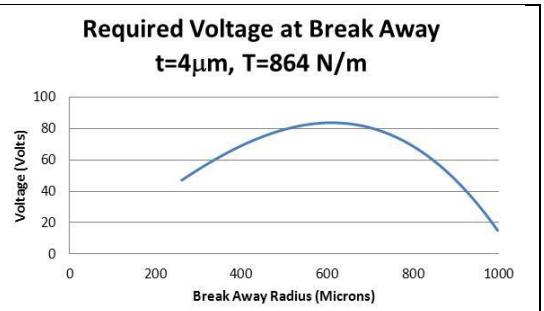

Fig. 8.5.6. Estimated max 84 volts, Case 6

8.6 Estimating Voltages and Breakaway Values for Plate Thickness 2 Microns

For the plate thickness $2\mu m$, we consider the two (2) cases given in Table 8.6.1. The plate thickness and the tension are the quantities used in estimating the maximum voltage needed to complete the full intake cycle (i.e., completely opening up the intake chamber) and the breakaway radius at which point the maximum voltage occurs. Applying the above equations of the analytical model from this chapter, we obtain the results given in Table 8.6.1 and Figs. 8.6.1 – 8.6.2.

Table 8.6.1. Compare voltages and breakaway points for plate thickness $t= 2\mu m$

			Simulation		Analytical Model	
Case	Plate Thickness t (μm)	Tension T (N/m)	Max Voltage V (volts)	Breakaway Radius r_ϕ (μm)	Max Voltage V (volts)	Breakaway Radius r_ϕ (μm)
1	2	4832.6	197	606.2	197	582
2	2	434.42	58.5	602.33	59	594

From Table 8.6.1, we see that the analytical model predicts values within about 2% of those from simulation.

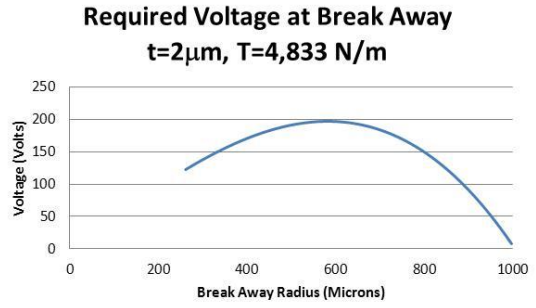

Fig. 8.6.1. Estimated max 197 volts, Case 1

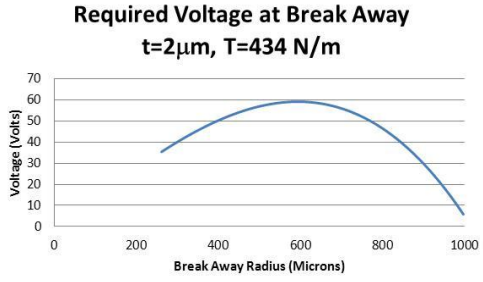

Fig. 8.6.2. Estimated max 59 volts, Case 2

8.7 Summary of Estimating Voltages and Breakaway Points

The analytical model approach was applied to plate thicknesses 2, 4, 6, 8, 10 μm and various tension stresses σ_T ranging between 200 MPa and 2,400 MPa, The analytical model estimated the maximum voltage needed to open up the intake chamber and it estimated the breakaway radius at which point the maximum voltage occurs. The estimates were within 5% in all cases considered. The analytical model approach confirmed the interesting phenomenon that was discovered in the simulations; that is, the voltage needed to electro-zip the plate up the chamber wall will increase up to a maximum value before the intake chamber is entirely open and then the voltage needed to continue electro-zipping the plate up the wall for the rest of the way will decrease until the intake chamber is completely open. The cause of this interesting phenomenon is due to the mechanism of required moments at the junction of the plate and the wall chamber. The required moment at a breakaway point is a function of the slope and the curvature of the chamber wall. The curvature starts out large and then decreases as the plate electro-zips up the chamber wall, and ends up being negative at the top. On the other hand, as the plate electro-zips up the chamber wall, the slope of the chamber wall increases up to a maximum value and then decreases to zero at the top. Since the require moment is a combination of these two effects, the net outcome is that the required moment reaches a maximum value before the slope reaches its maximum value. With the curvature starting out large and decreasing and with the slope starting out small and increasing, there is a tradeoff of the two effects that determine the point where the maximum moment occurs. The maximum voltage occurs at the point where the maximum moment occurs.

One of the reasons that the analytical modeling was undertaken in the first place was to help explain what was observed in the simulation work. The work in Chapters 5-8 was carried out for that reason. The simple models presented in these chapters have turned out to help explain the observed. For example, the simple models predict quite accurately (i.e., within 1-2%) the maximum bending stresses coming out of the simulations. They accurately predict within 5% the maximum voltages needed to completely open the intake chamber. And, furthermore, they accurately predict within 5% the radius at which the maximum voltage occurs that is needed to completely open the intake chamber.

CHAPTER 9

POWER STROKE ANALYSIS

9.1 Power Stroke Geometry

We consider the power stroke and let the variable x denote the distance from the side breakaway point (i.e., the point where the plate separates from the bottom electrode) as shown in Fig. 9.1.1.

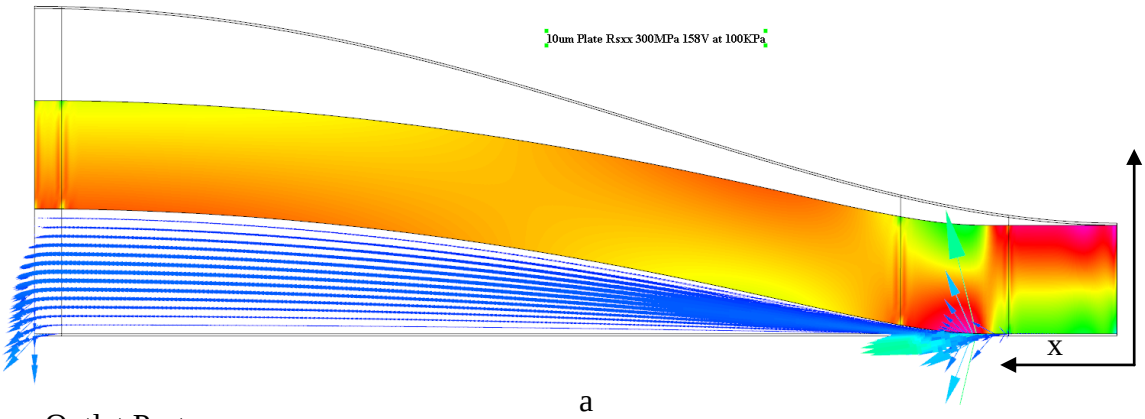

Fig. 9.1.1 Power Stroke Geometry of 2D Plate

We utilize the 4th order reduced von Kármán governing differential equations (6.1.1)

$$D\frac{d^4w}{dx^4} = T\frac{d^2w}{dx^2} + p_0 \tag{9.1.1}$$

where $w(x)$ is deflection respect to x, p_0 is the outlet pressure on the plate, T is the tension due to residual stresses in the plate, and D is the flexural rigidity of the plate.

The outlet pressure p_0 is assumed to be constant across the bottom surface of the plate. We let *M(x)* and *V(x)* be as defined in (6.1.2) and (6.1.3).

$$M(x) = D\frac{d^2w}{dx^2} \tag{9.1.2}$$

$$V(x) = \frac{dM(x)}{dx} = D\frac{d^3w}{dx^3} \tag{9.1.3}$$

We assume that the following boundary conditions hold at *x=0*:

$$\delta(0) \equiv w(0) = 0 \tag{9.1.4}$$

$$\theta(0) \equiv \frac{dw}{dx}(0) = 0 \tag{9.1.5}$$

Due to symmetry, we assume that the following boundary conditions hold at *x=a*:

$$V(a) = 0 \tag{9.1.6}$$

$$\theta(a) \equiv \frac{dw}{dx}(a) = 0 \tag{9.1.7}$$

$M(0)$ and *V(0)* satisfies (9.1.2) and (9.1.3) at the breakaway point *x=0*:

$$M(0) \equiv M_0 = D\frac{d^2w}{dx^2}(0) \tag{9.1.2}$$

$$V(0) \equiv V_0 = \frac{dM(0)}{dx} = D\frac{d^3w}{dx^3}(0) \tag{9.1.3}$$

9.2 Linear State Space Equation

Using definitions (9.1.2) and (9.1.3), we can rewrite (9.1.1) in the second order form

$$\frac{dM(x)}{dx} = V(x) \tag{9.2.1a}$$

$$\frac{dV(x)}{dx} = \lambda^2 M(x) + p_0 \tag{9.2.1b}$$

where

$$\lambda = \sqrt{\frac{T}{D}} \tag{9.2.2}$$

In state space matrix form, we can rewrite (9.2.1) as follows

$$\begin{bmatrix} \frac{dM(x)}{dx} \\ \frac{dV(x)}{dx} \end{bmatrix} = \lambda \begin{bmatrix} 0 & 1/\lambda \\ \lambda & 0 \end{bmatrix} \begin{bmatrix} M(x) \\ V(x) \end{bmatrix} + \begin{bmatrix} 0 \\ 1 \end{bmatrix} p_0 \tag{9.2.3}$$

By defining the state variable Z as the vector

$$Z = \begin{bmatrix} M(x) \\ V(x) \end{bmatrix} \tag{9.2.4}$$

Eq. (9.2.3) has the standard state space matric form which is linear in state Z and input p_0.

$$\frac{dZ}{dx} = \lambda AZ + Bp_0 \tag{9.2.5}$$

where

$$A = \begin{bmatrix} 0 & 1/\lambda \\ \lambda & 0 \end{bmatrix} \tag{9.2.6a}$$

$$B = \begin{bmatrix} 0 \\ 1 \end{bmatrix} \tag{9.2.6b}$$

9.3 Solution for the interval $0 \le x \le a$

The unique solution to (9.2.5) satisfies

$$e^{-A\lambda x} Z(x) = Z(0) + \int_0^x e^{-A\lambda \bar{x}} B p_0 d\bar{x}, 0 \le x \le a \tag{9.3.1}$$

Carrying out the integral on the second term, we get

$$e^{-A\lambda x} Z(x) = Z(0) + \frac{p_0}{\lambda^2}\left[I - e^{-A\lambda x} \right] \begin{bmatrix} 1 \\ 0 \end{bmatrix} \tag{9.3.2}$$

Which can also be written as

$$Z(x) = e^{A\lambda x} Z(0) + \frac{p_0}{\lambda^2}\left[e^{A\lambda x} - I \right] \begin{bmatrix} 1 \\ 0 \end{bmatrix} \tag{9.3.3}$$

Making use of (6.2.7a,b), we see that

$$\left[e^{A\lambda x} - I \right] \begin{bmatrix} 1 \\ 0 \end{bmatrix} = \begin{bmatrix} \cosh(\lambda x)\text{-}1 \\ \lambda \sinh(\lambda x) \end{bmatrix} \tag{9.3.4}$$

Using (9.3.4), (9.3.3) becomes

$$Z(x) = e^{A\lambda x} Z(0) + \frac{p_0}{\lambda^2} \begin{bmatrix} \cosh(\lambda x)\text{-}1 \\ \lambda \sinh(\lambda x) \end{bmatrix} \tag{9.3.5}$$

This can be rewitten as

$$\begin{bmatrix} M(x) \\ V(x) \end{bmatrix} = \begin{bmatrix} \cosh(\lambda x) & \frac{\sinh(\lambda x)}{\lambda} \\ \lambda \sinh(\lambda x) & \cosh(\lambda x) \end{bmatrix} \begin{bmatrix} M_0 \\ V_0 \end{bmatrix} + \frac{p_0}{\lambda^2} \begin{bmatrix} \cosh(\lambda x)\text{-}1 \\ \lambda \sinh(\lambda x) \end{bmatrix} \tag{9.3.6}$$

The matrix equation (9.3.6) yields the two scalar equations

$$M(x) = M_0 \cosh(\lambda x) + \frac{V_0}{\lambda} \sinh(\lambda x) + \frac{p_0}{\lambda^2} \left[\cosh(\lambda x)\text{-}1\right] \tag{9.3.7a}$$

$$V(x) = M_0 \lambda \sinh(\lambda x) + V_0 \cosh(\lambda x) + \frac{p_0}{\lambda^2} \lambda \sinh(\lambda x) \tag{9.3.7b}$$

Using *M(x)* from (9.3.7a) and the boundary condition (9.1.5), we integrate the following equation

$$D \frac{d\theta(x)}{dx} = M(x) \tag{9.3.8}$$

and obtain

$$D\theta(x) = M_0 \frac{\sinh(\lambda x)}{\lambda} + \frac{V_0}{\lambda^2} \left[\cosh(\lambda x)\text{-}1\right] + \frac{p_0}{\lambda^3} \left[\sinh(\lambda x)\text{-}\lambda x\right] \tag{9.3.8}$$

Using $\theta(x)$ from (9.3.8) and the boundary condition (9.1.4), we integrate the following equation

$$D \frac{d\delta(x)}{dx} = \theta(x) \tag{9.3.9}$$

and obtain

$$D\delta(x) = M_0 \frac{\left[\cosh(\lambda x)\text{-}1\right]}{\lambda^2} + \frac{V_0}{\lambda^3}\left[\sinh(\lambda x)\text{-}\lambda x\right] + \frac{p_0}{\lambda^4}\left[\cosh(\lambda x)\text{-}1\text{-}\frac{(\lambda x)^2}{2}\right]$$

(9.3.10)

Using boundary condition (9.1.7) in (9.3.8) gives

$$D\theta(a) = 0 = M_0 \frac{\sinh(\lambda a)}{\lambda} + \frac{V_0}{\lambda^2}\left[\cosh(\lambda a)\text{-}1\right] + \frac{p_0}{\lambda^3}\left[\sinh(\lambda a)\text{-}\lambda a\right] \qquad (9.3.11)$$

Using boundary condition (9.1.6) in (9.3.7b) yields

$$V(a) = 0 = M_0 \lambda \sinh(\lambda a) + V_0 \cosh(\lambda a) + \frac{p_0}{\lambda^2}\lambda \sinh(\lambda a) \qquad (9.3.12)$$

From (9.3.11) and (9.3.12), we obtain the initial values M_0 and V_0:

$$M_0 = \frac{p_0}{\lambda^2}\left[\frac{(\lambda a)\cosh(\lambda a)\text{-}\sinh(\lambda a)}{\sinh(\lambda a)}\right] = p_0 a^2\left[\frac{(\lambda a)\cosh(\lambda a)\text{-}\sinh(\lambda a)}{(\lambda a)^2 \sinh(\lambda a)}\right]$$

(9.3.13a)

$$V_0 = -p_0 a \qquad (9.3.13b)$$

By evaluating (9.3.10) at $x = a$, we obtain the maximum deflection $\delta_{\max}$

$$D\delta_{\max} = M_0 \frac{\left[\cosh(\lambda a)\text{-}1\right]}{\lambda^2} + \frac{V_0}{\lambda^3}\left[\sinh(\lambda a)\text{-}\lambda a\right] + \frac{p_0}{\lambda^4}\left[\cosh(\lambda a)\text{-}1\text{-}\frac{(\lambda a)^2}{2}\right]$$

(9.3.14)

For the special case that $\lambda = 0$ in (9.3.13a), it can be easily shown that M_0 has the special value $M_0(\lambda = 0) = \frac{p_0 a^2}{3}$ (9.3.15)

9.4 Deflection Approximation for Small *x*

The deflection $\delta(x)$, (9.3.10), can be written in the form of an infinite series as follows:

$$D\delta(x) = M_0\left[\frac{x^2}{2} + \lambda^2\frac{x^4}{24} + \bullet\bullet\bullet\right] + V_0\left[\frac{x^3}{6} + \lambda^2\frac{x^5}{120} + \bullet\bullet\bullet\right] + p_0\left[\frac{x^4}{24} + \lambda^2\frac{x^6}{720} + \bullet\bullet\bullet\right]$$

(9.4.1)

For the special case that $\lambda = 0$ and x=a in (9.4.1), it follows from (9.3.15) that $\delta(x = a)$ has the special value

$$\delta\left(x = 0 \text{ and } \lambda = 0\right) = \frac{p_0 a^4}{24D} \tag{9.4.2}$$

For x sufficiently small, (9.4.1) provides the following approximation for $\delta(x)$:

$$\Delta\delta(x) \cong \frac{M_0}{D}\frac{x^2}{2} \tag{9.4.3}$$

We consider the approximation for $\delta(x)$:

$$\Delta\delta(x) = k_0 x^2 \tag{9.4.4}$$

where

$$k_0 = \frac{M_0}{2D} \tag{9.4.5}$$

9.5 Electrostatic Distributive Force Model

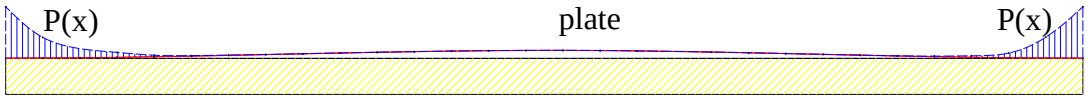

Fig.. 9.5.1. Electrostatic Distributive Force Model.

Recall the electrostatic distributive force model Eq. (5.4.5), Section 5.4 which we rewrite as follows:

$$p(x) = \frac{p_{e-\max}}{\left[1 + \frac{\alpha_0 \Delta\delta(x)}{1 + \alpha_0 gap}\right]^2} \tag{9.5.1}$$

where

$$p_{e-\max} = \frac{0.5\varepsilon_0 \varepsilon_a}{\left[1 + \alpha_0 gap\right]^2} (\alpha_0 V)^2 \tag{9.5.2}$$

$$\alpha_0 = \frac{\varepsilon_d}{\varepsilon_a d_0} \tag{9.5.3}$$

$$\alpha_1 = \frac{\alpha_0}{1 + \alpha_0 gap} \tag{9.5.3}$$

Using (9.5.3), (9.5.1) can be rewritten as

$$p(x) = \frac{p_{e-\max}}{\left[1 + \alpha_1 \Delta\delta(x)\right]^2} \tag{9.5.4}$$

Substituting (9.4.4) into (9.5.4) gives the electrostatic distributive force model for the power stroke, in its lowest order approximation, as a function of x^2 as follows.

$$p(x) = \frac{p_{e-\max}}{\left[1 + kx^2\right]^2} \tag{9.5.5}$$

where the constant k is defined as

$$k = \alpha_1 k_0 \tag{9.5.6}$$

where k_0 is defined by (9.4.5); that is,

$$k = \alpha_1 \frac{M_0}{2D} \tag{9.4.5}$$

where M_0 is defined by (9.3.13a)

9.6 Quadratic Approximation Model for Electrostatic Distributive Force

Similar to the development in Section 5.5, we consider a quadratic approximation model for the electrostatic distributive force so that it can be used in deriving closed form analytical solutions when it is used together with the 4th order differential equations such as the reduced Von Karman equation (5.1.2). For that purpose, we consider a similar quadratic model of the distributive forces acting on the plate at the floor junction during the power stroke:

$$p(x) = p_{e-\max}\left[1 - \frac{x}{x_1}\right]^2, \ 0 \le x \le x_1 \text{ and } p(x) = 0, \ x \ge x_1 \tag{9.6.1}$$

where the constant x_1 satisfies (5.5.15); that is,

$$x_1 = \sqrt{\frac{8.22}{k}} \tag{9.6.2}$$

As determined to be a better approximation in Chapter 7, we will use the approximation

$$x_1 = \sqrt{\frac{8.70}{k}} \tag{9.6.3}$$

where in the power stroke case of this chapter, k is given by (9.4.5).

9.7 Required Voltage Condition For Power Stroke

The condition for the required moment M_R is given by:

$$M_R = M_0 \quad (9.7.1)$$

where M_0 is given by (9.3.13a); that is,

$$M_0 = p_0 a^2 \left[\frac{(\lambda a)\cosh(\lambda a)\text{-}\sinh(\lambda a)}{(\lambda a)^2 \sinh(\lambda a)} \right] \quad (9.7.2a)$$

For λa larger than 2, M_0 can be approximated by

$$M_0 \cong p_0 a^2 \left[\frac{1}{\lambda a}\left(1 - \frac{1}{\lambda a}\right) \right], \text{ for } \lambda a \geq 2 \quad (9.7.2b)$$

The relationship between the required moment M_R and the required voltage V is given by (5.5.12) with *x=0*; that is,

$$M_0 = p_{e-\max} x_1^2 / 12 \quad (9.7.3)$$

The resulting condition for $p_{e-\max}$ satisfies

$$p_{e-\max} = M_0 \frac{12}{x_1^2} = M_0 \frac{12k}{8.70} = M_0 \frac{12\alpha_1 M_0}{8.70[2D]} = {M_0}^2 \frac{6}{8.70} \frac{\alpha_1}{D} \quad (9.7.4)$$

where

$$p_{e-\max} = \frac{0.5\varepsilon_0 \varepsilon_a}{[1 + \alpha_0 gap]^2} (\alpha_0 V_R)^2 = 0.5\varepsilon_0 \varepsilon_a {\alpha_1}^2 {V_R}^2 \quad (9.7.5)$$

Equating (9.7.4) and (9.7.5), the required voltage V_R is found to be given by

$$V_R^{\,2} = M_0^{\,2}\,\frac{12}{8.70\varepsilon_0\varepsilon_a\alpha_1 D} \tag{9.7.6}$$

$$V_R = |M_0|\sqrt{\frac{12}{8.70\varepsilon_0\varepsilon_a\alpha_1 D}} \tag{9.7.7}$$

where

$$M_0 = p_0 a^2\left[\frac{(\lambda a)\cosh(\lambda a)\text{-}\sinh(\lambda a)}{(\lambda a)^2\sinh(\lambda a)}\right] \tag{9.7.8a}$$

or, where the approximation holds

$$M_0 \cong p_0 a^2\left[\frac{1}{\lambda a}\left(1-\frac{1}{\lambda a}\right)\right],\ \text{for } \lambda a \geq 2 \tag{9.7.8b}$$

9.8 Outlet Pressure For Power Stroke Re Analytical Model

We consider the same conditions (e.g., applied voltage *V* and tension *T* loading) required in Ch. 8 to open the plate in the intake phase and compute the amount of differential pressure *p0* available in the power stroke phase to close the plate.

Table 9.10.1. Compare voltages and breakaway points for plate thickness *t= 10μm*

	Intake Conditions in Simulations				Analytical Model	
Case	Plate Thickness *t* (*μm*)	Tension *T* (*N/m*)	Residual Stress σ_T (MPa)	Pressure calculated (atm)	Applied Voltage *V* (volts)	Outlet Pressure p0 (atm)
1	10	5136	513.6	1.55	199	1.615
2	10	4142	414.2	1.30	179	1.31
3	10	3144	314.4	1.0	157	1.01
4	10	2147	214.7	0.70	131	0.71

Table 9.10.2. Compare voltages and breakaway points for plate thickness *t= 8μm*

	Intake Conditions in Simulations				Analytical Model	
Case	Plate Thickness *t* (*μm*)	Tension *T* (*N/m*)	Residual Stress σ_T (MPa)	Pressure calculated (atm)	Applied Voltage *V* (volts)	Outlet Pressure p0 (atm)
1	8	4922.4	615.3		195	1.526
2	8	3323.2	415.4		160.5	1.0413
3	8	1715.2	214.4		116	0.551

Table 9.10.3. Compare voltages and breakaway points for plate thickness *t= 6μm*

	Intake Conditions in Simulations				Analytical Model	
Case	Plate Thickness *t* (*μm*)	Tension *T* (*N/m*)	Residual Stress σ_T (MPa)	Pressure calculated (atm)	Applied Voltage *V* (volts)	Outlet Pressure p0 (atm)
1	6	4899.6	816.6		195	1.502
2	6	3691.8	615.3		169	1.134
3	6	2487.6	414.6		139	0.771
4	6	1299	216.5		100.5	0.4084

Table 9.10.4. Compare voltages and breakaway points for plate thickness $t = 4\mu m$

	Intake Conditions in Simulations				Analytical Model	
Case	Plate Thickness t (μm)	Tension T (N/m)	Residual Stress σ_T (MPa)	Pressure calculated (atm)	Applied Voltage V (volts)	Outlet Pressure p0 (atm)
1	4	4866.8	1216.7		195.5	1.4836
2	4	4064.8	1016.2		178.5	1.2396
3	4	3268.4	817.1		160	0.9981
4	4	2462	615.5		138.5	0.7518
5	4	1666.4	416.6		114	0.5112
6	4	864.4	216.1		82	0.2673

Table 9.10.5. Compare voltages and breakaway points for plate thickness $t = 2\mu m$

	Intake Conditions in Simulations				Analytical Model	
Case	Plate Thickness t (μm)	Tension T (N/m)	Residual Stress σ_T (MPa)	Pressure calculated (atm)	Applied Voltage V (volts)	Outlet Pressure p0 (atm)
1	2	4832.6	2416.3		197	1.4766
2	2	434.42	217.21		58.5	0.133

The multiphysics simulation results for the plate of 10μ*m* the case 1, 2 , 3 and 4 are presented en Fig.s 9.8.1 , Fig. 9.8.2, Fig. 9.8.3, and Fig. 9.8.4througth for Simulation result.

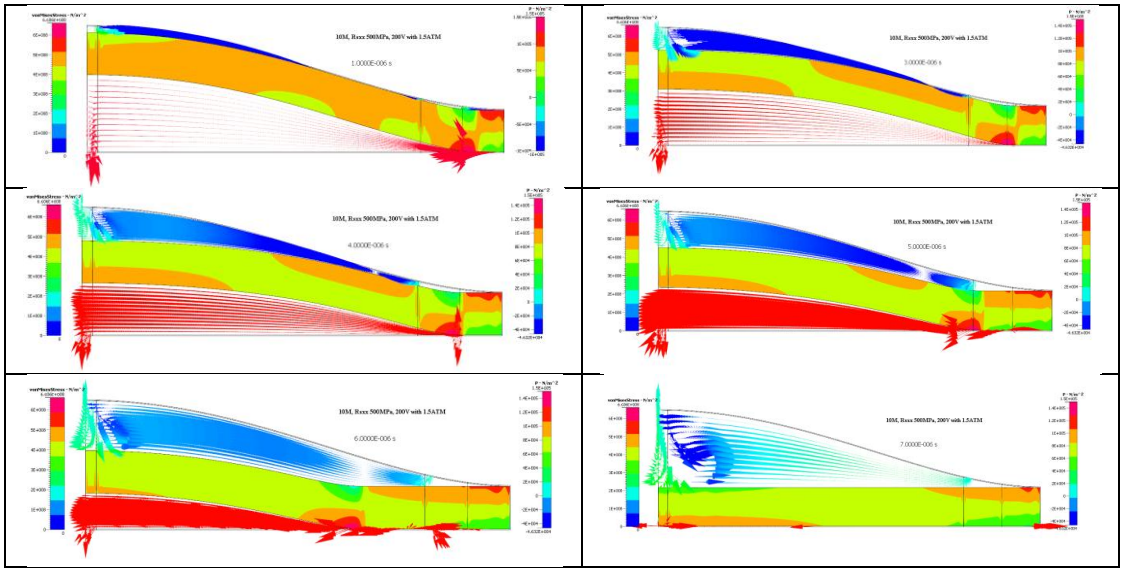

Fig. 9.8.1 Transient closing power stroke with 10μ*m* case 1: 200V, Rsxx500MPA, 1.5 ATM

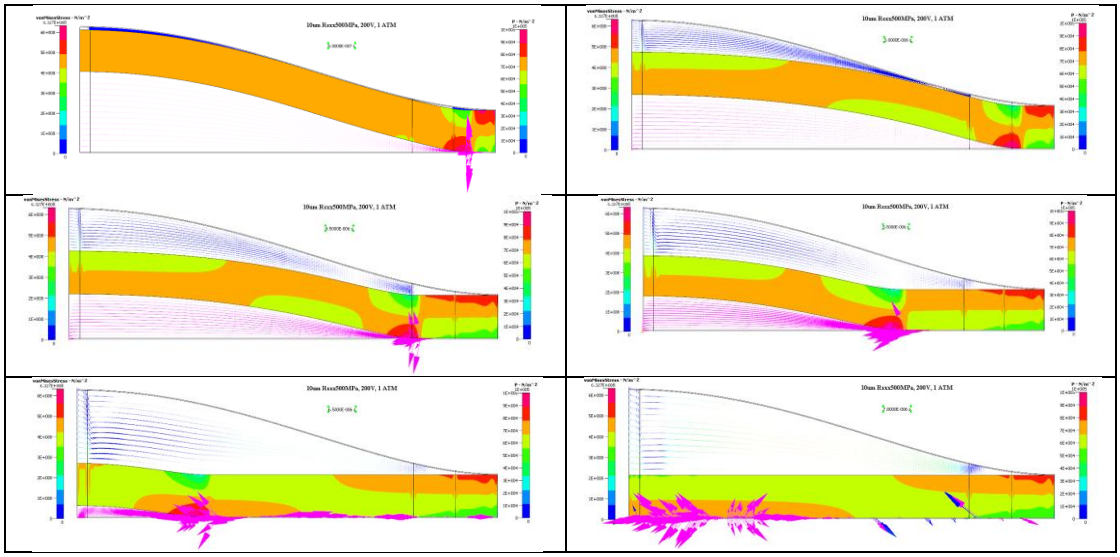

Fig. 9.8.2 Transient closing power stroke with 10μ*m* case 1*: 200V, Rsxx500MPA, 1 ATM.

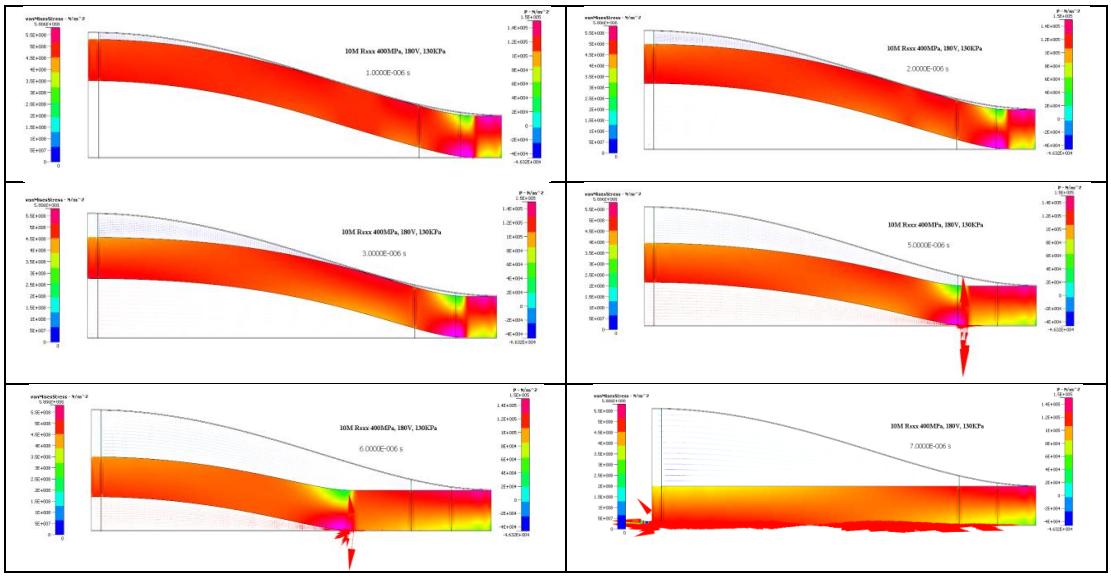

Fig. 9.8.3 Transient closing power stroke with 10μ*m* case 2: 180V, Rsxx400MPA, 1.3 ATM.

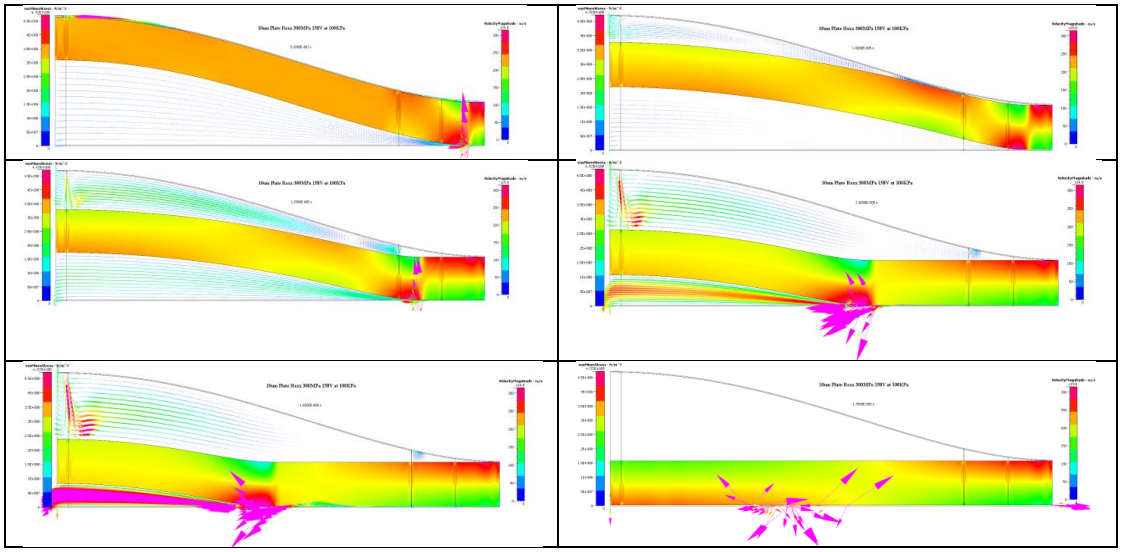

Fig. 9.8.4 Transient closing power stroke with 10μ*m* case 3: 158V, Rsxx300MPA, 1 ATM.

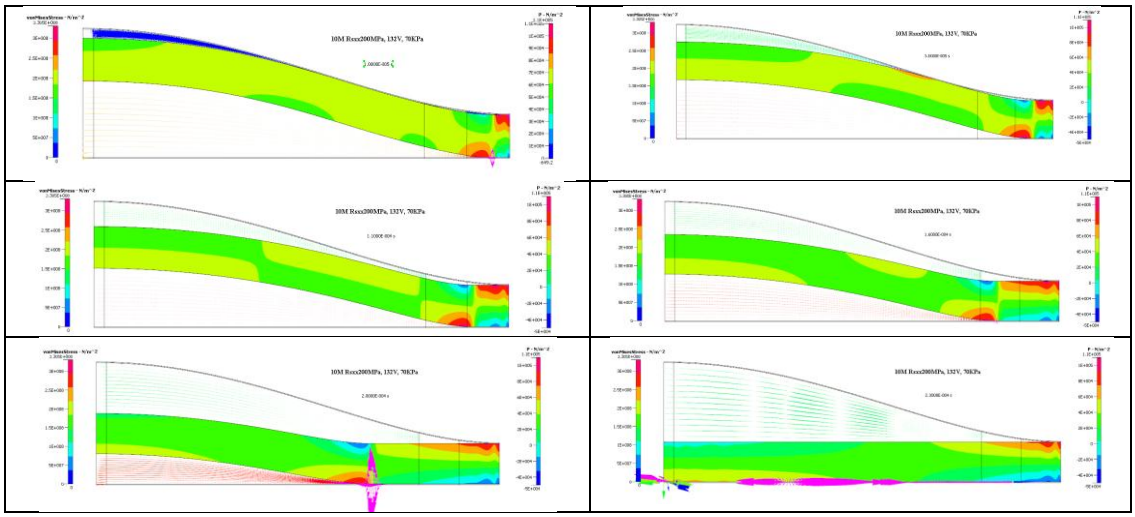

Fig. 9.8.5 Transient closing power stroke with 10μ*m* case 3: 132V, Rsxx200MPA, 0.7 ATM

CHAPTER 10

MICROPUMP DESIGN BEYOND THE BASELINE

The baseline design parameters, Table 10.0.1, has been utilized in the previous chapters to determine performance characteristics of our micropump concept. Complex multiphysics simulations have been run for the intake and power strokes. Furthermore, analytical models have been derived for the intake and power strokes. The results presented in Chapters 7, 8, and 9 show that the analytical models provide satisfactory comparable results with those from the multiphysics simulation. The satisfactory comparison has increased the confidence in the use of the analytical models. As a consequence, we use the analytical models, in this chapter, to explore the performance characteristics of our micropump concept beyond the baseline design parameters. For example, it is shown in Section 9.10 that the baseline design achieves an outlet differential pressure of 1.6 atm. One question is the following. What would the design parameters look like to achieve a greater differential pressure? The development in this chapter answers this question and others like it.

Table 10.0.1 Baseline Micropump Design Parameters

Plate Radius	a	1000	um
Chamber Height	δmax	20	um
Plate Thickness	t	10	um
Young's Modulus	E	1.60e11	N/m^2
Poisson's Ratio	υ	0.23	
Permittivity	ε_0	8.85e-12	F/m
Dielectric Permittivity	ε_d	3.9	
Air Permittivity	ε_{air}	1	
Max Residual Stresses	σ_T	500+	MPa
Ultimate Strength, Poly	σ_u	1550	MPa
Applied Voltage	V	200	volts
Dielectric Thickness	d_0	200	nm
Simulation Gap	gap	3	nm

10.1 Intake Analytical Model

From intake analytical equations (8.0.7) to (8.0.10), we can derive the following relationships.

$$p_{e-\max} = \frac{12ka^2}{8.7a^2}\left[\frac{D}{a}\right]\left[\frac{a\lambda\phi}{\tanh\left(a\lambda r_\phi / a\right)} + \frac{4\delta_{\max}}{a}\left[\frac{3r_\phi^2}{a^2} - 1\right]\left[\frac{1}{\left[1+\phi^2\right]^{3/2}}\right]\right] \tag{10.1.1}$$

$$p_{e-\max} = \frac{6}{8.7}\phi\alpha_1 a\left[\frac{D}{a^3}\right]\left[a\lambda + \frac{\left[3R_\phi^2 - 1\right]}{R_\phi\left[1-\left(R_\phi\right)^2\right]}\right]\left[\frac{a\lambda\phi}{\tanh\left(a\lambda R_\phi\right)} + \frac{4\delta_{\max}}{a}\left[\frac{\left[3R_\phi^2 - 1\right]}{\left[1+\phi^2\right]^{3/2}}\right]\right]$$

(10.1.2)

$$p_{e-\max} = \frac{6\alpha_1 a\phi^2}{8.7\tanh\left(a\lambda R_\phi\right)}\left(a\lambda\right)^2\left[\frac{D}{a^3}\right]\left[1+Term1\right]\left[1+Term2\right] \tag{10.1.3}$$

where

$$Term1 = \frac{\left[3R_\phi^2 - 1\right]}{a\lambda R_\phi\left[1-\left(R_\phi\right)^2\right]} \tag{10.1.4}$$

$$Term2 = \frac{\tanh\left(a\lambda R_\phi\right)4\delta_{\max}}{a\lambda a}\left[\frac{\left[3R_\phi^2 - 1\right]}{\left[1+\phi^2\right]^{3/2}}\right] \tag{10.1.5}$$

It can be shown that the terms Term1 and Term2 in the brackets of (10.1.3) are small compared to unity. That is, the following is a good approximation.

$$p_{e-\max} \cong \frac{6\phi^2\alpha_1 a}{8.7\tanh\left(a\lambda R_\phi\right)}\left(a\lambda\right)^2\left[\frac{D}{a^3}\right] \tag{10.1.6}$$

Since

$$\left(a\lambda\right)^2\left[\frac{D}{a^3}\right]=\sigma_T\,\frac{t}{a} \tag{10.1.7}$$

(10.1.6) becomes

$$p_{e-\max}\cong\frac{6\phi^2\sigma_T\alpha_1 a}{8.7\tanh\left(a\lambda R_\phi\right)}\frac{t}{a} \tag{10.1.8}$$

The worst case for the plate opening on intake is near the point where the tangent angle is at its maximum value. That is,

$$\phi\cong\phi_{\max}=\frac{8}{9}\sqrt{3}\,\frac{\delta_{\max}}{a} \tag{10.1.9}$$

The point where the tangent angle is at its maximum value has R_ϕ=0.577.

We substitute (10.1.9) into (10.1.8) and obtain

$$p_{e-\max}\cong\frac{6}{8.7}\left[\frac{64}{27}\right]\left[\frac{\delta_{\max}}{a}\right]^2\sigma_T\,\frac{t}{a}\,\alpha_1 a\left[\frac{1}{\tanh\left(a\lambda R_\phi\right)}\right] \tag{10.1.10}$$

or, equivalently,

$$p_{e-\max}\cong\left[\frac{128}{78.3}\right]\left[\frac{\delta_{\max}}{a}\right]^2\sigma_T\alpha_1 t\left[\frac{1}{\tanh\left(a\lambda R_\phi\right)}\right] \tag{10.1.11}$$

Recall that

$$p_{e-\max}=0.5\varepsilon_0\varepsilon_a\left(\alpha_1 V\right)^2,\ \text{where}\ \alpha_1=\frac{\alpha_0}{1+\alpha_0 gap}\ \text{and}\ \alpha_0=\frac{\varepsilon_d}{\varepsilon_a d_0} \tag{10.1.12}$$

For the purpose of exposing important ratios, we make the following definitions.

$$\alpha_0^*=\frac{\varepsilon_d}{\varepsilon_a} \tag{10.1.13}$$

$$\alpha_1^* = \frac{\alpha_0^*}{1 + \alpha_0^* \frac{gap}{d_0}} \tag{10.1.14}$$

Using the above definitions, (10.1.11) and (10.1.12) become

$$p_{e-\max} \cong \sigma_T \left(\frac{6}{8.7}\right)\left(\frac{64}{27}\right)\left[\left(\frac{\delta_{\max}}{a}\right)\left(\frac{t}{a}\right)\right]\left(\frac{\delta_{\max}}{d_0}\right)\left[\frac{\alpha_1^*}{\tanh\left(a\lambda R_\phi\right)}\right] \tag{10.1.15}$$

$$p_{e-\max} = 0.5\varepsilon_0\varepsilon_a\left(\alpha_1^*\right)^2\left(\frac{V}{d_0}\right)^2 \tag{10.1.16}$$

Recall the following definition; it exposes the ratio (*a/t*).

$$a\lambda = \sqrt{a^2\frac{T}{D}} = \left(\frac{a}{t}\right)\sqrt{12\left(1-\nu^2\right)}\sqrt{\frac{\sigma_T}{E}} \tag{10.1.17}$$

The intake equations (10.1.15), (10.1.17) are embedded with the three design ratios listed in Table 10.1.1. In addition, the ratio of the applied voltage to the dielectric thickness (i.e., V/d_0) is limited by the dielectric breakdown limit of 1 volt per nm. Furthermore, the residual stress parameter σ_T has a maximum value limited by yield stress (e.g., 500 to 600 MPa).

Table 10.1.1. Design ratios embedded in the Intake Stroke Equations

Description		Baseline Ratio
Chamber Height/ Plate Radius	$\delta max/a$	0.02
Dielectric Thickness / Chamber Height	$d_0/\delta max$	0.01
Plate Thickness/ Plate Radius	t/a	0.01

10.2 Power Stroke Analytical Model

From power stroke analytical equations (9.7.2b) and (9.7.4), we can derive the following relationship.

$$p_{e-\max} = [p_0]^2 \frac{6}{8.70} \frac{(\alpha_1 a) a^3}{(a\lambda)^2 D} \left(1 - \frac{1}{\lambda a}\right)^2 \tag{10.2.1}$$

Using (10.1.7), (10.1.13), and (10.1.14), Eq. (10.2.1) can be rewritten as

$$p_{e-\max} = \frac{[p_0]^2}{\sigma_T} \frac{6}{8.70} \left(\frac{a}{d_0}\right)\left(\frac{a}{t}\right) \alpha_1^* \left(1 - \frac{1}{\lambda a}\right)^2 \tag{10.2.2}$$

The power stroke equation (10.2.2) is embedded with the two design ratios listed in Table 10.2.1. In addition, the ratio of the applied voltage to the dielectric thickness (i.e., V/d_0) is limited by the dielectric breakdown limit of 1 volt per nm. Furthermore, the residual stress parameter σ_T has a maximum value limited by yield stress (e.g., 500 to 600 MPa).

Table 10.2.1. Design ratios embedded in the power stroke equations

Description		Baseline Ratio
Dielectric Thickness / Plate Radius	d_0/a	0.0002
Plate Thickness/ Plate Radius	t/a	0.01

10.3 Equal Voltages in Intake and Power Strokes

Consider the design objective to maximize the differential pressure on the outlet pressure stroke. This requires that the residual stresses σ_T in the plate and the applied voltage V be at maximum values. It turns out that the maximum thickness of the plate

is determined by those maximum values. For the purpose of illustration, let us assume that the maximum residual stresses σ_T allowed in the plate is 500 MPa and that the maximum allowed voltage is 1 volt per nm of dielectric thickness d_0. For a dielectric thickness d_0 = 200 nm, the maximum allowable voltage would be V=200 volts. During the intake stroke, the maximum allowable voltage V must be able to operate the plate under the condition of maximum residual stresses σ_T == 500 MPa. The results in Table 8.2.1 show that 199 volts are sufficient to perform the intake stroke with a plate thickness of 10 microns and residual stresses of 513.6 MPa. As shown in Table 9.10.1, 1.55 atm differential pressure is achievable at the outlet by operating with 200 volts in the power stroke with 513.6 MPa residual stresses and a 10 micron plate thickness. That is, the 1.55 atm differential pressure is achieved by using equal voltages for both the intake and the power strokes and by using a 10 micron plate thickness along with the 513.6 MPa residual stresses.

Consider the case of applying the same voltage for the intake and the power strokes. Equating (10.1.15) with (10.2.2), we obtain the following equation for p_0.

$$p_0 = \sigma_T \left(\frac{64}{27}\right)\left[\left(\frac{\delta_{\max}}{a}\right)\left(\frac{t}{a}\right)\right]\left[\frac{1}{\sqrt{\tanh\left(a\lambda R_\phi\right)}}\right]\left[\frac{1}{\left(1-\frac{1}{\lambda a}\right)}\right] \tag{10.3.1}$$

Consider the design problem of doubling the differential pressure p_0 by changing the design parameters from their baseline values. From (10.3.1) we see that doubling the differential pressure p_0 requires that the following new ratios be double their baseline ratios as given by the following equation.

$$\left[\left(\frac{\delta_{\max}}{a}\right)\left(\frac{t}{a}\right)\right]_{New} = 2\left[\left(\frac{\delta_{\max}}{a}\right)\left(\frac{t}{a}\right)\right]_{baseline} \tag{10.3.2}$$

One way to achieve the doubling in (10.3.2) is to double the plate thickness t over its baseline value and hold the other design parameters a and δmax to their baseline values. [An alternate way to achieve the doubling in (10.3.2) is to reduce both a and δmax to half of their baseline values while holding the plate thickness t at its baseline value.] From (10.1.15) we see that doubling the ratio factors given in (10.3.2) requires that the following new ratio be doubled over that of the baseline ratio.

$$\left[\frac{d_0}{\delta_{\max}}\right]_{New} = 2\left[\frac{d_0}{\delta_{\max}}\right]_{baseline} \tag{10.3.3}$$

One way to achieve the doubling in (10.3.3) is to double the dielectric thickness d_0 over its baseline value and hold δmax to its baseline value. [The alternate way of reducing δmax to half its baseline value while holding the dielectric thickness d_0 to its baseline value would achieve the doubling in (10.3.3) as well]

From the above analysis, we see that the differential pressure p_0 can be doubled over that which is achievable by the baseline design by doubling the dielectric thickness d_0 and the plate thickness t over their baseline values while holding the other design parameters a and δmax to their baseline values. That is, the dielectric thickness d_0 would be doubled from 200 nm to 400 nm and the plate thickness t would be doubled from 10 um to 20 um. We note that doubling the dielectric thickness d_0 requires doubling the applied voltage V at the same time so that the ratio V/d_0 remains constant. That is, doubling the dielectric thickness d_0 from 200 nm to 400 nm requires doubling the applied voltage V from 200 volts to 400 volts. Consequently, the required power

would double in order to double the differential pressure; the flow rate would be the same as in the baseline design. From Table 9.10.1 for the residual stress case σ_T =513.6 MPa, we see that the outlet pressure would be doubled from 1.55 atm to over 3 atm by doubling the dielectric thickness, the plate thickness, and the applied voltage. [Using the alternate way, the differential pressure p_0 can be doubled over that which is achievable by the baseline design by halving both the plate radius a and the plate height δmax relative to their baseline values while holding the other design parameters dielectric thickness d_0 and plate thickness t to their baseline values. Using the alternate way, the applied voltage V would remain at 200 volts; that is, the power requirements would remain the same as in the baseline design. The outlet pressure would be doubled, but the flow rate would be cut in half. That is, from Table 9.10.1 for the residual stress case σ_T =513.6 MPa, we see that the outlet pressure would be doubled from 1.55 atm to over 3 atm by halving both the plate radius a and the plate height δmax relative to their baseline values. The other design parameters dielectric thickness d_0, plate thickness t, and applied voltage V would remain at their baseline values (i.e., d_0=200 nm, t=10 microns, and V=200 volts).

CHAPTER 11

VACUUM PUMP DESIGN

The results of chapters 8 and 9 show that our micropump design with the baseline parameters can achieve differential pressures greater than 1.5 atm, notably with a 10 micron plate thickness. Consequently, it has the potential to pump vacuum pressure levels from the inlet side against 1.0 atm pressures at the outlet side. In this chapter, we examine that potential. Throughout this chapter, we assume micropump design parameters are being used that provide differential pressures greater than 1.5 atm. The following set of baseline design parameters is one such example.

Table 11.1 Baseline Micropump Design Parameters

Plate Radius	a	1000	um
Chamber Height	δmax	20	um
Plate Thickness	t	10	um
Young's Modulus	E	1.60e11	N/m^2
Poisson's Ratio	υ	0.23	
Permittivity	ε_0	8.85e-12	F/m
Dielectric Permittivity	ε_d	3.9	
Air Permittivity	ε_{air}	1	
Max Residual Stresses	σ_T	500+	MPa
Ultimate Strength, Poly	σ_u	1550	MPa
Applied Voltage	V	200	volts
Dielectric Thickness	d_0	200	nm
Simulation Gap	gap	3	nm

At the end of the power stroke, with the plate electro-zipped tightly against the bottom of the chamber, molecules are flowing through the roughness topography between the plate and the bottom of the chamber. That is, molecules leak back into the dead volume of the roughness topography between the plate and the bottom of the pump chamber. The molecules are always there and they are always flowing back into the vacuum

reservoir at rates that require some form of pumping mechanism to maintain required vacuum levels. Such leak rates are considered in this chapter. Roughness slit heights of 1 nm, $\sqrt{10}$ *nm* and 10 nm are considered in the leak rate feedback calculations.

In a vacuum pump design, the volume of the sensor vacuum reservoir plus all volumes connected to the sensor vacuum reservoir before the start of the intake stroke must be pumped down. Before the start of the intake stroke and at the end of the power stroke, the plate is flat against the floor of the chamber. The volume above the plate which is flat against the floor is the entire volume in the chamber; it is referred to as the chamber volume. We denote the entire volume of the chamber as V_P. Note that the volume above the plate is connected to the sensor vacuum reservoir whose volume is designated below as V_S. It is the pressure in the volume $V_P + V_S$ that must be pumped down in a vacuum pump application. At the start of the pump down, the volume $V_P + V_S$ is at an initial pressure P_0. At the end of the pump down, the pressure in the volume $V_P + V_S$ is required to be at or below a designed final pressure P_F. The intake volume V_I of the micropump is the volume available for pumping down the pressure in the volume $V_P + V_S$. These volumes are calculated in the next section. Afterwards, it is determined how much the pressure in the sensor reservoir decreases over one pump cycle of the intake plus the pressure stroke. An example is given of the number of cycles required to pump the pressure in the sensor chamber down from 760 Torr to a vacuum pressure of 10^{-6} Torr. The number of molecules pumped out in one cycle is calculated. Leak back rates through the pump are also determined using roughness slits of 1 nm, $\sqrt{10}$ nm and 10 nm. The pump cycle frequency needed to counter act leak back rates is computed for several vacuum pressure cases.

11.1 Chamber Volumes

We consider the vacuum pump aspect of our design. The footprint of the intake chamber, Fig. 11.1.1, has an intake volume that can be approximated with the sum of two volumes, V_1 and V_2. The volume V_1 has a circular footprint of radius a and the volume V_2 has a rectangular footprint with sides $2a$ and $20a$.

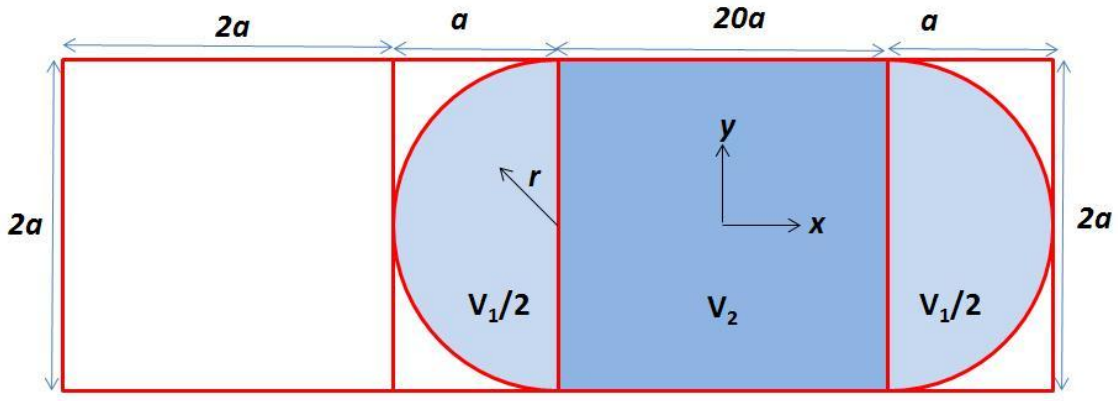

Fig. 11.1.1 Intake Chamber dimensions

The height of the chamber over the circular footprint depends on the radius r and is given by

$$\delta(r) = \delta_{\max}\left[1-\left(\frac{r}{a}\right)^2\right]^2, \quad -a \le r \le a \tag{11.1.1}$$

The volume V_1 is determined by the integral

$$V_1 = \int_0^{2\pi} \int_0^a \delta_{\max} \left[1 - \left(\frac{r}{a} \right)^2 \right]^2 r dr d\theta \tag{11.1.2}$$

$$V_1 = 2\pi \delta_{\max} \int_0^a \left[1 - \left(\frac{r}{a} \right)^2 \right]^2 r dr \tag{11.1.3}$$

Using the integration variable $z=(r/a)^2$, (11.1.3) can be rewritten as

$$V_1 = \pi a^2 \delta_{\max} \int_0^1 \left[1 - z \right]^2 dz \tag{11.1.4}$$

Carrying out the integral, we have

$$V_1 = \frac{\pi a^2 \delta_{\max}}{3} \tag{11.1.5}$$

The height of the chamber over the square footprint depends on *y* only and is given by

$$\delta(y) = \delta_{\max} \left[1 - \left(\frac{y}{a} \right)^2 \right]^2, \quad -a \le y \le a \tag{11.1.6}$$

The volume V_2 is determined by the integral

$$V_2 = 40a \int_0^a \delta_{\max} \left[1 - \left(\frac{y}{a} \right)^2 \right]^2 dy \tag{11.1.7}$$

Using the integration variable $z=(y/a)$, (11.1.7) can be rewritten as

$$V_2 = 40a^2 \delta_{\max} \int_0^1 \left[1 - z^2 \right]^2 dz \tag{11.1.8}$$

Carrying out the integral, we have

$$V_2 = \frac{320a^2\delta_{\max}}{15} \tag{11.1.9}$$

The volume of the intake chamber is approximated by the sum of volumes V_1 and V_2, and is given by

$$V_{\mathrm{I}} \cong V_1 + V_2 = \frac{(320+5\pi)a^2\delta_{\max}}{15} \tag{11.1.10}$$

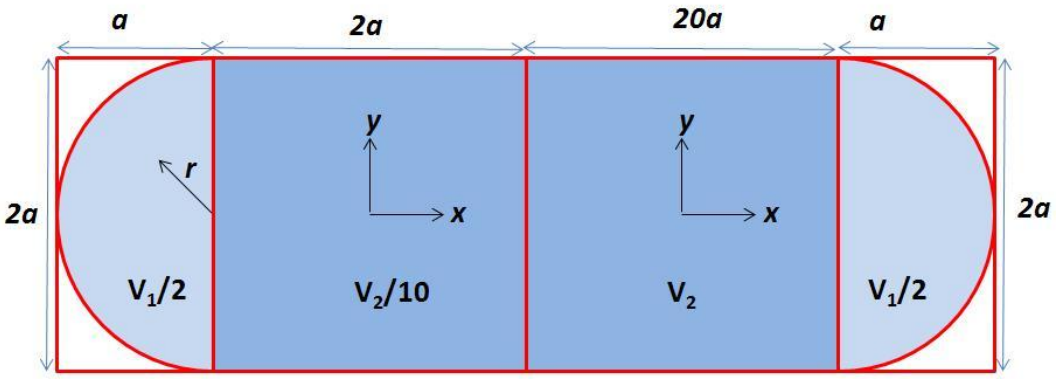

Fig. 11.1.2 Volume V_P above the plate at the end of the power stroke; it is the entire volume of the chamber

The volume V_P above the plate at the end of the power stroke is approximated by the sum of volumes V_1, V_2, and one-tenth the volume of V_2; it is given by

$$V_{\mathrm{P}} \cong V_1 + 1.1V_2 = \frac{(352+5\pi)a^2\delta_{\max}}{15} \tag{11.1.11}$$

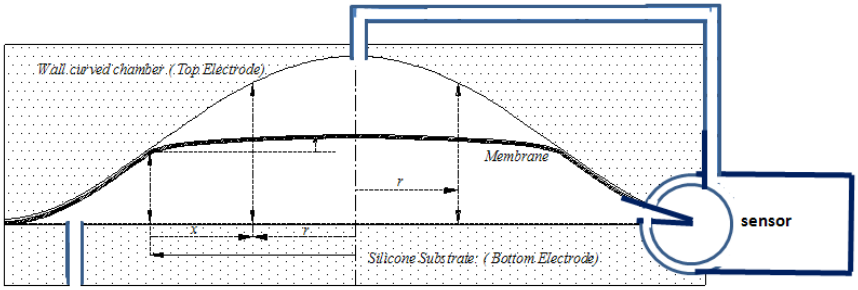

Fig. 11.1.3 Sensor Reservoir

For a radius of *a=1.0mm* and a maximum chamber height $\delta_{\max} = 0.02mm$, the volume V_I of the intake chamber and the volume V_P of the power stroke chamber are given by

$$V_{\mathrm{I}} = 0.4476mm^3 \tag{11.1.12}$$

$$V_{\mathrm{P}} = 0.4903mm^3 \tag{11.1.13}$$

The volume of the sensor chamber, including all conduits and connections to pump chamber is assumed to be less than a third that of the intake chamber. For example, suppose the sensor volume has dimensions 1mm by 1mm microns by 20 microns.

$$V_S = 0.02mm^3 \tag{11.1.14}$$

The volume taken up by the sensor reservoir and the volume in the chamber above the plate flat against the floor at the end of the power stroke is

$$V_{\mathrm{SP}} = 0.5103mm^3 \tag{11.1.15}$$

The ratio of the intake volume over the sensor-chamber volume is

$$\frac{V_{\mathrm{I}}}{V_{\mathrm{SP}}} = 0.8772 \tag{11.1.16}$$

11.2 Ideal Gas Law And Pumping Vacuum Reservoir Down

In this section, we determine how much the pressure in the sensor reservoir decreases over one pump cycle of the intake plus the pressure stroke. The ideal gas law states

$$PV = nRT \tag{11.2.1}$$

where P is pressure in pascals, V is volume in cubic meters, n is the number of moles, R is the universal gas constant 8.314 J/(K*mole), and T is the absolute temperature in degrees Kelvin.

Let n_0 be number of moles and P_0 be the pressure in the volume V_{SP} before the start of the intake stroke; the following ideal gas law is satisfied.

$$P_0 V_{SP} = n_0 RT \tag{11.2.2}$$

At the end of the intake stroke, let n_I be number of moles in the volume V_I. It is the moles n_I that is pumped out by the power stroke. The following ideal gas law is satisfied at the end of the intake stroke.

$$P_0 V_I = n_I RT \tag{11.2.3}$$

Subtracting (11.2.3) from (11.2.2) gives the following equation.

$$P_0 \left(V_{SP} - V_I \right) = \left(n_0 - n_I \right) RT \tag{11.2.4}$$

At the end of the power stroke, let P_1 be the pressure in the volume V_{SP} before the start of the next intake stroke. Since n_I moles are pumped out by the pressure stroke, the number of moles in the volume V_{SP} is n_0- n_I at the start of the next intake stroke. The ideal gas law is satisfied at the start of the next intake stroke.

$$P_1 V_{SP} = \left(n_0 - n_I\right) RT \tag{11.2.5}$$

After one complete cycle of intake and power stroke, we see from (11.2.4) and (11.2.5) that the pressure P_1 in the volume V_{SP} satisfies

$$P_1 = P_0 \frac{\left(V_{SP} - V_I\right)}{V_{SP}} \tag{11.2.6}$$

After N complete cycles, the pressure P_N in the volume V_{SP} satisfies

$$P_N = P_0 \left[\frac{V_{SP} - V_I}{V_{SP}}\right]^N \tag{11.2.7}$$

Consider a vacuum pump specification that the initial pressure P_0 =760 Torr is to be pumped down to a vacuum pressure of pressure $P_N = P_F = 10^{-6}$ Torr in the volume V_{SP}. The number of cycles required is determined from (11.2.7):

$$10^{-6} = 760\left[\frac{V_{SP} - V_I}{V_{SP}}\right]^N \tag{11.2.8}$$

For the parameters considered in the above volumes of (11.1.12) and (11.1.13), the number of cycles required satisfies

$$10^{-6} = 760\left[0.12281\right]^N \tag{11.2.9}$$

or, equivalently,

$$\left[1/0.12281\right]^N = \left[8.1427\right]^N = 760\times10^6 \tag{11.2.10}$$

$$N = \frac{\ln\left[760\times10^6\right]}{\ln\left[8.1427\right]} = \frac{\ln\left[760\right]+6\ln\left[10\right]}{\ln\left[8.1427\right]} = \frac{6.6333+6\left(2.3026\right)}{2.097} = 9.75 \tag{11.2.11}$$

The number of cycles required to pump the pressure in the sensor chamber down from 760 Torr to a vacuum pressure of 10^{-6} Torr is 10 cycles.

The ideal gas law can also be written as

$$PV = NkT \tag{11.2.12}$$

where N is the number of molecules, and where *k* is the Boltzmann constant

$$k = \frac{R}{N_A} = 1.38066\times10^{-23}\,J/K \tag{11.2.13}$$

where N_A is Avogadro's number 6.0221×10^{-23} molecules per mole.

The number density of molecules per unit volume is given by

$$\frac{N}{V} = \frac{PN_A}{RT} \tag{11.2.14}$$

The number of molecules *N* in a given volume V satisfies

$$N = \left[\frac{PN_A}{RT}\right]V \tag{11.2.15}$$

Consider a vacuum pressure P_1=1.0×10^{-6} Torr in the volume V_{SP} =0.510277 mm^3. The number of molecules N_1 in V_{SP} under pressure P_1 and temperature 300K is given by

$$N_1 = \left[\frac{P_1 N_A}{RT}\right] V_{SP} = \left[\frac{P_1}{kT}\right] V_{SP} = \frac{10^{-6} Torr \times 101,325 Pa \times 0.510277 \times 10^{-9} m^3}{760 Torr \times \left(1.38066 \times 10^{-23} J/K\right) 300K} \text{ molecules} \tag{11.2.16a}$$

$$N_1 = 16.4 \times 10^6 \text{ molecules} \tag{11.2.16b}$$

Consider an outlet pressure P_0=760 Torr in some volume V_0. The number density of molecules N_0 in V_0 under pressure P_0 and temperature 300K is given by

$$\frac{N_0}{V_0} = \left[\frac{P_0 N_A}{RT}\right] = \frac{760 Torr \times 101,325 Pa}{760 Torr \times \left(1.38066 \times 10^{-23} J/K\right) 300K} \frac{10^{-6} m^3}{cm^3} \tag{11.2.17a}$$

$$\frac{N_0}{V_0} = 2.45 \times 10^{19} \frac{\text{molecules}}{cm^3} \tag{11.2.17b}$$

Next, we consider leak back rates through the pump.

11.3 Leak Back Rates

For air at 1 atm and 20°C (i.e., 293.15°K), Eq. 3.96a in [Roth, 1990] provides leak back rates (cm^3 per second):

$$C_{air}\left(293.15°K\right) = 30.9\left[\frac{wh^2}{L}\right] 1.444 \times 10^3 \text{ cm}^3 \text{ per second} \tag{11.3.1}$$

where w is the width of the leak channel, L is the length of the leak channel, h is the height of the leak channel and where w, L, h are in units of centimeters. For air at 1 atm and 300°K, the leak rate back to the vacuum reservoir is given by

$$C_{air}\left(300°K\right) = 30.9\left[\frac{wh^2}{L}\right]1.444\sqrt{\frac{300}{293.15}}\times 10^3 \text{ cm}^3 \text{ per second} \tag{11.3.2}$$

For $w=2mm$, $L=24mm$ and $h=1nm$, C_{air} is given by

$$C_{air} = 4.10345\times 10^{-11}\text{cm}^3/\text{s} \tag{11.3.3}$$

The number of molecules per second being leak back from the outlet under 1 atm pressure to the inlet is given by

$$\frac{N_0}{V_0}C_{air} = 2.45\times 10^{19}\,\frac{\text{molecules}}{cm^3}\times 4.10345\times 10^{-11}\text{cm}^3/\text{s}=1.0038\times 10^9\,\frac{\text{molecules}}{\text{s}} \tag{11.3.4}$$

The above holds for a roughness slit height of $h=1nm$. For a roughness slit height of $h=\sqrt{10}\ nm$ the number of molecules per second being leak back would be 10 times higher. For a roughness slit height of $h=10\ nm$, the number of molecules per second being leak back would be 100 times higher.

11.4 Pump Frequency To Maintain 10^{-6} Torr Inlet With 1 ATM Outlet

The number of molecules per unit time (Δt) being pumped out of the vacuum reservoir under a vacuum pressure $P_1=1.0\times 10^{-6}$ Torr and temperature $300K$ by the intake volume V_I is given by

$$\frac{N_I}{\Delta t} = \left[\frac{P_1 N_A}{RT}\right]\frac{V_I}{\Delta t} \text{ molecules per s} \qquad 11.4.1)$$

The rate of molecules being leaked into the vacuum reservoir under an outlet pressure P_0=760 Torr and temperature 300K is given by

$$\frac{N_0}{V_0} C_{air} = \left[\frac{P_0 N_A}{RT}\right] C_{air} \text{ molecules per s} \qquad (11.4.2)$$

One requirement of a vacuum pump is that its pump rate must keep up with leak back rate. This requires

$$\frac{N_I}{\Delta t} = \frac{N_0}{V_0} C_{air} \text{ or } \left[\frac{P_1 N_A}{RT}\right]\frac{V_I}{\Delta t} = \left[\frac{P_0 N_A}{RT}\right] C_{air} \qquad (11.4.3)$$

Solving for the require pump rate, we get the following rate for an outlet pressure P_0=760 Torr and vacuum reservoir pressure P_1=1.0×10^{-6} Torr

$$\frac{V_I}{\Delta t} = \left[\frac{P_0}{P_1}\right] C_{air} = \left[\frac{760}{10^{-6}}\right] 4.10345 \times 10^{-11} \text{cm}^3/\text{s} = 0.0312 \text{ cm}^3/\text{s} \qquad (11.4.4)$$

The intake volume per cycle is given by (11.1.12). Dividing the intake volume per cycle by the required pump rate to maintain a vacuum reservoir pressure P_1=1.0×10^{-6} Torr, we obtain the required the pump cycle frequency

$$\frac{V_I}{\Delta t}\frac{1}{V_I} = \left[\frac{P_0}{P_1}\right]\frac{C_{air}}{V_I} = \frac{0.0312 \text{ cm}^3/\text{s}}{0.4476 \times 10^{-3} cm^3} = 69.7 \frac{\text{cycles}}{\text{s}} \qquad (11.4.5)$$

The above holds for a roughness slit height of h=1nm. For a roughness slit height of h=$\sqrt{10}$ nm the required the pump cycle frequency would be 697 cycles per second. For a

roughness slit height of *h=10 nm* the required the pump cycle frequency would be 6970 cycles per second which is more that the rates obtained in the multiphysics simulations. For the most part, 1000 Hz pump rate is a conservative value. But, for a 1 Torr inlet reservoir, much higher pump rates are possible, particularly with the use of a check value at the outlet for applications where the outlet reservoir is at 1 atm pressures. It is recommended to employ multiple cascaded vacuum pumps to pull 10^{-6} Torr vacuum reservoir pressure for roughness slit heights as large as a few nm.

11.5 Pump Frequency To Maintain 10^{-3} Torr Inlet With 1 ATM Outlet

Next, we consider the pump frequency required to maintain vacuum reservoir pressure P_1=1.0×10^{-3} Torr at the inlet with 1 atm at the outlet.

The required the pump cycle frequency is determined using Eqs. (11.4.4) and (11.4.5). Using P_1=1.0×10^{-3} Torr at the inlet, Eqs. (11.4.4) and (11.4.5) yield

$$\frac{V_I}{\Delta t}=\left[\frac{P_0}{P_1}\right]C_{air}=\left[\frac{760}{10^{-3}}\right]4.10345\times10^{-11}\text{cm}^3/\text{s}=0.0312\times10^{-3}\ \text{cm}^3/\text{s} \tag{11.5.1}$$

$$\frac{V_I}{\Delta t}\frac{1}{V_I}=\left[\frac{P_0}{P_1}\right]\frac{C_{air}}{V_I}=\frac{0.0312\times10^{-3}\ \text{cm}^3/\text{s}}{0.4476\times10^{-3}cm^3}=69.7\times10^{-3}\frac{\text{cycles}}{\text{s}} \tag{11.5.2}$$

This shows that one pump cycle every 10 seconds will maintain vacuum reservoir pressure P_1=1.0×10^{-3} Torr at the inlet with 1 atm at the outlet.

The above holds for a roughness slit height of *h=1nm*. For a roughness slit height of *h=* $\sqrt{10}$ *nm* the required the pump cycle frequency would be 0.697 cycles per second. For a roughness slit height of *h=10 nm* the required the pump cycle frequency would be 6.97 cycles per second.

11.6 Pump Frequency To Maintain 10^{-9} Torr Inlet With 10^{-3} Torr Outlet

Next, we consider the pump frequency required to maintain vacuum reservoir pressure P_1=1.0×10^{-9} Torr at the inlet with 10^{-3} Torr at the outlet. The required the pump cycle frequency is determined using Eqs. (11.4.4) and (11.4.5). Using P_1=1.0×10^{-9} Torr at the inlet with 10^{-3} Torr at the outlet, Eqs. (11.4.4) and (11.4.5) yield

$$\frac{V_I}{\Delta t}=\left[\frac{P_0}{P_1}\right]C_{air}=\left[\frac{760}{10^{-3}}\right]\left[\frac{10^{-3}}{10^{-9}}\right]4.10345\times10^{-11}\text{cm}^3/\text{s}=\left[\frac{1000}{760}\right]0.0312\times10^{-3}\ \text{cm}^3/\text{s} \tag{11.6.1}$$

$$\frac{V_I}{\Delta t}=\left[\frac{P_0}{P_1}\right]C_{air}=\left[\frac{1000}{760}\right]0.0312\times10^{-3}\ \text{cm}^3/\text{s}=0.0410\times10^{-3}\ \text{cm}^3/\text{s} \tag{11.6.2}$$

$$\frac{V_I}{\Delta t}\frac{1}{V_I}=\left[\frac{P_0}{P_1}\right]\frac{C_{air}}{V_I}=\frac{0.0410\times10^{-3}\ \text{cm}^3/\text{s}}{0.4476\times10^{-3}cm^3}=91.7\times10^{-3}\,\frac{\text{cycles}}{\text{s}} \tag{11.6.3}$$

This shows that one pump cycle every 10 seconds will maintain vacuum reservoir pressure P_1=1.0×10^{-9} Torr at the inlet with 10^{-3} Torr at the outlet.

The above holds for a roughness slit height of *h=1nm*. For a roughness slit height of *h=* $\sqrt{10}$ *nm* the required the pump cycle frequency would be 0.917 cycles per second. For

a roughness slit height of *h=10 nm* the required the pump cycle frequency would be 9.17 cycles per second.

11.7 Two Pumps in Series to Maintain 10^{-9} Torr Inlet With 1 ATM Outlet Pressure

The above two section suggests cascading pumps in series to maintain very high vacuum pressures in the vacuum reservoir. One vacuum pump could maintain an inlet vacuum pressure of 10^{-9} Torr at the inlet with 10^{-3} Torr at the outlet. A second vacuum pump could maintain an inlet vacuum pressure of 10^{-3} Torr at the inlet with 760 Torr at the outlet. Taken in series together, the cascaded vacuum pumps would provide 10^{-9} Torr at the inlet of the first pump while 760 Torr exists as the pressure at the outlet of the second pump.

CHAPTER 12

HIGH PRESSURE HIGH FLOW RATE DESIGN

12.1 Design Parameters for High Pressure High Flow Rates

In this chapter, we show that our micropump concept can be designed for high differential pressure and high flow rates. The first example (Section 12.2) considers vacuum pressures at the inlet reservoir with 1 atm pressure at the outlet. The second example (Section 12.3) considers 1 atm pressures at the inlet reservoir with 2 atm pressure at the outlet. We consider an intake chamber *V2* that has a square footprint 20 mm by 20 mm. In this case, the parameter a=20/2 mm=10mm. We desire to maintain the following ratio of the baseline design

$$\frac{\delta_{\max}}{a} = \frac{1}{50} \tag{12.1.1}$$

Maintaining this ratio requires that the chamber height satisfy

$$\delta_{\max} = 200 \; microns \tag{12.1.2}$$

We recall the baseline micropump design parameters, Table 12.1.1.

Table 12.1.1 Baseline Micropump Design Parameters

Plate Radius	a	1000	um
Chamber Height	δmax	20	um
Plate Thickness	t	10	um
Young's Modulus	E	1.60e11	N/m^2
Poisson's Ratio	υ	0.23	
Permittivity	ε_0	8.85e-12	F/m
Dielectric Permittivity	ε_d	3.9	
Air Permittivity	ε_{air}	1	
Max Residual Stresses	σ_T	500+	MPa
Ultimate Strength, Poly	σ_u	1550	MPa
Applied Voltage	V	200	volts
Dielectric Thickness	d_0	200	nm
Simulation Gap	gap	3	nm

From Chapter 10, we see that the differential pressure at the outlet achieved by the baseline design parameters is also achieved by a new set of design parameters provided that the same ratios in Table 12.1.2 are maintained by the new set. The new set of design parameters given in Table 12.1.3 satisfies the requirement that the design ratios in Table 12.1.2 have the same values for both the baseline and the new set of design parameters. Since the design parameters of the new set meet this requirement, the resulting micropump achieves differential pressures p_0=1.55 atm at the outlet as shown by the results in Table 9.10.1. That is, the same differential pressure p_0=1.55 atm result is achieved by the new design parameters: plate thickness t= 100 microns, residual stresses σ_T = 513.6 MPa, dielectric thickness d_0 = 2000 nm, maximum applied voltage V=2000 volts, plate radius a=10,000 microns, and chamber height δmax =200 microns. That is, these parameters have all been increased by a factor of 10. Consequently, the results given in Chapters 8 and 9 for the plate thickness t= 10 microns also hold for the new set of parameters given in Table 12.1.3.

Table 12.1.2. Baseline design ratios

Description		Baseline Ratio
Chamber Height/ Plate Radius	$\delta max/a$	0.02
Dielectric Thickness / Chamber Height	$d_0/\delta max$	0.01
Plate Thickness/ Plate Radius	t/a	0.01

Table 12.1.3 New Set of Micropump Design Parameters

Plate Radius	a	10000	um
Chamber Height	δmax	200	um
Plate Thickness	t	100	um
Young's Modulus	E	1.60e11	N/m^2
Poisson's Ratio	υ	0.23	
Permittivity	ε_0	8.85e-12	F/m
Dielectric Permittivity	ε_d	3.9	
Air Permittivity	ε_{air}	1	
Max Residual Stresses	σ_T	500+	MPa
Ultimate Strength, Poly	σ_u	1550	MPa
Applied Voltage	V	2000	volts
Dielectric Thickness	d_0	2000	nm
Simulation Gap	gap	3	nm

In all that follows in this chapter, we make use of the fact that the micropump as defined by the new set of parameters given in Table 12.1.3 has the capability to achieve 1.55 atm differential pressure at the output. That is, it will pump gas from an inlet 1 Torr reservoir to a 760 Torr outlet reservoir with a pumping frequency at least as much as 1000 Hz. For the purposes of calculating the flow rate from the inlet to the outlet, we need to compute the intake volume.

The intake volume V_2 is determined by the integral

$$V_2 = 2a\int_0^a \delta_{\max}\left[1-\left(\frac{y}{a}\right)^2\right]^2 dy \tag{12.1.3}$$

Using the integration variable z=*(y/a)*, (12.1.3) can be rewritten as

$$V_2 = 2a^2\delta_{\max}\int_0^1\left[1-z^2\right]^2 dz \tag{12.1.4}$$

Carrying out the integral, we have

$$V_2 = \frac{16a^2\delta_{\max}}{15} \tag{12.1.5}$$

The intake volume V_2 is given by

$$V_2 = \frac{16a^3}{15*50} = \frac{16}{15*50}\ CC \tag{12.1.6}$$

where CC stands for cubic centimeters at the inlet 1 Torr pressure.

12.2 Flow Rates Greater Than 1 SCCM

We consider the following high pressure high flow rate design problem. Design a micropump that will pump at a 1 SCCM (cubic centimeters per minute at standard atmospheric conditions) flow rate from an inlet reservoir with 1 Torr pressure to an outlet reservoir with 1 atm pressure. In this example, the inlet volume will be compressed by the factor 760 as it is pumped from the inlet 1 Torr pressure to the outlet 760 Torr pressure. That is, the volume V_{outlet} at the outlet is given by

$$V_{outlet} = \frac{16}{760*15*50}\ SCC \tag{12.2.1}$$

where SCC stands for cubic centimeters at the outlet standard 760 Torr pressure.

Assuming a pumping frequency of 1000 Hz, the flow rate at the outlet in units of cubic centimeters per minute is given by

$$\textit{flow rate}\ \text{at the outlet}=Q_{outlet} = \frac{1000*16*60}{760*15*50}\ SCCM = 1.68\ SCCM \tag{12.2.2}$$

In summary, the micropump with the design parameters as given in Table 12.1.3, has a flow rate greater than 1 SCCM from an inlet 1 Torr reservoir to an outlet 760 Torr reservoir. This example shows that a vacuum micropump can be designed with a high flow rate (i.e., 1.7 SCCM) as well as a high differential pressure (i.e., 1.55 atm) capability at the outlet. Since the differential pressure capability of 1.55 atm is much greater than 1.0 atm, the micropump is capable of providing at least a 1000 Hz pumping frequency and considerably higher since it is pumping from an inlet reservoir with 1 Torr pressure, provided a check value is used at the outlet.

12.3 Flow Rates Greater Than 1000 SCCM

Next, we consider the following high pressure high flow rate design problem. Design a micropump that will pump at a 1000 SCCM (cubic centimeters per minute at standard atmospheric conditions) flow rate from an inlet reservoir with 1 atm pressure to an outlet reservoir with 2 atm pressure. The design parameters in Table 12.1.3 apply. We consider the flow rate referenced at the inlet since the inlet reservoir is at standard atmospheric conditions (e.g., 1 atm). [In this case, it is not necessary to consider that the inlet volume is compressed by the factor 2 as it is pumped from the inlet 1 atm pressure to the outlet 2 atm pressure.] The inlet volume V_{inlet} being pumped from the inlet reservoir (which is at 1 atm pressure) is given by

$$V_{inlet} = \frac{16}{15*50}\ \mathrm{S}CC \tag{12.3.1}$$

Assuming a pumping frequency of 1000 Hz, the flow rate from the inlet in units of cubic centimeters per minute is given by

$$\textit{flow rate}\ \text{at the outlet}=\mathrm{Q}_{outlet} = \frac{1000*16*60}{15*50}\ \mathrm{S}CCM = 1280\ SCCM \tag{12.3.2}$$

In summary, the micropump with the design parameters as given in Table 12.1.3, has a flow rate greater than 1000 SCCM from an inlet 1 atm reservoir to an outlet 2 atm reservoir. This example shows that a vacuum micropump can be designed with a high flow rate (i.e., 1280 SCCM) reference to the inlet reservoir pressure (1 atm) as well as a high differential pressure (i.e., 1.55 atm) capability at the outlet.

CHAPTER 13

CONCLUSIONS

A novel peristaltic micropump concept has been investigated in this dissertation that is based on the "electrozipper" type of actuating mechanism. Significant performance results in terms of high differential pressures (e.g., 1.5 atm) and high flow rates (1-1000 SCCM) have been obtained with a baseline design configuration of this concept by employing the new idea of preloaded tension (i.e., tensile residual stresses) in the pumping plate. The inclusion of the preloaded tension as a design parameter was instrumental in achieving large differential pressure performance. The stored energy provided by the preloaded tension significantly increases the differential pressure performance of the baseline configuration as compared with zero tension (e.g., from 0.3 atm to 1.55 atm) for the same power requirements.

The following baseline design parameters were used throughout the study. The polysilicon plate material has the properties: Young's modulus=160 GPa; Poisson's ratio=0.23; ultimate strength (tension) 1.55 GPa. The silicon dioxide (SiO_2) dielectric material has a relative dielectric permittivity of 3.9. Geometry parameters were set as follows: Plate radius=1000 microns (um); chamber height=20 microns; plate thickness=10 microns; dielectric thickness=200 nanometers (nm). The applied voltage per dielectric thickness was limited to 1 volt per nm, limiting the applied voltage to a maximum of 200 volts.

Extensive multiphysics simulations were performed on the baseline configuration for both intake and outlet power strokes. Multiphysics interactions of electrostatics, structures, fluid flow, and moving boundaries were carried out in the simulations. Early on in the simulations, a surprising simulation result was observed during the intake stroke. As the applied voltage was increased, the micropump plate electrozipped up the walls of the intake chamber with increasing height. But, when the plate reached a certain point along the chamber wall, the plate would then electrozip all the way up the chamber wall to maximum height without any additional increase in applied voltage. In the beginning of the study, we had not expected such change in intake volume to take place without an increase in applied voltage. That particular observation in the multiphysics simulations was what initiated the analytical modeling of the intake stroke. The work of developing the analytical models derived in Chapters 5-7 for the intake stroke was initially carried out to help understand and explain the nature of that surprising result. It turned out that the results from the analytical modeling matched the results observed in the simulations, Chapters 7 and 8. The analytical modeling revealed that the nature of the surprising phenomenon was due to the maximum moment required to hold the plate against the chamber wall and that the point of occurrence depended on the tangent and the curvature of the chamber wall as well as the tension in plate. The analytical modeling showed that the moment required to hold the plate against the wall reached a maximum value at the same point as observed in the simulations. As shown in Chapters 7 and 8, the analytical modeling predicted the same maximum voltage and bending stresses as those calculated by the multiphysics simulations as well as the surprising result described above. The results of

the analytical modeling matched those of the simulations, qualitatively and quantitatively, in all 19 cases considered in Chapters 7 and 8.

The analytical model for the intake stroke was derived using a quadratic electrostatic distributive force model in the 4^{th} order reduced Von Karman governing differential equations that was analytically integrated for conditions under bending, stretching, and quadratic electrostatic pressure forces on the plate. The analytical model for the pressure power stroke was derived by integrating a 4^{th} order reduced Von Karman governing differential equations with constant differential pressure p_0 acting on the plate.

The 2D multiphysics simulation modeling of the micropump captured the most relevant properties and behavior occurring during the intake stroke and it provided insight into the parametric study of the baseline design configuration for the new micropump concept. The 2D multiphysics simulations developed to handle high loads and large deflections in large aspect ratios were found to be computationally time consuming due to the complexity of the fluid, structure, electrostatic and moving plate boundaries interactions. The results from the analytical models for the intake and power strokes, Chapters 7-9 were shown to match the results of the multiphysics simulations to within a few per cent. Since the analytical models were able to match the simulation results so well for both intake and power outlet strokes over many cases and conditions, it showed that they could be used beyond the baseline values to evaluate quite accurately the performances of many other different and alternate design

configurations rather easily and quickly, avoiding the large expenditure of computational time and cost needed by the multiphysics simulation approach. The numerical simulations basically validated the use of the analytical models as a design tool for the extended applications beyond the baseline configuration given in Chapters 10-12 for vacuum pump and high flow rate designs. In Chapter 10, it is shown that the analytical models contain non-dimensional parameters that can be used in designing parameters for new micropump configurations for applications requiring different differential pressures and flow rates. That is, the non-dimensional parameters of the analytical models can be used to scale the baseline design to other micropump configurations and achieve specified and targeted performance characteristics (differential pressures and flow rates). This new design methodology provides rapid determination of ballpark values for the design parameters needed for achieving specified performance requirements in new micropump applications.

Major goals achieved by the work herein include the following. The micropump baseline configuration was shown to produce more than 1.5 atm differential pressure using a 10 microns plate thickness, 199 volts applied, and 514 MPa residual stresses. For such a case, it is shown that fatigue safety limits are satisfied for multimillions life-cycles. The micropump baseline configuration is shown in Chapter 11 that it can function as a vacuum pump on-chip for the sensor industry. In the vacuum pump applications given in Chapter 11, leak back rates are based on surface roughness heights from 1nm to 10 nm. It is shown that the baseline configuration can pull vacuum pressures on the order of 10^{-3} Torr and that high vacuum pressures on the order of 10^{-9}

Torr are achievable by cascading two such vacuum pumps in series. Micropump designs are presented in Chapter 12 that provide high flow rates in the range 1-1000 SCCM in pumping from a 1 atm inlet reservoir to a 2 atm outlet reservoir. The fatigue aspects of polysilicon and its use as a material for the micropump plate in the baseline design was investigated in Chapter 4 and was shown to have good fatigue characteristics for multi-millions cycles, especially for the 10 micron plate thickness.

REFERENCES

[Accoto, Carrozza, et al., 2000] D. Accoto, M. C. Carrozza, and P. Dario, "Modelling of Micropumps using Unimorph Piezoelectric Actuator and Ball Valves," J. Micromechanics and Microengineering, 10, 2000, pp. 277-281.

[Acero, Plaza, et al., 1997] M. C. Acero, J. A. Plaza, J. Esteve, M. Carmona, S. Marco, and J. Samitier, "Design of a Modular Micropump Based on Anodic Bonding," J. Micromech. Microeng., Vol. **7**, 1997, pp. 179-182.

[Ahn and Kim, 1997] Ahn, S.-H. and Y.-K. Kim, "Fabrication and Experiment of Planar Micro Ion Drag Pump," Tranducers '97, 1997 International Conference on Solid-State Sensors and Actuators, Chicago, June 16-19, 1997, pp. 373-376.

[Angel, Terry, Barth, 1983] J.B. Angel, S.C. Terry, and P.W. Barth, "Silicon Micromechanical Devices," *Scientific American*, Vol. 248, p. 44, April 1983.

[Ballantine, et al., 1997] Ballantine, Jr., S. J. Martin, A. J. Ricco, G. C. Frye, R. M. White, E. T. Zellers, *Acoustic Wave Sensors, Theory, Design, and Physico-Chemical Applications*, Academic Press, San Diego, CA, 1997.

[Bart, et al., 1990] Stephen F. Bart, Lee S. Tavrow, Mehran Mehregany and Jefrey H. Lang, "Microfabricated Electrohydrodynamic Pumps," Sensors and Actuators, A21-A23, 1990, pp. 193-197.

[Barth, 1995] Phillip W. Barth, “Silicon Microvalves for Gas Flow Control,” Transducers ’95, Eurosensors IX, Stockholm, Sweden, June 25-29, 1995, pp. 276-279.

[Barth, et al., 1994] Phillip W. Barth, Christopher C. Beatty, Leslie A. Field, James W. Baker, and Gary B. Gordon, A Robost Nornally-Closed Silicon Microvalve,” Solid-State Sensor and Actuator Workshop, Hilton Head, South Carolina, June 13-16, 1994, pp. 248-250.

[Benard, 1997] William L. Benard, “Thin-Film Shape Memory Alloy Actuated Microfluidics Devices,” Dept. of Electrical Engineering and Applied Physics, Cleveland, Case Western Reserve University, 1997.

[Benard, et al., 1997a] William L. Benard, Harold Kahn, “A Titanium-Nickel Shape-Memory Alloy Actuated Micropump,” Proc. IEEE 9th International Conference on Solid State Sensors and Actuators, Transducers’97, Chicago, 1997.

[Benard, Kahn, et al., 1997b] William L. Benard, Harold Kahn, Arthur H. Heuer, and Michael A. Huff, “A Titanium-Nickel Shape-Memory Alloy Actuated Micropumps,” Int. Conf. Solid-State Sensors and Actuators, 1997, pp. 361-364.

[Benard, et al., 1997c] William L. Benard, Harold Kahn, et al., “A Ti-Ni Shape-Memory Alloy Actuated Micropump with Fluid Isolation,” **3046**, 1997, pp. 156-164.

[Benard, et al., 1998] William L. Benard, Harold Kahn, Arthur H. Heuer, and Michael A. Huff, “Thin-Film Shape-Memory Alloy Actuated Micropumps,” J. Microelectromechanical Systems, Vol. 7, No. 2, June 1998, pp. 245-251.

[Berg, et al., 2003] J. M. Berg, R. Anderson, M. Anaya, B. Lahlouh, M. Holtz, and T. Dallas, “A two-stage discrete peristaltic micropump,” Sensors and Actuators A, Vol. 104, 2003, pp. 6-10.

[Bergstrom, Ji, Kaviany,Wise, 1995] Paul L. Bergstrom, Jin Ji, Yu-Ning Liu, Massoud Kaviany, and Kensall D. Wise, “Thermally Driven Phase-Change Microactuation,” J. Microelectromechanical Systems, Vol. 4, No. 1, March 1995, pp 10-17.

[Beskok, et al., 1996] Ali Beskok, George Em Karniadakis, and William Trimmer, “Rarefaction and Compressibility Effects in Gas Microflows,” J. Fluids Engr., Transactions ASME, Vol. 118, September, 1996, pp. 448-456.

[Böhm, Olthuis, et al., 1999] Sebastian Böhm, Wouter Olthuis, and Piet Bergveld, “A plastic micropump constructed with conventional techniques and materials,” Sensors and Actuators A Physical, Vol. 77, 1999, pp. 223-228.

[Böhm, Timmer, et al., 2000] Sebastian Böhm, Björn Timmer, Wouter Olthuis, and Piet Bergveld, “A Closed-Loop Controlled Electrochemically Actuated Micro-Dosing System, J. Micromechanics and Microengineering, **10**, 2000, pp. 498-504.

[Bosch, et al., 1993] D. Bosch, B. Heimhofer, G. Muck, H. Seidel, U. Thumser, and W. Welser, “A silicon microvalve with combined electromagnetic/electrostatic actuation,” Sensors and Actuators A, 37-38, 1993, pp. 684-692.

[Bousse, Dijkstra, et al. 1996] L. Bousse, E. Dijkstra, and O. Guenat, “High-Density Arrays of Valves and Interconnects for Fluid Switching,” Proc. IEEE Solid-State Sensor and Actuator Workshop, Hilton Head Island, SC, June 3-6, 1996, pp. 272-275.

[Bourouina, Bosseboeuf, et al., 1997] Tarik Bourouina, Alain Bosseboeuf, and Jean-Paul Grandchamp, “Design and Simulation of an Electrostatic Micropump for Drug-Delivery Applications,” J. Micromech. Microeng., Vol. **7**, 1997, pp. 186-188.

[Bradley, et al., 1995] C. E. Bradley, J. M. Bustillo, and R. M. White, IEEE Ultrasonics Symposium 1, 505 (1995).

[Boresi, et al ., 1978] Arthur P. Boresi., Omar M. SideBottom., Fred B. Seely., James O. Smith., “Advanced Mechanics of Materials”., 2 Edition, John Wiley and Sons., 1978

[Buchaillot, Nakamura, et al., 1996] L. BUCHAILLOT, Y. NAKAMURA, S. NAKAMURA, H. FUJITA, “**Thin film SMA actuators for MEMS applications,”** 3rd France-Japan Congress, 1st Europe-Asia Congress on Mechatronics, Vol. 2, pp. 627-630, Besançon, France, Oct. 1-3, 1996.

[Busch and Johnson, 1990] John D. Busch and A. David Johnson, “Prototype Micro-Valve Actuator,” IEEE Proceedings, CH2832-4, Napa, USA, 1990, pp. 40-41.

[Büstgens, et al., 1994] B. Büstgens, W. Bacher, W. Menz, and W. K. Schomburg, “Micropump Manfactured by Thermoplastic Molding,” Proc. IEEE MEMS-94, Oiso, Japan, 1994, pp. 18-21.

[Bush and Johnson, 1990] Bush, J. D. and A. D. Johnson, “Propotype Microvalve Actuator,” MEMS’90, NAPA, CA, IEEE, 1990.

[Cabuz, et al., 2001] Cleopatra Cabuz, William R. Herb, Eugen I. Cabuz, and Son Thai Lu, “The Dual Diaphragm Pump,” Proc. IEEE 2001 Micro Electro Mechanical Systems Workshop (MEMS’01), 2001, pp. 519-522.

[Carlen, 2001] E. T. Carlen, " Electrothermally actuated polymer microvalves," PhD Thesis, University of Michigan, 2001.

[C. H. Ng, et al., 2003] C. H. Ng, K.W. Chew, and S.F. Chu, "Characterization and Comparison of PECVD Silicon Nitride and Silicon Oxynitride Dielectric for MIM Capacitors", IEEE Electron Device Letters, Vol. 23, Issue 8, Aug. 2003, pp. 506-508.

[Ceriotti, Lichtenberg, et al., 2002] Laura Ceriotti, Jan Lichtenberg, Takayuki Shibata, Vincent Linder, Wolfgang Thormann, Hans Sigrist, Nico F. de Rooij, Elisabeth Verpoorte, "Towards analysis of real clinical samples with microfluidic devices," **NanoTech 2002, 6th Annual Conference on Micro and Nanoscale Technologies for the Biosciences,** November 26-28, 2002, Montreux, Switzerland.

[Chakraborty, et al., 1999] Chakraborty, I., Tang, W., Bame, D., and Tang, T., "MEMS Micro-Valve For Space Applications," Technical Digest, Transducers'99, Sendai, Japan, June 7-11, 1999, pp. 1820-1823.

[Chen,et al., 1998] Kuo-Shen Chen, Arturo A. Ayon, S. Mark Spearing, "Silicon Strength Testing for Mesoscale Structural Applications,"Microelectromechanical Structures for Materials Research, Mat. Res. Soc. Symp. Proc. Vol. 518, 1998, pp. 123-130.

[Chen and Santiago, 2002] Chuan-Hua Chen and Juan G. Santiago, "A Planar Electroosmotic Micropump," J. Microelectromechanical Systems, Vol. 11, No. 6, December 2002, pp. 672-683.

[Chia, 1973] Chen-Yuan Chia "Large deformation of rectangular orthotropic plates"., Journal of the Engineering Mechanics Division, Vol 99, No. 4 July 1973, pp 890-891.

[Chiao and Lin, 2000] Mu Chiao and Liwei Lin, “Self-Buckling of Micromachined Beams Under Resistive Heating,” J. Microelectromechanical Systems, Vol. 9, No. 1, March 2000, pp.146-151.

[Cousseau, Hirsch, et al., 2001] P. Cousseau, R. Hirsch, B. Frehner, S. Gamper, D. Maillefer, “Improved Micro-Flow Regulator for Drug Delivery Systems,” Proc. IEEE 2001 Micro Electro Mechanical Systems Workshop (MEMS’01), 2001, pp. 527-530.

[Darabi, et al., 2001] J. Darabi, M.M. Ohadi, and D. DeVoe, “An Electrohydrodynamic Polarization Micropump for Electronic Cooling,” J. Microelectromechanical Systems, Vol. 10, No. 1, March 2001, pp 98-106.

[Dario, Carrozza, et al., 2000] , Paolo Dario, Maria Chiara Carrozza, Antonella Benvenuto and Arianna Menciassi, “Micro-Systems in Biomedical Applications,” J. Micromechanics and Microengineering, **10**, 2000, pp. 235-244.

[DeCourtye, Sen, et al., 1998] D. DeCourtye, M. Sen and M. Gad-El-Hak, “Analysis of Viscous Micropumps and Microturbines,” IJCFD, Vol. 10, 1998, pp. 13-25.

[Dewa, Deng, et al., 1997] Andrew S. Dewa, Keren Deng, Darren C. Ritter, Charles Bonham, Henry Guckel, and Sombol Massood-Ansari, “Development of LIGA-Fabricated, Self-Priming, In-Line Gear Pumps,” Transducers ’97, 1997 International Conference on Solid-State Sensors and Actuators, Chicago, June 16-19, 1997, pp. 757-760.

[Dhuler, Mehregany, et al., 1992] Vijay R. Dhuler, Mehran Mehregany, Stephen M. Phillips, Jeffrey H. Lang, “Micromotor Operation in a Liquid Environment,” Technical Digest of the 5th IEEE Solid State Sensor and Actuator Workshop, Hilton Head, South Carolina, June, 1992, pp. 10-13.

[Dubois, et al., 2001] Ph. Dubois, B. Guldimann, M.-A. Gretillat, N.F. de Rooij, "Electrostatically Actuated Gas Microvalve Based on a TA-SI-N Membrane," Proc. 14th IEEE MEMS 2001 Technical Digest, 2001, pp. 535-538.

[Elwenspoek, et al., 1994] M. Elwenspoek, T. S. J. Lammerink, R. Miyake, and J. H. J. Fluitman, "Towards integrated microliquid handling systems," J. Micromech. Microeng., Vol. 4, 1994, pp. 227-245.

[Enikov and Lazarov, 2003] Eniko T. Enikov and Kalin Lazarov, "PCB-integrated metallic thermal micro-actuators," Sensors and Actuators A, Vol. 105, 2003, pp. 79-82.

[Esashi, et al., 1989] Esashi, M., Shoji, S., and Nakano, A., "Normally-Closed Microvalve and Micropump Fabricated on a Silicon Wafer," Sensors and Actuators, Vol. 20, 1989, pp. 163-169.

[Eto, et al., 1993] T. K. Eto, B. J. Costello, S. W. Wenzel, R. M. While, and B. Rubinsky, "Viscosity Sensing With Lamb-Wave Microsensor: Dimethylsulfoxide Solution Viscosity as a Function of Temperature," J. Biomechanical Engineering, August 1993, Vol. 115, pp. 329-331.

[Evans, et al., 1997] J. Evans, D. Liepmann, and A. P. Pisano, Proc. Micro Electro Mechanical Systems (Nagoya, Japan, 1997), p. 96.

[Field, White, et al., 1991] Leslie A. Field, Richard M. White, and Albert P. Pisano, "Fluid-Powered Rotary Gears and Micro-Flow Channels," Transducers '91, 6th International Conference on Solid-State Sensors and Actuators, Digest of Technical Papers, San Francisco, California, June, 1991, pp. 1033-1036.

[Folta, Raley, et al., 1992] Folta, James A., Norman F. Raley, Edmund W. Hee, “Design, Fabrication and Testing of a Miniature Peristaltic Membrane Pump,” Proc. MEMS ’92, 1992, 186-189.

[Francais, Dufour, et al., 1997] Olivier Francais, Isabelle Dufour, and Emmanuel Sarraute, “Analytical Static Modelling and Optimization of Electrostatic Micropumps,” J. Micromech. Microeng., Vol. **7**, 1997, pp. 183-185.

[Francais, and Dufour, 2000] Francais, O. and I. Dufour, “Enhancement of Elementary Displaced Colume with Electrostatically actuated Diaphragms: Application to Electrostatic Micropumps,” J. Micromechanics and Microengineering, 10, 2000, pp. 282-286.

[Franz, et al., 1995] Franz, J., Baumann, H., and Trah, H., “A Silicon Microvalve with Integrated Flow Sensor,” Transducers’ 95, Stockholm, Sweden, June 25-29, 1995.

[Fu, et al., 2003] Yongqing Fu, Hejun Du, and Sam Zhang, “Functionally graded TiN/TiNi shape memory alloy films,” Materials Letters, Vol. 57, 2003, pp. 2995-2999.

[Fuhr, et al., 1992] G. Fuhr, R. Hagedorn, T. Muller, W. Benecke, and B. Wagner, Proc. Micro Electro Mechanical Systems (Travemunde, Germany, 1992), p. 25.

[Fuhr, Hagedorn, et al., 1992] Günter Fuhr, Rolf Hagedorn, Torsten Müller, and Bernd Wagner, “Microfabricated Electrohydrodynamic (EHD) Pumps for Liquids of Higher Conductivity,” Journal of microelectromechanical systems, 1 (3), 1992, pp. 141-145.

[Fuhr, Schnelle, et al., 1994] G. Fuhr, T. Schnelle, and B. Wagner, “Travelling wave-driven microfabricated electrohydrodynamic pumps for liquids,” *J. Micromech. Microeng.* **4,** 1994, pp. 217-226.

[Furuya and Shimada, 1990] Furuya, Y. and H. Shimada, “Shape Memory Actuators for Robotic Applications,” Engineering Aspects of Shape Memory Alloys, T. W. Duerig, Butterworth-Heinemann, 1990, pp. 338-355.

[Garcia-Blanco, et al 2008] S. Garcia-Blanco, P. Topart, Y. Desroches, J. S. Caron, F. Williamson, C. Alaain, “A. Roth, *Vacuum Technology”*, 3rd edition, North-Holland, Amsterdam, 1990.

[Gad-El-Hak, 1999] Mohamed Gad-El-Hak, “The Fluid Mechanics of Microdevices-The Freeman Scholar Lecture,” J. Fluids Engineering, March 1999, Vol. 121, pp. 5-33.

[Gass, et al., 1993] V. Gass, B. H. van der Schoot, S. Jeanneret, and N. F. de Rooij, Tech. Digest IEEE Transducers (Yokohama, 1993), p. 1048.

[Geng, Yuan, et al., 2001] Geng, X., H. Yuan, H. N. Oguz, A. Prosperetti, “Bubble-Based Micropump for Electrically Conducting Liquids,” J. Micromechanics and Microengineering, 11, 2001, pp. 270-276.

[Gerlach and Wurmus, 1995] Torsten Gerlach and Helmut Wurmus, “Working Principle and Performance of the Dynamic Micropump,” Sensors and Actuators A, Vol. 50, 1995, pp. 135-140.

[Gilbertson and Busch, 1996] Roger G. Gilbertson and John D. Busch , “A Survey of Micro-Actuator Technologies for Future Spacecraft Missions,” J. of the British Interplanetary Society, Vol. 49, 1996, pp. 129-138.

[Gilbert, Ananthasuresh, and Senturia, 1996] J. R. Gilbert, G. K. Ananthasuresh, and S. D. Senturia, "3D Modeling of Contact Problems and Hysteresis in Coupled Electro-Mechanics," MEMS '96, 1996, pp. 127-132.

[Gogoi and Mastrangelo, 1996] B. P. Gogoi and C. H. Mastrangelo, "A Low-Voltage Force-Balanced Barometric Pressure Sensor," Tech. Dig. 1996 IEDM Conf., pg. 529-532, San Francisco, CA, Dec. 8-11, 1996.

[Gogoi and Mastrangelo, 2000?] B. P. Gogoi and C. H. Mastrangelo, "Force Balanced Micromachined Pressure Sensors," IEEE Transactions on Electron Devices, 2000?, accepted, December, 1999.

[Gong, et al., 2000] Gong, Q., Z. Zhou, et al., "Design, Optimization and simulation on Microelectromagnetic pump," Sensors and Actuators A, 83, 2000, pp. 200-203.

[Goto, et al., 2002] Akira Goto, Motohiko Nohmi, Takaki Sakurai, Yoshiyasu Sogawa, "Hydrodynamic Design System for Pumps Based on 3-D CAD, CFD, and Inverse Design Method, J. Fluids Engineering, June 2002, Vol. 124, pp. 329-335.

[Goto and Zangeneh, 2002] Akira Goto and Mehrdad Zangeneh, "Hydrodynamic Design of Pump Diffuser Using Inverse Design Method and CFD," J. Fluids Engineering, June 2002, Vol. 124, pp. 319-328.

[Grate, et al., 1991] Jay W. Grate, Stuart W. Wenzel, and Richard M. White, "Flexural Plate Wave Devices for Cemical Analysis," Analytical Chemistry, Vol. 63, No. 15, August 1, 1991, pp. 1552-1561.

[Gravesen, et al., 1993] Peter Gravesen, Jens Branebjerg and Ole Sondergard Jensen, "Microfluidics-a review," J. Micromech. Microeng., Vol. 3, 1993, pp. 168-182.

[Griffel1968] William Griffel., "Plate Formulas"., Frederick Ungar Publising Co., New York., 1968.

[Grosjean, et al., 1999] Charles Grosjean, Xing Yang, and Yu-Chong Tai, "A Practical Thermopneumatic Valve," Technical Digest of IEEE International MEMS'99 Conference, Orlando, Florida, January, 1999.

[Gupta, et al., ?] A. Gupta, R. Bashir, G. W. Neudeck, and M. McElfresh, "Design of Piezoresistive Silicon Cantilevers with Stress Concentration Region (SCR) for Scanning Probe Microscopy (SPM) Applications,"

[Habermehl, et al., 2009] S. Habermehl, R. T. Apodaca, and R. J. Kaplar, "On dielectric breakdown in Silicon-rich Silicon nitride thin films," to be published in Applied Physics Letters, 94, 1 (2009).

[Habermehl, et al., 2005] S. Habermehl and R. T. Apodaca, "**Dielectric breakdown and Poole–Frenkel field saturation in silicon oxynitride thin films**," Applied Physics Letters, 86, 072103 (14 February 2005).

[Hagood IV, et al., 1999] Nesbitt W. Hagood IV, Davud C. Roberts, Laxman Saggere, Martin A. Schmidt, Mark Spearing, Kenneth S. Breuer, Richard Mlcak, Jorge A. Carretero, Farid Ganji, Hanqing Li, Kuo-Shen, Yu-Hsuan Su, Seward Pulitzer, ""Development of Micro-Hydraulic Transducer Technology," 10th International Conference on Adaptive Structures and Technologies, ICAST'99, Paris, France, October 11-13, 1999, pp. .

[Hahm, 2000] Geon Hahm, “Microfabricated, Silicon Spring Biased, Shape Memory Actuated Microvalve,” Proceedings of the IEEE Solid-State Sensor and Actuator Workshop, 230-233, June, 2000.

[Hahm, et al., 2000] Geon Hahm, Hal Kahn, Stephen M. Phillips, Arthur H. Heuer, “Fully Microfabricated, Silicon Spring Biased, Shape Memory Actuated Microvalve,” Solid-State Sensor and Actuator Workshop, Hilton Head Island, South Carolina, June 4-8, 2000, pp. 230-233.

[Haller and Moesner, 1998] Kristian K. Haller and Felix M. Moesner, “Theoretical Considerations on the Electrohydrodynamic Propulsion,” Institute of Robotics, Swiss Federal Institute of Technology Zurich (ETHZ), CH-8092 Zurich, Switzerland, Proc. ?, pp. 1121-1126.

[Hatch, Kamholz, et al., 2001] Hatch, Anson, Andrew Evan Kamholz, Gary Holman, Paul Yager, and Karl F. Böhringer, “A Ferrofluidic Magnetic Micropump,” Journal of microelectromechanical systems, 10 (2), 2001, pp. 215-221.

[Hayamizu, et al., 2003] Shunichi Hayamizu, Kusunoki Higashino, Yasuhisa Fujii, Yasuhiro Sando, Koji Yamamoto, “Development of a bi-directional valve-less silicon micro pump controlled by a driving waveform,” Sensors and Actuators A, Vol. 103, 2003, pp. 83-87.

[Henning, 1998] Henning, Albert K., “Microfluidic MEMS,” Proc. IEEE Aerospace Conference, paper 4.906, 1998.

[Herman, 1991] J. S. Herman and F. L. Terry, “A two-temperature technique for PECVD deposition of silicon dioxide,” IEEE Electron Device Letters, vol. 12, no. 5, pp. 236-237, May 1991.

[Ho and Tai, 1998] Chih-Ming Ho and Yu-Chong Tai, "Micro-Electro-Mechanical-Systems (MEMS) and Fluid Flows," Annu. Rev. Fluid Mech. 1998, Vol. 30, pp. 579-612.

[Hock, et al., 1997] Hock, T. E., Francis, et al., "Designing a Fluid Pump for Microfluidic cooling systems," Proc. MEMS'97 IEEE, 1997.

[Hosokawa and Maeda, 2001] Hosokawa K and Maeda R., "In-line pressure monitoring for microfluidic devices using a deformable diffraction grating," *Proc. IEEE Micro Electro Mechanical Systems (Interlaken, Switzerland)* (New York: IEEE), 2001, pp 174-177.

[Hughes, 2000] Michael Pycraft Hughes, "AC Electrokinetics: Applications for Nanotechnology," Nanotechnology, **11**, 2000, pp. 124-132.

[Huff, et al., 1990] Michael A. Huff, Michael S. Mettner, Theresa A. Lober, and Martin A. Schmidt, "A Pressure-Balanced Electrostatically-Actuated Microvalve, IEEE Solid-State Sensor and Actuator Workshop, 1990, pp. 123-127.

[Huff and Schmidt, 1992] Huff, M. and Schmidt, M., (Michael A. Huff, Michael S. Mettner, Theresa A. Lober, and Martin A. Schmidt) "Fabrication, Packaging, and Testing of a Wafer-Bonded Microvalve," Technical Digest, Solid-State Sensor and Actuator Workshop, p. 194, Hilton Head, SC, June 22-25, 1992. Correct authors?

[Huff, et al., 1993] Huff, M., Gilbert, J., and Schmidt, M., "Flow Characteristics of a Pressure-Balanced Microvalve," Digest of Techical Papers, Transducers' 93, Yokohama, Japan, June 7-10, 1993.

[Hunter and Lafontaine, 1992] Hunter, I. W. and S. Lafontaine, "A Comparison of Muscle with Artificial Actuators, Solid-State Sensor and Actuator, Hilton Head Island, IEEE, 1992, p. 178-185.

[Ikuta, et al., 2000] Koji Ikuta, Tadahiro Hasegawa and Takao Adachi, "SMA Micro Pumps and Switching Valves for Biochemical IC Family," 2000 International Symposium on Micromechatronics and Human Science, IEEE, 2000, pp. 169-174.

[Ishida and Martynov, 2002] Akira Ishida and Valery Martynov, "Sputter-Deposited Shape-Memory Alloy Thin Films: Properties and Applications," MRS Bulletin, February 2002, pp. 111-114.

[Jen and Lin, 2002] Chun-Ping and Yu-Cheng Lin, "Design and Simulation of Bi-Directional Microfluid Driving Systems," J. Micromechanics and Microengineering, **12**, 2002, pp. 115-121.

[Jansen, 2001] J. F. Jansen, "New Piezoelectric Pump," Final Report, FY 2001 ORNL Laboratory Directed Research and Development Annual Report, Project Number: 00-3210-005C, 2001.

[Jensen and Howell, 2003?] Brian D. Jensen and Larry L. Howell, "Bistable Configurations of Compliant Mechanisms with Translational Joints," submitted to J. Mechanical Design, 2003.

[Jensen, et al., 2001] Brian D. Jensen, Matthew B. Parkinson, Katsuo Kurabayashi, Larry L. Howell, Michael S. Baker, "Design Optimization of a Fully-Compliant Bistable Micro-Mechanism," Proc. 2001 ASME International Mechanical Engineering Congress and Exposition, November 11-16, 2001, New York, NY.

[Jeong and Yang, 2000] Ok Chan Jeong and Sang Sik Yang, “Fabrication of a thermopneumatic microactuator with a corrugated p+ silicon diaphragm,” Sensors and Actuators, Vol. 80, 2000, pp. 62-67.

[Jeong and Yang, 2000] Ok Chan Jeong and Sang Sik Yang, “Fabrication and Test of a thermopneumatic micropump with a corrugated p+ diaphragm,” Sensors and Actuators, Vol. 83, 2000, pp. 249-255.

[Jerman, 1990] Jerman, H., “Electrically-Activated Micromachined Diaphragm Valves,” J. Micromech. Microeng. 4, 1994, pp. 210-216 and [Technical Digest, Solid-State Sensor and Actuator Workshop, pp. 67, Hilton Head, SC, June 4-7, 1990.]

[Jerman, 1991] Hal Jerman, “Electrically-Activated, Normally-Closed Diaphragm Valves,” Transducers ’91, 1991 International Conference on Solid-State Sensors, and Actuators, pp. 1045-1048.

[Jerominek, 2008] Jerominek., “Low temperature vacuum hermetic wafer-level package for uncooled microbolometer FPAs,” *Proceedings of SPIE*, 6884 (2008) 1-8.

[Jie, Diao, et al., 2000] Dai Jie, Xu Diao, Khoo Cheong, and Lam Khin Yong, “Navier-Stokes Simulations of Gas Flow in Micro Devices,” J. Micromechanics and Microengineering, **10**, 2000, pp. 372-379.

[Jiang, Ng, Lam, after 1999] T. Y. Jiang, T. Y. Ng and K. Y. Lam, “Dynamic Analysis of an Electrostatic Micropump,” after 1999

[Johnson and Bokaie, 1998] John, D. and Bokaie, M. “Valves for Instrumentation and Propulsion Systems in Microspacecraft,” Proceedings, 9th Advanced Space Propulsion Workshop, JPL D-15671, Jet Propulsion Laboratory, Pasadena, CA, March 11-13, 1998.

[Johnson and Warne, 1995] William A. Johnson and Larry K. Warne, “Electrophysics of Micromechanical Comb Actuators,” *Journal of Microelectromechanical Systems*, Vol. 4, No. 1, pp. 49-59, 1995.

[Joung, Shen, et al., 2000] Joung, J., J. Shen, and Piotr Grodzinski, “Micropumps Based on Alternating High-Gradient Magnetic Fields,” IEEE Transactions on Magnetics, 36 (4), 2000, pp. 2012-2014.

[Judy, Tamagawa, et al., 1991] Jack W. Judy, T. Tamagawa, Dennis L. Polla, “Surface-Machined Micromechanical Membrane Pump,” Proceedings of the IEEE 1991 Micro Electro Mechanical Systems Workshop (MEMS’91), Nara, Japan, 1991.

[Judy and Muller, 1996] Jack W. Judy and Richard. S. Muller, “Magnetic microactuation of torsional polysilicon structures,” *Sensors and Actuators A (Physical)*, vol. A53, no. 1-4, pp. 392-396, 1996.

[Judy and Muller, 1997] Jack W. Judy and Richard. S. Muller, “Magnetically Actuated, Addressable Microstructures” *IEEE Journal of Microelectromechanical Systems*, vol. 6, no. 3, pp. 249-256, 1997.

[Judy, Yang, et al., 2000] Jack W. Judy, Henry Yang, Nosang V. Myung, Ken C.-K. Yang, Morton Schwartz, and Ken Nobe, “Integrated Ferromagnetic Microsensors and Microactuators”, *Proceedings of the Fifth International Symposium on Magnetic Materials, Processes, and*

Devices, 198th Meeting of the Electrochemical Society, Phoenix, AZ (October 22-27, 2000), pp. 456-468.

[Judy, 2001] Jack W. Judy, "Microelectromechanical Systems (MEMS): fabrication, design and applications, Smart Materials and Structures, Vol. 10, 2001, pp. 1115-1134.

[Kahn, et al., 1997] H. Kahn, W. L. Benard, M. A. Huff, and A. H. Heuer, "Titanium-Nickel Shape Memory Thin Film Actuators for Micromachined Valves," Mat. Res. Soc. Symp. Proc., Vol. 444, 1997, pp. 227-232.

[Kahn, et al., 1998] H. Kahn, M. A. Huff, and A. H. Heuer, "The TiNi shape-memory alloy and its applications for MEMS," J. Micromech. Microeng., Vol. 8, 1998, pp. 213-221.

[Kamper, Döpper, et al., 1998] Kamper, K.-P., J. Döpper, W. Ehrfeld, and S. Oberbeck., "A self-Filling Low-Cost Membrane Micropump," Proc. of the 11th IEEE MEMS 1998 Technical Digest, Heidelberg, Germany, January 25-29, 1998, pp 432-437.

[Kapels, et al, 2000] Hergen Kapels, Robert Aigner, and Josef Binder, "Fracture Strength and Fatigue of Polysilicon Determined by a Novel Thermal Actuator", IEEE Transactions on Electron Devices, Vol. 47, No. 7, July 2000, pp. 1522-1528.

[Karniadakis and Beskok, 2002] George Em Karniadakis and Ali Beskok, *Micro Flows, Fundamentals and Simulation*, Springer-Verlag, New York, 2002.

[Kim, Lee, at al., 2002] Dong Sung Kim, Kwang-Cheol Lee, Tai Hun Kwon, and Seung S. Lee, "Micro-Channel Filling Flow Considering Surface Tension Effect," J. Micromechanics and Microengineering, **12**, 2002, pp. 236-246.

[Khoo and Liu, 2000] Melvin Khoo and Chang Liu, "A Novel Micromachined Magnetic Membrane Microfluid Pump," 22nd Annual International Conference of the IEEE Engineering in Medicine and Biology Society, Chicago, IL, 2000. pp. 1-4.

[Kluge, et al., 1998] Stefan Kluge, Gerhard Klink, and Peter Woias, "A fast-switching, low-power pneumatic microvalve with electrostatic actuation made by silicon micromachining," American Laboratory, March 1998, pp. 17-18.

[Ko, et al., 2003] Sang Choon Ko, Yong Chul Kim, Seung Seob Lee, Seung Ho Choi, Sang Ryong Kim, "Micromachined piezoelectric membrane acoustic device, Sensors and Actuators A, Vol. 103, 2003, pp. 130-134.

[Koch, Harris, et al., 1997] M. Koch, N. Harris, R. Maas, A G R Evans, N.M. White, and A. Brunnschweiler, "A novel micropump design with thick-film piezoelectric actuation," Meas. Sci. Technol., Vol. 8, 1997, pp. 49-57.

[Koch, Evans, et al., 1998] M. Koch, A G R Evans, and A. Brunnschweiler, "The Dynamic Micropump Driven with A Screen Printed PZT Actuator," J. Micromechanics and Microengineering, **8**, 1998, pp. 119-122.

[Koch, Harris, et al., 1998] Michael Koch, Nich Harris, Alan G R Evans, Neil M. White, and Arthur Brunnschweiler, "A novel micromachined pump based on thick-film piezoelectric actuation," Sensors and Actuators A Physical, Vol. 70, 1998, pp. 98-103.

[Koch, Schabmuller, et al., 1999] M. Koch, C.G.J. Schabmuller, A.G.R. Evans, A. Brunnschweiler, "Micromachined chemical reaction system," Sensors and Actuators A Physical, Vol. 74, 1999, pp. 207-210.

[Koeneman, Busch-Vishnaic, et al., 1997] Paul B. Koeneman, Ilene J.Busch-Vishnaic, and Kristin L. Wood, “Feasibility of Micro Power Supplies for MEMS, J. Microelectromechanical Systems, Vol. 6, No. 4, December 1997, pp. 355-362.

[Kohl and Skrobanek, 1998] Kohl, M. and K. D. Skrobanek, “Linear Microactuators Based on the Shape Memory Effect,” Sensors and Actuators A, 70, 1998, pp.104-111.

[Koltay,Taoufik, et al., 2003] P. Koltay, S. Taoufik, G. Birkle, R. Steger, H. Sandmaier, R. Zengerle, “Dispensing Well Plate (DWP): A highly integrated nanoliter dispensing system,” Proc. of TRANSDUCERS 2003, Boston, 2003, pp. 16-19.

[Kraus, Baltzer, et al., 1997] Th. Kraus, M. Baltzer, and E. Obermeier, “”Design and Fabrication of Surface Micromachined Micromotors with Large Dimensions, J. Micromech. Microeng., Vol. **7**, 1997, pp. 196-199.

[Krulevitch, 1994] Krulevitch, Peter Allen, *Micromechanical Investigations of Silicon and Ni-Ti-Cu Thin Films*, Ph.D. Dissertation, Univ. Calif., Berkeley, 1994.

[Krulevitch, et al., 1996] Peter Krulevitch, Abraham P. Lee, Philip B. Ramsey, James C. Trevino, Julie Hamilton, and M. Allen Northrup, “Thin Film Shape Memory Alloy Microactuators,” J. Microelectromechanical Systems, Vol. 5, No. 4, December 1996, pp. 270-282.

[Kuribayashi, 2000] Kuribayashi, Katsutoshi, “Micro SMA Actuator and Motion Control,” Proc. 2000 International Symposium on Micromechanatronics and Human Science, Nagoya, Japan, Oct. 22-25, 2000, pp. 35-42.

[Lai, et al., 2001] B.-K. Lai, G. Hahm, L. You, C.-L. Shih, H. Kahn, S. M. Phillips, and A. H. Heuer, "The Characterization of TiNi Shape-Memory Actuated Microvalves," Mat. Res. Soc. Symp. Proc., Vol. 657, 2001, EE8.3.1-EE8.3.6.

[Lee and Kim, 1998] Junghoon Lee and Chang-Jin (CJ) Kim, "Liquid Micromotor Driven by Continuous Electrowetting," MEMS'98, Heidelberg, Germany, 1998.

[Lee and Kim, 2000] Junghoon Lee and Chang-Jin (CJ) Kim, "Surface-Tension-Driven Microactuation Based on Continuous Electrowetting," J. Microelectromechanical Systems, Vol. 9, No. 2, June 2000, pp 171-180.

[Lee, Wong, et al., 2001a] Sylvanus Yuk Kwan Lee, Man Wong, and Yitshak Zohar, "Pressure Losses in Microchannels with Bends," 14th **IEEE** Int. Conf. on Micro Electro Mechanical Systems, MEMS'01, Jan. 2001 pp 491-494.

[Lee, Wong, et al., 2001b] Wing Yin Lee, Man Wong, and Yitshak Zohar, "Flow Separation in Constriction Microchannels," Proc. 14th Int. Conf. on Micro. Electro. Mechanical Systems, MEMS'01, 2001, pp 495-498.

[Lee, Wong, et al., 2001c] Sylvanus Yuk Kwan Lee, Man Wong, and Yitshak Zohar, "Gas Flow in a Microchannels with Bends," J. Micromechanics and Microengineering, **11**, 2001, pp. 635-644.

[Lee, Yu, et al., 2002] Sylvanus Yuk Kwan Lee, Zeta Tak For Yu, Man Wong, and Yitshak Zohar, "Gas Flow in a Microdevice with a Mixing Layer Configuation," J. Micromechanics and Microengineering, **12**, 2002, pp. 96-102.

[Lemoff and Lee, 2000] Asuncion V. Lemoff and Abraham P. Lee, "An AC magnetohydrodynamic micropump," Sensors and Actuators B Chemical, Vol. 63, 2000, pp. 178-185.

[Li, et al., 2001] Shifeng Li, Yang Liu, and Shaochen Chen, "Dynamic Modeling and Optimization of a Valveless PZT Micropump," Microfluidics and BioMEMS, Proc. Of SPIE, Vol. 4560, 2001, pp. 67-74.

[Li and Chen, 2003] Shifeng Li and Shaochen Chen, "Analytical analysis of a circular PZT actuator for valveless micropumps," Sensors and Actuators A, Vol. 104, 2003, pp. 151-161.

[Li, et al., 2000] H. Q. Li, D.C. Roberts, J.L. Steyn, K.T. Turner, J.A. Carretero, O. Yaglioglu, Y.-H. Su, L. Saggere, N.W. Hagood, S.M. Spearing, and M.A. Schmidt, "A High Frequency High Flow Rate Piezoelectrically Driven MEMS Micropump," Proceedings IEEE Solid State Sensors and Actuators Workshop, Hilton Head, June 2000.

[Li, Lin, et al., 2002] Wang-Long Li, Jau-Wen Lin, Shun-Ching Lee, and Ming-Da Chen, "Effects of Roughness on Rarefied Gas Flow in Long Microtubes," J. Micromechanics and Microengineering, **12**, 2002, pp. 149-156.

[Lin, et al., 1991] L. Lin, A. P. Pisano, and A. P. Lee, "Microbubble Powerd Actuator," Tech. Digest. IEEE Transducers (San Francisco, CA, 1991), pp. 1041-1044.

[Lin, et al., 1996] Lin, Y. C., Hesketh, P., Boyd, J., Lunte, S., and Wilson, G., "Characteristics of a Polyimide Microvalve," Technical Digest, Solid State Sensor and Actuator Workshop, Hilton Head, SC, June 3-6, 1996, pp. 113-116.

[Lin, 2000] Liwei Lin, “MEMS Post-Packaging by Localized Heating and Bonding,” IEEE Transactions on Advanced Packaging, Vol. 23, No. 4, November 2000, pp. 608-616.

[Linderman, Sett, et al., 2001] Ryan J. Linderman, Subbam Sett, and Victor M. Bright, “The Resonant Micro Fan for Fluidic Transport, Mixing and Particle Filtering,” Proc. 2001 ASME International Mechanical Engineering Congress and Exposition, IMECE2001/MEMS-23868, New York, November 11-16, 2001, pp. 1-8.

[Linderman, Kladitis, et al., 2002] Ryan J. Linderman, Paul E. Kladitis, and Victor M. Bright, “Development of the Micro Rotary Fan,” Sensors and Actuators A, **95**, 2002, pp. 135-142.

[Linnemann, Woias, et al., 1998] Linnemann, R., P. Woias, C.-D. Senfft, and J. A. Ditterich, “A Self-Priming and Bubble-Tolerant Piezoelectric Silicon Micropump for Liquids and Gases,” Proc. of the MEMS ´98, 25.-29 January, 1998, Heidelberg, pp. 532-537

[Löfdahl and Gad-El-Hak, 1999] Lennart Löfdahl and Mohamed Gad-El-Hak, ”MEMS Applications in Turbulence and Flow Control,” in Progress in Aerospace Sciences, 35, 1999, pp. 101-203.

[Luginbuhl, Collins, et al., 1997] Philippe Luginbuhl, Scott D. Collins, Georges-Andre Racine, and Marc-Alexis Gretillat, Nicolaas F. de Rooij, Keith G. Brooks, and Nava Setter, “Microfabricated Lamb Wave Device Based on PZT Sol-Gel Thin Film for Mechanical Transport of Solid Particles and Liquids,” Journal of Microelectromechanical Systems 6, (4), 1997, pp. 337-346.

[Maillefer, Lintel, et al., 1999] Maillefer, D., Harald van Lintel, Gilles Rey-Mermet, and Roland Hirschi, “A High-Performance Silicon Micropump for an Implantable Drug Delivery System,”

Proc. 1999 IEEE Conference on MicroElectroMechanical Systems (MEMS'99), Orlando, Florida, pp. 541-546.

[Maillefer, Gamper, et al., 2001] Maillefer, Didier, Stephan Gamper, Beatrice Frehner, Patrick Balmer, Harald van Lintel, Philippe Renaud, "A High-Performance Silicon Micropump for Disposable Drug Delivery System," Proc. MEMS'01, 2001, pp. 413-417.

[Makino, et al., 1999] Eiji Makino, Kazuhiro Kato, and Takayuki Shibata, "Thermo-mechanical properties of TiNi shape memory thin film formed by flash evaporation," Sensors and Actuators A (Physical), Vol. 75, 1999, 156-161.

[Makino, et al., 2001] Eiji Makino, Takashi Mitsuya, and Takayuki Shibata, "Fabrication of TiNi shape memory micropump, Sensors and Actuators A, Vol. 88, 2001, pp. 256-262.

[Makino, et al., 2000a] Eiji Makino, Takashi Mitsuya, and Takayuki Shibata, "Micromachining of TiNi shape memory thin film for fabrication of micropump," Sensors and Actuators A Physical, Vol. 79, 2000, pp. 251-259.

[Makino, et al., 2000b] Eiji Makino, Takashi Mitsuya, and Takayuki Shibata, "Dynamic actuation properties of TiNi shape memory diaphragm," Sensors and Actuators A Physical, Vol. 79, 2000, pp. 128-135.

[Makino, et al., 1999] Eiji Makino, Takayuki Shibata, and Kazuhiro Kato, "Dynamic thermo-mechanical properties of evaporated TiNi shape memory thin film," Sensors and Actuators A (Physical), Vol. 78, 1999, 163-167.

[Makino, et al., 1998] Eiji Makino, M. Uenoyama, and Takayuki Shibata, "Flash evaporation of TiNi shape memory thin film for microactuators," Sensors and Actuators A (Physical), Vol. 71, 1998, 187-192.

[Makino and Shibata, in press] Eiji Makino and Takayuki Shibata, “Fusion Bonding of Si Wafers and fabrication of Checkvalve for Micropump,” J. Surf. Finish. Soc. Jpn., in press (in Japanese).

[Manz and Effenhauser, 1994] A. Manz, C. S. Effenhauser, N. Burggraf, D. J. Harrison, K. Seiler, and K. Fluri , “Electroosmotic pumping and electrophoretic separations for miniaturized chemical analysis systems,” *J. Micromech. Microeng.* **4,** 1994, 257-264.

[Manz, Harrison, et al., 1990] A. Manz, D. J. Harrison, J. C. Fettinger, E. Verpoorten, H. Ludi, and H. M. Widner, “Integrated Electroosmotic Pumps and Flows Manifolds for Total Chemical Analysis Systems,” Tech, Digest IEEE Transducers (San Franciso, CA, 1991), pp. 939-941.

[Martin, et al., 1990] Bret A. Martin, Stuart W. Wenzel, and Richard M. White, “Viscosity and Density Sensing with Ultrasonic Plate Waves,” Sensors and Actuators, A21-A23, 1990, pp. 704-708.

[Matsumoto and Colgate, 1990] Matsumoto, M. and J.E. Colgate, “Preliminary Investigations of Micropumping Based on Electrical Control of Interfacial Tension,” MEMS’90, Napa Valley, CA, IEEE, 1990.

[McNamara and Gianchandani, 2003] Shamus McNamara and Yogesh B. Gianchandani, “A Micromachined Knudsen Pump for On-Chip Vacuum,” Transducers ’03, 12th International Conference on Solid State Sensors, Actuators and Microsystems, Boston, June 8-12, 2003, pp. 1919-1922.

[Meckes, et al., 1997] Andreas Meckes, Jörg Behrems, and Wolfgang Benecke, “Electromagnetically Driven Microvalve Fabricated in Silicon,” Transducers ’97, 1997

International Conference on Solid-State Sensors and Actuators, Chicago, June 16-19, 1997, pp. 821-824.

[Meng, et al., 1997] Audra H. Meng and Richard M. White, "Cell growth assay using the ultrasonic flexural plate-wave device," Micro- and Nanofabricated Electro-Optical Mechanical Systems for Biomedical and Environmental Applications for Biomedical and Environmental Applications, SPIE Vol. 2978, 1997, pp. 227-233.

[Meng, et al., 2000] Audra H. Meng, Nam-Trung Nguyen, and Richard M. White, "Focused Flow Micropump Using Ultrasonic Flexural Plate Waves," Biomedical Microdevices, Vol. 2, No. 3, 2000, pp. 169-174.

[Messner, et al., 1998] S. Messner, M. Muller, V. Burger, J. Schaible, H. Sandmaier, R. Zengerle, "A Normally-Closed, Bimetallically Actuated 3-Way Microvalve for Pneumatic Applications," Proc. 11th IEEE MEMS 1998 Technical Digest, Heideberg, Germany, 1998, pp. 40-44.

[Messner, Schaible, et al., 2003] S. Messner, J. Schaible, J. Vollmer, H. Sandmaier, R. Zengerle, "Electrostatic Driven 3-Way Silicon Microvalve for Pneumatic Applications," Proc. IEEE The Sixteenth Annual International Conference on Micro Electro Mechanical Systems, MEMS2003, Kyoto, Japan, January 20- 23, 2003, pp. 88-91.

[Morita, 2003] Takeshi Morita, "Miniature Piezoelectric Motors," Sensors and Actuators A, Vol. 103, 2003, pp. 291-300.

[Moroney, et al., 1991] R. M. Moroney, R.M. White, and R.T. Howe, ASME Winter Annual Meeting DSC-32, 181, 1991.

[Moroney, 1995] Richard Morgan Moroney, III, *Ultrasonic Microtransport*, Ph.D. Dissertation, EECS Department, University of California, Berkeley, 1995.

[Moroney, et al., 1991a] R. M. Moroney, R.M. White, and R.T. Howe, "Microtransport induced by ultrasonic Lamb waves," Applied Physics Letters, Vol. 59, No. 7, 12 August 1991, pp. 774-776.

[Moroney, et al., 1991b] R. M. Moroney, R.M. White, and R.T. Howe, "Ultrasonically Induced Microtransport," Proc. IEEE 1991 Micro Electro Mechanical Systems Workshop (MEMS'91), Nara, Japan, 1991, pp. 277-282.

[Morris and Forster, 2000] Christopher J. Morris and Fred K. Forster, "Optimization of a circular piezoelectric bimorph for a micropump driver," J. Micromech. Microeng., Vol. 10, 2000, pp. 459-465.

[Mourlas, Stark, et al.,1996] Nicholas Mourlas, Kevin C. Stark, Mehran Mehregany, Stephen M. Phillips, "Exploring Polysilicon Micromotors for Data Storage Microdisks," Proceedings of the 9th IEEE International Workshop on MEMS, MEMS96 digest, San Diego, California, February, 1996, pp. 198-203.

[Mu, Hung, et al., 1999] Mu, Y. H., N. P. Hung, et al., "Optimisation Design of a Piezoelectric Micropump," The International Journal of Advanced Manufacturing Technology, 15, 1999, pp. 573-576.

[Mueller, 1997] Juergen Mueller, J., "Thruster Options for Microspacecraft: A review and Evaluation of Existing Hardware and Emerging Technologies," 33rd AIAA/ASME/SAE/ASEE Joint Propulsion Conf., Seattle, WA, July 6-9, 1997, AIAA 97-3058.

[Mueller, 2000] Juergen Mueller, “Review and Applicability Assessment of MEMS-Based Microvalve Technologies for Microspacecraft Propulsion,” Micropropulsion for Small Spacecraft, Progress in Astronautics and Aeronautics, Vol. 187, edited by Micci, M. and Ketsdever, A., AIAA, Reston, VA, 2000, Chap. 19, pp. 449-476.

[Mueller, et al., 2002] Juergen Mueller, Colleen Marrese, John Ziemer, Amanda Green, et al., “JPL Micro-Thrust Propulsion Activities,” AIAA 2002-5714, Nanotech 2002, Sept. 9-12, 2002, Houston, TX, pp. 74-87.

[Mutlu, Yu, et al., 2002] Mutlu, S., Yu, Cong, Selvaganapathy, P., Svec, F; Mastrangelo, C. H.; Frechet, J. M. J., “Micromachined porous polymer for bubble free electro-osmotic pump,” IEEE International Conference on Micro Electro Mechanical Systems, Technical Digest, 15th, Las Vegas, NV, , Jan. 20-24, 2002 (2002), pp. 19-23.

[Morishita, et al., 1997] S. Morishita, S. Sugahara, M. Matsumura, “Atomic-layer chemicals-vapor-deposition of silicon-nitride,” Applied Surface Science, 112 (1997), pp. 198-204.

[Najafi, 2003] A. Selvakumar, and K. Najafi, "Vertical Comb Array Microactuators," IEEE/ASME Journal of Microelectromechanical Systems (JMEMS), Volume: 12 Issue: 4, pp. 440-449, 08/2003

[Najafi, 1992] S.T. Cho, K. Najafi, C.L. Lowman, K.D. Wise, "An Ultrasensitive Silicon Pressure-Based Microflow Sensor," IEEE Trans. Electron Devices, Vol. ED-39, No. 4, pp. 825-835, 04/1992

[Najafi, 1991] K. Najafi, "Smart Sensors," Micromech. & Microeng., 1, pp. 86-102, 06/1991.

[Ng, 2003] W. C. H. Ng, K. W. Chew, and S. F. Chu, “Characterization and comparison of PECVD silicon nitride and silicon oxynitride dielectric for MIM capacitors,” IEEE Electron Device Letters, vol. 24, no. 8, pp. 506-508, Aug. 2003.

[Nakamura, Nakamura, et al., 1997] Nakamura, Yousuke, Shigeo Nakamura, Lionel Buchaillot, and Hiroyuki Fujita, “A Three-Dimensional Shape Memory Alloy Loop Actuator,” Proc. IEEE Int. Workshop on Micro Electro Mechanical Systems (MEMS 97), Nagoya, Japan, January 26-30, 1997, pp. 262-266.

[National Academy Press, 1977] Microelectromechanical Systems: Advanced Materials and Fabrication Methods, National Materials Advisory Board, National Academy Press, 1997.

[Neagu, 1998] Cristina Rodica Neagu, *A Medical Microactuator Based on an Electrochemical Principle*, PhD Dissertation, Micromechanics of the MESA Research Institute, University of Twente, Enschede, The Netherlands, 1998.

[Nguyen, et al., 1998a] N. T. Nguyen, R. G. Doering, and R. M. White, Supplement Digest, Hilton Head Workshop, Hilton Head, 31 (1998).

[Nguyen, et al., 1998b] N. T. Nguyen, R. G. Doering, A. Lai, and R. M. White, “Computational Fluid Dynamics Modeling of Flexural Plate Wave Pumps,” IEEE International Ultrasonics Symposium (Sendai, Japan, 1998). Pp. 431-434.

[Nguyen, et al., 2002] Nam-Trung Nguyen, Xiaoyang Huang, Toh Kok Chuan, “MEMS-Micropumps: A Review,” Transactions of the ASME, Vol. 124, June 2002, pp. 384-392.

[Nguyen, et al., 2000] Nam-Trung Nguyen, Audra H. Meng, Justin Black, Richard M. White, "Integrated flow sensor for in situ measurement and control of acoustic streaming in flexural plate wave micropumps," Sensors and Actuators, Vol. 79, 2000, pp. 115-121.

[Nguyen and Huang, 2000] Nam-Trung Nguyen and Xiaoyang Huang, "Numerical Simulation of Pulse-Width-Modulated micropumps with Diffuser/Nozzle Elements," Technical Proceedings of the 2000 International Conference on Modeling and Simulation of Microsystems, San Diego, CA, March 27-29, 2000, pp. 636-639.

[Ohnstein, et al., 1990] Ohnstein, T., Fukiura, T., Ridley, J., and Bonne, U., "Micromachined Silicon Microvalve," IEEE Proceedings, CH2832-4/90, Napa Valley, CA, Feb. 11-14, 1990, pp. 95-98.

[Olsson, Stemme, et al., 1995] Olsson, Anders, Göran Stemme, and Erik Stemme, "A Valve-Less Fluid Pump with Two Pump Chambers," Sensors and Actuators A, 47 (1-3), 1995, pp. 549-556.

[Olsson, Enoksson, et al., 1995] Olsson, Anders, Peter Enoksson, Göran Stemme, and Erik Stemme, "A Valve-Less Planar Pump in Silicon," Trandsducers '95 - Eurosensors IX, The 8th International Conference on Solid-State Sensors and Actuators, and Eurosensors IX, Stockholm, Sweden, June 25-29, 1995, pp. 291-294.

[Olsson, Enoksson, et al., 1996] Olsson, Anders, Peter Enoksson, Göran Stemme, and Erik Stemme, "A Valve-Less Planar Pump, Isotropically Etched in Silicon," J. Micromechanics and Microengineering, 6, pp. 87-91.

[Olsson, Larsson, et al., 1998] Olsson, Anders, Olle Larsson, Johan Holm, Lars Lundbladh, Ove Öhman, Göran Stemme, “Valve-Less Diffuser Micropump Fabricated Using Thermoplastic Replication,” Sensors and Actuators A, 64, 1998, pp. 63-68.

[Olsson, Stemme, et al., 1999] Anders Olsson, Göran Stemme and Erik Stemme, “A Numerical Design Study of the Valveless Diffuser Pump Using a Lumped-Mass Model,” J. Micromechanics and Microengineering, **9**, 1999, pp. 34-44.

[Olsson, Stemme, et al., 2000] Anders Olsson, Göran Stemme and Erik Stemme, “Numerical and Experimental Studies of Flat-Walled Diffuser Elements for Valve-Less Micropumps,” Sensors and Actuators A, 84, 2000, pp. 165-175.

[Oosterbroek, Berenschot, et al., 1999] R. E. Oosterbroek, J. W. Berenschot, S. Schlautmann, G. J. M. Krijnen, T. S. J. Lammerink, M. C. Elwenspoek, and A van den Berg, “Designing, Simulation and Realization of In-Plane Operating Micro Valves, using New Etching Techniques,” J. Micromechanics and Microengineering, **9**, 1999, pp. 194-198.

[Osterberg, et al., 1994] P. Osterberg, H. Yie, X. Cai, J. White, and S. Senturia, “Self-Consistent Simulation and Modeling of Electrostatically Deformed Diaphragms,” Proc. IEEE Micro Electro Mechanical Systems Workshop, Oiso, Japan, Jan. 25-28, 1994, pp. 28-32.

[Papageorgiou, Bledsoe, et al., 2001] , D. Papageorgiou, S. C. Bledsoe, M. Gulari, J. F. Hetke, D. J. Anderson, and K. D. Wise,“A Shuttered Probe with In-Line Flowmeter for Chronic In-Vivo Drug Delivery” Proc. IEEE 2001 Micro Electro Mechanical Systems Workshop (MEMS’01), 2001, pp. 212-215.

[Papavasiliou, 2001] Alexandros Prodromos Papavasiliou, *Bubble-Actuated Planar Microvalves*, PhD Dissertation, Mechanical Engineering, University of California, Berkeley, Spring 2001.

[Paul C. H. Li, 2006]. Paul C. H. Li., "Microfluidic lab-on-a-Chip" Taylor & Francis Group., Boca Raton, FL., 2006.

[Park and Prahl, 1988] S. Park, W. Ko, and J. Prahl, "A Constant Flow-rate microvalve Actuator Based on Silicon and Micromachining Technology," Proc. IEEE Solid-State Sensor and Actuator Workshop, Hilton Head Island, SC, June 6-9, 1988, pp. 136-139.

[Parkinson, et al., 2000] Matthew B. Parkinson, Brian D. Jensen, Gregory M. Roach, "Optimization-Based design of a Fully-Compliant Bistable Micromechanism," Proc. DETC'00, ASME 2000 Design Engineering Technical Conferences and Computers and Information in Engineering Conference, Baltimore, Maryland, September 10-13, 2000.

[Parr, 1998] A. G. Parr Jr., *Design and Characterization of a Patterned Actuator and the Design and Development of a Smart Controller for a Microfluidic Valve*, MS Thesis, Case Western Reserve University, Department of Electrical Engineering and Applied Physics, 1998.

[Potapov and de Silva, 2000] Potapov, P. L. and E. P. de Silva, "Time Response of Shape Memory Alloy Actuators," J. of Intelligent Materials Systems and Structures, 11 (Feb.), 2000, pp. 125-134.

[Pourahmadi, et al., 1990] Fazad Pourahmadi, Lee Christel, Kurt Petersen, Joseph Mallon, Janusz Bryzek, "Variable-Flow with Silicon Fusion Bonding," Technical Digest, Solid-State Sensor and Actuator Workshop, Hilton Head, SC, June 4-7, 1990, pp. 78-81.

[Puntambekar and Ahn, 2002] Aniruddha Puntambekar and Chong H. Ahn, “Self-Aligning Microfluidic Interconnects for glass- and plastic-based Microfluidic Systems,” J. Micromechanics and Microengineering, **12**, 2002, pp. 35-40.

[Quandt and Seemann, 1995] E. Quandt and K. Seemann, “Fabrication of Giant Magnetostrictive Thin Film Actuators,” Proc. IEEE MEMS 1995, 1995, pp. 273-277.

[Ray, et al., 1992] Curtis A. Ray, Charles L. Sloan, A. David Johnson, John D. Busch, Bruce R. Petty,”A Silicon-Based Shape Memory Alloy Microvalve,” Mat. Res. Soc. Symp. Proc., Vol. 276, 1992, pp. 161-166.

[Reynaerts, Peirs, et al., 1996a] Dominiek Reynaerts, Jan Peirs, and Hendrik Van Brussel, “A SMA-Actuated Implantable System For Delivery of Liquid Drugs,” Actuator 96, 5th International Conference on New Actuators, Bremen, Germany, 26-28 June 1996, pp. 379-382.

[Reynaerts, Peirs, et al., 1996b] Dominiek Reynaerts, Jan Peirs, and Hendrik Van Brussel, “Design of a Shape Memory Alloy Actuated Implantable Drug Delivery System,” Eurosensors X, Leuven, Belgium, 8-11 September 1996, pp. 1185-1188.

[Richter, et al., 1990] A. Richter, H. Sandmaier, and A. Plettner, Proc. Micro System Technologies 90 (Berlin, 1990), p. 812.

[Richter, Plettner, et al., 1991] A. Richter, A. Plettner, et al., “Electrodynamic (EHD) Pumping and Flow Measurement,” Proc. IEEE Micro Electro Mechanical Systems Workshop (MEMS’91), Nara, Japan, 1991, 271-276.

[Richter, et al., 1991] A. Richter, A. Plettner, et al., " A Micromachined Electrodynamic (EHD) Pump," Sensors and Actuators A, 29 (2), 1991, pp. 159-168.

[Richter, et al., 1997] Richter, M., R. Linnemann, et al., "Design Methodology for Gas and Liquid Micropumps," Proc. Eurosensors XI, Warsaw, 1997.

[Richter, Linnemann, et al., 1998] Richter, M., R. Linnemann, and P. Woias, "Robust Design of Gas and Liquid Micropumps," Sensors and Actuators A, 68, 1998, pp. 480-486.

[Robert, Danel, et al., 1997] Ph. Robert, J. S. Danel, and P. Villard, "The Electrostatic Ultrasonic Micromotor," J. Micromech. Microeng. Vol. **7**, 1997, pp. 170-172.

[Roth, 1990] A. Roth, *Vacuum Technology*, 3rd edition, North-Holland, Amsterdam, 1990.

[Sadler, et al., 1999] Daniel J. Sadler, Kwang W. Oh, and Chong H. Ahn, "A New Magnetically Actuated Microvalve for Gas and Liguid Control Applications," Symposium on Nano-, Micro-, and Mesoscale Technologies in Science and Engineering," May 13, 1999.

[Saif, Alaca, et al., 1999] Saif, M. T. A., B. Erdem Alaca, and Huseyin Sehitoglu, "Analytical Modeling of Electrostatic Membrane Actuator for Micro Pumps," Journal of microelectromechanical systems, 8 (3), pp. 335-345.

[Sammarco and Burns, 2000] Timothy S. Sammarco and Mark A. Burns, "Heat-Transfer Analysis of Microfabricated Thermocapillary Pumping and Reaction Devices," J. Micromechanics and Microengineering, **10**, 2000, pp. 42-55.

[Sashida and Kenjo, 1993] Toshiiku Sashida and Takashi Kenjo, *An Introduction to Ultrasonic Motors*, Claredon Press, Oxford, 1993.

[Sato and Shikida, 1994] K. Sato and M. Shikida, “An electrostatically actuated gas valve with an S-shaped film element,” *J. Micromech. Microeng.* **4,** 1994, 205-209.

[Schabmueller, Koch, et al., 1999] C. G. J. Schabmueller, M. Koch, , A. G. R. Evans, and A. Brunnschweiler, “Design and Fabrication of a Microfluidic Circuitboard,” J. Micromechanics and Microengineering, **12**, 1999, pp. 176-179.

[Schabmueller, Koch, et al., 2002] C. G. J. Schabmueller, M. Koch, M. E. Mokhtari, A. G. R. Evans, A. Brunnschweiler, and H. Sehr, “Self-Aligning Gas/Liquid Micropump,” J. Micromechanics and Microengineering, **12**, 2002, pp. 420-424.

[Schaible, Vollmer, et al., 2001] J. Schaible, J. Vollmer, R. Zengerle, H. Sandmaier, and T. Strobelt , “Electrostatic Microvalves in Silicon with 2-Way Function for Industrial Applications,” Proc. Transducers 2001, Munich, pp. 928-931.

[Schmidt, 1998] Martin A. Schmidt, “Wafer-to-Wafer Bonding for Microstructure Formation,” Proceedings of the IEEE, Vol. 86, No. 8, August 1998, pp. 1575-1585.

[Schmidt, Holtkamp, et al., 1997] H.-J. Schmidt, F. Holtkamp, and W. Benecke, “Flow Measurement in Micromachined Orifices,” J. Micromech. Microeng., Vol. **7,** 1997, pp. 189–192.

[Sen, Wajerski, et al., 2003] Mihir Sen, Daniel Wajerski, and Mohamed Gad-el-Hak, “A Novel Pump for MEMS Applications,” Department of Aerospace and Mechanical Engineering, University of Notre Dame, unpublished paper, 2003.

[Shih, 1999] C.-L. Shih, *Deposition and Characterization of TiNi Shape Memory Alloy Thin Film for MEMS Annlications*, MS Thesis, Case Western Reserve University, Department of Materials Science and Engineering, 1999.

[Shih and Lai, et al., 2001] Chen-Luen Shih, Bo-Kuai, Harold Kahn, Stephen M. Phillips, and Arthur H. Heuer, "A Robust Co-Sputtering Fabrication Produre for TiNi Shape Memory All oys for MEMS," IEEE J. Microelectromechanical Systems, Vol. 10, No. 1, March 2001, pp. 69-79.

[Shikida, et al., 1993] Shikida, M., Sato, K., Tanaka, S., Kawamura, Y., and Fujisaki, Y., "Electrostatically-Actuated Gas Valve with Large Conductance," Digest of Technical Papers, Transducers'93, Yokohama, Japan, June 7-10, 1993.

[Shinohara, et al., 2000] Jun Shinohara, Masayuki Suda, Kazuyoshi Furuta, Toshihiko Sakuhara, "A High Pressure-Resistance Micropump using Active and Normally-Closed Valves," IEEE, 2000, pp. 86-91.

[Shoji and Esashi, 1994] Shuchi Shoji and Masayoshi Esashi,, "Microflow devices and systems," J. Micromech. Microeng., Vol. 4, 1994, pp. 157-171.

[Skrobanek, et al., 1997] K.D. Skrobanek, M. Kohl, and S. Miyazaki, "Stress-Opimised Shape Memory Microvalves," Proc. 10th IEEE MEMS 1997 Technical Digest, 1997, pp. 256-261.

[Smith, Bower, et al., 1990] Smith, R., Bower, R., and Collins, S., "The Design and Fabrication of a Magnetically Actuated Micromachined Flow Valve," Sensors and Actuators A, Vol. 24, 1990, pp. 47-53.

[Smits, 1985] Smits, J. G., Piezoelectric Pump for Peristaltic Fluid Displacements," Dutch, 1985.

[Smits, 1989] Smits, J. G., Piezoelectric Micropumps with Microvalves," Eighth Biennial University/Government/Industry Symposium, IEEE, 1989.

[Smits, 1990] Smits, J. G., "Piezoelectric Micropump with Three Valves Working Peristaltically," Sensors and Actuators A, 21-23, 1990, pp. 203-206.

[Stark, Mehregany, et al., 1997] K. C. Stark, M. Mehregany, and S. M. Phillips, "Mechanical Coupling and Direct Torque Measurement of Outer-Rotor Polysilicon Micromotors," Proceedings of the 10th IEEE International Workshop on MEMS, MEMS97 digest, pp. 221-226.

[Stehr, Ulrich, et al., 1996] M. Stehr, S. Messner, J. Ulrich, H. Sandmaier, R. Zengerle; A microvalve with bidirectional pump effect; Proc. EUROSENSORS X; 8-11 September 1996; Leuven, Belgium, pp. 845-848

[Stemme and Stemme, 1993], Stemme, G. and E. Stemme, "Valveless Diffuser/Nozzle-Based Fluid Pump," Sensors and Actuators A, 39 (2), 1993, pp. 159-167.

[Stenmark and Lang, 1997] Stenmark, L. and Lang, M., "Micro Propulsion Thrusters and Technologies," Proc. Second European Spacecraft Propulsion Conference, ESTEC, Noordwijk, The Netherlands, ESA SP-398, May 27-29, 1997, pp. 399-405.

[Stenmark, et al., 1997] Stenmark, L., Lang, M., Köhler, J., and Simu, U., "Micro Machined Propulsion Components," Proc. Second Round Table on Micro/Nano Technologies for Space, ESTEC, Noordwijk, The Netherlands, ESA WPP-132, Oct. 15-17, 1997, pp. 69-76.

[Stenmark 1998] Stenmark, L., “Micro Machined Cold Gas Thrusters,” Proc. Workshop on Low Cost Propulsion Technologies for Small Satellites, ESA-ESTEC, Noordwijk, The Netherlands, ESA SP-398, March 19-20, 1998.

[Sung, et al., 1993] K.T. Sung, W.Q. Li, S.H. Li, S.W. Pang, and P.K. Bhattacharya, “Application of High-Quality SiO2 Grown by Multipolar ECR Source to Si/SiGe MISFET,” Electronic Letters, Vol. 29, No. 3, 1993, pp. 277-278.

[Szilard 1974] Szilard , Rudolph.,” Theory and Analysis of Plates”., Prentice Hall INC., Englewood Cliffs, New Jersey, 1974.

[Tay, 2002] Francis Eng Hock Tay, *Microfluidics and BioMEMS Applications*, Microsystems, Vol, 10, Kluwer Academic Publishers, 2002.

[Terry, et al., 1979] Stephen C. Terry, John H. Jerman, and James B. Angell, “A Gas Chromatographic Air Analyzer Fabricated on a Silicon Wafer,” IEEE Transactions on Electron Devices, Vol. Ed-26, No. 12, December 1979, pp. 1880-1886.

[Thielicke and Obermeier, 2000] E. Thielicke and E. Obermeier, “Microactuators and Their Technologies,” Mechatronics 10, 2000, pp. 431 – 455.

[Trah, et al., 1993] H.-P. Trah, H. Baumann, C. Döring, H. Goebel, T. Grauer and M. Mettner, “Micromachined valve with hydraulically actuated membrane subsequent to a thermoelectrically controlled bimorph cantilever,” Sens. Actuators A, Phys., Vol. 39, 1993, pp. 169-176.

[Timoshenko, et al., 1959] S. Timoshenko., S. Woinowsky Krieger., " Theory of Plates and Shells"., Mac Graw Hill, New York, 1959.

[Tiren, et al., 1989] Tiren, J., Tenerz, L., and Hök, B., "A Batch-Fabricated Non-Reverse Valve with Cantilever Beam Manufactured by Micromachining of Silicon," Sensors and Actuators A, Vol. 18, 1989, pp. 389-396.

[Tsao, et al., 1991] T. R. Tsao, R. M. Moroney, B. A. Moroney, B. A. Martin, and R. M. White, Proc. IEEE Ultrasonics Symposium 2, 937 (1991).

[Tipirneni, et al., 2007] N. Tipirneni, V. Adivarahan, G. Simin, and A. Khan, "Silicon Dioxide-Encapsulated High-Voltage AlGaN/GaN HFETs for Power-Switching Applications," IEEE Electron Device Letters, Vol. 28, No. 9, September 2007.

[Toshiyoshi, Fujita, and Ueda, 1995] Hiroshi Toshiyoyuki, Hiroyuki Fujita, and Toshitsugu Ueda, "A Piezoelectrically operated Optical Chopper by Quartz Micromachining," Journal of Microelectromechanical Systems, 4 (1), 1995, pp. 3-9.

[Troitsky 1976] M. S. Troitsky., " Stiffened Plates bending, stability and vibrations"., Elsevier Scientific Publishing Co. 1976

[Ullmann, 1998] Ullmann, A., "The Piezoelectric Valve-Less Pump – Performance Enhancement Analysis," Sensors and Actuators A, 69, 1998, pp. 97-105.

[Ulrich, Stehr, et al., 1996] J. Ulrich, M. Stehr, R. Zengerle; Simulation of a bidirectional pumping microvalve using FEM; Proc. EUROSENSORS X; 8-11 September 1996; Leuven, Belgium, pp. 1241-1244

[van Lintel, et al., 1988] H. T. G. van Lintel, F. C. M. van de Pol, and S. Bouwstra, "A Piezoelectric Micropump Based on Micromachining of Silicon," Sensors and Actuators, Vol. 15, 1988, pp. 153-167.

[van de Pol, et al., 1989] F. C. M. van de Pol, D. G. J. Wonnink, M. Elwenspoek, and J. H. J. Fluitman, "A Thermo-Pneumatic Actuation Principle For A Microminiature Pump and Other Micromechanical Devices," Sensors and Actuators, Vol. 17, 1989, pp. 139-143.

[van de Pol, et al., 1990] F. C. M. van de Pol, H. T. G. van Lintel, M. Elwenspoek, J. H. J. Fluitman, "A Thermopneumatic Micropump Based on Micro-engineering Techniques," Sens. Actuators A21-23, 1990, pp. 198-202.

[van Toor, Lammerink, et al., 1997] M. W. van Toor, T. S. J. Lammerink, J. G. E. Gardeniers, M. Elwenspoek, and D. Monsma, "A Novel Micromechanical Flow Controller," J. Micromech. Microeng., Vol. **7**, 1997, pp. 165-169.

[van der Wijngaart, 2002] Wouter van der Wijngaart, *Designing Microfluidic Control Components*, PhD Dissertation, Microsystem Technology, Department of Signals, Sensors and Systems, Computer Science-Electrical Engineering-Engineering Physics, Royal Institute of Technology, Stockholm, Sweden, 2002.

[van der Wijngaart, et al., 2000] Wouter van der Wijngaart, Helene Andersson, Peter Enoksson, Kjell Noren, and Goran Stemme, "The First self-priming and bi-directional valve-less diffuser micropump for both liquid and gas," Proc. MEMS'00, IEEE, 2000.

[Vandelli, et al., 1998] Nelsimar Vandelli, Donald Wroblewski, Margo Velonis, and Thomas Bifano, "Development of a MEMS Microvalve Array for Fluid Flow Control," J. Microelectromechanical Systems, Vol. 7, No. 4, December 1998, pp. 395-403.

[Verpoorte, Van Der Schoot, et a., 1994] E M J Verpoorte, B H VanDerSchoot, S Jeanneret, A Manz, H M Widmer, N F DeRooij, "Three-dimensional micro flow manifolds for miniaturized chemical analysis systems," *J. Micromech. Microeng.* **4,** 1994**,** 246-256.

[Vinson, 1974] Jack R. Vinson., "Structural mechanics: The Behavior of Plates and Shells"., John Wiley & Sons, New York 1974.

[Waibel, Kohnle, Cernosa, et al., 2003] G. Waibel, J. Kohnle, R. Cernosa, M. Storz, M. Schmitt, H. Ernst, H.Sandmaier, R. Zengerle, T. Strobelt; "Electronic Fountain Pen – A Highly Integrated Stand-Alone Microdosage System," Sensors & Actuators A 103 (2003); pp. 225 - 230

[Wego and Pagel, 2001] Wego, A. and L. Pagel, "A Self-Filling Micropump Based on PCB Technology," Sensors and Actuators A, 88, 2001, pp. 220-226.

[Wenzel and White, 1988] S. W. Wenzel and R. M. White, IEEE Trans. Electron Devices, ED-35, 735 (1988).

[Woias, 2001] Peter Woias, "Micropumps – Summarizing the First Two Decades," Microfluidics and BioMEMS, Proc. Of SPIE, Vol. 4560, 2001, pp. 39-52.

[Xu, Wong, et al., 1999] , B. Xu, K. T. Ooi, T. N. Wong, and C. Y. Liu, "Study on the Viscosity of the Liquid Flowing in Microgeometry," J. Micromechanics and Microengineering, **9**, 1999, pp. 377-384.

[Xu and Choong, et al., 2001] Yuan Xu; Wen On Choong; Francis Eng Hock Tay; Xuan Xiong Zhang; Yen Ping Kong; and Haiqing Gong, Thomas, “Simulations of a Micro Valve and a Micro Pump,” Microfluidics and BioMEMS, Proc. Of SPIE, Vol. 4560, 2001, pp. 53-60.

[Xu, Kong, et al., 2001] Xu, Yuan; Kong, Yen Peng; Zhang, Xuan Xiong; Yao, Kui; Choong, Wen On; Tay, Francis Eng Hock; and Wang, Wen Ping, “Three-Dimensional Simulation of Micro Pumps,” Microfluidics and BioMEMS, Proc. Of SPIE, Vol. 4560, 2001, pp. 61-66.

[Xu, Wang, et al., 2001] Dong Xu, Li Wang, Guifu Ding, Yong Zhou, Aibing Yu, Bingchu Cai, “Characteristics and fabrication of NiTi/Si diaphragm micropump, Sensors and Actuators A Physical, Vol. 93, 2001, pp. 87-92.

[Yanagisawa, et al., 1993] Yanagisawa, K., Kuwano, H., and Tago, A., “An Electromagnetically Driven Microvalve,” Digest of Technical Papers, Transducers ’93, Yokohama, Japan, June 7-10, 1993.

[Yang, et al., 2002] X. Yang, A. Holke, and M. A. Schmidt, “An Electrostatic, On/Off MEMS Valve for Gas Fuel Delivery of a Microengine,” Solid-State Sensor and Actuator Workshop, Hilton Head Island, South Carolina, USA, June 2-6, 2002, pp. 19-22.

[Yang, Lee, et al., 2003] Eui-Hyeok (EH) Yang, Choonsup Lee and Juergen Mueller, “Normally-Closed, leak-Tight Piezoelectric Microvalve under Ultra-High Upstream Pressure for Integrated Micropropulsion, IEEE International Conference on Microelectromechanical Systems (MEMS ’03) Conference, Kyoto, Japan, Jan. 2003, pp. 80-83.

[Yang, et al., 2002] Eui-Hyeok Yang, Nishant Rohatgi, and Larry Wild, “A Piezoelectric Microvalve for Micropropulsion,” AIAA, NanoTech 2002, 9-12 September 2002, Houston, Tx.

[Yang, et al., 1997] Xing Yang, Charles Grosjean, Yu-Chong Tai, and Chih-Ming Ho, "A MEMS Thermopneumatic Silicone Membrane Valve," MEMS'97, Nagoya, Japan, 1997.

[Yang, Grosjean and Tai, 1999] Xing Yang, Charles Grosjean, Yu-Chong Tai, and Chih-Ming Ho, "Design, Fabrication, and Testing of Micromachined Silicone Rubber Membrane Valves," J. Microelectromechanical Systems, Vol. 8, No. 4, Decenber, 1999, pp. 393-402.

[Yu, Mutlu, 2003] Yu, C.; Mutlu, S.; Selvaganapathy, P.; Mastrangelo, C.H.; Svec, F.; Fréchet, J.M.J., "Flow Control Valves for Analytical Microfluidic Chips Without Mechanical Parts Based on Thermally Responsive Monolithic Polymers," Analytical Chemistry, 2003, in press.

[Yuan and Prosperetti, 1999] H. Yuan and A. Prosperetti, "The Pumping Effect of a Growing and Collapsing Bubbles in a Tube," J. Micromechanics and Microengineering, **9**, 1999, pp. 402-413.

[Yun, Cho, et al., 2001] Kwang-Seok Yun.-S., Il-Joo Cho, Jong-Uk Bu, Geun-Ho Kim, Young-Sam Jeon, Chang-Jin (CJ) Kim, and Euisik Yoon, "A Micropump Driven by Continuous Electrowetting Actuation for Low Voltage and Low Power Operations," IEEE, 2001.

[Yuen, et al., 2000] Po Ki Yuen, Larry J. Kricka, and Peter Wilding, "Semi-disposable microvalves for use with microfabricated devices or microchips," J. Micromech. Microeng., Vol. 10, 2000, pp. 401-409.

[Zdebkick and Angell, 1987] Mark J. Zdebkick and J. B. Angell, "A Microminiature Electric-to-Fluid Valve," Transducers'97, 1987.

[Zdebkick, et al., 1994] Mark J. Zdebkick, Rolfe Anderson, Joe Jankowski, Bob Kline-Schoder, Lee Christel, Robin Miles, Walter Weber, "Thermpneumatically actuated microvalves and integrated electro-fluidic circuits," Technical Digest, Solid-State Sensor and Actuator Workshop, Hilton Head, South Carolina, June 13-16, 1994, pp. 251-255.

[Zeng, et al., 2000] Shulin Zeng, Chuan-Hua Chen, James C. Mikkelsen, Jr., and Juan G. Santiago, "Fabrication and Characterization of Electrokinetic Micro Pumps," Sensors and Actuators B, v.79, 2001, pp.107-114, and 2000 Inter Society Conference on Thermal Phenomena," 2000, pp. 31-36.

[Zengerle, et al., 1992] R. Zengerle, A. Richter, and H. Sandmaier, "A Micro Membrane Pump With Electrostatic Actuation," Proc. IEEE MEMS-92, Micro Electro Mechanical Systems '92, Travemunde, Germany, February 4-7, 1992, pp. 19-24.

[Zengerle, et al., 1993] Zengerle, M., M. Richter, F. Brosmger, A. Richter, and H. Sandmaier, Tech,. Digest IEEE Transducers (Yokohama, 1993), p. 106.

[Zengerle and Richter, 1994] Zengerle R and Richter M 1994 Simulation of microfluid systems *J. Micromech. Microeng.* **4**, 1994, 192-204.

[Zengerle, et al., 1995] Zengerle, R., J. Ulrich, et al., "A bidirectional silicon micropump, "Sensors and Actuators A, 50, 1995, pp. 81-86.

[Zengerle, et al., 1995] R. Zengerle, S. Kluge, M. Richter, and A. Richter, "A Bidirectional Silicon Micropump," Proc. IEEE MEMS-95, Amsterdam, The Netherlands, 1995, pp. 19-24.

[Zhao and Liao, 2002] T. S. Zhao and Q. Liao, "Thermal Effects on Electro-Osmotic Pumping of Liquids in Microchannels," J. Micromechanics and Microengineering, **12**, 2002, pp. 962-970.

APPENDIX A

PATTENT LIST MICROPOUMPS

[Cabuz, Eugen I, et al., 2003]., Cabuz, Cleopatra., " Electrostatically actuated pump with elastic restoring forces"., 2002, U.S. Patent No. 20030068231.

[Cabuz, Cleopatra, et al., 2003]., Horning, Robert D., Herb, William R., " Polymer microactuator array with microscopic force and displacement"., 2001., US Patent No. 6,184,608.

[Cabuz, Cleopatra, et al., 2001]., Cabuz, Eugen I.," Electrrostatic actuators for active surfaces".,2002., US Patent No. 6,358,021.

[Cabuz, Cleopatra, et al., 2002]., Cabuz, Eugen I., " Compounded AC driving signal for increased reliability and lifetime in touch mode electrostatic actuators"., 2002, U.S. Patent No. 6,351,054.

[Cabuz, Cleopatra, et al., 2001]., Cabuz, Eugen I.," Electrrostatic/ pneumatic actuators for active surfaces".,2001., US Patent No. 6,288.472.

[Cabuz, Cleopatra, et al., 2001]., Cabuz, Eugen I.," Driving strage for non-paralell array of electrostatic actuators sharing a common electrode"., 2001., US Patent No. 6,184,607.

[Cabuz, Cleopatra, et al., 2001]., Cabuz, Eugen I., " Polymer microactuator array with macroscopy force and displacement"., 2001., US Patent No. 6,184,608.

[Cabuz, Cleopatra, 2000], “ Low cost, high pumping rate electrostatically actuated mesopump”., 2000, US Patent No. 6,106,245.

[Cabuz, Cleopatra, 1999], “ Bucked actuator with enhanced restoring force”., 1999, US Patent No. 5,901,939.

[Cabuz, Cleopatra, 1998], “ Electrostatically actuated mesopump having a plurality of elementary cells”., 1998., US Patent No. 5,836,750.

[Cabuz, Cleopatra, et al., 1998]., Ohnstein , Thomas R., Cabuz, Eugen I., ” Hydrophobic coating for reducing humidity effect in electrostatic actuators”., 1998., US. Patent No. 5,822,170.

[Bossini, Leonardo, 2001]. “ Showerv with nozzles for delivery of atomized jets of water”., 2001., US Patent No. 6,328,228.

[Laumann, Jr., et al., 1990[., Carl ,W.., “ Micro miniature implantable pump”., 1990., US Patent No. 4,911,616.

[Mercer, Mark J., “ Reference voltage circuit”., 2001., US Patent No. 6,215,291.

[Herb, William R., et al , 2001], Zook, J. David., Cabuz, Cleopatra., “ Dual; diaphragm, single chamber mesopump”., 2001, US Patent No. 6,179,586.

[Najafi, et al., 2003], Kim Hanseups S., Bernal, Luios P., astle, Aaron A., Washabaugh, Peter D., ”Micropump assembly for a microgas chromatograph and the like”., 2003. U.S. Patent No. 20030231967.

[Ohnstein, et al., 2001]., Cabuz, Eugen I., “ Addressable valve array for proportional pressure or flow ontrol”.,2001., US Patent No. 6,2408944

[Quenzer, Hans Joachim, et al., 2001]., Wagner, Bernd., " Bistable microactuator with coupled membranes

[Richter, Axel.,et al., 1993]., Sandmeier, Herrmann., " Microminiaturtized electrostically pump"., 1998., US Patent No. 5,180,288.

[Zengerle, Roland., et al., 1996], " Micro-miniaturized, electrostatically driven diaphragm micropump"., 1996, US Patent No. 5,529,465.